

The Impact of Selected Environmental Severity Factors on Paint Scribe Creep, Polymer
Degradation and Corrosion of Epoxy Coated 1018 Steel

A Dissertation

Presented to
the faculty of the School of Engineering and Applied Science
University of Virginia

in partial fulfillment
of the requirements for the degree

Doctor of Philosophy

by

Merrill L. Tayler

May

2014

APPROVAL SHEET

The dissertation
is submitted in partial fulfillment of the requirements
for the degree of
Doctor of Philosophy

AUTHOR

The dissertation has been read and approved by the examining committee:

John R. Scully

Advisor

Robert G. Kelly

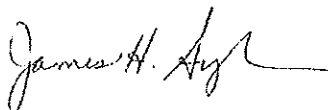
Elizabeth J. Opila

James M. Fitz-Gerald

Larry G. Richards

James W. Rawlins

Accepted for the School of Engineering and Applied Science:



Dean, School of Engineering and Applied Science

May

2014

Abstract

The discrepancy between lab accelerated life tests (LALTs) and field exposures of organically coated aerospace alloys subjected to corrosion is a well-known problem. For example, some Mg-based chromate-free primers for AA2024-T351 perform well in field corrosion testing but perform poorly in LALTs such as the ASTM B-117. Conversely, some primer coatings on metals have been found to perform well from a corrosion standpoint in LALTs but poorly in the field. Currently, it is not well understood whether various differences in environmental severity factors (ESFs), such as chloride and UV, cause such discrepancies. A lack of understanding of how ESFs affect the coating/substrate system is a consequence of previous studies' reliance on low fidelity interrogation methods, such as visual inspection and coating gloss measurements, which do not adequately capture the entire range of interactions between ESFs, the coating and the substrate. Subsequent LALTs are developed by trial and error. This research seeks to take the first steps to understand the influence of selected specific ESFs on metal corrosion and polymer degradation in scribe creep.

To begin to understand the influence of environmental severity factors on underpaint corrosion, we compare the similarities and differences in corrosion and scribe creep results from standard LALTs, field sites and lab full immersion tests (FIT). Ultra-high molecular weight epoxy resin (Poly(Bisphenol A-co-epichlorohydrin) glycidyl end-capped ($\text{C}_{18}\text{H}_{22}\text{O}_3$) $_n$ • $\text{C}_{22}\text{H}_{26}\text{O}_4$; CAS No. 25036-25-3, trade name Eponol) coated AISI 1018 steel samples (UNS# G10180; 0.15% C, 0.7% Mn, Fe; wt. %), with controlled scribes to expose the bare metal, were used in all tasks. In this initial investigation, comparisons between

standard LALTs, FITs and field exposures were made using a suite of high-level surveillance methods: electrochemical impedance spectroscopy (EIS), Fourier Transform Infrared Spectroscopy (FTIR), X-Ray diffraction (XRD), and Raman spectroscopy. These methods maximize the ability to detect corrosive degradation both to the bare substrate at the scribe and to the substrate under the coating, as well as improve detection of degradation of the coating itself. By elucidating corrosive changes at a high level that could be missed with low fidelity surveillance techniques, these methods also improve our ability to make comparisons between LALT, FIT and field tests, and demonstrated a methodological improvement upon previous studies. Tests were conducted according to the LALT standards and were interrogated at predetermined time points (i.e., 0, 1, 3, 5, 10 and 15 days) during a total exposure time of 15 days. Briefly, results from this work demonstrate that there is a positive correlation between mass loss on bare 1018 steel samples and scribe creep length on coated steel for both lab- and field- exposed samples. Additionally, there is an inverse correlation between scribe creep length and the low frequency electrochemical impedance of the coating for coated steel near the scribe for lab and field samples. Concerning field vs. LALTs, the results demonstrate that LALT's without UV radiation do not correlate as well with field exposure in terms of polymer coating degradation. This points to the need for UV radiation to damage the polymer coating. Comparison of LALT results to full immersion tests (FITs) helped to clarify the mechanism of scribe creep in these lab and field exposures.

LALT, FIT and field comparisons demonstrate that while the effects of ESFs on the corrosion of bare steel are straightforward, their effects on the scribe creep of coated steel are more complex. Therefore, systematic variation of ESFs in non-standard LALTs and statistical

analysis of the resulting data were conducted to better understand the effects of ESFs on scribe creep of ultra-high molecular weight epoxy resin coated AISI 1018 steel. The role of ESFs in scribe line corrosion and corrosion of “intact” organic coatings was studied using 3D optical microscopy, EIS, XRD and Raman microscopy while parallel studies at the University of Southern Mississippi examined coating degradation with FTIR. Samples were exposed to various levels of ESFs in a set non-standard LALTs, in a fractional factorial design. The effect of UV light, temperature, relative humidity, chloride, and wet/dry cycling on underpaint corrosion and degradation of electrical properties of organic coatings were investigated using the high-level surveillance methods noted previously. Differences in corrosion morphology, corrosion products formed, and rates of scribe creep were examined as a function of ESFs with the objective to produce a parametric model that could relate scribe creep length to ESFs. It was found that temperature and cycling had the largest effect on scribe creep. Temperature and cycling in combination interacted to produce an effect on scribe creep that was greater than the additive effects of each.

Finally, the data from the non-standard LALTs was used to develop an empirical model of scribe creep of Eponol coated 1018 steel. This is the first empirical model to relate scribe creep to ESFs for an organically coated steel system known to the author, similar to those constructed in the past for bare steel. The model assesses the relative strength of individual and combined ESFs on scribe creep of coated steel. The model found that cycling had the biggest effect on scribe creep. The model also indicated the possible interaction between temperature and cycling. Field behavior was subsequently predicted using the model. By highlighting which ESFs most greatly impact scribe creep, the model provides guidelines for creating future LALTs that better mimic important aspects of the field environment. The

model also serves as a template for creating scribe creep models for other commonly used coating schemes. Finally, the model highlights ESF interactions that should be further investigated in future research.

Overall, this body of work adds to the understanding of the effects of ESFs on scribe creep and the relationship between anodic wedging and cathodic delamination on scribe creep. This work also demonstrates the applicability of fractional factorial design for quickly and efficiently investigating multiple ESFs in relatively few experiments. Insights gained can be used in the construction of future LALTs.

Acknowledgements

The first paragraph goes to my adviser, John Scully, for all of his help and support. He always pushed me a little farther than I thought I could go which expanded both my abilities and my confidence. His willingness to let me take the work in my own direction when I thought it best allowed me to grow as a researcher. I know he truly cared about me as a researcher, but more importantly, care about me as a person, as a husband and as a father. Thanks John.

Thank you to my committee for all of their help and support. Dr. Elizabeth Opila whose questions and advice helped me to make a thesis that was readable to non “scribe creepers” and helped me to clarify my ideas. Dr. James Rawlins at the University of Southern Mississippi whose support in coatings from selection to analysis was a huge part of my work and was essential to my thesis. Dr. Rob Kelly whose door was always open for discussion and who challenged me at every step. Dr. Jim Fitz-Gerald who chaired my committee (and two others that same week) and advised the characterization work. Finally, Dr. Larry Richards who not only advised me on statistics but also introduced me to the American Society of Engineering Education and ended up being one of the largest influences in my academic life at UVa.

Thanks also to everyone in CESE. Being in such a great research center made life better. Everyone made themselves available to answer questions and help me when I needed it.

The camaraderie of all the students is what makes CESE such a great place to work.

Everyone in CESE helped me in some way.

Jay Srinivasan gets his own paragraph. He was a great person to have in the office to bounce ideas off of, give advice or to just have intelligent conversations about any topic imaginable. His gift to and traditional Hindu blessing of Leif was extremely touching for us. Leif will always remember his Uncle Jay.

Other important CESEers are: Eric Schindleholtz for conversations both technical and not, Amber Lass, Greg Pioszak and Marcel Mibus for letting me bother them constantly in their office (thanks for the Squirt, Amber), previous officemates Mara Shedd and Katie Fleming for keeping me sane and making the office a great place to be, Andrew King who was the most knowledgeable and helpful person in the lab, Arwen Wilson who loved to commiserate about the annoyances of graduate life, Sam Madden and Rebecca Schaller for being fun to hang out with, Hung Ha for being immensely helpful and also the nicest person I've ever met, and Mary Lyn Lim, maraming salamat sa lahat, kaibigan ko. Hanggang sa muling pagkikita.

Thanks to all those that helped do all the little things like purchase orders and paperwork that made this possible: Shelley Mendez, Kim Fitzhugh-Higgins, Susan Bagby, Frances Cruz, Jeannie Reese and Eric Newsome. Thanks also to Richard White for putting up with me never signing in to use the scopes and Rusty Wright for keeping everything running and helping to modify my exposure chambers

Barry Baber, the amazing building manager, needs special recognition. In addition to helping me set up my chambers and keeping the labs running and having intelligent discussions on topics from research to married life, it was Barry who, after the fire, got the lab and my equipment back up and running in record time. I would not have been able to graduate this May without all of the work that he did. Thanks, Barry.

Our friends outside the academic sphere were a huge support for me and my family. Calvin and Sara Simmons for camping and spontaneity, Heather and George Glass for all the help with the newborn, and Doug and Lindsey Sorensen, Chris and Rachel Bailey, Dr. Michael Shirts and Natalie Brown and Paul and Charlotte Baker (and Thomplekins) for being great friends. Ben Abruzzo and Hetal Kapadia were not only great friends, but were supportive and great to commiserate with and always made us laugh. Brian and Stacy Wotring deserve special recognition for being great friends and also letting us crash at their place at the beach. Some of the best times in Charlottesville were shooting hoops with Brian and shooting other people when we were a roving two man paintball wrecking machine.

My family was a huge support for me during my entire academic career, both family by blood and by marriage. I had my first fried turkey and first crawfish boil with the Kuss family. Those Cajuns sure know how to cook. I was given nothing but support and encouragement from the Kuss clan through everything I went through. Special thanks to Mr. Brad and Miss Kathy.

My mom and dad have been amazing parents and so supportive of my academic goals and choices even when they took me to the other side of the country. Thanks to my mom for

being there whenever I needed her. She was always happy to talk for hours. Thanks to my dad for his advice and help, and also for being an inspiration for me. I wouldn't have even thought about getting a Ph.D. when I was younger if it weren't for him. I love you both.

My brand new son, Leif, deserves his own paragraph. You didn't help with anything, in fact you probably made things harder as you are just two months old as I finish this. But, coming home to you, crying or happy, always made me remember what was most important in life. You reminded me that as important as this degree is to me, it means nothing compared to you. I love you.

Lastly, and probably most importantly, thanks to my wife Kaycie. I could not have done this without her. She helped me every step of the way from application to dissertation. She is also an amazing cook who kept me well fed, and an amazing wife who kept my spirits up. She did all this while getting a Ph.D. of her own (we are now the Dr.'s Tayler!). She also has been the best mother to my little son that I could ever hope for. I love you more than anything.

Table of Contents

Abstract.....	i
Acknowledgements.....	v
Table of Contents	ix
Table of Figures	xv
Table of Tables.....	xxxviii
List of Symbols.....	xli
List of Iron Compounds.....	xliv
1 Chapter 1 – Introduction.....	1
1.1 Summary	1
1.2 Background:.....	1
1.2.1 Necessary Development of LALTs for New Coating Systems	1
1.2.2 Current Approaches to LALT Design	3
1.2.3 Drawbacks to Current LALT Design Methods.....	8
1.2.4 Use of Models in Atmospheric Corrosion	13
1.3 Scribe Creep Mechanisms for Steel.....	15
1.4 Influence of Environmental Severity Factors on Scribe Creep and Bare Steel	
Corrosion.....	18
1.4.1 Temperature	19
1.4.2 pH	21
1.4.3 UV Radiation	23
1.4.4 Ozone	26

1.4.5	Chloride.....	30
1.4.6	Relative Humidity and Time of Wetness.....	33
1.4.7	Wet/Dry Cycling.....	37
1.5	Overall Critical Unresolved Issues.....	39
1.6	Overall Problem Statement.....	41
1.7	Overall Objective.....	42
1.8	General Approach.....	43
1.8.1	A “Bottom Up” Approach.....	43
1.9	Thesis Organization.....	60
1.10	References	61
2	Chapter 2 – Comparison of Scribe Creep and Underpaint Corrosion on Eponol Coated 1018 Steel in Field Exposures vs. LALTs.....	68
2.1	Summary of Chapter 2.....	68
2.2	Background – The Need to Understand the Roles of ESFs in Underpaint Corrosion 69	
2.3	Objective.....	74
2.4	Experimental Methods	74
2.4.1	Materials.....	74
2.4.2	Sample Preparation Procedure.....	75
2.4.3	High Level Surveillance Testing Methods.....	76
2.4.4	Sample Exposure Conditions	81
2.5	Results.....	85
2.5.1	Mass Loss of Uncoated Steel.....	85

2.5.2	Corrosion Product Analysis.....	86
2.5.3	Scribe Creep Behavior	96
2.5.4	Coating Analysis	125
2.6	Discussion.....	134
2.6.1	Environmental Severity Factors	134
2.6.2	Correlation of Mass Loss with Scribe Creep	137
2.6.3	Corrosion Product Analysis.....	139
2.6.4	Scribe Creep Behavior of Coated Steel.....	141
2.6.5	Coating Degradation During Exposure	143
2.6.6	Anodic Wedging vs. Cathodic Delamination as a Main Factor in Scribe Creep 144	
2.6.7	LALTs that Simulate Field Tests	146
2.7	Conclusions	147
2.8	References	150
3	Chapter 3 – Isolation and Systematic Analysis of Corrosion Factors in LALTs.....	155
3.1	Summary of Chapter 3.....	155
3.2	Background.....	156
3.2.1	Isolation of Corrosion Factors	156
3.2.2	ESF Level Selection.....	158
3.2.3	Theory of Factorial Design.....	166
3.3	Objective.....	169
3.4	Experimental Methods	169
3.4.1	Materials.....	169

3.4.2	Sample Preparation	170
3.4.3	High-Level Surveillance Testing Methods	171
3.4.4	Sample Exposure Conditions	175
3.5	Results.....	182
3.5.1	Mass Loss of Bare Steel.....	182
3.5.2	Corrosion Product Analysis.....	183
3.5.3	Scribe Creep Behavior	190
3.5.4	Coating Analysis	210
3.6	Discussion.....	220
3.6.1	Corrosion Product Analysis.....	220
3.6.2	Correlation of Mass Loss and Scribe Creep.....	221
3.6.3	Scribe Creep Behavior of Coated Steel.....	226
3.6.4	Coating Degradation.....	226
3.6.5	Anodic Wedging vs. Cathodic Delamination as a Main Factor in Scribe Creep 228	
3.6.6	The Need for Statistical Analysis	229
3.7	Conclusions	230
3.8	References	231
4	Chapter 4–Construction of an Empirical Scribe Creep Model as a Function of ESFs for Eponol Coated 1018 Steel	234
4.1	Summary of Chapter 4.....	234
4.2	Background.....	235
4.2.1	The Need for a Scribe Creep Model.....	235

4.2.2	Theory of Linear Regression	237
4.3	Objective.....	244
4.4	Experimental Methods	245
4.5	Results.....	245
4.5.1	Mass Loss Model Results	245
4.5.2	Scribe Creep Model Results	254
4.6	Discussion.....	264
4.6.1	Mass Loss Model.....	264
4.6.2	Scribe Creep Model	266
4.7	Conclusions	269
4.8	References	270
5	Chapter 5 – Summary and Future Work.....	272
5.1	Summary	272
5.1.1	Comparison of Standard LALTs, FITs and Field Sites	273
5.1.2	Systematic Analysis of the Roles of ESFs in Scribe Creep	275
5.1.3	Statistical Analysis and Modeling of Mass Loss of Bare Steel and Scribe Creep of Coated Steel	277
5.2	Future Work	278
5.3	Significance	281
5.4	References	283
6	Appendix A - Scribe Creep and Underpaint Corrosion on Eponol Coated AA2024-T3	284
6.1	Summary of Appendix A.....	284

6.2	Background.....	284
6.2.1	Mechanism of Scribe Creep on Coated Aluminum	284
6.3	Objective.....	287
6.4	Experimental Methods	287
6.4.1	Sample Preparation	287
6.4.2	High-Level Surveillance Testing Methods	289
6.4.3	Sample Exposure Conditions	294
6.5	Results.....	297
6.5.1	Scribe Creep Analysis.....	297
6.5.2	Pitting Analysis	304
6.5.3	Corrosion Analysis by SEM and EDS.....	313
6.5.4	Coating Analysis	319
6.6	Discussion.....	338
6.6.1	Visual Analysis	338
6.6.2	EIS Analysis.....	339
6.6.3	Importance of UV	339
6.6.4	Role of Chloride	341
6.6.5	Analysis of Corrosion on Bare AA2024-T351	342
6.7	Conclusions	343
6.8	References	344

Table of Figures

Figure 1.1 Correlation plot showing the values of scribe creep of phosphated and galvanized cold-rolled steel coated with an automotive primer and a clear topcoat for 5 year on vehicle field tests compared with 80 cycles of SAE J2334. For this plot, $R^2=0.98$ and $C=0.97$. ¹⁴ See Table 1 for explanation of R^2 and C .	8
Figure 1.2 Low-Frequency Impedance Modulus as a function of UV irradiation time for galvanized and polyester-coated steel. ¹⁸	10
Figure 1.3 Schematic of cathodic disbondment and corrosion product wedging on organically coated steel. ³² Reprinted with permission from D.A. Jones, Principles and Prevention of Corrosion. 2nd ed. 1996: Prentice Hall. Copyright 2014 Pearson Educational.	16
Figure 1.4 Optical micrograph showing the structure of a growing filament on an epoxy coated 1045 carbon steel. ³⁵ A distinct transition region between the head and the tail can be seen with a noticeable V-shape. This may be a $\text{Fe}(\text{OH})_3$ membrane.	18
Figure 1.5 Graph showing the effects of temperature and sulfur dioxide on the corrosion rate of bare mild steel. ³⁸ Reprinted with permission from P.J. Sereda, <i>Atmospheric factors affecting the corrosion of steel</i> . Industrial & Engineering Chemistry, 1960. 52(2): p. 157-160. Copyright 2014 American Chemical Society.	20
Figure 1.6 Pourbaix diagram for iron. ⁴³	21
Figure 1.7 Graph of the effect of corrosion rate of bare iron as a function of pH. ⁴⁴	22
Figure 1.8 Graph of the effect of UV light ($\lambda=340$ nm) on the corrosion of bare 1010 steel at various salt loading densities with and without ozone.	24

Figure 1.9 The pore resistance for polyester resin-coated galvanized and phosphated steel as a function of time. Three different UV irradiation times are shown. The samples were immersed in 5% sodium chloride solution. ⁵⁷	26
Figure 1.10 Graph of the corrosion rate of bare 1010 steel at various relative humidities and salt loading densities for three ozone levels. The colored lines across the graph show the corrosion rates of bare steel at Kennedy Space Center and in the ASTM B-117. Figure adapted from ⁵⁵	27
Figure 1.11 Graph showing the relative material loss of pure aluminum exposed to different pollutant gases (left), and a table showing the pH of the surface water films produced in each exposure environment (right) after 4 weeks of exposure. ⁶¹	29
Figure 1.12 Concentration of NaCl in water droplets as a function of %RH. Values predicted using OLI software. ⁷⁰	31
Figure 1.13 The effect of chloride deposition rate on mild steel corrosion rate in atmospheric exposure. ²⁹ The authors combined data from many literature sources.....	31
Figure 1.14 Plot showing the correlation of delamination rates of polybutadiene coatings on steel with the diffusion coefficient of the electrolyte in solution. ⁷⁷	33
Figure 1.15 Graph of mass change of a sodium chloride particle with respect to relative humidity. The deliquescence point is 75% RH and the efflorescence point is 43% RH. ⁸⁵	35
Figure 1.16 A Campbell Scientific 237L leaf wetness sensor.	36
Figure 1.17 Images of a scratch on the surface of a 1018 steel sample. The left image shows the bare surface before the clear coating was applied. The right image shows the same sample after it has been coated with a clear epoxy coating. Images taken with a confocal laser scanning microscope using a HeNe laser ($\lambda = 542 \text{ nm}$).....	46

Figure 1.18 Schematic showing locations where EIS was performed on coated and scribed samples.	48
Figure 1.19 Molecular structure of the ultra-high molecular weight epoxy resin used as a coating in this study.....	49
Figure 1.20 Schematic of coated and scribed 1018 steel sample.	50
Figure 1.21 Schematic of Eponol coated and scribed 1018 steel sample. The substrate is roughly 1 mm thick and the Eponol topcoat is $30\pm5\text{ }\mu\text{m}$. The scribe line is $150\pm50\text{ }\mu\text{m}$ in width.	50
Figure 1.22 Spectrum of the lamps used in the QUV™ and salt spray chamber compared to natural sunlight. ¹⁰¹ Image reprinted with permission of Q-Lab Corporation, copyright 2014 (www.q-lab.com).	51
Figure 1.23 Mass loss data for standard LALTs plotted against Equation 1.16. Each curve for Equation 1.16 uses as inputs the same environmental parameters as the standard LALT it is plotted against. Results demonstrate strong agreement between the model and the LALTs.	55
Figure 2.1 Schematic of coated and scribed 1018 steel sample.	76
Figure 2.2 Schematic of Eponol coated and scribed 1018 steel sample. The substrate is roughly 1 mm thick and the Eponol topcoat is $30\pm5\text{ }\mu\text{m}$. The scribe line is $150\pm50\text{ }\mu\text{m}$ in width.	76
Figure 2.3 Graph of mass loss versus exposure time for bare 1018 steel in various environments. Error bars represent standard error for environments with multiple exposures.	86

Figure 2.4 XRD spectra for all standard LALTs, field sites and standard powders for iron based corrosion products. No results are shown for FIT at -1 V because only iron peaks were detected.....	88
Figure 2.5 XRD spectra of standard powders individually (iron III hydroxide α and γ phase) compared to a 50/50 by weight mix of the two powders. Iron III hydroxide γ phase peaks at 9, 28 and 47 degrees appear to be greatly reduced in intensity in the mix relative to the pure powder.....	89
Figure 2.6 XRD spectra of standard powders individually (iron (II) oxide and iron (III) oxide) compared to a 50/50 by volume mix of the two powders.	89
Figure 2.7 Experimental Raman spectra for standard powders.....	91
Figure 2.8 Raman spectra for bare 1018 steel exposed at KSC for 6 weeks. “exp” indicates experimental spectra, “std” indicates standard powder spectra, “lit” indicates spectra from literature.....	92
Figure 2.9 Raman spectra for bare 1018 steel exposed at BRD for 9 months. “exp” indicates experimental spectra, “std” indicates standard powder spectra.....	92
Figure 2.10 Raman spectra for bare 1018 steel exposed in ASTM B-117 for 15 days. “exp” indicates experimental spectra, “std” indicates standard powder spectra.	93
Figure 2.11 Raman spectra for bare 1018 steel samples exposed in ASTM G-85 Annex 5 for 15 days. “exp” indicates experimental spectra, “std” indicates standard powder spectra....	93
Figure 2.12 Raman spectrum for bare 1018 steel exposed in ASTM G-85 Annex 5+UV for 15 days. “exp” indicates experimental spectra, “std” indicates standard powder spectra.....	94
Figure 2.13 Raman Spectra for bare 1018 steel exposed in FIT at OCP for 15 days. “exp” indicates experimental spectra, “std” indicates standard powder spectra.....	94

Figure 2.14 Optical images of the progression of scribe creep for Eponol coated steel exposed at KSC as a function of exposure time. Scale bars show 3000 μm	97
Figure 2.15 Optical images of the progression of scribe creep for Eponol coated steel exposed at BRD as a function of exposure time. Scale bars show 3000 μm	98
Figure 2.16 Optical images of the progression of scribe creep for Eponol coated steel exposed in ASTM B-117 as a function of exposure time. Scale bars show 3000 μm	99
Figure 2.17 Optical images of the progression of scribe creep for Eponol coated steel exposed in ASTM G-85 Annex 5 as a function of exposure time. Scale bars show 3000 μm	100
Figure 2.18 Optical images of the progression of scribe creep for Eponol coated steel exposed in ASTM G-85 Annex 5+UV as a function of exposure time. Scale bars show 3000 μm	100
Figure 2.19 Optical images of the progression of scribe creep for Eponol coated steel exposed in ASTM G-85 Annex 3 as a function of exposure time. Scale bars show 3000 μm	101
Figure 2.20 Optical images of the progression of scribe creep for Eponol coated steel exposed in full immersion test in 0.3 wt% NaCl solution held at -1 V vs. SCE as a function of exposure time. Scale bars show 3000 μm	102
Figure 2.21 Optical images of the progression of scribe creep for Eponol coated steel exposed in full immersion test in 0.3 wt% NaCl solution held at OCP as a function of exposure time. Scale bars show 3000 μm	103
Figure 2.22 Optical images of the progression of scribe creep for Eponol coated steel exposed in full immersion test in 5% NaCl solution held at OCP as a function of exposure time. Scale bars show 3000 μm	103

Figure 2.23 Optical images of the progression of scribe creep for Eponol coated steel exposed in ASTM D-5894 as a function of exposure time. Scale bars show 3000 μm	104
Figure 2.24 Plot of average scribe creep length vs. time for coated 1018 steel exposed to various LALT, field and full immersion environments. Error bars show standard error. ..	105
Figure 2.25 3D images of the scribe on epoxy resin coated 1018 steel exposed at KSC for 8 weeks. The units of the images are micrometers. Dashed lines show the location of the scribe.....	107
Figure 2.26 Selected line profiles for Eponol coated steel exposed at KSC. Vertical offset for data from each day reported is 50 μm . Dashed lines indicate original scribe location.....	108
Figure 2.27 3D images of the scribe on epoxy resin coated 1018 steel exposed at BRD for 8 weeks. The units of the images are micrometers. Dashed lines show the location of the scribe.....	109
Figure 2.28 Selected line profiles for Eponol coated steel exposed at BRD. Vertical offset for data from each day reported is 30 μm . Dashed lines indicate original scribe location.....	110
Figure 2.29 3D images of the scribe on epoxy resin coated 1018 steel exposed to ASTM B-117 for 15 days. The units of the images are micrometers. Dashed lines show the location of the scribe.....	111
Figure 2.30 Selected line profiles for Eponol coated steel exposed in ASTM B-117. Vertical offset for data from each day reported is 40 μm . Dashed lines indicate original scribe location.....	112
Figure 2.31 3D images of the scribe on epoxy resin coated 1018 steel exposed to ASTM G-85 Annex 5 for 15 days. The units of the images are micrometers. Dashed lines show the location of the scribe.	113

Figure 2.32 Selected line profiles for Eponol coated steel exposed in ASTM G-85 Annex 5. Vertical offset for data from each day reported is 20 μm . Dashed lines indicate original scribe location.....	114
Figure 2.33 3D images of the scribe on epoxy resin coated 1018 steel exposed to ASTM G-85 Annex 5+UV for 15 days. The units of the images are micrometers. Dashed lines show the location of the scribe.	115
Figure 2.34 Selected line profiles for Eponol coated steel exposed in ASTM G-85 Annex 5+UV. Vertical offset for data from each day reported is 20 μm . Dashed lines indicate original scribe location.....	116
Figure 2.35 3D images of the scribe on epoxy resin coated 1018 steel exposed to ASTM G-85 Annex 3 for 15 days. The units of the images are micrometers. Dashed lines show the location of the scribe.	117
Figure 2.36 Selected line profiles for Eponol coated steel exposed in ASTM G-85 Annex 3. Vertical offset for data from each day reported is 60 μm . Dashed lines indicate original scribe location.....	118
Figure 2.37 3D images of the scribe on epoxy resin coated 1018 steel exposed in full immersion in aerated 0.3 wt% NaCl solution at 25°C held at -1 V vs. SCE as a function of exposure time. The units of the images are micrometers. Dashed lines show the location of the scribe.....	119
Figure 2.38 Selected line profiles for Eponol coated steel exposed in full immersion test in 0.3 wt% NaCl solution held at -1 V vs. SCE. Vertical offset for data from each day reported is 10 μm . Dashed lines indicate original scribe location.	120
Figure 2.39 3D images of the scribe on epoxy resin coated 1018 steel exposed in full immersion in aerated 0.3 wt% NaCl solution at 25°C held at OCP as a function of exposure	

time. The units of the images are micrometers. Dashed lines show the location of the scribe.	
.....	121
Figure 2.40 Selected line profiles for Eponol coated steel exposed in full immersion test in 0.3 wt% NaCl solution held at OCP. Vertical offset for data from each day reported is 100 μm . Dashed lines indicate original scribe location.	122
Figure 2.41 3D images of the scribe on epoxy resin coated 1018 steel exposed in full immersion in aerated 5% NaCl solution at 25°C held at OCP as a function of exposure time. The units of the images are micrometers. Dashed lines show the location of the scribe.	123
Figure 2.42 Selected line profiles for Eponol coated steel exposed in full immersion test in 5% NaCl solution held at OCP. Vertical offset for data from each day reported is 100 μm . Dashed lines indicate original scribe location.	124
Figure 2.43 Raw EIS data from samples exposed at KSC. Data were taken from the near location (left) and far location (right).	126
Figure 2.44 Raw EIS data for samples exposed at BRD. Data were taken from the near location (left) and far location (right).	127
Figure 2.45 Raw EIS data from samples exposed in ASTM B-117. Data were taken from the near location (left) and far location (right).	127
Figure 2.46 Raw EIS data from exposed in ASTM G-85 Annex 5. Data were taken from the near location (left) and far location (right).	128
Figure 2.47 Raw EIS data from samples exposed in ASTM G-85 Annex 5+UV. Data were taken from the near location (left) and far location (right).	128
Figure 2.48 Raw EIS data from samples exposed in ASTM G-85 Annex 3. Data were taken from the near location (left) and far location (right).	129

Figure 2.49 Raw EIS data from samples exposed in full immersion at OCP in aerated 0.3 wt% NaCl solution at 25°C. Data were taken from the near location (left) and far location (right).	129
Figure 2.50 Raw EIS data from samples exposed in full immersion at OCP in aerated 5% NaCl solution at 25°C. Data were taken from the near location (left) and far location (right).	130
Figure 2.51 Raw EIS data from samples exposed in full immersion at -1 V vs. SCE in aerated 0.3 wt% NaCl solution at 25°C. Data were taken from the near location (left) and far location (right).....	130
Figure 2.52 Normalized low frequency impedance values over time for Eponol coated steel samples exposed in various standard LALTs. EIS readings taken at near location. Normalization was $ Z_{0.01} (\text{day})/ Z_{0.01} (\text{initial})$ for all days of the test. Time for KSC and BRD are shown on the top axis.....	131
Figure 2.53 Normalized low frequency impedance values over time for Eponol coated steel samples exposed in various standard LALTs. EIS readings taken at far location. Normalization was $ Z_{0.01} (\text{day})/ Z_{0.01} (\text{initial})$ for all days of the test.	132
Figure 2.54 FTIR spectra of Eponol films exposed in ASTM B-117 and G-85 A5 for 15 days. Data taken at UVa.	133
Figure 2.55 FTIR spectra of Eponol films exposed in various conditions. Data taken at USM.	134
Figure 2.56 Correlation chart showing a positive correlation between mass loss and scribe creep. Exposure conditions are labeled. Equation for fit line and R^2 value are given. Error bars represent standard error. Values for KSC are at 6 weeks, while values for LALTs are at 10 days. *interpolated value.	138

Figure 2.57 Bar graph showing positive correlation and similarity of rank order between mass loss and scribe creep for 1018 steel after 10 days of exposure in various environments. Values for KSC are at 6 weeks, while values for LALTs are at 10 days.	
*interpolated value.	139
Figure 2.58 Schematic of underpaint corrosion and scribe creep processes on Eponol coated 1018 steel. Diagram adapted from. ⁵⁶	147
Figure 3.1 Mass loss data for standard LALTs plotted against Equation 3.1. Each curve for Equation 3.1 uses the same environmental parameters as the standard LALT (listed in Table 3.4) it is plotted against. Results demonstrate strong agreement between the model and the LALTs.	162
Figure 3.2 Mass loss of bare steel for the first four conditions in the fractional factorial test matrix.	165
Figure 3.3 FTIR spectra for Eponol coated polypropylene samples unexposed and exposed in 500 ppb ozone for 15 days.	166
Figure 3.4 Chart of relative humidity during one day for high and low cycling for a mean relative humidity of 70%.	179
Figure 3.5 Graph of mass loss versus time for bare 1018 steel exposed in various FFA environments (Table 3.9). The error bars shown above the data are the standard error from mass loss results for ASTM G-85 Annex 5.	183
Figure 3.6 XRD spectra for standard powders and all FFA experiments. Vertical lines indicate peaks for α -FeOOH (blue) and γ -FeOOH (red).....	184
Figure 3.7 Experimental Raman spectra for standard powders.....	185

Figure 3.8 Raman spectra for bare 1018 steel exposed in FFA1 for 15 days. “exp” indicates experimental spectra from this study, “std” indicates standard powder spectra from this study. Conditions: T(-), %RH(+), Cl(-), UV(+), Cycling(-).....	186
Figure 3.9 Raman spectra for bare 1018 steel exposed in FFA2 for 15 days. “exp” indicates experimental spectra from this study, “std” indicates standard powder spectra from this study, “lit” indicates spectra from literature. Conditions: T(-), %RH(-), Cl(+), UV(+), Cycling(-).....	186
Figure 3.10 Raman spectra for bare steel exposed in FFA3 for 15 days. “exp” indicates experimental spectra from this study, “std” indicates standard powder spectra from this study, “lit” indicates spectra from literature. Conditions: T(+), %RH(+), Cl(+), UV(-), Cycling(-).....	187
Figure 3.11 Raman spectra bare steel exposed in FFA4 for 15 days. “exp” indicates experimental spectra from this study, “std” indicates standard powder spectra from this study. Conditions: T(+), %RH(-), Cl(+), UV(-), Cycling(+)......	187
Figure 3.12 Raman spectra bare steel exposed in FFA5 for 15 days. “exp” indicates experimental spectra from this study, “std” indicates standard powder spectra from this study, “lit” indicates spectra from literature. T(-), %RH(-), Cl(+), UV(-), Cycling(+)......	188
Figure 3.13 Raman spectra bare steel exposed in FFA6 for 15 days. “exp” indicates experimental spectra from this study, “std” indicates standard powder spectra from this study. Conditions: T(+), %RH(+), Cl(-), UV(+), Cycling(+)......	188
Figure 3.14 Optical images of the progression of scribe creep for Eponol coated steel exposed in FFA1 for 15 days. Conditions: T(-), %RH(+), Cl(-), UV(+), Cycling(-)......	190
Figure 3.15 Optical images of the progression of scribe creep for Eponol coated steel exposed in FFA2 for 15 days. Conditions: T(-), %RH(-), Cl(+), UV(+), Cycling(-)......	191

Figure 3.16 Optical images of the progression of scribe creep for Eponol coated steel exposed in FFA3 for 15 days. Conditions: T(+), %RH(+), Cl(+), UV(-), Cycling(-).....	192
Figure 3.17 Optical images of the progression of scribe creep for Eponol coated steel exposed in FFA4 for 15 days. Conditions: T(+), %RH(-), Cl(+), UV(-), Cycling(+)......	193
Figure 3.18 Optical images of the progression of scribe creep for Eponol coated steel exposed in FFA5 for 15 days. Conditions: T(-), %RH(-), Cl(+), UV(-), Cycling(+)......	194
Figure 3.19 Optical images of the progression of scribe creep for Eponol coated steel exposed in FFA6 for 15 days. Conditions: T(+), %RH(+), Cl(-), UV(+), Cycling(+)......	195
Figure 3.20 Images of Eponol coated 1018 steel. Sample was exposed for three days in FFA6 and then coated with gold-palladium over the polymer coating. Dotted lines mark where the boundary where the Au-Pd film was deposited.....	196
Figure 3.21 Graph of scribe creep for coated 1018 steel replicate samples exposed in FFA5 and FFA6. Error bars show standard error.	197
Figure 3.22 Graph of average scribe creep length versus time for 1018 steel samples exposed in FFA environments. The metal test was under FFA6 exposure conditions. Error bars show standard error.....	198
Figure 3.23 3D images of the scribe on epoxy resin coated 1018 steel exposed in FFA1 for 15 weeks. The units of the images are micrometers.....	199
Figure 3.24 Selected line profiles for Eponol coated steel exposed at FFA1 Vertical offset for data from each day reported is 20 μm . Dashed lines indicate original scribe location..	200
Figure 3.25 3D images of the scribe on epoxy resin coated 1018 steel exposed in FFA2 for 15 weeks. The units of the images are micrometers.....	201
Figure 3.26 Selected line profiles for Eponol coated steel exposed at FFA2 Vertical offset for data from each day reported is 30 μm . Dashed lines indicate original scribe location..	202

Figure 3.27 3D images of the scribe on epoxy resin coated 1018 steel exposed in FFA3 for 15 weeks. The units of the images are micrometers.....	203
Figure 3.28 Selected line profiles for Eponol coated steel exposed at FFA3 Vertical offset for data from each day reported is 20 μm . Dashed lines indicate original scribe location..	204
Figure 3.29 3D images of the scribe on epoxy resin coated 1018 steel exposed in FFA4 for 15 weeks. The units of the images are micrometers.....	205
Figure 3.30 Selected line profiles for Eponol coated steel exposed at FFA4 Vertical offset for data from each day reported is 25 μm . Dashed lines indicate original scribe location..	206
Figure 3.31 3D images of the scribe on epoxy resin coated 1018 steel exposed in FFA5 for 15 weeks. The units of the images are micrometers.....	207
Figure 3.32 Selected line profiles for Eponol coated steel exposed at FFA5 Vertical offset for data from each day reported is 20 μm . Dashed lines indicate original scribe location..	208
Figure 3.33 3D images of the scribe on epoxy resin coated 1018 steel exposed in FFA6 for 15 weeks. The units of the images are micrometers.....	209
Figure 3.34 Selected line profiles for Eponol coated steel exposed at FFA6 Vertical offset for data from each day reported is 20 μm . Dashed lines indicate original scribe location..	210
Figure 3.35 Raw EIS data from samples exposed in FFA1. Data were taken from the near location (left) and far location (right).....	211
Figure 3.36 Raw EIS data from samples exposed in FFA2. Data were taken from the near location (left) and far location (right).....	212
Figure 3.37 Raw EIS data from samples exposed in FFA3. Data were taken from the near location (left) and far location (right).....	212
Figure 3.38 Raw EIS data from samples exposed in FFA4. Data were taken from the near location (left) and far location (right).....	213

Figure 3.39 Raw EIS data from samples exposed in FFA5. Data were taken from the near location (left) and far location (right).....	213
Figure 3.40 Raw EIS data from samples exposed in FFA6. Data were taken from the near location (left) and far location (right).....	214
Figure 3.41 Normalized EIS data from samples exposed in FFA5 and FFA6. Data were taken from the near location (top) and far location (bottom).....	215
Figure 3.42 Normalized low frequency impedance values over time for Eponol coated steel samples exposed in FFAs. EIS readings taken at near location. Normalization was $ Z_{0.01} (\text{day})/ Z_{0.01} (\text{initial})$ for all days of the test. The error bars below the graph shows the error bars for four identical samples exposed to ASTM B-117 at each time indicated.....	216
Figure 3.43 Normalized low frequency impedance values over time for Eponol coated steel samples exposed in FFAs. EIS readings taken at far location. Normalization was $ Z_{0.01} (\text{day})/ Z_{0.01} (\text{initial})$ for all days of the test. The error bars below the graph shows the error bars for four identical samples exposed to ASTM B-117 for each time indicated.....	217
Figure 3.44 FTIR spectra of Eponol films exposed FFAs.....	218
Figure 3.45 FTIR spectra of Eponol films exposed in FFAs. The graph has been rescaled to show the changes at the 1717 cm^{-1} peak.	219
Figure 3.46 Graph of low frequency impedance ($Z_{0.01}$) and cathodic current density measured at -0.8 V vs. SCE over time for all FFA exposures.....	220
Figure 3.47 Plot of corrosion rate and corrosion potential over time for iron with 1 g/m^2 of SO_2 on the surface as the relative humidity drops from 95% to 40%. The solid line shows the corrosion rate and the dashed line shows the corrosion potential. ³⁸	223
Figure 3.48 Thermodynamic equilibrium concentration of various saltwater solutions relative to the relative humidity in equilibrium at $25\text{ }^\circ\text{C}$. Calculated by OLI. ⁴¹	223

Figure 3.49 Bar chart showing the correlation between mass loss and scribe creep for all FFA exposures at 15 days. Error bars are standard error.....	225
Figure 3.50 Correlation chart of mass loss with scribe creep for all FFA exposures.	225
Figure 4.1 Example graphs of residual error versus predicted values to test for linearity. The left graph shows data that is linear. The right graph shows data that has a nonlinear relationship.....	238
Figure 4.2 Example autocorrelation plots. The top plot shows correlated data while the bottom plot shows uncorrelated data.....	240
Figure 4.3 Example graphs of residuals vs. predicted values of y. The left graph shows homoscedastic data and the right graph shows heteroscedastic data.	241
Figure 4.4 Example normal probability plots. The top plot shows non-normal data while the bottom shows normal data.	242
Figure 4.5 Box-Cox log likelihood plot for determining the exponent of a power transformation. λ is the value of the exponent for the transformation (y^λ). The estimated value of λ is 0.23-0.45.	244
Figure 4.6 Box-Cox plot of FFA mass loss data showing the proper transform for the data is between $\lambda = 0.37$ and $\lambda = 0.71$. λ is the value of the exponent for the transformation (y^λ).	246
Figure 4.7 Plot of standardized residuals versus fitted values (values predicted by Equation 4.3, or $ML^{1/2}$) for transformed FFA mass loss data showing that the data is linear and homoscedastic.....	247
Figure 4.8 Autocorrelation plot of transformed FFA mass loss data showing that the data is independent. The x axis shows the lag, or time periods between the values that are being analyzed for correlation.....	248

Figure 4.9 Normal probability plot for transformed FFA mass loss data showing that the errors are normal. The x axis is the theoretical values of the residuals if they are normal and the y axis is the actual values of the residuals.	249
Figure 4.10 Graph of mass loss predicted by Equation 4.3 for bare 1018 steel compared with experimental results for 1018 steel in FFA exposures. The error bars shown above the data are from mass loss results for ASTM G-85 Annex 5.	250
Figure 4.11 Graph showing the sensitivity of the model of mass loss of bare steel to temperature. High temperature is 40°C and low is 25°C. All other ESFs are at baseline values.	251
Figure 4.12 Graph showing the sensitivity of mass loss of bare steel to cycling. High cycling level is 4 wet/dry cycles per day and low is 1 cycle per day. All other ESFs are at baseline values.	252
Figure 4.13 Graph showing the sensitivity of mass loss of bare steel to relative humidity. High relative humidity is 85% and low is 70%. All other ESFs are at baseline values.	252
Figure 4.14 Graph showing the sensitivity of mass loss of bare steel to chloride. High chloride level is 2.3×10^{-4} g/cm ² /day and the low level is 2.3×10^{-4} g/cm ² /day. All other ESFs are at baseline values.	253
Figure 4.15 Graph of mass loss results for ASTM G-85 Annex 5 and KSC plotted against the model predictions for those exposures. The model inputs were the same ESF parameters as the exposure environments reported in Table 3.1. The model for ASTM G-85 Annex 5 used $t^{0.5}$ while the model for KSC used $t^{0.35}$	254
Figure 4.16 Box-Cox plot of FFA1, 2, 3, and 5 scribe creep data for Eponol coated steel indicating that the proper transform is between $\lambda = 0.35$ and $\lambda = 0.92$. λ is the value of the exponent for the transformation (y^λ).	256

Figure 4.17 Graph of standardized residuals versus fitted values (the values predicted by Equation 4.4, or $SC^{1/2}$) for transformed FFA1, 2, 3, and 5 scribe creep data indicating that the residuals are linear and homoscedastic.	257
Figure 4.18 Autocorrelation plot of transformed FFA1, 2, 3, and 5 scribe creep data for coated steel showing that the errors are independent.	258
Figure 4.19 Normal probability plot of transformed FFA1, 2, 3, and 5 scribe creep data showing that the residuals are normally distributed.	259
Figure 4.20 Graph of model values plotted against observed values of scribe creep for Eponol coated steel exposed to FFA1, 2, 3, and 5 test environments.	260
Figure 4.21 Graph showing the sensitivity of scribe creep of coated steel exposed in FFA1, 2, 3, and 5 to temperature. High temperature is 40°C and low is 25°C. All other ESFs are at baseline values.	261
Figure 4.22 Graph showing the sensitivity of scribe creep of coated steel exposed in FFA1, 2, 3, and 5 to cycling. High cycling level is 4 wet/dry cycles per day and low is 1 cycle per day. All other ESFs are at baseline values.	262
Figure 4.23 Graph showing the sensitivity of scribe creep of coated steel exposed in FFA1, 2, 3, and 5 to relative humidity. High relative humidity is 85% and low is 70%. All other ESFs are at baseline values.	262
Figure 4.24 Graph showing the sensitivity of scribe creep of coated steel exposed in FFA1, 2, 3, and 5 to UV. High UV is 0.28 W/m ² and low UV is 0.16 W/m ² . All other ESFs are at baseline values.	263
Figure 4.25 Graph showing the sensitivity of scribe creep of coated steel exposed in FFA1, 2, 3, and 5 to chloride. High chloride level is 2.3x10 ⁻⁴ g/cm ² /day and the low level is 2.3x10 ⁻⁴ g/cm ² /day. All other ESFs are at baseline values.	263

Figure 4.26 Graph of observed values of scribe creep plotted against predicted model values. The model inputs are the same ESF parameters present in exposures summarized in Table 3.1.	264
Figure 4.27 Thermodynamic equilibrium concentration of various saltwater solutions relative to the relative humidity in equilibrium at 25 °C. Calculated by OLI. ²⁰	265
Figure 6.1. Schematic of filiform corrosion on an aluminum alloy. ⁵	286
Figure 6.2. Schematic of Eponol coated and scribed AA2024-T351 sample. The sample is a square that is 2.5 cm on a side.	288
Figure 6.3. Schematic of Eponol coated and scribed AA2024-T351 sample. The substrate is roughly 1 mm thick and the Eponol topcoat is 30±5 µm. The scribe line is 150±50 µm in width.	289
Figure 6.4. Schematic showing locations where EIS was performed on coated and scribed samples.	291
Figure 6.5. Optical Images of scribe creep over time for Eponol coated AA2024-T351 exposed at KSC.	298
Figure 6.6. Optical Images of scribe creep over time for Eponol coated AA2024-T351 exposed at BRD.	299
Figure 6.7. Optical images of Eponol coated AA2024-T351 exposed in ASTM B-117.	300
Figure 6.8. Optical Images of scribe creep over time for Eponol coated AA2024-T351 exposed to ASTM G-85 Annex 3.	300
Figure 6.9. Optical images of the scribe on Eponol coated AA2024-T351 exposed to ASTM G-85 Annex 5.	301
Figure 6.10. Optical images of the scribe on Eponol coated AA2024-T351 exposed to ASTM D-5894.	301

Figure 6.11. Optical images of the scribe on Eponol coated AA2024-T351 exposed to CC+O ₃ (0.7-2.5 ppm).....	302
Figure 6.12. Optical images of eponol coated AA2024-T351 exposed in various LALTs showing the extent of scribe creep after 15 days.....	302
Figure 6.13. Optical images of eponol coated AA2024-T351 exposed at various field sites showing the extent of corrosion and scribe creep over time.....	303
Figure 6.14. Scribe creep length over time for Eponol coated AA2024-T351 for all LALTs and field sites. The KSC and BRD data points correspond to the upper X axis, as indicated by the arrows.....	303
Figure 6.15. Optical image (left) and CSLM image (right) of pitting on bare AA2024 exposed to CC+O ₃ (10-25 ppm) for 5 days. All samples rinsed in DI water before imaging.....	305
Figure 6.16. Optical images of pitting on bare AA2024-T351 exposed in CC+O ₃ (0.7-2.5 ppm) for 15 days (left) and CC+O ₃ (10-25 ppm) for 5 days (right). All samples rinsed in DI water before imaging.....	305
Figure 6.17. Optical image (left) and CLSM image (right) of pitting on bare AA2024 exposed at LA for 9 months. All samples rinsed in DI water before imaging.....	306
Figure 6.18. Optical images of pitting on bare AA2024-T351. a) unexposed sample, b) exposed at BRD for 1 month, c) Exposed at BRD for 3 months, d) Exposed at KSC for 1 month, e) exposed at KSC for 3 months, f) exposed at KSC for 3 months. All samples rinsed in DI water before imaging.....	307
Figure 6.19. Optical images of pitting on bare AA2024-T351 a) unexposed, b) exposed at LA for 9 months, c) exposed at KSC for 3 months, d) exposed at PJ for 9 months. All samples rinsed in DI water before imaging.....	308

Figure 6.20. Optical images of pitting on bare AA2024-T351 a) unexposed, b) exposed in ASTM D-5894 for 1 cycle (14 days), c) exposed in ASTM D-4587 for 15 days, d) exposed in ASTM G-85 Annex 5 for 10 days, e) exposed in ASTM G-85 Annex 3 for 15 days, f) exposed in ASTM B-117 for 15 days. All samples rinsed in DI water before imaging.	309
Figure 6.21. Optical image (left) and binary image (right) of pitting on bare AA2024-T351 exposed to CC+UV+O ₃ (0.7-2.5 ppm) for 15 days. All samples rinsed in DI water before imaging.....	310
Figure 6.22. Histogram of pit area for bare AA2024-T351 exposed at KSC for 3 months. .	311
Figure 6.23. Histograms of pit area for bare AA2024-T351 exposed in ASTM D-5894 for 1 cycle (14 days) (left) and for samples exposed at KSC for 3 months (right). Note that the x axis scales are equal in this figure and that the x axis scales for samples exposed at KSC is different in this figure compared with Figure 6.22.	312
Figure 6.24. Histogram of pit area for bare AA2024-T351 exposed in ASTM B-117 for 15 days.....	312
Figure 6.25. Optical image of AA2024-T351 exposed in CC+O ₃ (10-25 ppm) for 5 days showing open pits, copper replating and oxide filled pits. Sample was rinsed with DI water before imaging.	313
Figure 6.26. SEM image of pit that is filled with oxide. Sample exposed in CC+O ₃ (10-25 ppm) for 5 days. Sample was rinsed with DI water before imaging.....	314
Figure 6.27. EDS linescan of oxide filled pit of a bare AA2024-T351 sample exposed in CC+O ₃ (10-25 ppm) for 5 days. The spectra on the left show the relative abundances of oxygen, magnesium, aluminum and copper. The image on the right shows the length and direction of the scan. Sample was rinsed with DI water before imaging.	315

Figure 6.28. Images of small pits growing by undercutting the surface oxide layer on bare AA2024-T351 exposed to CC+O ₃ (10-25 ppm) for 5 days. Sample was rinsed with DI water before imaging.	316
Figure 6.29. SEM images of AA2024-T351 exposed in CC+UV+O ₃ (0.7-2.5 ppm) for 15 days and then immersed in 60% nitric acid solution to remove the surface oxide. Sample was rinsed with DI water before imaging.....	317
Figure 6.30. SEM images of bare AA2024-T351 exposed to CC+UV+O ₃ (0.7-2.5 ppm) for 15 days showing oxide particles on the surface of the sample. The particles were absent from samples exposed in other conditions. Sample was rinsed with DI water before imaging. ..	318
Figure 6.31. SEM images of bare AA2024-T351 exposed at LA for nine months showing pit morphology characteristic of samples exposed at field sites. Sample was rinsed with DI water before imaging.	318
Figure 6.32. EDS spectra (right) of a pit on bare AA2024-T351 exposed at LA field site for 9 months. The image on the right shows the direction of the scan. Sample was rinsed with DI water before imaging.	319
Figure 6.33. EIS data for coated AA2024 exposed at Kennedy Space Center, FL. Left is near and right is far.	321
Figure 6.34. EIS data for coated AA2024 exposed at Birdwood Golf Course, Charlottesville VA (BRD). Left is near and right is far.	321
Figure 6.35. EIS data for coated AA2024 exposed to ASTM B-117. Left is near and right is far.	322
Figure 6.36. EIS data for coated AA2024 exposed to ASTM G-85 Annex 3. Left is near and right is far.....	322

Figure 6.37. EIS data for coated AA2024 exposed to ASTM G-85 Annex 5. Left is near and right is far.....	323
Figure 6.38. EIS data for coated AA2024 exposed in ASTM D-5894. Left is near and right is far.	323
Figure 6.39. EIS data for coated AA2024 exposed to CC. Left is near and right is far.	324
Figure 6.40. EIS data for coated AA2024 exposed to CC+UV. Left is near and right is far.	324
Figure 6.41. EIS data for coated AA2024 exposed to CC+O ₃ (0.7-2.5ppm). Left is near and right is far.....	325
Figure 6.42. EIS data for coated AA2024 exposed to CC+UV+O ₃ (0.7-2.5ppm). Left is near and right is far.....	325
Figure 6.43. The equivalent circuit model for an organically coated metal. R(soln) is the solution resistance, R(pore) is the resistance of the pores in the coating, R _{dl} is the double layer resistance, CPE2 is the coating capacitance and CPE1 is the double layer capacitance.	327
Figure 6.44. Example of the data that can be obtained from EIS. Saddle frequency decreases as R _{pore} decreases. For this simulation, R _s was 10 Ω-cm ² , R _{pore} varied from 10 ¹² to 10 ³ Ω-cm ² , R _{dl} varied from 10 ⁸ to 10 ⁴ Ω-cm ² , and the total area was 1 cm ²	328
Figure 6.45. Saddle frequency plots for coated AA2024 exposed to various environments. The top plot is data taken from the Near location. The bottom plot is data taken from the Far location. Open symbols represent data for samples exposed at field sites; time is on the top axis for the field sites.....	330
Figure 6.46. EIS data and equivalent circuit fit Eponol coated AA2024-T351 exposed to CC+O ₃ (0.7-2.5 ppm) for 3 days. Data taken at the far location (see Figure 6.4).	332

Figure 6.47. R_{pore} values for Eponol coated AA2024-T351 exposed in CC+O ₃ (0.7-2.5 ppm). EIS scans were performed near and far from the scribe and then fit to an equivalent circuit to obtain R_{pore}	332
Figure 6.48. Graph of Equation 6.5 showing the increase in electrical defect area associated with the decrease of R_{pore}	333
Figure 6.49. Plot of saddle frequency and high and low breakpoint frequency (f_{45}) for the model presented in Figure 6.44. The parameters are identical; R_s was 10 Ω -cm ² , R_{pore} varied from 10 ¹² to 10 ³ Ω -cm ² , R_{dl} varied from 10 ⁸ to 10 ⁴ Ω -cm ² , and the area was 1 cm ²	334
Figure 6.50. FTIR spectra of Eponol films exposed in ASTM B-117 and G-85 A5 for 15 days. Data taken at UVa.	335
Figure 6.51. FTIR spectra of Eponol films exposed in various conditions. Data taken at USM.	336
Figure 6.52. FTIR spectra of Eponol films on inert polypropylene substrates exposed in various conditions. Arrows indicate peaks that are expected to change with exposure to UV.	340
Figure 6.53. Optical images showing the comparison of pitting/corrosion morphology on bare AA2024-T351 exposed at KSC (left) and in CC+UV+O ₃ (0.7-2.5 ppm) (right).....	343

Table of Tables

Table 1.1 Table showing the correlation of many different LALTs and fixed atmospheric exposures to cosmetic corrosion on phosphated cold-rolled steel samples coated with an automotive primer and a clear topcoat and mounted on vehicles in the Midwest for 5 years. R^2 is the correlation coefficient for a least-squares linear regression. C is the ratio of the average scribe creep from the real world exposure to the values of scribe creep predicted by the LALT. A sum of R^2 and C equaling 2 implies perfect correlation. ¹⁴	7
Table 1.2 The variables tested during the creation of the SAE J2334 and the two levels of the variables used.	8
Table 1.3 Table of empirical equations for corrosion rate from various sources.....	14
Table 1.4 Table of the mobility of fluorescent tracer molecules in PVP films as a function of %RH. ⁸⁹ Numbers indicate the fraction of tracer molecules undergoing each kind of motion.	37
Table 1.5 List of all standard LALTs used in this study.	52
Table 1.6 Environmental severity factors for field sites.....	53
Table 1.7 Table of levels for variables in eight experiments for 2^{7-4} fractional factorial design. “+” denotes the high level and “-” denotes the low level.....	57
Table 2.1 List of all LALTs used in this study.	83
Table 2.2 Environmental severity factors for field sites.....	84
Table 2.3 Table of Raman peaks of iron corrosion products.....	95
Table 2.4 Table of corrosion products found with XRD and Raman. X indicates that the species was found with XRD, and R indicates that it was found with Raman.	96
Table 3.1 ESF levels for selected LALTs and field sties.....	157

Table 3.2 Table of International Organization for Standardization (ISO) rankings (ISO 9223) for chloride levels. ¹²	159
Table 3.3 Chloride deposition rates and ISO classifications for various exposures.	160
Table 3.4 Table of ESF parameters in standard LALTs. These values were used with Equation 3.1 to determine the model predicted curves in Figure 3.1.	162
Table 3.5 The selected levels of variables for the fractional factorial design of experiment.	164
Table 3.6 Factorial design test matrix for testing three variables in eight experiments.	167
Table 3.7 Test matrix for fractional factorial experiments in this study.	177
Table 3.8 Revised test matrix for fractional factorial experiments in this study.	181
Table 3.9 Revised table of variable levels for fractional factorial experiments.	181
Table 3.10 Table of iron oxide species found on bare steel with XRD and Raman spectroscopy compared to KSC, ASTM B-117 and ASTM G-85 Annex 5. (X) indicates species found with XRD, (R) indicates species found with Raman, and (–) indicates that the species was not detected.	189
Table 3.11 Calculated Piling-Bedworth ratios for iron oxides. The PB ratio is the ratio of the molar volume of the oxide to the molar volume of the metal.	226
Table 4.1 ESF levels for the model baseline. Baseline values are the mean values of the high and low levels.	251
Table 4.2 ESF levels for the scribe creep model baseline. Baseline values are the mean values of the high and low levels.	261
Table 5.1 Test matrix for a 2 ³ full factorial design.	280
Table 6.1. List of all standard LALTs used in this study.	295
Table 6.2. List of all non-standard LALTs used in this study.	296

Table 6.3. Environmental severity factors for field sites.....	297
Table 6.4. Acceleration factors for LALTs with respect to KSC based on scribe creep length.	304
Table 6.5. Summary of Image Analysis of Pitting on bare AA2024-T351	311
Table 6.6. Acceleration factors for AA2024-T351 based on low frequency impedance ($Z_{0.01}$).	326
Table 6.7. Acceleration factors for AA2024-T351 based on saddle frequency.....	331
Table 6.8. DSC and MDSC results showing the glass transition temperature for eponol exposed to various conditions.....	337
Table 6.9. TGA results on Eponol films showing the amounts of residual solvents, organic material and inorganic material.	338

List of Symbols

A	area of electrodes (mm^2)
A_a	area of anode (cm^2)
A_c	area of cathode (cm^2)
A_{total}	total area (cm^2)
C_{bulk}	Concentration of electrolyte (mol/L)
C_{coat}	coating capacitance (F)
C_{dl}	double layer capacitance (F)
C_{sol}	solution capacitance (F)
D	diffusion coefficient
E	potential (mV)
E_{ocp}	open circuit potential (mV)
f	frequency (Hz)
I	current (A)
i	current density (A/cm^2)
M	molarity (mol/L)
ML	mass loss (g/cm^2)
R	gas constant ($8.314 \text{ J}/\text{mol}\cdot\text{K}$)
R	resistance (Ω)
R^2	coefficient of determination
R_{coat}	resistance of the coating ($\Omega\text{-cm}^2$)
R_p	polarization resistance ($\Omega\text{-cm}^2$)
R_s	ohmic resistance of the solution ($\Omega\text{-cm}^2$)
T	temperature ($^{\circ}\text{C}$)
t	time (day)
T_g	glass transition temperature
T_m	melting temperature
$ Z $	impedance (Ω)
$ Z_{0.01} $	impedance at a frequency of 0.01 Hz
$Z(C)$	impedance of capacitor (Ω)

Greek Symbols

λ	incident radiation wavelength (nm)
λ	statistics total population average
ρ	resistivity of the electrolyte
Σ	summation
2θ	diffraction angle

Acronyms

3DOM.....	3D optical microscopy
AISI.....	American Iron and Steel Institute
ASTM.....	American Society of Testing and Materials
BPA.....	Bisphenol-A
BRD.....	Birdwood Golf Course, Charlottesville VA
CC.....	cyclic condensation
CCC.....	chromate conversion coating
CLSM.....	confocal scanning laser microscope
CPE.....	constant phase element
CV.....	cyclic voltammetry
DSC.....	differential scanning calorimetry
EDS.....	energy dispersive spectroscopy
EIS.....	electrochemical impedance spectroscopy
ESF.....	environmental severity factor
FFC.....	filiform corrosion
f.c.c.....	face center cubic crystal structure
FFA.....	fractional factorial analysis
FIT.....	full immersion test
FTIR.....	Fourier transform infrared spectroscopy
HER.....	hydrogen evolution reaction
HI.....	Coconut Island, Hawaii
HLS.....	high-level surveillance

IMCs.....	intermetallic compounds
KSC.....	Kennedy Space Center
LA.....	Los Angeles, Ca
LALT.....	lab accelerated life test
MDSC.....	modified differential scanning calorimetry
OCP.....	open circuit potential
ORR.....	oxygen reduction reaction
PJ.....	Point Judith, Rhode Island
PMMA.....	Poly(methyl methacrylate)
ppb.....	parts per billion
ppm.....	parts per million
PVB.....	polyvinyl butyral
PVP.....	poly(vinylpyrrolidone)
QUV.....	UV weathering chamber made by Q-Lab Corporation
RH.....	relative humidity
SAE.....	Society of Automotive Engineers
SCE.....	Saturated Calomel Electrode
SEM.....	scanning electron microscopy
SHE.....	standard hydrogen electrode
SKP.....	Scanning Kelvin Probe
TGA.....	thermogravimetric analysis
ToW.....	time of wetness
UNS.....	unified numbering system
USM.....	University of Southern Mississippi
UV.....	ultraviolet light
UVa.....	University of Virginia
VOC.....	volatile organic compound
XRD.....	x-ray diffraction

List of Iron Compounds

α -Fe ₂ O ₃	hematite
α -FeOOH.....	Goethite
β -FeOOH.....	Akaganeite
γ -FeOOH.....	Lepidrocite
γ -Fe ₂ O ₃	Maghemite
FeO.....	ferrous oxide
Fe ₃ O ₄	magnetite

1 Chapter 1 – Introduction

1.1 Summary

In this chapter, the mechanisms of scribe creep on organically coated steel are reviewed. Important environmental factors affecting scribe creep, including UV radiation, ozone, chloride, time of wetness, relative humidity, and cycling are reviewed. Their effects both bare steel and on the degradation of the polymer coating itself are addressed. The processes by which environmental severity factors (ESF) affect the overall rate of scribe creep are not well understood. Subsequently, lab accelerated life tests (LALT) do not adequately mimic real world atmospheric exposure and correlation between the two are poor. Systematic studies of ESFs that drive scribe creep have not been performed with high level surveillance techniques. The first step towards designing LALTs that correlate better with field exposure is to establish an approach to understand the effects of environmental severity factors on scribe creep. Current standard LALTs are compared with field exposure to determine potential important ESFs. This review will point to the need to design an experimental matrix using fractional factorial design of experiment.

1.2 Background:

1.2.1 Necessary Development of LALTs for New Coating Systems

Recent changes to environmental regulations regarding hexavalent chromium (Cr⁺⁶) and volatile organic compounds (VOC) dictate that current generation coating systems used in defense applications must be rapidly replaced with new coating and pretreatment systems

capable of protecting metals from corrosive attack by the environment.¹⁻⁴ Chromate conversion coatings (CCCs) are one example of a system that must be replaced. CCCs have been used since the early 1900s to protect metal alloys from corrosion.⁵ They increase the corrosion resistance of steel and 2xxx series aluminum alloys, among others. Hexavalent chromium (Cr^{6+}) is the main protective component in CCCs. However, it has been found to be a carcinogen and has recently become a highly regulated substance.⁶ The US Department of Labor recently issued a new regulation that limits the amount of Cr^{6+} exposure for workers, cutting the permissible limit from $100 \mu\text{g}/\text{m}^3$ of air to $5 \mu\text{g}/\text{m}^3$ of air.¹ In addition, the EPA has set the permissible amount of Cr^{6+} in drinking water at 100 ppb and has established guidelines for enhanced monitoring of Cr^{6+} levels.^{2, 7} Finally, the Undersecretary of Defense has issued a memorandum which instructs the military to reduce its use of hexavalent chromium and find alternatives to CCCs.⁸

The drive to move away from coating and pretreatment systems containing hexavalent chromium and VOCs has led to an increase in the diversity of pretreatments and coating primers for corrosion protection on steel and aluminum alloys. Chromate-free pretreatments that promote adhesion of paint to the metal surface⁹ and Mg rich primers¹⁰ are two examples. New coating systems must still protect against scribe creep on steel and aluminum alloys over their service lives. Therefore, the service lifetimes of these new coating systems must be established. Field exposures, however, take many years to complete. As a result, the development of new priming and coating schemes has required the use of accelerated life corrosion tests (LALTs).

1.2.2 Current Approaches to LALT Design

Cabinet tests, lot acceptance tests, and other forms of accelerated tests are often used to predict the long-term performance of coatings. Accelerated testing saves time and reduces cost.¹¹ By understanding the limits of materials and products, companies can accurately gauge warranty and production costs.¹¹ However, discrepancies between such tests and field exposures undermine the utility and accuracy of accelerated testing.^{10, 12-14} A recent study for the Department of Defense attempted to address these discrepancies by examining the correlation in scribe creep between field exposed and ASTM B-117¹⁵ tested samples of coated 2xxx and 5xxx series aluminum alloys.¹² The authors examined differences in scribe creep using the ASTM D-1654 Procedure A,¹⁶ which involves removing the coating using compressed air or mechanical scraping and then visually rating the extent of corrosion. Based on their observations, two ways to improve correlation with field exposures were suggested: a) evaluate additional replicates of the substrate for each coating system to reduce sample to sample variability in the ASTM D-1654 Procedure A, and b) expose samples to at least two different LALTs, for example ASTM B-117 and GM 9540P.¹² These proposed solutions, however, represent brute force approaches to remedy a lack of correlation. The authors advocate testing more of the same samples and conducting a greater variety of LALTs without understanding the underlying corrosive mechanisms at work or how each environmental severity factor (ESF) affects the unit processes driving scribe creep.

Discrepancies between LALT and field exposures for coated metals have led to many attempts within industry to develop more accurate LALTs using a “top down” approach similar to the study described above. In the “top down” method, creation of a new LALT is approached by comparing existing LALT results to field exposures, usually by visual inspection, and then modifying the LALTs using trial and error approaches in an attempt to more accurately predict the service life of materials.^{12, 17-19} In a “top down” approach the impact of individual environmental factors is rarely studied systematically. Instead, the engineer’s past experience or knowledge dictates, in a “top down” manner, the environmental factors to be modified in the LALT. An alternative approach to improving field and test correlation would be to work from the “bottom up”: one would first elucidate similarities and differences in corrosive drivers and products in the lab versus field in order to understand the specific coating degradation mechanisms and processes occurring in each type of test. Knowledge of such differences could then be used to update an existing LALT or create an entirely new test with improved correlation of corrosion between the lab and field environments.

Townsend et al. use a “bottom up” approach in their attempt to improve LALT performance for the auto and steel industries.¹⁴ The goal of their study was to create a LALT (i.e., SAE J2334) that could more accurately predict the rate and mode of corrosion attack for cosmetic corrosion on automotive sheet steel in relation to the severe environments of Ontario and St. Johns, Canada. Canadian sites were chosen for their temperature extremes and the large amount of deicing salt used on the roadways in the winter: conditions that make Canada one of the most corrosive environments in the world.¹⁴ The material used was automotive sheet steel galvanized with Zn, ZnFe, or ZnNi. All samples were

electrophorically primed, and sprayed with a base paint coat and a clear top coat. The samples were scribed down to the steel.

The authors measured the extent of scribe creep (at 1 cm intervals along the scribe) from samples deployed at multiple sites of varying corrosive severity and various LALTs, including AISI A to E, which are cyclic tests (Table 1.1). They then compared correlation in scribe creep between the LALTs or various field sites and their “real world” samples that were mounted on vehicles in Canada and driven for 5 years. The LALTs and field tests were ranked according to the sum of R^2 (how well scribe creep in each test correlated with the Canada car tests) and C (the ratio of average creep of the samples to the value predicted by a least-squares line for the data). It is worth noting that ASTM B-117 was the worst performer of all of the exposures tested. In the second phase of their study, the authors performed a partial factorial experiment in an attempt to create a LALT with even stronger correlation than the existing AISI tests. In the partial factorial experimental design, the authors ran eight experiments to determine which of 7 environmental severity factors (i.e., Wet Stage temperature, Wet Stage humidity, Dry Stage temperature, Dry Stage humidity, NaCl concentration, salt solution composition and the number of dryouts per cycle) were most important to producing strong correlation between real world vehicle exposures and variations of the AISI B cyclic test. The variables were tested at two levels as shown in Table 1.2. The statistical design of the experiment allowed for examination of the effects of 128 combinations of the seven variables in eight non-standard LALTs. Each of the LALTs was run for 80 cycles with automotive sheet steel. By performing analysis of variance (ANOVA) statistical method on the results, the authors were able to rank the relative importance of each variable.¹⁴ Using these data, a new LALT, the SAE J2334, was developed

to optimize the variables identified in the statistical analysis. Figure 1.1 shows the correlation between SAE J2334 and the Canadian field exposures.

In their final set of analyses, the authors use light microscopy, SEM and three methods of chemical characterization: energy dispersive x-ray spectroscopy (EDS), X-ray diffraction (XRD), and Mossbauer spectroscopy to examine corrosive products and morphologies between their new SAE J2334 test and on-vehicle samples.¹⁴ The authors state that results showed similarities in corrosion morphology and products, which supports the strong correlation in corrosion rate between SAE J2334 and on-vehicle samples.¹⁴ However, their study does not elaborate on which types of morphologies or products were present.¹⁴

Overall, the study by Townsend, et al. is a positive example of engineers approaching LALT creation from a novel, “bottom up” perspective. Their approach represents two major advances in LALT design. First, rather than making a priori assumptions about environmental factors and adjusting the LALT through trial and error, Townsend et al. use partial factorial design and statistical analysis to determine which environmental severity factors are most important to consider in LALT design. Second, the authors move beyond basic visual inspection to perform some high level surveillance of corrosion morphology and products to identify corrosion similarities between their new LALT and field results.

Table 1.1 Table showing the correlation of many different LALTs and fixed atmospheric exposures to cosmetic corrosion on phosphated cold-rolled steel samples coated with an automotive primer and a clear topcoat and mounted on vehicles in the Midwest for 5 years. R^2 is the correlation coefficient for a least-squares linear regression. C is the ratio of the average scribe creep from the real world exposure to the values of scribe creep predicted by the LALT. A sum of R^2 and C equaling 2 implies perfect correlation.¹⁴

Test	Duration	R^2	C	Sum
SAE J2334	80 cycles	0.96	0.97	1.93
Acid Rain CCT	45 cycles	0.78	0.97	1.75
CCT-IV	35 cycles	0.74	0.86	1.6
GM9540P(B) (GM)	50 cycles	0.84	0.59	1.43
JASO M610	45 cycles	0.44	0.98	1.42
AISI-A	50 cycles	0.46	0.75	1.21
AISI-C	50 cycles	0.74	0.41	1.15
Michigan Suburban	24 months	0.61	0.51	1.12
GM9540P(B) (ACT)	50 cycles	0.44	0.67	1.11
Chrysler Chipping	25 cycles	0.54	0.56	1.1
AISI-B	70 cycles	0.74	0.29	1.03
Proving Ground 2	5-yr equivalent	0.64	0.39	1.03
AISI-E	50 cycles	0.62	0.38	1
Proving Ground 3	8-yr equivalent	0.37	0.59	0.96
Hoogovens Method 1	20 weeks	0.01	0.91	0.92
Montreal	24 months	0.62	0.28	0.9
Michigan Rural	24 months	0.68	0.19	0.87
AISI-D	70 cycles	0.45	0.41	0.86
West Virginia	24 months	0.58	0.25	0.83
QUV-Prohesion	12 weeks	0.62	0.2	0.82
Proving Ground 1	10-yr equivalent	0.1	0.72	0.82
CCT-1	60 cycles	0.56	0.21	0.77
Michigan Urban	24 months	0.61	0.15	0.76
South Florida	24 months	0.34	0.4	0.74
Navistar CCT	100 cycles	0.49	0.24	0.73
Philadelphia	24 months	0.49	0.23	0.72
GM9511P	20 cycles	0.35	0.18	0.53
Hoogovens Method 2	20 cycles	0.02	0.37	0.39
B117 Salt Spray	4 weeks	0.19	0.05	0.24

Table 1.2 The variables tested during the creation of the SAE J2334 and the two levels of the variables used.

Variable	Levels	
	1	2
Wet-Stage Temperature, °C	38	60
Wet-Stage Humidity, %RH	85	100
Dry-Stage Temperature, °C	30	60
Dry-Stage Humidity, %RH	25	50
NaCl Concentration, %	0.5	5
Salt Composition	NaCl only	NaCl+0.25%NaHCO ₃ +0.1% CaCl ₂
Number of Dryouts per Cycle	1	3

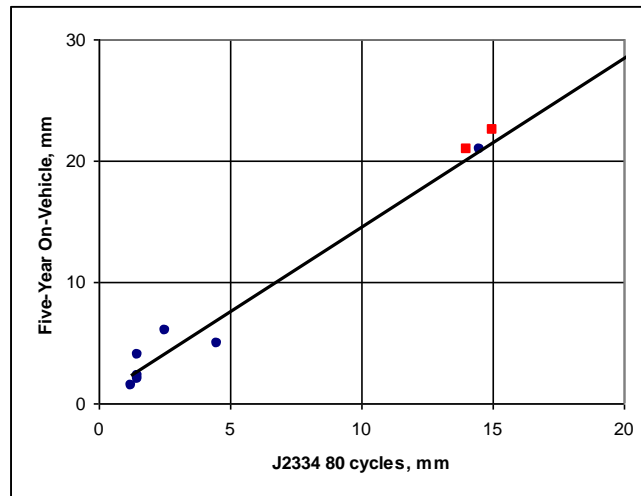


Figure 1.1 Correlation plot showing the values of scribe creep of phosphated and galvanized cold-rolled steel coated with an automotive primer and a clear topcoat for 5 year on vehicle field tests compared with 80 cycles of SAE J2334. For this plot, $R^2=0.98$ and $C=0.97$.¹⁴ See Table 1 for explanation of R^2 and C.

1.2.3 Drawbacks to Current LALT Design Methods

The “bottom up” approach used by Townsend et al. created an improved LALT that is still in use by the automotive industry. However, the study is not without limitations. First, when the SAE J2334 was actually conducted with coated samples, it was determined that the

corrosion rate of coated steel was too slow compared with the field and therefore did not correlate well with the field results. Additionally, the SAE J2334 corroded the uncoated steel samples much too quickly to provide a meaningful correlation to field results. The authors were forced to run variations on the LALT to determine through trial and error that dry stage humidity of 50% RH and 50°C wet-stage temperature were critical factors in achieving good correlation with field results. Changes to the salt solution, which the authors thought would improve the LALT's performance with coated metal based on "expertise within the committee indicating other ions [besides NaCl] are important for the evaluation of other materials such as polymers...", did not actually improve performance when compared with the SAE J2334 run using only NaCl.¹⁴ This trial and error approach could have potentially been avoided had the authors chosen to study isolated environmental corrosion factors, themselves, to understand how specific ESFs individually drive the corrosion of coated steel.

A second drawback to Townsend et al. and other attempts to improve LALT correlation with the field is an over-reliance on basic visual inspection methods to determine the extent of corrosion and coating degradation. Visual inspection methods are difficult to quantify and lack insight into underpaint corrosion. For example, it has been shown that a loss of coating gloss does not necessarily give a good indication of the extent of coating degradation.¹⁸ This is because gloss shows degradation at the surface of the coating but does not give a good description of the extent of degradation into or under the coating. Visual inspection of blistering can also be misleading. In the study performed for the Department of Defense discussed previously,¹⁸ zinc-coated steel samples were coated with polyurethane primers and polyester topcoats. The samples were exposed to cycles of UV

and condensation in a UV weathering tester followed by B-117 or to B-117 alone. Despite the large difference in the number of blisters between UV exposure followed by B-117 and B-117 alone, changes in gloss measurements from sample to sample were so minor that they did not provide any information on the corrosion barrier properties of the coatings. Additionally, coatings exposed only to UV showed no visual differences upon changes in irradiation time. However, the barrier properties of the coating, as measured with electrochemical impedance spectroscopy (EIS), decreased noticeably (Figure 1.2).¹⁸ For these reasons, using visual inspection methods alone to quantify corrosion or give a ranking of coating performance (as done by Townsend et al.) could yield imprecise or misleading results.

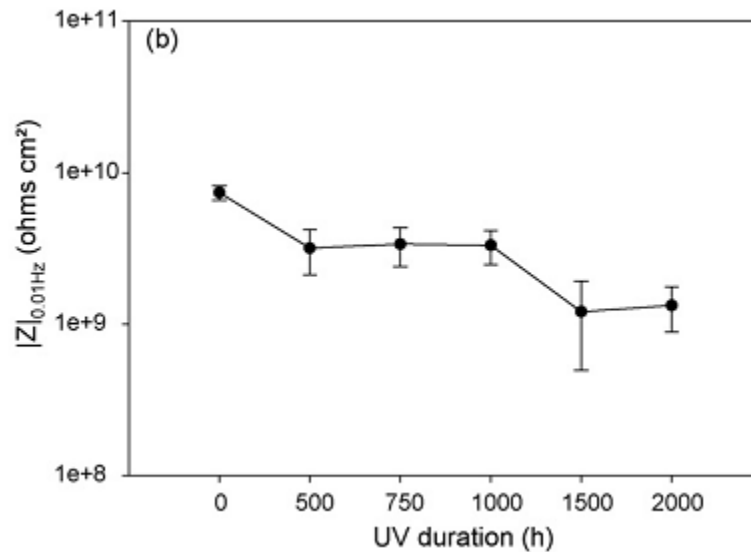


Figure 1.2 Low-Frequency Impedance Modulus as a function of UV irradiation time for galvanized and polyester-coated steel. ¹⁸

A third drawback to current methods for improving LALTs is the comparison of new LALT performance with results from the ASTM B-117. The B-117 salt fog test is the most

commonly used cabinet corrosion test,¹⁷ and is used by many industries including automotive, paint and coating vendors, and aerospace as a corrosion performance standard. The ASTM B-117 test consists of a constant fog of 5% sodium chloride solution in a cabinet kept at 35°C.¹⁵ Test runs last from a few hours to thousands of hours. Since its adoption as an official ASTM standard in 1939,¹⁷ the ASTM B-117 has been modified numerous times in an effort to more accurately mimic environmental corrosion attack observed in field environments. For example, in an attempt to mimic natural environmental pH variance and accelerate corrosion, the ASTM B-117 was modified to include acetic acid in the salt solution (ASTM G-85). Even the modified B-117 tests, however, have been shown to exhibit corrosion attack that is different from that seen in field exposures, as well as to produce different corrosion products.²⁰ The ASTM B-117 standard, itself, states that “prediction of performance in natural environments has seldom been correlated with salt spray results when used as standalone data. Correlation and extrapolation of corrosion performance based on exposure to the [ASTM B-117] test environment are not always predictable.”¹⁵ Even when used only as a process control test, the reproducibility of the ASTM B-117 can vary from lab to lab, and even from chamber to chamber “even [when] the testing conditions are nominally similar within the ranges specified in [the ASTM B-117] practice.”¹⁵ Despite these limitations, the ASTM B-117 test method is still used in industry to rank corrosion performance of materials and is one of the top ten bestselling ASTM standards of all time.¹⁷ Due to the limitations described above, comparison of new LALTs to ASTM B-117 cannot be relied upon to give meaningful results as to the efficacy of the new LALT.

Finally, the use of modeling is largely lacking in the creation of new LALTs. For example, although Townsend et al. ran statistical analyses to identify ESFs important to corrosion of a coated system, they did not take the next step to use their analyses to create an empirical model of scribe creep. In addition to using a model in a predictive fashion, the act of constructing the model often gives insights to the system behavior that would not have been apparent without modeling and the statistical analysis that it requires.

Until a LALT that correlates well with long term field results can be designed, accelerated testing is not exact and is only “...a balance between science and judgment.”¹¹ It is therefore necessary to develop better LALTs that more accurately mimic and predict service life. As described above, current approaches for developing improved LALTs are flawed in their a) use of trial and error to adjust testing parameters, b) failure to evaluate the impact of individual ESFs on corrosive processes, c) over-reliance on visual inspection methods, d) dependency on the ASTM B-117 in the comparison of new LALT performance to industry standards, and e) lack of predictive modeling that could be applied to multiple coating systems or closely related alloys. To overcome these issues and improve the process of creating future LALTs, engineers should focus first on understanding the influence of ESFs on the rates and unit processes of degradation of the coating and substrate. This understanding can only be gained if high level surveillance methods are used to compare corrosion products, morphologies, and processes between the lab and field. Second, engineers should create empirical models relating corrosion of coated systems (e.g., scribe creep) to specific levels and combinations of environmental severity factors. Such models give insight into the behavior of the system being modeled and could ultimately guide the creation of improved LALTs.

1.2.4 Use of Models in Atmospheric Corrosion

A number of expressions have been constructed to relate mass loss of bare steel to ESFs.²¹⁻²⁷

Mass loss is used as a measure of severity of corrosive attack in the environment. One example for unsheltered weathering steel is given in Equation 1.1: where ML is mass loss in g/m², t is time in years, [SO₂] is the concentration of gas in µg/m³, RH is % relative humidity and T is temperature in degrees Celsius.²¹

$$\ln(ML) = 3.54 + 0.33 \ln(t) + 0.13 \ln[SO_2] + 0.020RH - 0.036 (T - 10) \quad 1.1$$

Such equations are useful in predicting corrosion rates for various exposure locations.

Similar equations have been used in other dose-response type equations for bare steel in different environments. A brief list of some of those equations is given in Table 1.3.

Table 1.3 Table of empirical equations for corrosion rate from various sources.

Equation	Constants	Environment	Reference
$C = 4.15 + 0.88T - 0.073\%RH - 0.032RF + 2.913[Cl] + 4.921[SO_2]$	C=Penetration rate (mm/yr), T=temp in C, %RH=relative humidity, RF=rainfall (mm/month), [Cl]=conc. of Cl ⁻ (ppm), [SO ₂]=SO ₂ dep. rate (mg/dm ² /day)	Japan, industrial	28
$C = 5.61 + 2.754[Cl] + 6.155[SO_2]$	C=Penetration rate (mm/yr), [Cl]=conc. of Cl ⁻ (ppm), [SO ₂]=SO ₂ dep. rate (mg/dm ² /day)	Japan, marine	28
$C = C_0 \exp(-\beta x) + A$	C=mass loss rate (g/m ² -yr), C ₀ and β = constants, x=distance from shoreline (m), A=corrosion rate at zero salinity	Lagos Nigeria, Aracaju Brazil, Western Cuba, Digha and Mandapam Camp, India and Murmansk Russia	29
$\ln(ML) = 3.54 + 0.33 \ln(t) + 0.13 \ln[SO_2] + 0.020RH - 0.036(T - 10)$	ML=mass loss (g/m ²), t=time (yr), [SO ₂]=conc. of gas (μg/m ³), RH=relative humidity, T=temp (°C)	Average of many sites across Europe and North America	21
$C = ABt^{B-1}$	C=Penetration rate (μm/yr), A,B=constants, t=time (yr)	Bethlehem PA, Newark NJ, Saylorsburg PA, Kure Beach N.C.	30

Dose-Response type models for scribe creep that incorporate multiple ESFs have not been created yet. Several models have been developed which relate the rate of scribe creep to individual corrosive factors such as NaCl concentration.²⁶ Other models were developed using scanning Kelvin probe (SKP) results on polymer coated iron continuously immersed in deaerated phosphorus- or sulfur- based acid solutions.²⁷ However, these models do not take into account real-world conditions such as temperature or relative humidity, cycling, exposure to UV or dissolved oxygen in the electrolyte.

A model that could estimate scribe creep based on ESFs would be of great use to the corrosion community. By gaining a better understanding of the effects of ESFs through high level surveillance and efficient experimentation a model of scribe creep could be constructed that would provide guidance for the creation of new LALTs from the “bottom up.”

1.3 **Scribe Creep Mechanisms for Steel**

Steel, an alloy ubiquitous in structural and defense applications, is vulnerable to scribe creep. Scribe creep is the loss of adhesion of the organic coating and underpaint corrosion proceeding away from a defect or scribe.³¹ There are two general forms of underpaint corrosion on carbon steels: cathodic disbondment and corrosion product wedging or oxide lifting.³² In cathodic disbondment, water and oxygen penetrate the coating through micro or macro defects in the coating where they come in contact with the substrate.^{31, 32}

Hydroxyl ions are formed by the reduction of oxygen and water (Equation 1.2) which then break the bonds between the coating and the substrate causing disbondment.³² The accompanying anodic reaction is the dissolution of iron at the site of the defect (Equation 1.3) and is coupled to the nearby cathode, which is under the coating surrounding the defect (see Figure 1.3).³²

Corrosion product wedging occurs when accumulated corrosion products, which occupy more volume than the metal, exert stresses which reduce the adhesive strength of the coating (see Figure 1.3).^{32, 33} The lifting action of oxides and the subsequent undercutting is

seen with wet-dry cycling, and not in continuous immersion.³² It is believed that the reason for this is that colloidal corrosion products are deposited during drying and then do not dissolve upon rewetting.³² It is this constant buildup of corrosion products under the coating that leads to corrosion product wedging as shown in Figure 1.3. When corrosion product wedging occurs, scribe creep is caused by the mechanical stress of the corrosion products exceeding the adhesive strength of the coating to the substrate.

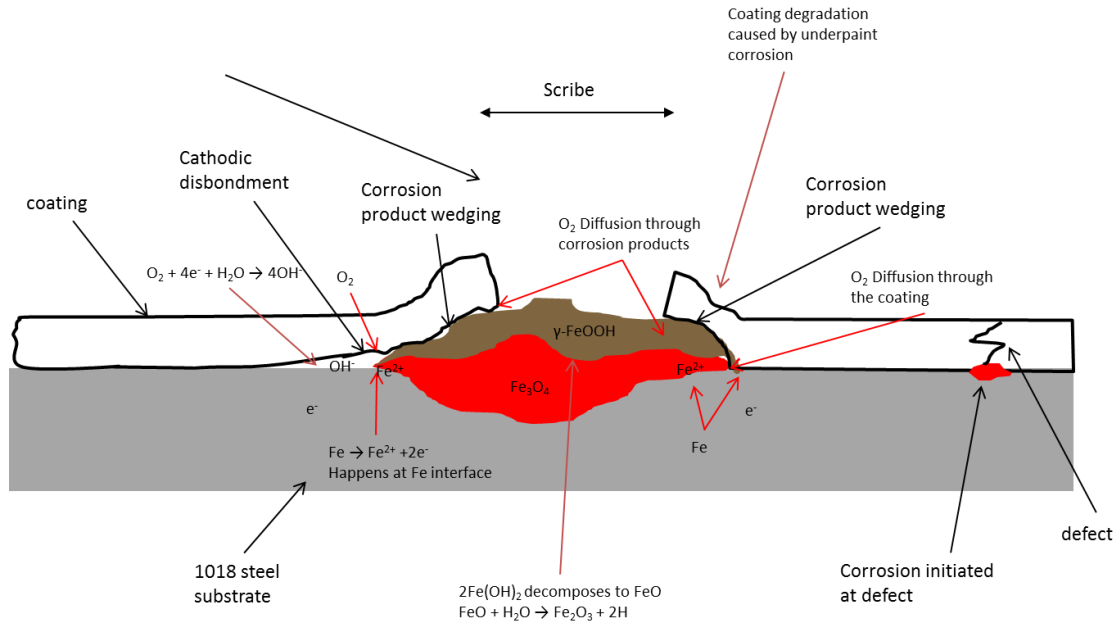
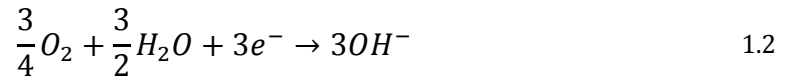
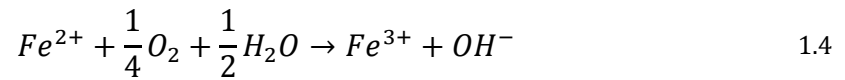
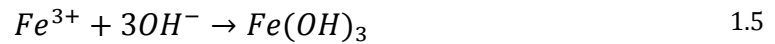


Figure 1.3 Schematic of cathodic disbondment and corrosion product wedging on organically coated steel.³²

Another form of corrosion commonly seen in organically coated steel is filiform corrosion (FFC). Because iron has two oxidation states (Fe^{2+} and Fe^{3+}) and can form various oxides and hydroxides, the mechanism of FFC is somewhat complex. Iron dissolves at the head of the filament to Fe^{2+} (Equation 1.3) where there is less oxygen. These ions then move to the back of the head where there is more oxygen and are further oxidized to Fe^{3+} (Equation 1.4).³⁴



FCC filaments in iron have a noticeable V shape that separates the head of the filament from the tail (visible in Figure 1.4).³⁵ It has been suggested that the cause of this V-shaped region is a membrane of $Fe(OH)_3$ (Equation 1.5).³⁶



The ferric hydroxide can further react to form ferric oxide corrosion product (Equation 1.6).³⁴

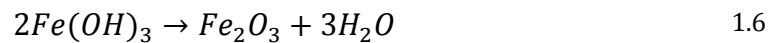


Figure 1.4 shows an optical micrograph that shows structure of a growing filament on epoxy coated 1045 steel.³⁵

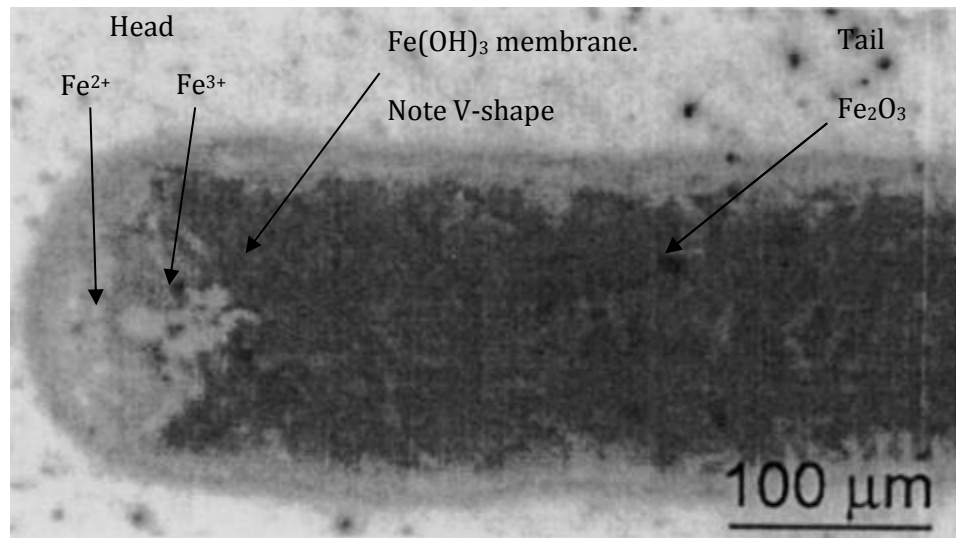


Figure 1.4 Optical micrograph showing the structure of a growing filament on an epoxy coated 1045 carbon steel.³⁵ A distinct transition region between the head and the tail can be seen with a noticeable V-shape. This may be a $\text{Fe}(\text{OH})_3$ membrane.

Although the mechanisms of cathodic disbondment, anodic wedging and FFC are well defined,^{31, 32} the effects of environmental severity factors on these processes are not well understood. ESFs that attack the coating specifically, like ozone and UV, could cause defects that allow the penetration of water and oxygen. Other factors that attack the substrate, such as chloride, could facilitate the accompanying anodic reaction at the defect. It is therefore necessary to elucidate the impact of individual ESFs on unit corrosive processes that affect scribe creep.

1.4 Influence of Environmental Severity Factors on Scribe Creep and Bare Steel Corrosion

Literature on the corrosion of coated metal systems and LALTs has provided a number of ESFs that affect corrosion of bare metals and underpaint corrosion. However, the singular

effects of isolated corrosion drivers on coated metal systems are poorly understood. To address this issue, this thesis has investigated the following ESFs individually and in combinations. A brief review of the effects of ESFs on organic coating degradation and metallic substrate corrosion is presented.

1.4.1 Temperature

Temperature is known to increase the rate of chemical reactions, including corrosion reactions.³¹ The reaction rate of a corrosion reaction approximately doubles for each 10°C rise in temperature for all types of corrosive attack.³⁷ Additionally, not only does temperature itself affect the corrosion rate, but increased temperature also increases the corrosivity of other environmental factors.³⁸ For example, in a study of temperature and sulfur dioxide on mild steel, it was found that the change in corrosion rate caused by a specific increase in sulfur dioxide was greater at higher temperatures (Figure 1.5).³⁸ Many standard LALTs, including the ASTM B-117, ASTM D-5894, and the ASTM G-85 Annex 1 through Annex 5, specify elevated temperatures.^{15, 39, 40} The effect of temperature is of considerable importance in atmospheric exposures where the temperature cycles throughout the day and throughout the year. Most models of the atmospheric corrosion of bare steel have temperature as an integral component, like the model given in Equation 1.7 (where ML is mass loss, t is time, $[SO_2]$ is the concentration of SO_2 , RH is the % relative humidity, and T is temperature).^{21, 28, 29}

$$\ln(ML) = 3.54 + 0.33 \ln(t) + 0.13 \ln[SO_2] + 0.020RH - 0.036 (T - 10) \quad 1.7$$

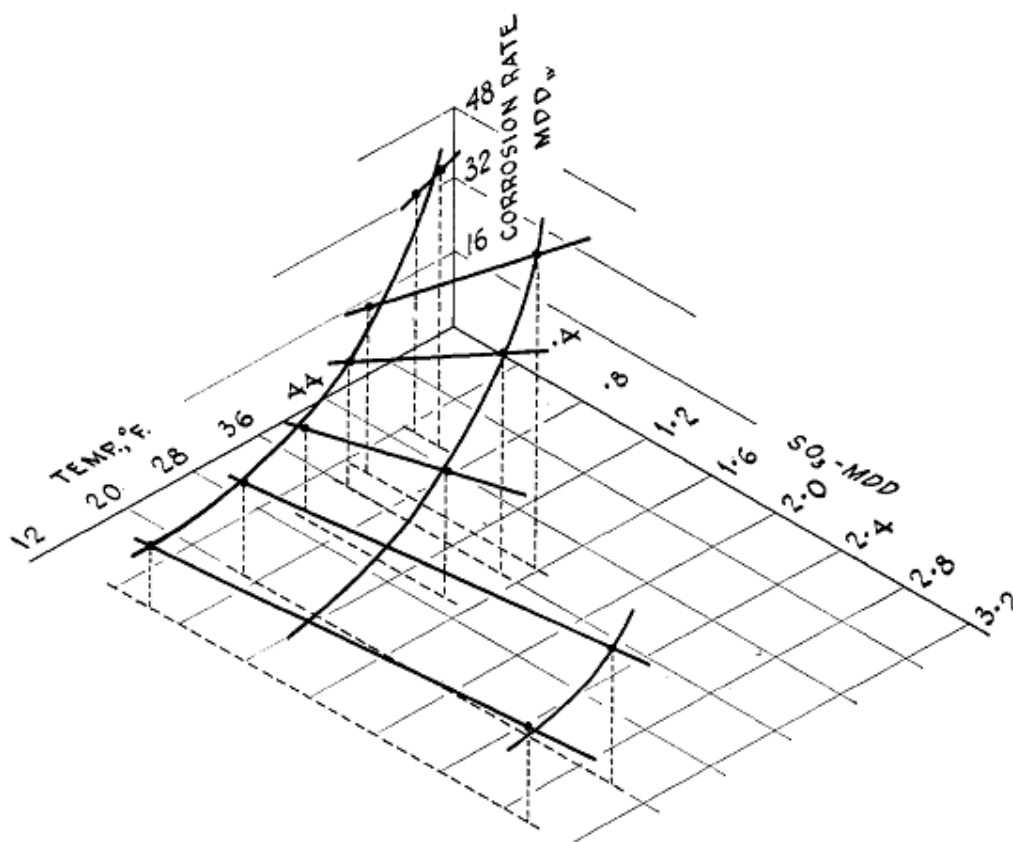


Figure 1.5 Graph showing the effects of temperature and sulfur dioxide on the corrosion rate of bare mild steel.³⁸ Reprinted with permission from P.J. Sereda, *Atmospheric factors affecting the corrosion of steel*. Industrial & Engineering Chemistry, 1960. 52(2): p. 157-160. Copyright 2014 American Chemical Society.

It is also important to consider the effect of temperature on the polymer coating. Generally, polymers have much lower melting temperatures than metals.⁴¹ Polymers have an important parameter called the glass transition temperature (T_g); the temperature at which an amorphous solid polymer transforms from a stiff state to a rubbery state.⁴¹ For the bisphenol-A (BPA) based polymer used in this study, the glass transition temperature is 149°C.⁴² This means that the mechanical and chemical properties of the polymer coating were not likely altered in any significant way by the temperatures encountered in this study.

1.4.2 pH

The effect of pH on iron is well known.⁴³ In aerated solutions at low pH iron corrodes freely, while at high pH iron forms a passive oxide on its surface (Figure 1.6).⁴³ The effect of pH on the corrosion rate of bare iron in aerated water is shown in Figure 1.7.⁴⁴ This figure shows that iron will corrode freely across much of the pH range. However, once the hydrogen evolution reaction (HER) begins (Equation 1.8), iron corrosion proceeds at a greater rate. Other reactions that often take place in corrosion can both raise or lower the pH of the electrolyte solution. For example, the oxygen reduction reaction (ORR) causes an increase in the pH either by consuming hydrogen ions in acidic solutions (Equation 1.9) or by producing hydroxyl ions in neutral or alkaline solutions (Equation 1.10).³²

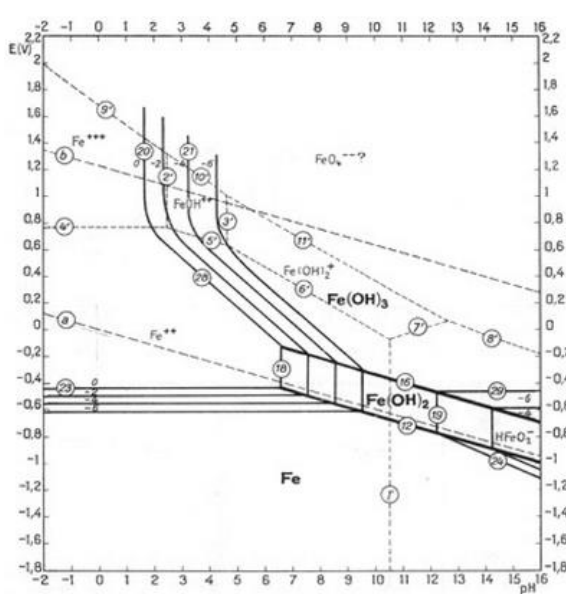


Figure 1.6 Pourbaix diagram for iron.⁴³

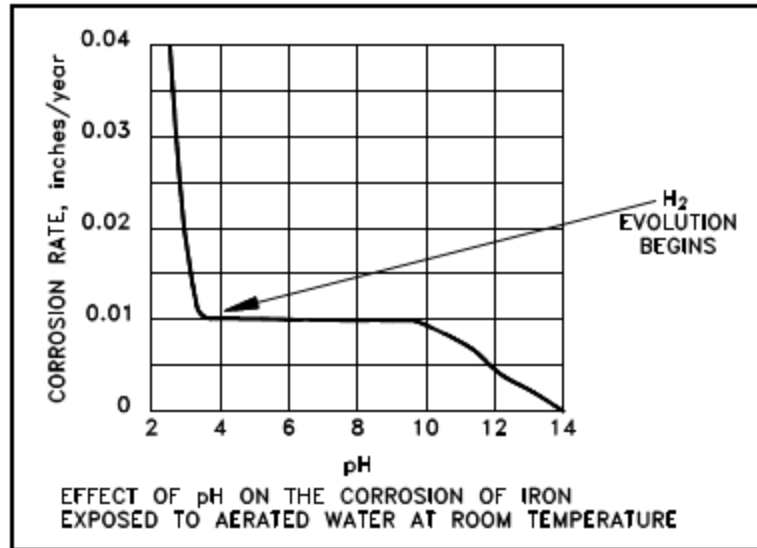


Figure 1.7 Graph of the effect of corrosion rate of bare iron as a function of pH.⁴⁴



In atmospheric corrosion there are many factors that can influence pH. An aqueous solution exposed to air will become acidic due to carbon dioxide being absorbed and converted to carbonic acid.²¹ At normal atmospheric concentrations, pure water exposed to air will equilibrate at pH 5.7.²¹ Additionally, aerosol particles in the atmosphere can introduce sulfate or nitrate species that can also lower the pH of the water layer on the surface of a metal sample.²¹ Sulfate and nitrate species can lower the pH of rainwater as

low as 4 in some marine and industrial locations, and in some instances individual droplets on the surface can become even more acidic.^{45, 46}

The effect of pH on the polymer must also be considered. Generally, polymers are more resistant to acid attack than metals.⁴¹ Many different polymer coatings, including polypropylene (PP) and polyaniline, are used to protect steels and other metals from acid attack.⁴⁷⁻⁵⁰ In one example, mild steel was coated with PP or polyethylene tetracarboxylate (PET) and exposed to acetic acid to simulate the conditions often found in canned goods.⁴⁷ It was found that PP was more resistant to acid attack and therefore protected the steel substrate better than PET. Bisphenol-A based coatings, such as the one used in this study, have been found to be resistant to attack by solutions of 10% hydrochloric acid, 10% sulfuric acid, and 2% lactic acid.⁵¹

1.4.3 UV Radiation

UV radiation was not considered in many early LALTs, such as the ASTM B-117. While it has since been found to be an important factor of degradation of organic-coated metals that are exposed in the field, it was never considered to be a significant factor in the corrosion of bare metals.^{18, 52-54} Recent work at UVa, however, indicates that UV can lower the corrosion rate of bare steel.⁵⁵ In one study, bare 1010 steel samples were sprayed with a saline solution and placed in a chamber with constant 98% RH for 100 hours. When the samples were exposed to UV light ($\lambda=340$ nm, 50 W/m²) for the duration of the test the corrosion rate was lowered from 13.03 MPY to 6.94 MPY for a salt loading density of 350 $\mu\text{g}/\text{cm}^2$ and from 11.62 MPY to 9.28 MPY for a salt loading density of 700 $\mu\text{g}/\text{cm}^2$.⁵⁵ When 8 ppm ozone

was added to the exposure chamber, UV light once again lowered the corrosion rates from 30.34 MPY to 15.53 MPY for a salt loading density of 350 $\mu\text{g}/\text{cm}^2$ and from 29.49 MPY to 21.34 MPY for a salt loading density of 700 $\mu\text{g}/\text{cm}^2$ (Figure 1.8).⁵⁵ No mechanism for this effect was proposed by the authors.

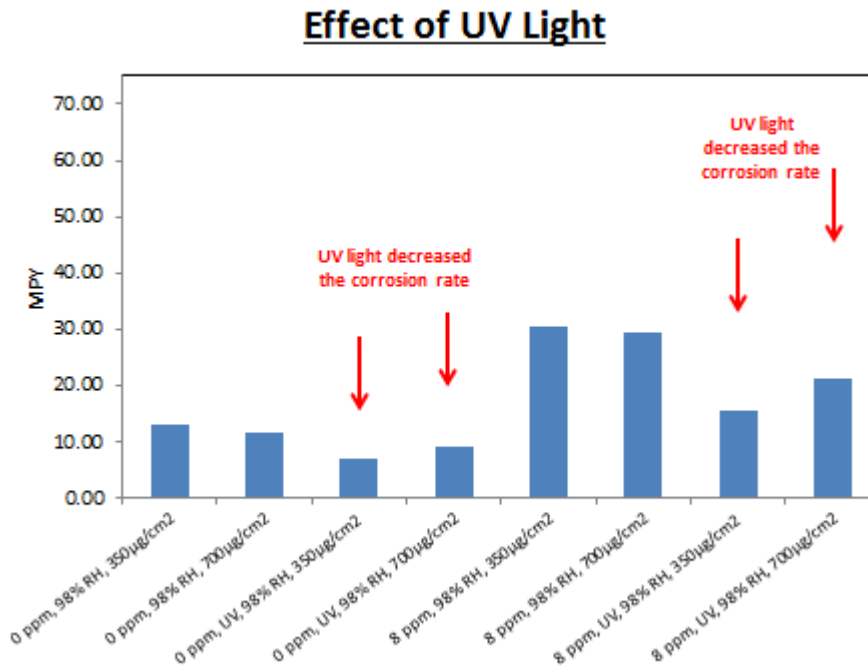


Figure 1.8 Graph of the effect of UV light ($\lambda=340\text{ nm}$) on the corrosion of bare 1010 steel at various salt loading densities with and without ozone.

UV radiation is also known to be an important factor in the degradation of organic coatings on metals in field exposures.^{18, 52-54} UV radiation reduces barrier properties of organic coatings by breaking bonds in the polymer, causing damage to crosslinking chains and polymer backbones.¹⁸ UV driven reduction in coating barrier properties has been demonstrated in previous work examining melamine ($\text{C}_3\text{H}_6\text{N}_6$) bridges that form between polymer chains as polyester resins harden.¹⁸ Coating degradation can be monitored by

tracking the change in melamine quantity with FTIR as the coating is photo-oxidized by UV radiation.¹⁸ When melamine bridges irradiated with UV light break down, a coating's barrier properties to moisture and ionic species become compromised, resulting in the formation of blisters and corrosion.¹⁸ Photo-oxidation of polymer coatings begins at the surface and progresses downward into the coating.⁵³ Studies of coated systems exposed to UV reveal that coatings that show very good resistance to blistering in ASTM B-117 are far less protective after exposure to UV radiation.¹⁸

Other work in organically coated metals demonstrates that defect area, coating permeability, and water uptake amount and kinetics increase with increased exposure to UV irradiation.^{54, 56} One study on galvanized and phosphated steel coated with a polyester resin used EIS to measure the change in pore resistance as a function of exposure to UV radiation.⁵⁷ Pore resistance has been shown to be a measure of the defect area of the coating (a lower pore resistance corresponds to a higher defect area) and can be found by modeling the surface as an equivalent electrical circuit.^{58, 59} Using this method established by earlier groups, Deflorian et al. were able to find the pore resistance. Figure 1.9 shows the change in pore resistance over time for samples immersed in 5% sodium chloride solution for three different UV irradiation times. From Figure 1.9, it can be seen that the defect area of the coating increases with increased exposure to UV radiation. This is attributed to the photo-oxidation of the coating polymer causing defects (which the authors assumed to be micro-cracks) where corrosion can initiate.⁵⁷ Therefore, the primary effect of UV light on organically coated metals is degradation of the coating.

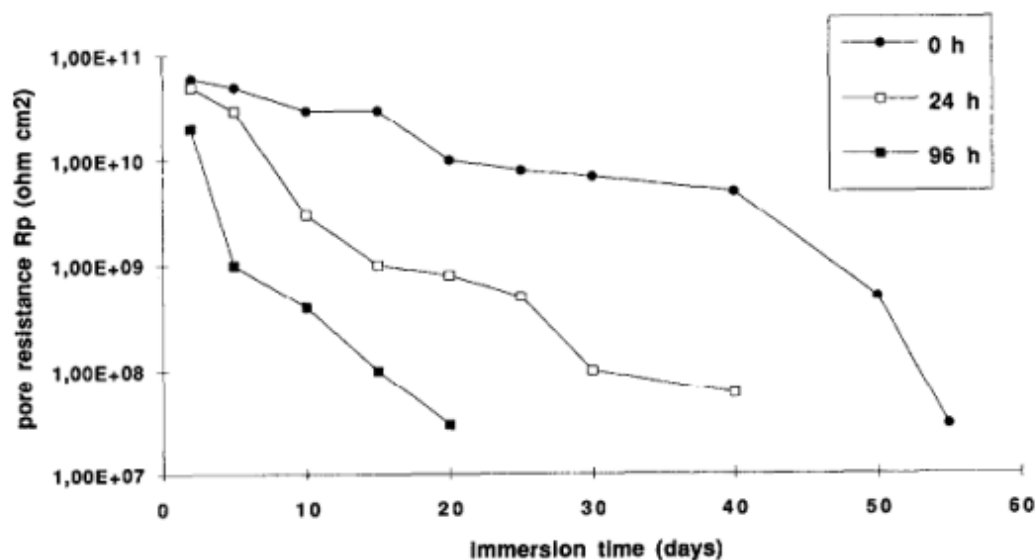


Figure 1.9 The pore resistance for polyester resin-coated galvanized and phosphated steel as a function of time. Three different UV irradiation times are shown. The samples were immersed in 5% sodium chloride solution.⁵⁷

1.4.4 Ozone

As a strong oxidizer, ozone can cause the corrosion of bare unalloyed carbon steel by itself.^{55, 60, 61} Other work with ozone and UV on silver found that ASTM B-117 with UV and ozone added produced corrosion products that matched those seen in field exposures, unlike ASTM B-117 without ozone and UV.⁶² Recent work with bare 1010 steel loaded with NaCl on the surface and placed in a controlled humidity chamber shows that 4 ppm greatly increases the corrosion rate (Figure 1.10).⁵⁵ However, when the ozone level is raised to 8 ppm, the corrosion rate is lower than with 4 ppm ozone (Figure 1.10).⁵⁵ The authors proposed that the ozone may have a passivating effect on the steel (e.g. the ozone may be creating a passive oxide on the surface).

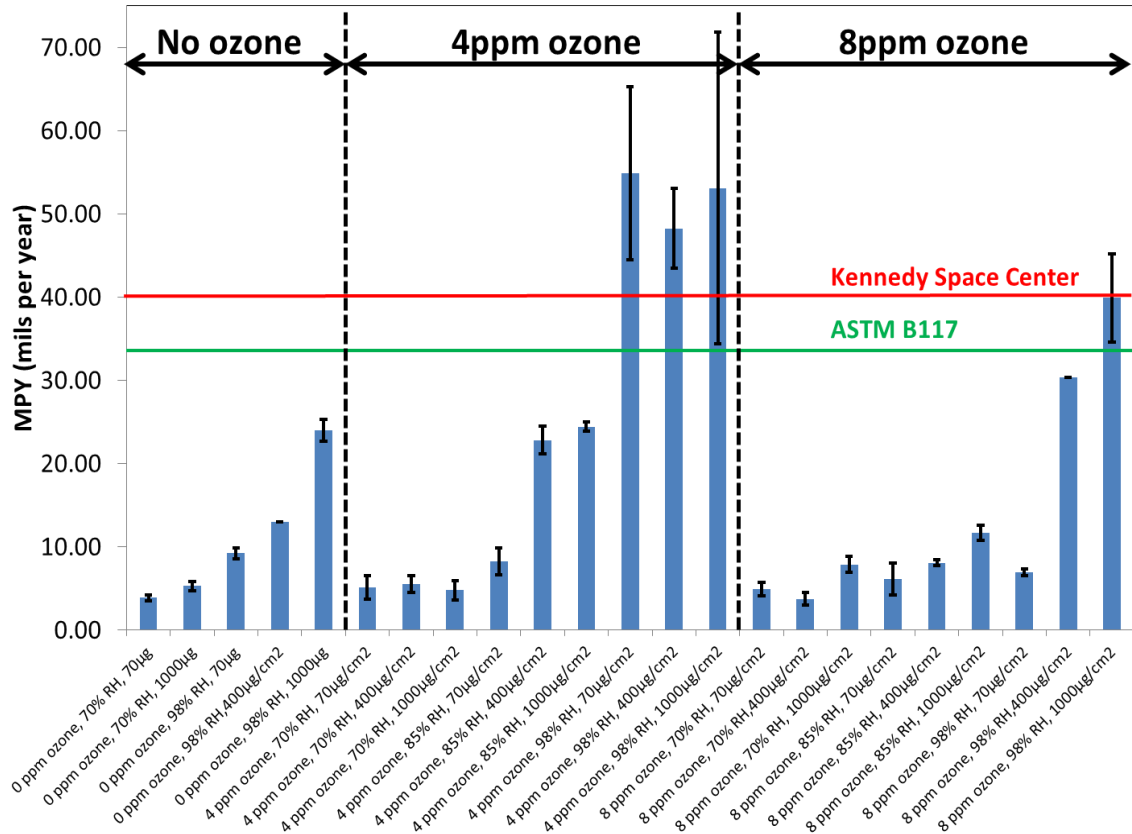


Figure 1.10 Graph of the corrosion rate of bare 1010 steel at various relative humidities and salt loading densities for three ozone levels. The colored lines across the graph show the corrosion rates of bare steel at Kennedy Space Center and in the ASTM B-117. Figure adapted from ⁵⁵.

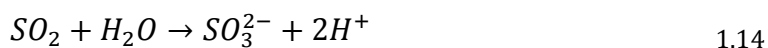
Ozone has also been shown to increase corrosion rates on bare steel by turning nitrogen dioxide (NO_2), a gaseous pollutant in the atmosphere, into nitric acid (HNO_3) (Equations 1.11, 1.12 and 1.13).⁶⁰





The oxidation of NO₂ to NO₃ by ozone occurs in the gas phase (Equation 1.11), as does the reaction of NO₃ with NO₂ to form N₂O₅ (Equation 1.12). N₂O₅ is a relatively unstable molecule and reacts quickly with H₂O in the air or in the aqueous film on the surface of the metal to create nitric acid (Equation 1.13).⁶⁰

Ozone can also react with sulfite ions (formed when sulfur dioxide reacts with water) in the water film to create sulfate ions, a known corrosion driver (Equation 1.14 and 1.15).⁶⁰



Ozone has been found to concentrate nitrogen- and sulfur-based corrosion species on the surface of steel,⁶⁰ even when the concentration of these species in lab air is 10 ppb and 0.6 ppb, respectively. Additionally, a study of atmospheric exposure of weathering steel found that as SO₂ concentration in the atmosphere decreases due to increased environmental air pollution standards, the influence of ozone on the corrosion of steel becomes more pronounced.²² On aluminum, 10 ppm ozone caused more material loss and a lower surface water film pH than sulfur- and nitrogen-based pollutants at equal amounts (Figure 1.11).⁶¹ The lower surface water film pH is believed to be caused by the fast oxidation of NO₂ by ozone.

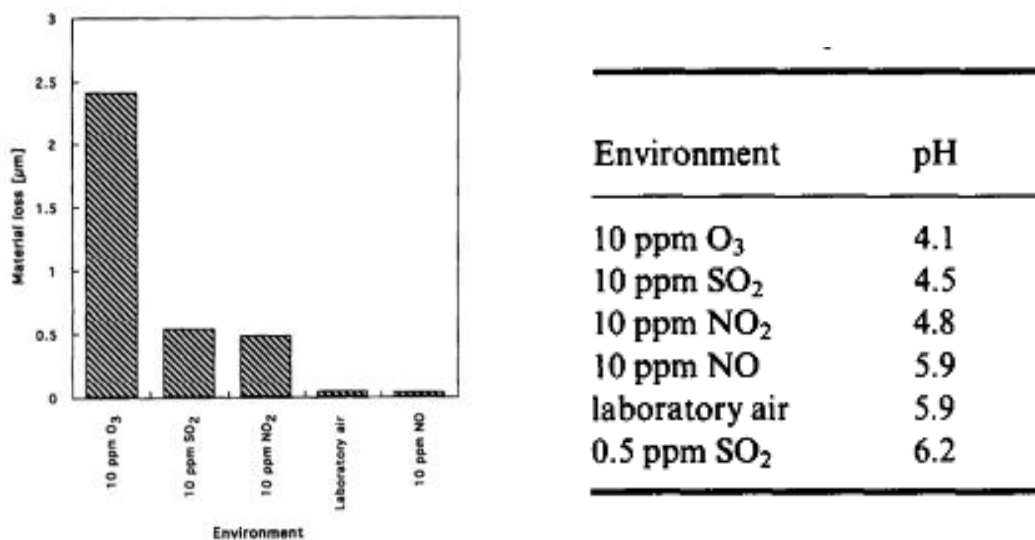


Figure 1.11 Graph showing the relative material loss of pure aluminum exposed to different pollutant gases (left), and a table showing the pH of the surface water films produced in each exposure environment (right) after 4 weeks of exposure.⁶¹

Although no studies of the effects of ozone on the corrosion of organically coated steel have been completed to date, there is literature on the effect of ozone on polymers. Ozone preferentially attacks double bonds found in many polymers.⁶³⁻⁶⁵ The oxidation of the double bonds in the polymer backbones and the crosslinking chains in organic coatings causes embrittlement of the coating.⁶⁵ Additionally, ozone has been shown to initiate chain oxidations, i.e., the reaction of ozone with polymers produces peroxyradicals that further oxidize the base resin and binders.⁶⁴ This damage to the coating creates defects where water and other ESFs can come into contact with the metal substrate and initiate corrosion. Studies of the effects of ozone on bisphenol-A in aqueous solution show that ozonation of water can break down BPA in water.⁶⁶⁻⁶⁸ However, to date there are no studies on the effects of ozone in the gas phase or dissolved in water on solid BPA. In summary, ozone is a very reactive ESF that can attack both the organic coating and the metal substrate.

1.4.5 Chloride

The addition of chloride ions has long been used in LALTs for steel alloys for many reasons. Chlorides are one of the principle pollutants in atmospheric corrosion and can accelerate the corrosion rate of metals by several orders of magnitude.⁶⁹ They are found in abundance in marine and coastal regions in the form of aerosol particles from the ocean, as well as in industrial areas from pollutant gases.⁶⁹ In temperate climates, chlorides come from de-icing salts used on roadways in urban areas. Chloride salts often dissociate in water films that form on the surface of metals exposed to the atmosphere creating an electrolyte solution, which is needed for corrosion to take place.⁶⁹ The concentration of chloride in the film or in droplets on the surface of the metal depends on %RH, with concentration increasing as %RH decreases (Figure 1.12).⁷⁰ Chloride ions have a high diffusivity and interfere with passivation.⁷¹ By compiling data from different sources, Feliu et al. showed the strong correlation between chloride deposition rate and corrosion rate on bare steel (see Figure 1.13).²⁹

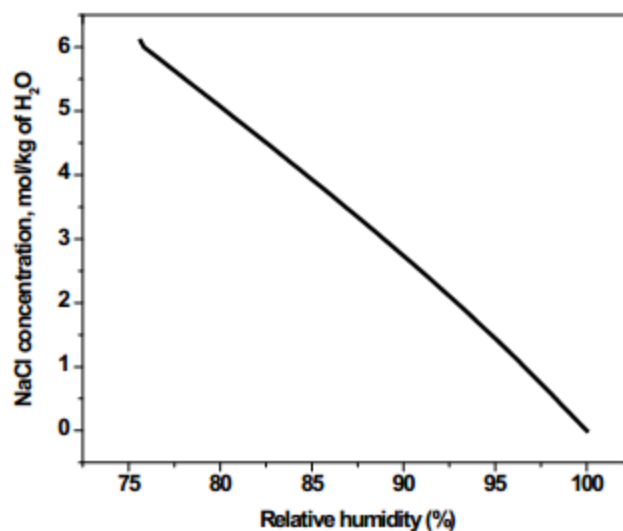


Figure 1.12 Concentration of NaCl in water droplets as a function of %RH. Values predicted using OLI software.⁷⁰

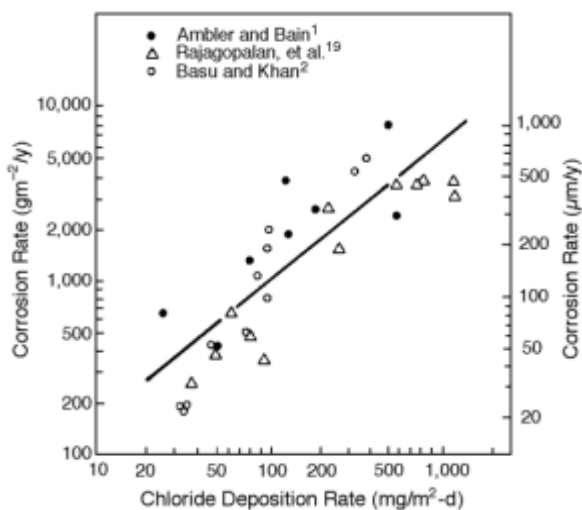


Figure 1.13 The effect of chloride deposition rate on mild steel corrosion rate in atmospheric exposure.²⁹ The authors combined data from many literature sources.

There is some literature on the effects of ions on polymer coatings.⁷²⁻⁷⁷ However, these works mainly look at the effect of positive ions on the coating. One study compared chloride salts to the delamination rate of polybutadiene coatings on steel.⁷⁷ It was shown

that the delamination rate correlates with the diffusion coefficient of the chloride ions in the electrolyte solution (Figure 1.14).⁷⁷ However, the effect was shown to be caused by the cation in the electrolyte and that any effect of the chloride ion was indistinguishable.⁷⁷ A later study proposed that the correlation of diffusion coefficient to delamination rate was due to galvanic current between the local anodes and local cathodes and was only possible if cations could be transferred from the anodes to the cathodes.⁷⁸ Another study showed that sodium ions (from NaCl) degrade polybutadiene coatings by either ion exchange reactions in the coating or by breaking the bonds at the polymer/metal interface.⁷³ When the polymer was exposed to BaCl₂ the same effects were not seen, ruling out the Cl⁻ ions as the cause of the coating degradation.⁷³ Other work showed that when mild steel coated with polybutadiene was polarized to -0.8 V vs. Ag/AgCl, not only was the rate of cation migration through the coating increased, but the rate of Cl⁻ ion migration increased as well.⁷⁴ The authors proposed three possible explanations: 1) the accumulation of positive charge at the coating/metal interface attracted the Cl⁻ anions, 2) the applied potential may enlarge minute pores in the coating allowing for greater diffusion rates, or 3) applied cathodic potential increased the diffusion rate of water through the coating, and the solvated Cl⁻ anions diffused with the water.⁷⁴ Lastly, a study of poly(methyl methacrylate) (PMMA) polymer for slow-release medicine applications showed that 0.1 M Cl⁻ slowed the diffusion rate of water through the coating, though no explanation was given.⁷⁹ There are no known studies on the effects of chloride ions on BPA specifically. In summary, chloride is very corrosive to the metal substrate in organically coated steel, but has an uncertain effect on the coating itself.

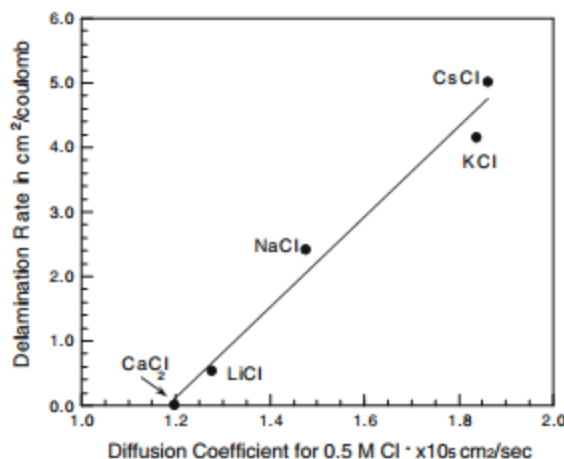


Figure 1.14 Plot showing the correlation of delamination rates of polybutadiene coatings on steel with the diffusion coefficient of the electrolyte in solution.⁷⁷

1.4.6 Relative Humidity and Time of Wetness

Electrochemical corrosion cannot occur without an electrolyte.^{21, 80, 81} The usual electrolyte is composed of thin films of water with impurities on the surface of the metal.⁸¹ In regards to atmospheric corrosion, it is important to know how often the surface of a metal is wet. Surfaces can be wetted by rain or dew. Water films can also form on the surfaces of metals due to humidity in the atmosphere.²¹ This has led to the concept of Time of Wetness (ToW). ToW is defined many different ways, but perhaps it is best defined by Leygraf et al. as “time during which a corrosion stimulating film exists on the surface.”²¹ Many aerosol particles that accumulate on metal surfaces are hygroscopic and absorb water from the atmosphere. Called deliquescence, this phenomenon can cause the surface of the metal to wet at a lower relative humidity than would be expected for a clean, bare metal surface.²¹ The deliquescence of hygroscopic species on a metal surface can cause corrosion at low relative humidity. Study of the relationship between relative humidity and deliquescence led to the development of the concept of critical relative humidity (% RH_{crit}). Vernon first observed

the existence of critical relative humidity in studies of bare copper exposed to varying levels of humidity and sulfur dioxide (SO_2), a common pollutant.^{82, 83} Samples were exposed at five different %RH levels; 50%, 63%, 75%, 99% and 100%. A “profound” difference in corrosion rate was found between 63% and 75% RH when sulfur dioxide was added to the exposure atmosphere. This was true for all levels of sulfur dioxide tested. The % RH level at which corrosion rate sharply increases is called the critical humidity. This critical humidity is the humidity level at which hygroscopic particles begin to absorb water from the air.^{82, 83}

Time of Wetness, however, is very difficult to accurately measure due to the following reasons. As noted above, different aerosol particulates that can be present on the surface of a sample deliquesce at different relative humidities. For example, the deliquescence point of NaCl is 75% RH.⁸⁴ For other common aerosol particles such as $(\text{NH}_4)_2\text{SO}_4$, NH_4Cl and $(\text{NH}_4)\text{HSO}_4$ the deliquescence points are 79%, 77%, and 39% respectively.²¹ Additionally, a fully dry NaCl particle will deliquesce at 75% RH, but a wetted NaCl particle may not fully dry out until 43% RH, allowing corrosion to continue below the deliquescence point of NaCl (Figure 1.15).⁸⁵ Another issue is that the wettability of the surface can change. For example, the wettability of water is much greater on rust than on bare steel, causing droplets to spread out more on rust than on bare steel.⁸⁶ Lastly, ToW sensors are limited in their practical ability to sense time of wetness. A common ToW sensor is an interdigitated array of metal electrodes embedded in an insulator (Figure 1.16).⁸⁷ When the electrodes are bridged by a water droplet or film, the electrical connection is completed and the sensor records the surface as being wet. However, the issues noted above, deliquescence and efflorescence, and the changing wettability of a corroding surface versus the wettability of

the metal electrodes or the insulator between them can cause discrepancies between the ToW measured by the sensor and the actual time that the sample is in a corroding state.⁸⁸

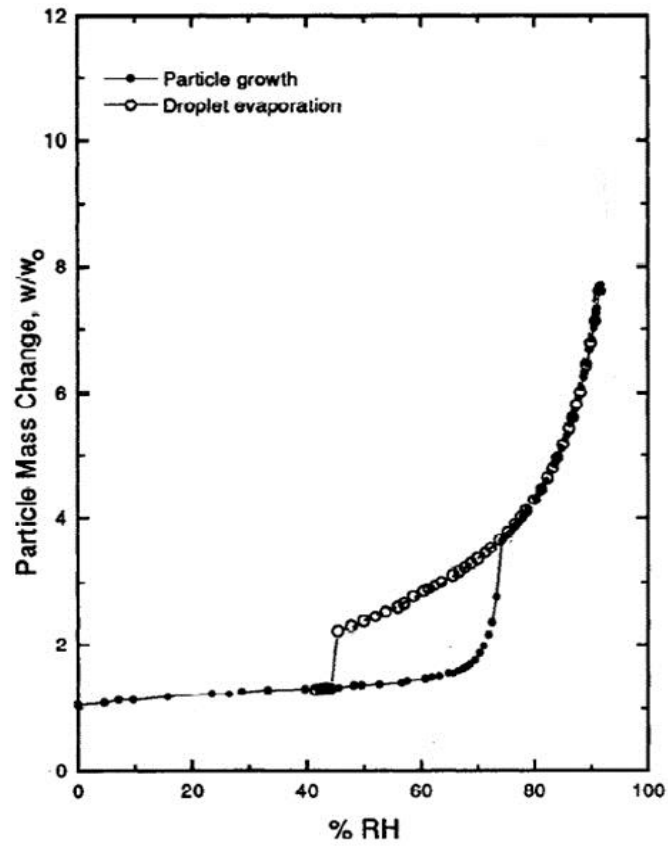


Figure 1.15 Graph of mass change of a sodium chloride particle with respect to relative humidity. The deliquescence point is 75% RH and the efflorescence point is 43% RH.⁸⁵

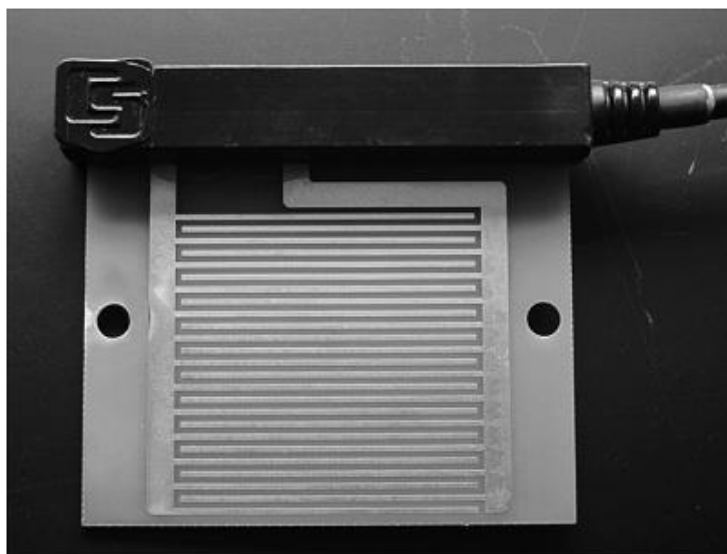


Figure 1.16 A Campbell Scientific 237L leaf wetness sensor.

Water vapor from the air can also be absorbed by polymers.⁸⁹⁻⁹¹ One study used fluorescent tracer molecules to track the changes in plasticity as a function of % RH in poly(vinylpyrrolidone) (PVP) films on glass substrates (Table 1.4).⁸⁹ It was found that at %RH above 50% the tracer molecules became mobile and were able to diffuse through the PVP and that as the % RH increased, more molecules were able to move.⁸⁹ This is because the water acts as a plasticizer, causing the film to swell and increasing the distance between the polymer chains, which makes the material more flexible.⁹¹ This uptake of water also allows dissolved ions to migrate through the coating, which in the case of coated metals, can cause corrosion initiation at coating defect sites.⁷⁴ Another study on the effects of cure time on bisphenol-a based epoxy resin sheets found that as the relative humidity increased, the equilibrium moisture level in the epoxy increased as well.⁹²

Table 1.4 Table of the mobility of fluorescent tracer molecules in PVP films as a function of %RH.⁸⁹ Numbers indicate the fraction of tracer molecules undergoing each kind of motion.

	Category of Motion			
RH (%)	Immobile	Confined Motion	Subdiffusion	Normal Diffusion
20-50	0.96	0.04	0	0
~55	0.64	0.31	0.04	0.01
60±2	0.23	0.06	0.47	0.24
75±2	0.08	0.04	0.57	0.31

1.4.7 Wet/Dry Cycling

When discussing the quantification of ESFs it is important to note that cycling is a different type of corrosion driver. ESFs such as chloride levels and UV exposure can be easily and accurately quantified. However, cycling is an action and must be expressed in terms of other quantities. For example, if we were to quantify running, we would do it in terms of distance covered or time spent running, but to directly quantify running in terms of itself has no actual meaning. Therefore, it is important that cycling is clearly defined in this work and is directly comparable to field exposure. As has been shown previously, the cycling of many different ESFs can play a role in the scribe creep of coated metal systems. To cycle every ESF that may have an effect on scribe creep rate and then quantify the effects would be a large task and is not in the scope of the current work. Wet/dry and temperature cycling are almost always encountered in the field. For steel, wet/dry cycling appears to

have the greatest effect on the scribe creep rate, while temperature appears to have a lesser effect.⁹³ In this work cycling was quantified by the effect of wet/dry cycling on scribe creep rate.

Materials exposed to the environment experience many natural cycles. Day and night leads to a cycling of UV irradiation, as well as temperature and humidity. Cycling in LALTs provides results that are closer than non-cycling LALTs to field results, as demonstrated in the following examples. Wet/dry cycling has been shown to increase the adhesion degradation and delamination of organic coatings on mild steel.⁹³⁻⁹⁵ The reason proposed for this is that during continuous exposure to salt spray the corrosion products at the scribe creep front are washed away, so there is little mechanical lifting of the film.⁹⁴ In contrast to wet/dry cycling, the corrosion product is able to precipitate during the dry cycle, resulting in much more voluminous corrosion product at the scribe creep front.⁹⁴ This corrosion product wedge creates more potential paths for oxygen and electrolyte to diffuse to the scribe creep front and exerts a mechanical stress on the coating.^{94, 95}

Wet/dry cycling has also been shown to increase the corrosion rate of bare metals.⁹⁶⁻⁹⁸ Using a Scanning Kelvin Probe (SKP), Stratmann et al. were able to show that the corrosion rate of pure iron increases as the metal surface dries.⁹⁷ As the surface electrolyte layer becomes thinner, salts concentrate and oxygen diffusion through the electrolyte becomes faster and allows for an increased corrosion rate.⁹⁷

Wet/dry cycling can also have an effect on polymers. In a recent study, the behavior of a commercial polymer membrane for fuel cells was subjected to repeated wet/dry cycles.⁹⁹

The membrane was mounted in a frame and subjected to cycles consisting of two hours at 90% RH and two hours at near 0% RH, both at 70°C. After 136 cycles, it was found that the mechanical strength of the membrane had decreased by roughly 15%. It is believed that the repeated swelling and shrinking of the membrane caused mechanical stress that degraded the mechanical strength.⁹⁹ For bisphenol-A based polymer films, there are no known studies on the effects of repeated wet/dry cycling.

For these reasons, wet/dry cycling is believed to be an important factor in scribe creep, but observation based empirical studies are unclear.

1.5 Overall Critical Unresolved Issues

To date, there has been little systematic variation and evaluation of corrosion drivers in the lab or field to study the effects of each ESF on the processes controlling scribe creep.

Although a few examples of individual corrosion drivers can be found in the literature, overall, widespread systematic studies have not been performed. Often, all the drivers that may affect a system have been “lumped together” in some combination at relatively high levels, which comprises the LALT.^{14, 100} As a result, LALTs are typically much more severe than field environments. The conventional notion has been that good coating performance in the severe LALTs will mean good performance in the comparatively benign field, even if the drivers differ. However, in reality combining all drivers obscures the impact of individual corrosion drivers on substrate corrosion and impairs understanding of the effects of individual corrosion drivers on the degradation of the coating itself, as well as the interactions between the coating and the substrate during the degradation of the system.

Moreover, many studies rely on visual inspection or a few limited interrogation methods.^{14,}

18, 100

In a coated system, the effects of corrosion drivers on the degradation of the coating itself must be studied in addition to the effects on the substrate. Factors such as UV may have a much greater effect on the degradation of the coating than on the corrosion of the metal substrate. Effects of underpaint corrosion and scribe creep on the resulting chemistry under the coating are also important aspects of the overall degradation of the coated metal system. Other factors affecting the coating are corrosion product wedging and physical damage to the coating caused by growth of corrosion product upwards into the coating. All these factors are presently poorly understood as a function of ESFs, and insight must be gained as to how they affect the degradation of the coating so that quantitative laws describing scribe creep and impedance decreases can be developed. No models that relate scribe creep length to the effects of ESFs have yet been constructed. Such models could be connected to the construction of LALTs that better mimic field environments if the relative influence of the drivers can be determined.

To accurately mimic field environments and systematically study the effects of isolated and combined corrosion drivers, a controlled cycling of the corrosion drivers is needed. There is no one lab exposure device that can cycle humidity, UV, condensation, chloride deposition and concentration of gases (e.g. ozone). Existing exposure systems must be modified and perhaps new systems made to accurately control and cycle the corrosion drivers needed for this study.

The following important issues must be resolved in order to properly begin to construct LALTs:

1. One must determine the effects of individual corrosion drivers on underpaint corrosion, scribe creep, and coating polymer degradation using high-level surveillance in order to understand their role and quantitative impact on the coating/substrate system.
2. An understanding of the combined effects of key corrosion drivers on underpaint corrosion using high-level surveillance must be gained. To do this, we must understand how the effects of corrosion drivers on the metal, the polymer coating, and the system as a whole interact to cause underpaint corrosion and scribe creep.
3. One must determine the extent of degradation of the organic coating triggered by the environment, versus degradation triggered by conditions developing at the coating/metal interface (i.e., caused by underpaint corrosion).
4. A scribe creep model based on the effects of corrosion drivers on the coating/substrate system must be developed for organically coated steel alloys. Such a model would shed light on the relative impact and interplay between various ESFs.

1.6 **Overall Problem Statement**

Field tests and LALTs to determine the service life of coated metals do not always produce the same mechanism of corrosion; specifically, field tests usually have limited agreement with the ASTM B-117 method despite its severity. A fundamental understanding of the

effects of corrosion drivers in terms of role and quantitative impact, both individually and in combination, must be gained in order to improve understanding of the differences between LALT and field exposures. Additionally, acceleration factors for many systems are unknown, even when the mode and mechanism of field and lab attack are similar.

1.7 **Overall Objective**

The overall objective of this work is to understand the role of environmental severity factors on scribe creep of coated steel in specific lab and field environments. Specific goals to accomplish this task include:

- Comparison of corrosion phenomena during standard lab tests and field exposures.
- Conduct high-level surveillance of degradation using a suite of characterization techniques suitable for both the polymer coating and the metal substrate in order to compare phenomena at the highest level possible.
- Selection of some of the ESFs important to corrosion in LALTs and field exposures.
- Setup and implementation of an experimental matrix to test the effects of selected ESFs.
- Construction of an empirical statistical model of scribe creep that accounts for selected environmental severity factors.

1.8 **General Approach**

As detailed previously in Section 1.2.3, there are many drawbacks to the traditional approaches to designing new LALTs. Briefly, they are 1) a lack of comprehensive and systematic study of the ESFs incorporated into LALTs, 2) a reliance on visual inspection and other low fidelity surveillance techniques and 3) comparing new LALTs to ASTM B-117 to determine the efficacy of the new LALT. These drawbacks must be overcome to build new and improved LALTs from the “bottom up.”

1.8.1 **A “Bottom Up” Approach**

Instead of a trial and error approach, the current study addresses the construction of LALTs in a “bottom up” fashion, whereby specific environmental corrosion factors are isolated, examined, and their effects elucidated. Ultimately, these data indicate the role and quantitative impact of specific environmental severity factors which impact the corrosion rate and thus service life of coated metal alloys.

In this study, selective testing with variation in environmental severity factors was used to identify key corrosion factors and elucidate their effects on a clear organic coating (Poly(Bisphenol A-co-epichlorohydrin) glycidyl end-capped $(C_{18}H_{22}O_3)_n \cdot C_{22}H_{26}O_4$; CAS No. 25036-25-3, trade name Eponol) and underlying steel substrate (UNS# G10180; 0.15% C, 0.7% Mn, Fe; wt. %). This clear coating system allowed for visual interrogation that would not have been possible with an opaque coating, giving real time data of the extent of scribe creep underneath the coating. Collaboration with James Rawlins and Michael Blanton at the University of Southern Mississippi (USM) School of Polymers has helped to determine

mechanism of degradation of the coating itself. USM specializes in polymer research and has the expertise and instrumentation to gather information about the coating that would not be possible at UVa. Free films were exposed at UVa and analyzed at UVa and USM to determine the environmental effects on the coatings without any coating/substrate interactions. Coated metal samples were also sent to USM to help elucidate the effects of the coating/substrate interaction on the overall degradation of the coated systems. Comparison of coating degradation mechanisms between lab and field provides insight into the overall degradation of the systems in field and LALT exposures.

The following sections present, in greater detail, how this “bottom up” approach was accomplished.

1.8.1.1 Importance of Using Multiple High-Level Surveillance Methods

In order to accurately characterize and understand the many different aspects of the metal/coating system and the processes that lead to scribe creep, many different high-level surveillance characterization techniques were used. These methods are able to give detailed characterization data about the substrate degradation, the coating (namely its molecular and electrical degradation), or both. These methods also make use of the advantages of using a clear coating system, namely that the extent of scribe creep can be monitored in real time and the morphology of scribe creep (i.e., filiform vs. a more uniform

scribe creep front) can be visualized underneath the coating. What follows here is a brief mention of each method and the reason they are used. An in depth description and detailed description of how each method was used appears in subsequent chapters. For this work, the following characterization methods have been used:

1.8.1.1.1 2D and 3D Digital Optical Microscopy

3D optical microscopy allows for the tracking and quantification of scribe creep and corroded area over time based on color change. The use of a clear coating allowed for visualization of the surface of the substrate underneath the coating that cannot be done with an opaque coating. 3D images were also used to create line profiles of the scribe lines over time. This was done to track the changes in topography as the scribe corroded and scribe creep progressed from the scribe. Figure 1.14 shows two images of a scratch on a 1018 steel sample. The left image is of a bare sample, the right is of the same sample after it has been coated with the clear Eponol coating. Figure 1.14 shows that the surface of the substrate can be easily imaged through the clear coating.

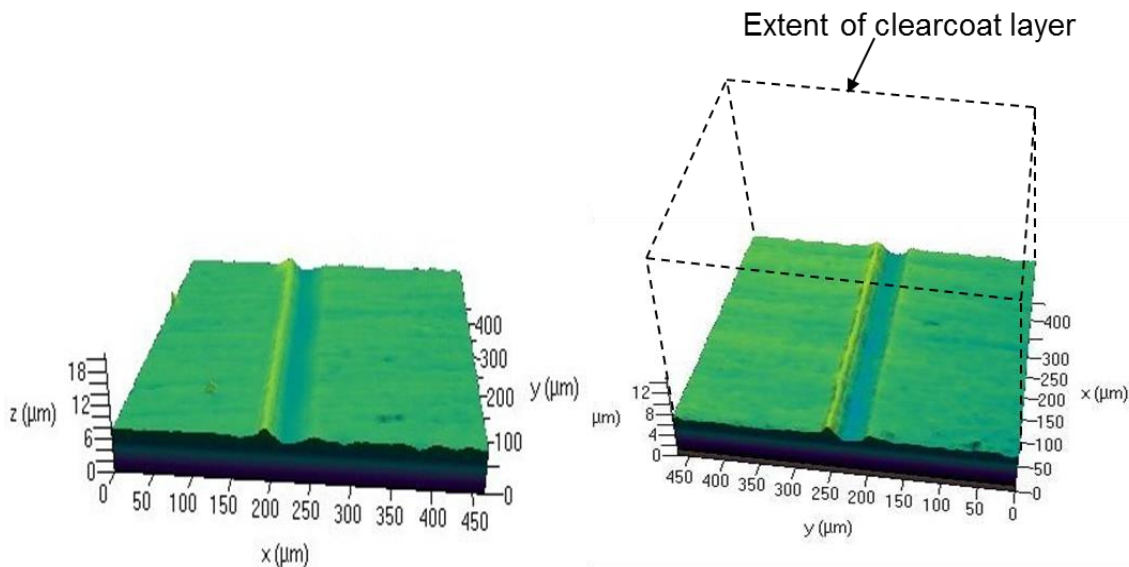


Figure 1.17 Images of a scratch on the surface of a 1018 steel sample. The left image shows the bare surface before the clear coating was applied. The right image shows the same sample after it has been coated with a clear epoxy coating. Images taken with a confocal laser scanning microscope using a HeNe laser ($\lambda = 542 \text{ nm}$).

1.8.1.1.2 X-Ray Diffraction (XRD)

XRD is a commonly used method of determining the identity of corrosion products as long as they are crystalline. XRD is quick and non-destructive and allows for an easy comparison to other studies.

1.8.1.1.3 Raman Microscopy

Raman microscopy is a surface sensitive spectroscopy method that detects the molecular identity of corrosion products. It is used to determine the species that form on the surface of the samples that are either amorphous or in limited quantities below the detection limits of XRD. Raman microscopy in conjunction with XRD allows for better detection of corrosion products than using XRD alone.

1.8.1.1.4 Fourier Transform Infrared Microscopy (FTIR)

Fourier Transform Infrared Microscopy detects molecular bonds and was used to monitor degradation of the coating over time. FTIR allows for the detection of coating degradation that is not visible with optical microscopy. Eponol films cast on inert polypropylene substrates were exposed, and, after exposure, the films were removed and analyzed. The polypropylene substrate on which the Epoxy resin coating was cast was inert, and thus has no effect on the degradation of the coating. This isolated the effects of the environment from the effects of underpaint corrosion on degradation of the coating. Degradation of the coating was observed by comparing the results of an unexposed coating to exposed coatings.

1.8.1.1.5 Electrochemical Impedance Spectroscopy (EIS)

Electrochemical Impedance Spectroscopy was used to measure the change in the electrical properties of the coating over time. EIS was performed at locations near to and far from the scribe (Figure 1.18). The measurements were conducted near to the scribe in order to sense coating damage due to corrosion, and far from the scribe to examine “intact” coatings.

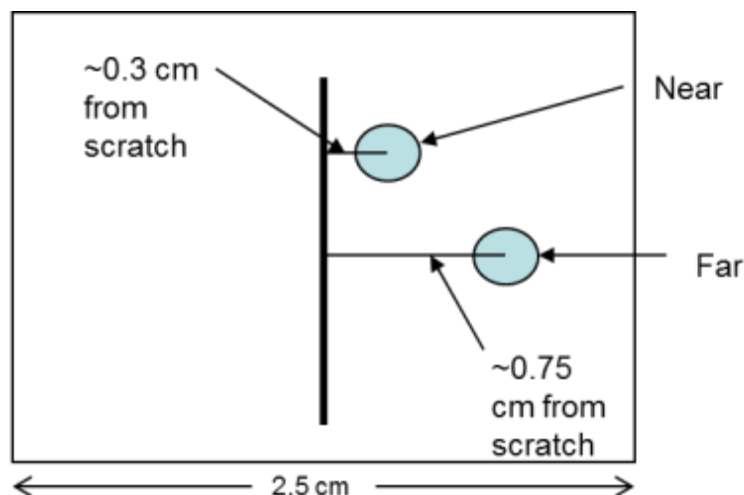


Figure 1.18 Schematic showing locations where EIS was performed on coated and scribed samples.

1.8.1.1.6 Mass Loss Test Procedure

Mass loss is commonly used to determine the corrosion severity of atmospheric exposure sites and LALTs on metallic substrates.²¹ Mass loss results show the relative severity of standard LALTs, non-standard LALTs, and field sites in terms of corrosivity. Mass loss results are also compared with scribe creep results to show the relative complexity of the processes governing scribe creep as opposed to the processes governing mass loss.

1.8.1.2 The Metal/Coating System

AISI 1018 steel (UNS# G10180; 0.15% C, 0.7% Mn, Fe; wt. %) was chosen as the substrate for all tests because it is used in many applications that require welding, forming, and machining. In collaboration with the University of Southern Mississippi, a clear epoxy resin (Poly(Bisphenol A-co-epichlorohydrin) glycidyl end-capped $(C_{18}H_{22}O_3)_n \cdot C_{22}H_{26}O_4$; Trade

name Eponol) (see Figure 1.19)) was chosen for use in coating samples of steel. The chosen epoxy resin is a high molecular weight resin used primarily as a constituent of paint coatings and is clear which allows for the visualization of corrosion underneath the coating in real time. The coating was applied to be 30 μm thick and had a high impedance of around $10^{11} \Omega\text{-cm}^2$. The choice of this clear resin as a coating for samples in field tests and LALTs allows the underpaint corrosion to be seen. It also enables interrogation of the underpaint environment by 3D optical microscopy and Raman microscopy, both of which penetrate the clear coating to interrogate the substrate.

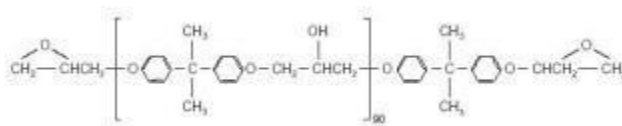


Figure 1.19 Molecular structure of the ultra-high molecular weight epoxy resin used as a coating in this study.

The surface of the metal samples were ground with 180, 240, 300, and 600 grit silicon carbide paper to remove any surface oxide, even out any imperfections and create a clean bare surface for the application of the coating. The samples were then blown with compressed air to remove any large debris from the grinding. The samples were washed with water and detergent soap and rinsed with Millipore water. After washing, the samples were immediately blown dry with compressed air. The Eponol was applied to 1018 steel samples by spin coating (early work) and by draw down bar (later work) to a thickness of 30 ± 5 microns. The latter method provided a much more uniform coating thickness. The metal samples were cured for five days in lab air and then cured at 60°C for 24 hours. After

curing, the samples were cut to 2.5 x 2.5 cm dimensions and then scribed by hand down the middle with a diamond scribe tool. Figure 1.20 shows a top-down diagram of the coated and scribed sample, while Figure 1.21 shows the sample and scribe in cross-section.



Figure 1.20 Schematic of coated and scribed 1018 steel sample.

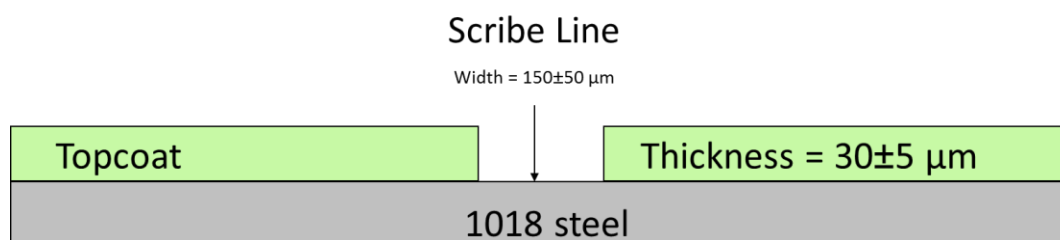


Figure 1.21 Schematic of Eponol coated and scribed 1018 steel sample. The substrate is roughly 1 mm thick and the Eponol topcoat is 30±5 µm. The scribe line is 150±50 µm in width.

Epoxy resin films were also cast on inert polypropylene substrates. These substrates were exposed along with the bare and coated metal samples and were interrogated with FTIR after exposure.

1.8.1.3 Exposure Conditions

1.8.1.3.1 LALT Environments

The suite of LALT exposure chambers includes a humidity chamber, a cyclic condensation (CC/UV) chamber, and a salt fog chamber. The salt fog chamber was modified by Ye Wan in the RGK group to include UV lights ($\lambda = 340$ nm) and an input for gases. The QUV™ allows the use of elevated temperatures, humidity and condensation cycling, and UV exposure ($\lambda = 340$ nm) in LALTs. Figure 1.22 shows the spectrum of the lamps used in the QUV™ and modified salt spray chamber compared with natural sunlight. It was also modified to enable the input of additional gases. These chambers can be used to perform standard LALTs such as ASTM B-117 and ASTM D5894, and also allow for modified versions of standard LALTs. Following a change in lab equipment, samples requiring both salt fog and UV exposure were removed from the salt fog chamber daily and dosed with UV in the QUV™ chamber. A full list and description of all standard LALTs used in this work is given in Table 1.5.

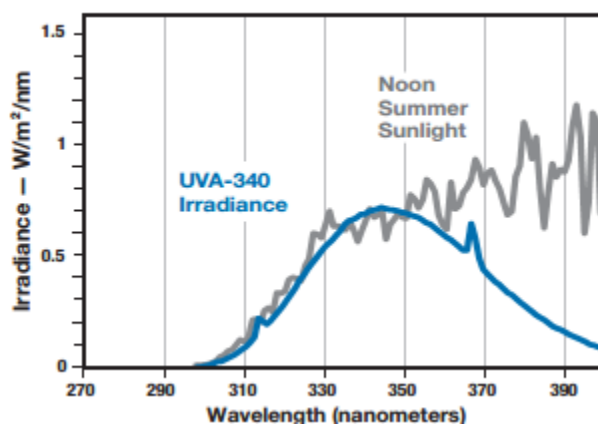


Figure 1.22 Spectrum of the lamps used in the QUV™ and salt spray chamber compared to natural sunlight.¹⁰¹ Image reprinted with permission of Q-Lab Corporation, copyright 2014 (www.q-lab.com).

Table 1.5 List of all standard LALTs used in this study.

Standard LALT	Conditions and Notes	Cl ⁻	UV	Cycling
ASTM B-117	Standard practice for operating salt spray (fog) apparatus. 5% NaCl solution, continuous spray. ¹⁵ ASTM B-117 SW used ASTM synthetic sea water solution in place of the 5% NaCl solution. ToW 75-100%	✓		
ASTM G-85 A3	Seawater acidified test, cyclic. Solution is 42 g of synthetic sea salt and 10 mL glacial acetic acid per liter of solution. $2.8 \leq \text{pH} \leq 3.0$. Test cycle is 0.5 hours spray of this solution followed by 1.5 hours soak at or above 98% RH. ⁴⁰	✓		✓
ASTM G-85 A5	Dilute electrolyte cyclic fog dry test. Test consists of two step cycles of 1 hour spray at room temperature and 1 hour dry off at 35°C. Solution of 0.05% sodium chloride and 0.35% ammonium sulfate. ⁴⁰	✓		✓
ASTM D-4587	Standard practice for fluorescent UV-condensation exposures of paint and related coatings. 4 hours of UV (340 nm) at 0.89 W/m ² at 60°C followed by 4 hours of condensation (dark) at 50°C. ¹⁰² Condensation comes from the heating of water in a tray below the samples.		✓	✓
ASTM D-5894	Standard practice for cyclic salt fog/UV exposure of painted metal (alternating exposures in a fog/dry cabinet and a UV/condensation cabinet). A combination of ASTM G-85 Annex 5 and ASTM D-4587 Cycle 2. One week of ASTM D-4587 (4 hours of UV (340 nm) at 0.89 W/m ² at 60°C followed by 4 hours of condensation (dark) at 50°C.) followed by one week of ASTM G-85 Annex 5. ³⁹	✓	✓	✓

1.8.1.3.2 Field Environments

Initially, 1018 steel samples were prepared and deployed to sites around the country. Point Judith, RI (PJ) is a harsh marine site that experiences large variations in temperature and UV irradiation through the year. Coconut Island, HI (HI) is a marine site that has relatively constant conditions all year long. Los Angeles, CA (LA) is a moderate industrial area about

three miles from the ocean. Conditions were too harsh for steel samples across all three of exposure sites listed above. After three months, the samples returned so corroded that the coating was severely degraded and little useful data could be taken from them. As a result, steel samples were sent to Kennedy Space Center (KSC), a harsh marine environment, with samples returned every two weeks for three months from November 2011 to January 2012. Steel samples were also deployed at Birdwood golf course in Charlottesville, a rural/suburban location. They were returned every two weeks for three months from April to June of 2012. A list of field sites used throughout this work and characterization data is given in Table 1.6.

Table 1.6 Environmental severity factors for field sites.

Site Location	Mean Temp °C	Mean RH (%)	Mean O ₃ Concentration (ppb)	Mean UV (W/m ²)	Mean Cl ⁻ deposition rate (mg/m ² /day)
Charlottesville, VA	15.6	64.6	47*	-	1.08
Kennedy Space Center, FL	23.6	77.2	75.3*	0.6	640

Note: “-” indicates that the data is not available. “*” indicates that the data were taken from nearby NOAA site.

1.8.1.3.3 Full Immersion Tests

Additionally, coated and bare steel samples were exposed to full immersion tests (FIT).

FITs are also a traditional method of exposure for corrosion analysis of coated systems.¹⁰³

¹⁰⁴ The FIT environment was 0.3 wt% NaCl solution, and the sample was exposed using an

ambient aerated flat cell at room temperature. The benefit of performing FITs is that the electrical potential can be controlled. This enables isolation of cathodic conditions with an applied potential of -1V vs. SCE (saturated calomel electrode), or coupled anodic and cathodic conditions with the potential allowed to float at open circuit potential (OCP). A FIT was also performed at OCP using 5 wt% NaCl for comparison to the ASTM B-117 which uses a NaCl solution of the same concentration.

1.8.1.4 Comparison of LALT, FIT and Field Results

By comparing the data gleaned from multiple high level surveillance techniques across all exposures (LALT, FIT and field) the important variables that warranted further investigation were made apparent. The comparisons were done in many ways. First correlations between mass loss and scribe creep were performed to establish any possible relationships between the two. The correlations are discussed in Chapter 2. Second, statistical models were constructed for both mass loss and scribe creep from the available data. The model for scribe creep can be found in Equation 1.16 where ML is mass loss in mg/cm², t is time in days, [Cl⁻] is chloride concentration in g/L, RH is mean % relative humidity, and cycling is the number of cycles per day. The mass loss predictions for Equation 1.16 for each LALT vs. the actual results is plotted in Figure 1.23. From this model, it was determined that temperature, %RH, chloride, ozone, UV and pH were ESFs that required further investigation. The model and reasoning for the ESFs chose are discussed in Chapter 3.

$$ML = 19.9(t^{1/2}) + 0.934[Cl^-] - 0.33RH - 2.95(pH) + 2.4(cycling) \quad 1.16$$

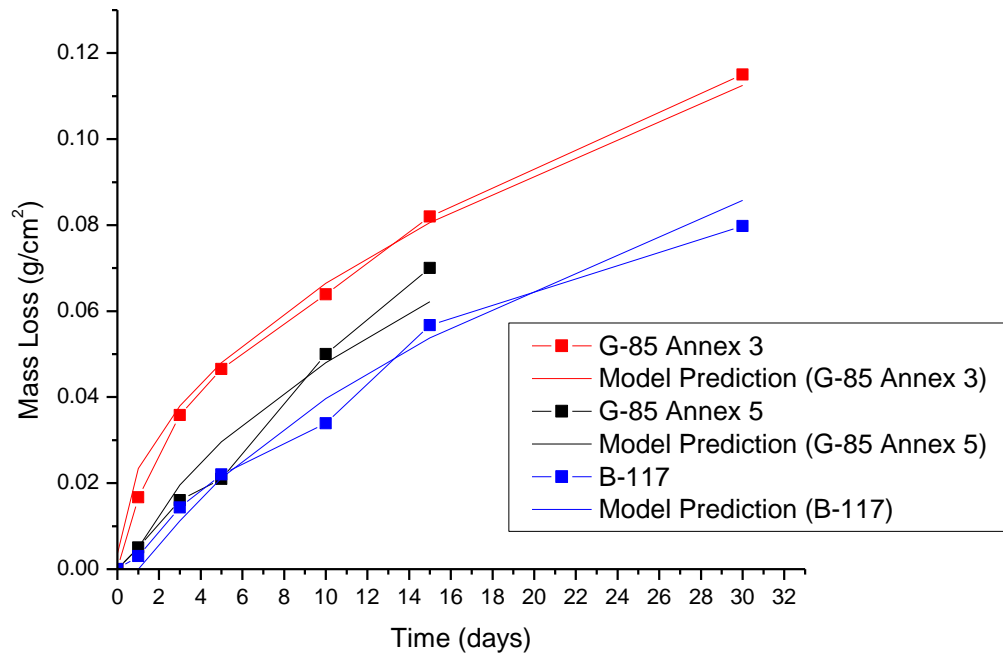


Figure 1.23 Mass loss data for standard LALTs plotted against Equation 1.16. Each curve for Equation 1.16 uses as inputs the same environmental parameters as the standard LALT it is plotted against. Results demonstrate strong agreement between the model and the LALTs.

1.8.1.5 Fractional Factorial Design of Experiment

Classical empirical experimental design involving the effects of multiple variable is called factorial design.¹⁰⁵ In factorial design, the experimenter selects the variables to be tested and the levels at which the variables will be used. The experimenter then performs experiments with all possible combinations of variables and levels. This method generates a great amount of data and, in theory, all main effects and all interactions between variables

can be estimated.¹⁰⁵ However, there are drawbacks to this type of experimental design. For example, to test all possible combinations of factors with six variables at two levels would require 64 individual experiments. The full 64 experiments would be needed to determine not only the main effects, but all of the interactions between three, four or more variables. Many of these interactions, especially higher-order interactions, generally have a negligible effect on the overall trends of the data and can be disregarded¹⁰⁵ (this is analogous to ignoring higher-order terms in a Taylor series expansion). Additionally, experiments that have many variables have some variables with limited or even indistinguishable effects.¹⁰⁵ However, using fractional factorial design of experiment, the same results from 64 factorial experiments can be obtained by performing just eight experiments.¹⁰⁵ Admittedly, fractional factorial experimental design may confound higher-level interactions, meaning that higher order interactions may be indistinguishable from each other, but the main effects will not be confounded with each other and will be distinguishable.¹⁰⁶ Performing eight experiments for seven variables at two levels, known as a 2^{7-4} factorial design, is a fairly common experimental design choice.¹⁰⁵ In this type of experimental setup, a high and low level for each selected variable is chosen, and then the experiments are designed so that the levels are varied systematically across all experiments. Any variable at a high or low level will be exposed to every other variable at both a high and low level, thus allowing for the determination of the main effects. The experimental design for these experiments can be seen in Table 1.7.

Table 1.7 Table of levels for variables in eight experiments for 2^{7-4} fractional factorial design. “+” denotes the high level and “-” denotes the low level.

Run	Temperature	Ozone	Mean %RH	Cl ⁻	UV	Cycling
1	-	-	+	-	+	-
2	-	+	-	+	+	-
3	+	+	+	+	-	-
4	+	-	-	+	-	+
5	+	+	+	-	-	+
6	+	-	-	-	+	+
7	-	-	+	-	-	+
8	-	-	+	+	+	+

1.8.1.6 Isolation of Effects of and Analysis of Corrosion Factors in LALTs

The analysis of the entire coated system, coating and substrate, and the interactions within can yield a more complete understanding of the roles of corrosion drivers present in field tests compared to lab tests. This task is complicated, however, by the likelihood that some ESFs affect the organic coating and some affect the corrosion of the metal. Those that affect the coating may indirectly cause corrosion. For example, UV has been shown to have a retarding effect on the corrosion of bare steel,⁵⁵ but UV damage can reduce a coating's barrier properties, leading to corrosion caused by other ESFs. Additionally, different pretreatments, primers and coating materials could have an effect on the scribe creep rate,

making these aspects difficult to incorporate into an all-encompassing model. Finally, a model incorporating many possible corrosion drivers would be difficult to create, due to the large amount of data that would need to be obtained to make the law usable in real-world applications. However, by focusing on the Eponol/1018 steel system, and by focusing on the strongest corrosion drivers, an empirical model will be constructed in this thesis.

Isolation of ESFs by testing each ESF individually (i.e., with no other ESFs) is not a feasible approach. Some ESFs cannot be uncoupled from other ESFs, such as chloride and time of wetness. This is because water is needed to create the electrolyte solution required for corrosion to take place (i.e., salt on the surface of steel in a perfectly dry environment would have limited, if any, corrosive effect).²¹ Additionally, testing all ESFs that could be uncoupled, such as temperature and UV, individually would only add to the 64 experiments required to test all variables together at two levels (see Section 1.8.1.5). However, isolation of the effects of ESFs is not the same as isolation of the ESFs themselves. With proper experimental set up (fractional factorial design of experiment) and proper statistical analysis, the effects of each ESF can be isolated.¹⁰⁵

To understand the effects of ESFs on the coating alone, polypropylene substrates were coated with Eponol. The polypropylene is an inert substrate and has no effect on coating degradation over the course of testing. These samples were exposed in all standard and non-standard LALTs for 15 days as well as at BRD and KSC for two to six weeks. The Eponol film was removed from the substrate and analyzed with FTIR, DSC, and TGA. These results show the effects of the exposure environments on the coating itself without any interactions with the corroding substrate.

Bare steel samples were also exposed to determine the effects of ESFs on the steel without any interactions with the coating. These samples were analyzed with mass loss, 3D microscopy, Raman microscopy and XRD.

The results from the bare steel samples and the coated polypropylene samples were compared to coated steel samples. This enabled the differentiation of mechanisms of degradation and the effects of ESFs on the coating/substrate system as a whole as opposed to the coating or substrate alone. Selected diagnostic tests were also performed.

1.8.1.7 Creation of an Empirical Scribe Creep Model

An empirical model was created using data from the experiments run in the fractional factorial design of experiment. Using R statistical software, the main effects of individual ESFs were determined.¹⁰⁷ Linear regression was used to create an empirical model that accepts ESFs as inputs and predicts scribe creep length over time

1.8.1.8 Importance of a Scribe Creep Model to the Corrosion Field

The scribe creep model based on multiple ESFs presented in this thesis provides insight into the effects of selected ESFs on the processes that govern scribe creep. These insights could be used to guide creation of future LALTs for environments in which coated steels are exposed to the selected ESFs. However, it is unclear whether the model will be robust enough to predict outside of the database or for different coatings. Future work could compare the model's predictions to long term field exposures, with the goal of further

refinement. Future work could also test the applicability of the model to other coating/substrate systems. The model could also be used as a foundation on which to create a model for other specific coated systems or perhaps even a generalized model.

1.9 **Thesis Organization**

Chapter 1 lays out the need for a “bottom up” approach to investigating scribe creep. Known effects of selected ESFs on steel corrosion and coating degradation are presented. The approach to be used in this work is presented.

Chapter 2 compares mass loss and scribe creep results for bare and coated steel samples exposed in standard LALTs and at KSC. A non-standard LALT is also used to determine the effects of UV on the system. High level surveillance methods are used to gain a more complete understanding of the effects of ESFs on the coating substrate system. The complexities of scribe creep compared with the corrosion of bare steel are discussed.

In Chapter 3, the data from LALTs and field exposures are analyzed to determine possible ESFs that have a strong role in scribe creep. Preliminary models for mass loss and scribe creep are constructed to determine ESF levels for future experiments. Fractional Factorial Design of Experiment is employed to create an experimental matrix to test the selected ESFs.

In Chapter 4, the data generated from the experiments run in Chapter 3 are analyzed and a model is constructed. The model shows the relative importance of each ESF on scribe creep and also investigates possible second order interactions.

In Chapter 5, conclusions are drawn and a discussion of future work is presented. A brief summary of the work laid out. Directions for future investigations into the effects of ESFs on the scribe creep of coated steel are proposed. The significance of this body of work is expounded.

1.10 **References**

1. U.S. Department of Labor. Revising the Notification Requirements in the Exposure Determination Provisions of the Hexavalent Chromium Standards, 75, Federal Register, 2010, 75:27188-27189.
2. US Environmental Protection Agency. Chromium-6 in Drinking Water, 2010, EPA 815-F-10-005.
3. Strategic Environmental Research and Development Program. Non-Chromate No-VOC Coating System for DoD Applications, 2009, WP-1521.
4. Environmental Security Technology Certification Program. Low VOC Barrier Coating for Industrial Maintainance, 2007, WP-0301.
5. R.G. Buchheit, *Conversion Coating Science and Technology - is it Evolving or is it Stuck?*, in *Corrosion Science: a Retrospective and Current Status in Honor of Robert P. Frankenthal*, G. Frankel, J.R. Scully, H.S. Issacs and J.D. Sinclair, Editors. 2002, Electrochemical Society: Pennington, New Jersey. p. 430-437.
6. Chromium Hexavalent Compounds, Report on Carcinogens, National Institute of Health.
7. P.S. Silva, *Guidance for Public Water Systems on Enhanced Monitoring for Chromium-6 (Hexavalent Chromium) in Drinking Water*, U.E.P. Agency, Editor. 2011, Office of Water.
8. J.J. Young, *Minimizing the Use of Hexavalent Chromium*. 2009.
9. M. Daniel E. Bullock, *Memorandum for distribution*, in *Subject: Adding PreKote SP to Technical Order (T.O.) 1-1-8*. 2004, Department of the Air Force. p. 1.
10. A. King and J.R. Scully, *Corrosion Protection of 2024-T351 by a Mg-Rich Primer: Discrepancies Between Field Versus Laboratory Exposures*, in *NACE 2010*. 2011: San Antonio Tx.
11. B. Dodson and H. Schwab, *Accelerated Testing - A Practitioner's Guide to Accelerated and Reliability Testing*. 2006: SAE International.

12. C.A. Matzdorf and C.W. Nickerson. *Assesment of Accelerated Tests Compared to Beachfront Test and Proposed Evaluation Method*. in *DoD Corrosion Conference*. 2009.
13. O. Guseva, S. Brunner and P. Richner, *Service life prediction for aircraft coatings*. Polymer Degradation and Stability, 2003. **82**.
14. H.E. Townsend. *Development of Laboratory Corrosion Tests by the Automotive and Steel Industries of North America*. in *Proceedings of The 4th International Conference on Zinc and Zinc-Alloy Coated Steel Sheet*. 1998.
15. ASTM Standard B117 2007a, "Standard Practice for Operating Salt Spray (Fog) Apparatus," ASTM International, West Conshohocken, PA, 2007, DOI: 10.1520/B0117-11, www.astm.org
16. ASTM Standard D1654, 2008, "Standard Test Method for Evaluation of Painted or Coated Specimens Subjected to Corrosive Environments," ASTM International, West Conshohocken, PA, 2008, DOI: 10.1520/D1654-08, www.astm.org
17. C.L. Meade, *Cabinet Tests*, in *Corrosion Tests and Standards: Application and Interpretation*, R. Baboian, Editor. 2005, ASTM International. p. 131-138.
18. J. Mallegol, M. Poelman and M.G. Olivier, *Influence of UV weathering on corrosion resistance of prepainted steel*. Progress in Organic Coatings, 2008. **61**(2-4): p. 126-135.
19. B. Boelen, B. Schmitz, J. Defourny and F. Blekkenhorst, *A literature survey on the development of an accelerated laboratory test method for atmospheric corrosion of precoated steel products*. Corrosion Science, 1993. **34**(11): p. 1923-1931.
20. B.R. Appleman, *Prediction Exterior Performance of Organic Coatings from Salt Spray: Two Types of Errors*. Journal of Protective Coatings and Linings, 1993: p. 134-143.
21. C. Leygraf and T.E. Graedel, *Atmospheric Corrosion*. 2000: John Wiley & Sons.
22. J.F. Henriksen and A.A. Mikhailov, *Atmospheric Corrosion Tests of Metals in SO₂-Polluted Cold Atmosphere in Northern Norway and along Its Border with Russia*. Protection of Metals, 2002. **38**(6): p. 579-589.
23. A.U. Leuenberger-Minger, *Dose-response functions for weathering steel, copper and zinc obtained from a four year exposure programme in Switzerland*. Corrosion Science, 2002. **44**: p. 675-687.
24. A.A. Mikhailov, *Dose-Response Functions as Estimates of the Effect of Acid Precipitates on Materials*. Protection of Metals, 2001. **37**(4): p. 357-366.
25. J. Tidblad, V. Kucera, A. Mikhailov, J. Henriksen, K. Kreislova, T. Yates, B. Stöckle and M. Schreiner, *UN ECE ICP Materials: Dose-Response Functions on Dry and Wet Acid Deposition Effects After 8 Years of Exposure*. Water, Air, & Soil Pollution, 2001. **130**(1): p. 1457-1462.
26. G. Williams and H.N. McMurray, *The Kinetics of Chloride-Induced Filiform Corrosion on Aluminum Alloy AA2024-T3*. Journal of the Electrochemical Society, 2003. **150**(8): p. B380-B388.
27. G. Williams, A. Gabriel, A. Cook and H.N. McMurray, *Dopant Effects in Polyaniline Inhibition of Corrosion-Driven Organic Coating Cathodic Delamination on Iron*. Journal of the Electrochemical Society, 2006. **153**(10): p. B425-B433.
28. I. Matsushima, *Carbon Steel—Atmospheric Corrosion*, in *Uhlig's Corrosion Handbook*. 2011, John Wiley & Sons, Inc. p. 579-588.
29. S. Feliu, M. Morcillo and B. Chico, *Effect of distance from sea on atmospheric corrosion rate*. Corrosion, 1999. **55**(9): p. 883-891.
30. H.E. Townsend and J.C. Zoccola, *Eight-Year Atmospheric Corrosion Performance of Weathering Steel in Industrial, Rural, and Marine Environments*, in *Atmospheric*

- Corrosion of Metals*, ASTM STP 767, S.W. Dean and E.C. Rhea, Editors. 1982, American Society for Testing and Materials: Philadelphia.
31. E. McCafferty, *Introduction to Corrosion Science*. 2010, New York: Springer.
 32. D.A. Jones, *Principles and Prevention of Corrosion*. 2nd ed. 1996: Prentice Hall.
 33. F. Mansfeld, *Corrosion Mechanisms*. 1987, New York: Marcel Dekker Inc.
 34. A. Bautista, *Filiform corrosion in polymer-coated metals*. Progress in Organic Coatings, 1996. **28**(1): p. 49-58.
 35. P.P. Leblanc and G.S. Frankel, *Investigation of filiform corrosion of epoxy-coated 1045 carbon steel by scanning Kelvin probe force microscopy*. Journal of the Electrochemical Society, 2004. **151**(3): p. B105-B113.
 36. C.F. Sharman, *Filiform Underfilm Corrosion of Lacquered Steel Surfaces*. Nature, 1944. **153**.
 37. *Temperature Influence on Corrosion* [website] 2010 [cited 2014 May]; Available from: <http://events.nace.org/library/corrosion/Design/Temperature-effects.asp>.
 38. P.J. Sereda, *Atmospheric factors affecting the corrosion of steel*. Industrial & Engineering Chemistry, 1960. **52**(2): p. 157-160.
 39. ASTM Standard D5894, 2001, "Standard Practice for Cyclic Salt Fog/UV Exposure of Painted Metal, (Alternating Exposures in a Fog/Dry Cabinet and a UV/Condensation Cabinet)," ASTM International, West Conshohocken, PA, 2010, DOI: 10.1520/D5894-10, www.astm.org
 40. ASTM Standard G-85, 2011, "Standard Practice for Modified Salt Spray Testing," ASTM International, West Conshohocken, PA, 2002, DOI: 10.1520/G0085-11, www.astm.org
 41. W.D.J. Callister, *Materials Science and Engineering An Introduction* 7th ed. 2007, New York: John Wiley and Sons, Inc.
 42. L. Delbreilh, E. Dargent, J. Grenet, J.M. Saiter, A. Bernès and C. Lacabanne, *Study of poly(bisphenol A carbonate) relaxation kinetics at the glass transition temperature*. European Polymer Journal, 2007. **43**(1): p. 249-254.
 43. M. Pourbaix, *Atlas of electrochemical equilibria in aqueous solutions*. 2nd ed. 1974, Houston: National Association of Corrosion Engineers.
 44. U.S. Department of Energy. DOE Fundamentals Handbook Chemistry, 1, Government Printing Office, 1993, DOE-HDBK-1015/1-93.
 45. I.S. Cole, *Mechanism of Atmospheric Corrosion in Tropical Environments*, in *Marine Corrosion in Tropical Environments*, ASTM STP 1399, S.W. Dean and J.B. Bushman, Editors. 2000, American Society for Testing and Materials: West Conshohocken, PA.
 46. N.S. Azmat, K.D. Ralston, B.C. Muddle and I.S. Cole, *Corrosion of Zn under acidified marine droplets*. Corrosion Science, 2011. **53**(4): p. 1604-1615.
 47. A. de Vooys, B. Boelen, J.P. Penning and H. van der Weijde, *Improving coating resistance to acetic acid sterilisation: An EIS approach*. Progress in Organic Coatings, 2009. **65**(1): p. 30-36.
 48. U. Riaz, S.M. Ashraf and S. Ahmad, *High performance corrosion protective DGEBA/polypyrrole composite coatings*. Progress in Organic Coatings, 2007. **59**(2): p. 138-145.
 49. B. Narayanasamy and S. Rajendran, *Electropolymerized bilayer coatings of polyaniline and poly(N-methylaniline) on mild steel and their corrosion protection performance*. Progress in Organic Coatings, 2010. **67**(3): p. 246-254.

50. A. Kumar S, H. Bhandari, C. Sharma, F. Khatoon and S.K. Dhawan, *A new smart coating of polyaniline-SiO₂ composite for protection of mild steel against corrosion in strong acidic medium*. Polymer International, 2013. **62**(8): p. 1192-1201.
51. A. Wegmann, *Chemical resistance of waterborne epoxy/amine coatings*. Progress in Organic Coatings, 1997. **32**(1-4): p. 231-239.
52. B.S. Skerry, *ACCELERATED TEST METHOD FOR ASSESSING CORROSION AND WEATHERING OF PAINTS FOR ATMOSPHERIC CORROSION CONTROL*. Corrosion, 1993. **49**(8): p. 663-674.
53. J. Pospíšil, J. Pilar, N.C. Billingham, A. Marek, Z. Horák and S. Nespurek, *Factors affecting accelerated testing of polymer photostability*. Polymer Degradation and Stability, 2006. **91**(3): p. 417-422.
54. B.R. Hinderliter, S.G. Croll, D.E. Tallman, Q. Su and G.P. Bierwagen, *Interpretation of EIS data from accelerated exposure of coated metals based on modeling of coating physical properties*. Electrochimica Acta, 2006. **51**(21): p. 4505-4515.
55. P. Khullar and R.G. Kelly. Accelerated Atmospheric Corrosion Testing of Steel. presented at Electrochemical Society, San Francisco, CA, October, 2013.
56. F. Deflorian, L. Fedrizzi and S. Rossi, *Electrochemical Impedance Spectroscopy and Fourier Transform Infrared Spectroscopy of Natural and Accelerated Weathering of Organic Coatings*. Corrosion, 1998. **54**(8): p. 598-605.
57. F. Deflorian, L. Fedrizzi and P.L. Bonora, *INFLUENCE OF THE PHOTO-OXIDATIVE DEGRADATION ON THE WATER BARRIER AND CORROSION PROTECTION PROPERTIES OF POLYESTER PAINTS* Corrosion Science, 1996. **38**(10): p. 1697-1708.
58. H.P. Hack and J.R. Scully, *Defect Area Determination of Organic Coated Steels in Seawater Using the Breakpoint Frequency Method*. Journal of the Electrochemical Society, 1991. **138**(1): p. 33-40.
59. F. Mansfeld and C.H. Tsai, *Determination of Coating Deterioration with EIS .1. Basic Relationships*. Corrosion, 1991. **47**(12): p. 958-963.
60. S. Oesch, *The effect of SO₂, NO₂, NO and O₃ on the corrosion of unalloyed carbon steel and weathering steel - The results of laboratory exposures*. Corrosion Science, 1996. **38**(8): p. 1357-1368.
61. S. Oesch and M. Faller, *ENVIRONMENTAL EFFECTS ON MATERIALS: THE EFFECT OF THE AIR POLLUTANTS SO₂, NO₂, NO AND O₃ ON THE CORROSION OF COPPER, ZINC AND ALUMINIUM. A SHORT LITERATURE SURVEY AND RESULTS OF LABORATORY EXPOSURES* Corrosion Science, 1997. **39**(9): p. 1505-1530.
62. Y. Wan, E.N. Macha and R.G. Kelly, *Modification of ASTM B117 Salt Spray Corrosion Test and Its Correlation to Field Measurements of Silver Corrosion*. Corrosion, 2012. **68**(3): p. 036001-1-036001-10.
63. J.J. Robin, *Overview of the Use of Ozone in the Synthesis of New Polymers and the Modification of Polymers* Advances in Polymer Science, 2004. **167**: p. 235.
64. S.D. Razumovskii, A.A. Kefeli and G.E. Zaikov, *Degradation of polymers in reactive gases*. European Polymer Journal, 1971. **7**(3): p. 275-285.
65. R.D. Edwards, N.L. Lam, L. Zhang, M.A. Johnson and M.T. Kleinman, *Nitrogen Dioxide and Ozone As Factors in the Availability of Lead from Lead-Based Paints*. Environmental Science & Technology, 2009. **43**(22): p. 8516-8521.
66. S. Irmak, O. Erbatur and A. Akgerman, *Degradation of 17 β -estradiol and bisphenol A in aqueous medium by using ozone and ozone/UV techniques*. Journal of Hazardous Materials, 2005. **126**(1-3): p. 54-62.

67. E. Kusvuran and D. Yildirim, *Degradation of bisphenol A by ozonation and determination of degradation intermediates by gas chromatography–mass spectrometry and liquid chromatography–mass spectrometry*. Chemical Engineering Journal, 2013. **220**(0): p. 6-14.
68. T. Garoma and S. Matsumoto, *Ozonation of aqueous solution containing bisphenol A: Effect of operational parameters*. Journal of Hazardous Materials, 2009. **167**(1–3): p. 1185-1191.
69. L. Veleva and R.D. Kane, *Atmospheric Corrosion in Corrosion: Fundamentals, Testing and Protection*, Various, Editor. 2003, ASM International: Materials Park, OH. p. 196-209.
70. M. Shedd, 2012, Modeling and Measurement of the Maximum Pit Size on Ferrous Alloys Exposed to Atmospheric Conditions. (Master's Thesis) University of Virginia, Charlottesville.
71. G.S. Frankel, *Pitting Corrosion in Corrosion: Fundamentals, Testing and Protection*, Various, Editor. 2003, ASM International: Materials Park, OH. p. 236-241.
72. H. Leidheiser and P.D. Deck, *Chemistry of the Metal-Polymer Interfacial Region*. Science, 1988. **241**(4870): p. 1176-1181.
73. H. Leidheiser, R.D. Granata and R. Turoscy, *Technical Note: Alkali Metal Ions as Aggressive Agents to Polymeric Corrosion Protective Coatings*. Corrosion, 1987. **43**(5): p. 296-297.
74. J. Parks and H. Leidheiser, *Ionic migration through organic coatings and its consequences to corrosion*. Industrial & Engineering Chemistry Product Research and Development, 1986. **25**(1): p. 1-6.
75. R. Turoscy, J. Henry Leidheiser and J.E. Roberts, *Solid-State Nuclear Magnetic Resonance Studies of Ions in Protective Coatings III: Sodium, Lithium, and Cesium Ions in Polyimide and Epoxy-Polyamide Coatings*. Journal of the Electrochemical Society, 1993. **140**(1): p. 149-154.
76. R. Turoscy, J. Henry Leidheiser and J.E. Roberts, *Solid-State NMR Studies of Sodium Ions in a Polybutadiene Matrix*. Journal of the Electrochemical Society, 1990. **137**(6): p. 1785-1788.
77. H. Leidheiser and W. Wang, *Some Substrate and Environmental Influences on the Cathodic Delamination of Organic Coatings*. Journal of Coatings Technology, 1981. **53**(672): p. 77-84.
78. M. Stratmann, A. Leng, W. Fürbeth, H. Streckel, H. Gehmecker and K.H. Große-Brinkhaus, *The scanning Kelvin probe; a new technique for the in situ analysis of the delamination of organic coatings*. Progress in Organic Coatings, 1996. **27**(1–4): p. 261-267.
79. K. Knop, *Influence of buffer solution composition on drug release from pellets coated with neutral and quaternary acrylic polymers and on swelling of free polymer films*. European Journal of Pharmaceutical Sciences, 1996. **4**(5): p. 293-300.
80. M. Tullmin and P.R. Roberge, *Atmospheric Corrosion*, in *Uhlig's Corrosion Handbook*, R.W. Revie, Editor. 2000, John Wiley & Sons.
81. E. Schindelholz and R.G. Kelly, *Wetting Phenomena and Time of Wetness in Atmospheric Corrosion*. 2010, Center for Electrochemical Science and Engineering, University of Virginia.
82. W.H.J. Vernon, *A laboratory study of the atmospheric corrosion of metals. Part I.-The Corrosion of copper in certain synthetic atmospheres, with particular reference to the*

- influence of sulphur dioxide in air of various relative humidities*. Transactions of the Faraday Society, 1931. **27**: p. 255-277.
83. W.H.J. Vernon, *A laboratory study of the atmospheric corrosion of metals. Part II.-Iron: the primary oxide film. Part III.-The secondary product or rust (influence of sulphur dioxide, carbon dioxide, and suspended particles on the rusting of iron)*. Transactions of the Faraday Society, 1935. **31**: p. 1668-1700.
 84. D.A. Bruzewicz, A. Checco, B.M. Ocko, E.R. Lewis, R.L. McGraw and S.E. Schwartz, *Reversible uptake of water on NaCl nanoparticles at relative humidity below deliquescence point observed by noncontact environmental atomic force microscopy*. The Journal of Chemical Physics, 2011. **134**(4): p. -.
 85. I.N. Tang, *Deliquescence Properties and Particle Size Change of Hygroscopic Aerosols*. in *Symposium on Biological Studies of Environmental Pollutants: Aerosol Generation and Exposure Facilities*. 1979. Honolulu, Hawaii.
 86. W. Lu and D.D.L. Chung, *Effect of Rust on the Wettability of Steel by Water*. Cement and Concrete Research, 1998. **28**(4): p. 477-480.
 87. E. Schindelholz, *Time of Wetness in Atmospheric Corrosion: Defining and Sensing*. 2011, University of Virginia. p. 38.
 88. E. Schindelholz, R.G. Kelly, I.S. Cole, W.D. Ganther and T.H. Muster, *Comparability and accuracy of time of wetness sensing methods relevant for atmospheric corrosion*. Corrosion Science, 2013. **67**(0): p. 233-241.
 89. S. Bhattacharya, D.K. Sharma, S. Saurabh, S. De, A. Sain, A. Nandi and A. Chowdhury, *Plasticization of Poly(vinylpyrrolidone) Thin Films under Ambient Humidity: Insight from Single-Molecule Tracer Diffusion Dynamics*. The Journal of Physical Chemistry B, 2013. **117**(25): p. 7771-7782.
 90. P. Nogueira, C. Ramírez, A. Torres, M.J. Abad, J. Cano, J. López, I. López-Bueno and L. Barral, *Effect of water sorption on the structure and mechanical properties of an epoxy resin system*. Journal of Applied Polymer Science, 2001. **80**(1): p. 71-80.
 91. G. Baschek, G. Hartwig and F. Zahradnik, *Effect of water absorption in polymers at low and high temperatures*. Polymer, 1999. **40**(12): p. 3433-3441.
 92. J.B. Enns and J.K. Gillham, *Effect of the extent of cure on the modulus, glass transition, water absorptio, and density of an amine-cured epoxy*. Journal of Applied Polymer Science, 1983. **28**(9): p. 2831-2846.
 93. N. LeBozec and D. Thierry, *Influence of climatic factors in cyclic accelerated corrosion test towards the development of a reliable and repeatable accelerated corrosion test for the automotive industry*. Materials and Corrosion-Werkstoffe Und Korrosion, 2010. **61**(10): p. 845-851.
 94. M. Kappes, G.S. Frankel and N. Sridhar, *Adhesion and adhesion degradation of a pressure sensitive tape on carbon steel*. Progress in Organic Coatings, 2010. **69**(1): p. 57-62.
 95. R.A. Dickie, *Paint adhesion, corrosion protection, and interfacial chemistry*. Progress in Organic Coatings, 1994. **25**(1): p. 3-22.
 96. M. Stratmann and H. Streckel, *On the atmospheric corrosion of metals which are covered with thin electrolyte layers—I. Verification of the experimental technique*. Corrosion Science, 1990. **30**(6-7): p. 681-696.
 97. M. Stratmann and H. Streckel, *On the atmospheric corrosion of metals which are covered with thin electrolyte layers—II. Experimental results*. Corrosion Science, 1990. **30**(6-7): p. 697-714.

98. M. Stratmann, H. Streckel, K.T. Kim and S. Crockett, *On the atmospheric corrosion of metals which are covered with thin electrolyte layers-iii. the measurement of polarisation curves on metal surfaces which are covered by thin electrolyte layers.* Corrosion Science, 1990. **30**(6-7): p. 715-734.
99. H. Lee, T. Kim, W. Sim, S. Kim, B. Ahn, T. Lim and K. Park, *Pinhole formation in PEMFC membrane after electrochemical degradation and wet/dry cycling test.* Korean Journal of Chemical Engineering, 2011. **28**(2): p. 487-491.
100. H.E. Townsend, M.W. Simpson, W.B. van der Linde and D.C. McCune, *License Plate Cosmetic Corrosion Test of Automotive Coated Steel Sheet.* Corrosion, 1998. **55**(4): p. 406.
101. *QUV Accelerated Weathering Tester.* 2006, Q-Lab Corporation.
102. ASTM Standard D4587, 2011, "Standard Practice for Fluorescent UV-Condensation Exposures of Paint and Related Coatings," ASTM International, West Conshohocken, PA, 2011, DOI: 10.1520/D4587-11, www.astm.org
103. J.N. Murray and H.P. Hack, *Long-Term Testing of Epoxy-Coated Steel in ASTM Seawater Using Electrochemical Impedance Spectroscopy.* Corrosion, 1991. **47**(6): p. 480-489.
104. J.N. Murray and H.P. Hack, *Testing Organic Architectural Coatings in ASTM Synthetic Seawater Immersion Conditions Using EIS.* Corrosion, 1992. **48**(8): p. 671-685.
105. G.E.P. Box, W.G. Hunter and J.S. Hunter, *Statistics for Experimenters.* 1976, New York: John Wiley and Sons.
106. R.A. Stowe and R.P. Mayer, *EFFICIENT SCREENING OF PROCESS VARIABLES.* Industrial & Engineering Chemistry, 1966. **58**(2): p. 36-40.
107. R. Ihaka and R. Gentleman, *R: A Language for Data Analysis and Graphics.* 1996.

2 Chapter 2 – Comparison of Scribe Creep and Underpaint Corrosion on Eponol Coated 1018 Steel in Field Exposures vs. LALTs

2.1 Summary of Chapter 2

Corrosion and scribe creep of ultra-high molecular weight epoxy resin (Poly(Bisphenol A-co-epichlorohydrin) glycidyl end-capped ($C_{18}H_{22}O_3$) $_n \bullet C_{22}H_{26}O_4$; CAS No. 25036-25-3, trade name Eponol) coated AISI 1018 steel (UNS# G10180; 0.15% C, 0.7% Mn, Fe; wt. %) was investigated. Selected standard laboratory accelerated life tests (LALTs) were compared to field exposures and full immersion tests (FITs) to elucidate similarities and differences between scribe creep and corrosion on bare steel. To accurately discern these phenomena, comparisons between LALT, FIT and field exposures were made using a suite of methods to interrogate both coating and substrate degradation. The methods included electrochemical impedance spectroscopy (EIS), X-ray diffraction (XRD), 3D optical microscopy, and Fourier Transform Infrared Spectroscopy (FTIR). Mass loss on bare samples correlated positively with scribe creep length on coated steel in the case of both lab and field exposure. The results also demonstrated that LALTs without UV radiation and wet/dry cycling did not correlate well with field exposure in terms of coating and corrosion degradation, as compared to tests that incorporated these environmental factors. For example, ASTM G-85 Annex 5 modified to incorporate UV correlated well with field sites. This points to the need for UV radiation to damage the polymer coating and wet/dry cycling to mimic the natural diurnal cycles found at field sites. Additionally, FITs produced differences in oxide species and scribe creep morphology compared to field exposures. By comparing similarities and

differences in scribe creep behavior and scribe corrosion products between field results and LALTs, and by identifying environmental severity factors critical to underpaint corrosion, the current study ultimately provides guidance that will enable the development of LALT methods that better simulate field chemistry and environmental conditions.

2.2 **Background – The Need to Understand the Roles of ESFs in Underpaint Corrosion**

The discrepancy between lab accelerated life tests (LALTs) and field tests of chromate-free organically coated metal alloys is a well-known problem.¹⁻¹² For example, a review of the development of accelerated test methods for atmospheric corrosion of organically coated steel found that the rank order of systems exposed in accelerated tests were often not the same rank order observed in field exposures.⁴ Currently, it is not understood how differences in environmental severity factors (ESFs) used in these tests cause such discrepancies. This research seeks to increase understanding of the influence of environmental stresses on the mechanisms and rates of scribe creep of coated steel and degradation of intact organic coatings.

Many forms of accelerated tests, including cabinet tests, lot acceptance tests, and others, are often used to predict the long term performance of coatings. However, discrepancies between LALTs and field exposures undermine the utility and accuracy of accelerated testing.^{3, 6, 11, 13} A recent study for the Department of Defense attempted to address these discrepancies by examining the correlation in scribe creep between field exposed and ASTM B-117¹⁴ tested samples of coated 2xxx and 5xxx series aluminum alloys.³ The authors examined differences in scribe creep using the ASTM D-1654 Procedure A, which involves

removing the coating using compressed air or mechanical scraping and then visually rating the extent of corrosion. Based on their observations, two ways to improve correlation with field exposures were suggested: a) evaluate additional replicates of the substrate for each coating system to reduce sample to sample variability in the ASTM D-1654 Procedure A,¹⁵ and b) expose samples to at least two different LALTs, for example ASTM B-117 and GM 9540P.³ However, these proposed solutions represent brute force approaches to remedy a lack of correlation. They advocated testing more of the same samples and conducting a greater variety of LALTs without understanding the underlying mechanisms nor how each ESF affects the unit processes that drive scribe creep. An alternative approach to improving field and test correlation is to elucidate individual differences in corrosive mechanisms, products, and coating degradation processes between lab and field.

Early work establishing atmospheric corrosion rates for bare metals was done through long-term atmospheric exposures and measurement of corrosion rates over time, sometimes as long as 30 years.¹⁶⁻¹⁹ From this long-term data, corrosivity maps and corrosivity classification systems for specific metals were constructed.^{20, 21} These long-term data have been used to create empirical equations relating corrosion rate for bare metals to time and ESFs (e.g., atmospheric characteristics).¹⁹⁻²³ A sampling of some of the relationships found in the literature is given in Table 1.3. Much work has also been done in comparing bare metals in LALT and field environments. As early as 1935 Vernon established corrosion rates by measuring the weight gain of iron plates in controlled atmospheres.²⁴ Since then, numerous studies have been conducted that sought to correlate lab and field environments,^{3, 4, 11, 22, 25} with the general consensus being that LALTs must be

tailored to each specific field environment to reduce discrepancy between corrosion behavior predicted by LALTs and the actual behavior observed in field environments .^{2, 4}

The empirical relationships relating ESFs to corrosion rate for bare steel unfortunately do not exist for scribe creep of coated steel. This is because the situation for organically coated systems is complicated by corrosion at the scribe, corrosion under the coating, coating degradation, anodic wedging and possible cathodic disbondment. All of these factors contribute to the rate of scribe creep observed. In order to accurately reproduce field exposures with industry standard LALTs, the same mechanisms of coating degradation, scribe and underpaint corrosion, and corrosion product identity and morphology must be present in both lab and field tests. In an ideal field predictive LALT, not only will the mechanisms of corrosion be the same as those seen in the field, but the relationship between acceleration factors and damage, such as chloride and scribe creep, will also be similar. To understand the mechanisms driving underpaint corrosion, the identity of corrosion products, and factors controlling scribe creep, a baseline comparison of standard LALTs to field sites is necessary. The effect of each ESF on the unit processes controlling scribe creep needs to be assessed by comparing the time dependent underpaint corrosion processes during standardized LALT and field site exposure. Subsequently, acceleration factors can be determined and simple rate laws for scribe creep can ultimately be derived. Ideally, such rate laws would establish a relationship between the extent of corrosive attack and exposure time based on the combinations of environmental drivers present.

Previous comparisons of LALT vs. field studies of coated metals have relied heavily on visual examination of corrosion and coating appearance, such as gloss measurements (ASTM D523-08),²⁶ a count of the number of blisters of a certain size (ASTM D714-02),²⁷ or the extent of visible rust (ASTM D610-08).²⁸ However, these approaches (i.e., optical images of opaque coatings at limited magnification) may not detect all of the important differences in corrosion mechanisms or products between LALTs and field exposures. For example, one study compared steel with a range of polyester based coatings exposed to either UV followed by B-117 or to B-117 alone.⁸ Large differences in blister counts were seen between the two sets of samples for some of the coatings, but were not accompanied by changes in coating gloss.⁸ Gloss measurements from sample to sample were so similar across the coatings tested that they did not provide any information on the degradation of the barrier properties of the coatings, let alone underpaint corrosion processes.⁸ Additionally, many coatings exposed to UV cycles showed no visual differences upon changes in irradiation time.⁸ Thus, the limited data that could be obtained through visual inspection methods as well as methods that focus only on coating evaluation make accurate comparisons between lab and field exposures difficult.

Corrosion differences between lab and field can be elucidated by taking advantage of a suite of methods suitable for sensitive evaluation of both coating degradation and steel corrosion. The benefit of using high-level surveillance test methods (HLS) over visual inspection of coated systems is the type of information and greater level of detail obtained. This is demonstrated in the above study of ASTM B-117,⁸ in which use of EIS and FTIR enabled the detection of changes in the electrical and molecular properties of the coating that were not detected with gloss measurements. Detailed HLS analysis of field samples is largely lacking,

however, in previous work,^{6, 25, 29-31} There are several reasons for this: (1) opaque pigments in the coating make it difficult to determine the corrosion mechanisms and analyze the corrosion products during underpaint corrosion, (2) non-destructive methods to monitor underpaint corrosion are limited, and (3) instruments that analyze the coating are often not useful in analysis of the substrate, requiring a suite of many different techniques to analyze the entire coated metal system (i.e., degradation of the properties of the coating, underpaint corrosion, scribe behavior, and corrosion product identities).

In this work, these challenges are overcome by 1) using a clear polymer coating that allows visual inspection of the substrate, and 2) using many different non-destructive characterization techniques including EIS, FTIR, XRD, Raman, and 3D microscopy to better understand the coating/substrate system. These methods maximize our ability to detect corrosive change and improve our ability to identify differences in the impact of corrosion drivers between lab and field. These methods also allow us to determine which environmental severity factors are important to incorporate into existing or future LALTs. Ultimately, knowledge gained using HLS can then be used to build more accurate LALTs that better correlate with field environments and improve comparisons between LALT, FIT and field tests.

Comparing standard LALTs to field exposures using high-level surveillance techniques is a first step in building more accurate LALTs. However, the advantages of this methodology cannot be fully realized without systematic evaluation and quantification of individual corrosion drivers in the lab or field. Although a few examples of individual corrosion drivers can be found in the literature,^{8, 22, 30, 32} overall, widespread systematic studies have

not been performed. Often, all drivers that may affect a system are combined in one LALT. As a result, LALTs are typically much more severe than field environments. The conventional notion has been that good coating performance in severe LALTs will mean good performance in the comparatively benign field, even if the drivers differ. However, in actuality, combining all drivers obfuscates the impact of individual corrosion drivers on the substrate, impairs our understanding of the effects of individual drivers on the degradation of the coating itself, and masks interactions between the coating and the substrate.

2.3 **Objective**

The objective of this study is to compare selected standardized LALTs to field environments. High-level surveillance techniques are used to closely examine coating degradation, corrosion rate and corrosion product behaviors between LALT and field exposures. Finally we demonstrate the need for systematic examination of individual corrosion drivers in order to understand their effects on scribe creep.

2.4 **Experimental Methods**

The experimental methods have been discussed at length in Chapter 1. However, a brief description of the methods will be stated here.

2.4.1 **Materials**

Organic coated and scribed AISI 1018 steel (UNS# G10180; 0.15% C, 0.7% Mn, Fe; wt. %) was used as a model coating system. A clear epoxy resin (Poly(Bisphenol A-co-

epichlorohydrin) glycidyl end-capped ($C_{18}H_{22}O_3$) $n \cdot C_{22}H_{26}O_4$; Trade name Eponol) was used. The chosen epoxy resin is a high molecular weight resin used primarily as a constituent of paint coatings.³³ The coating was applied to be $30 \pm 5 \mu\text{m}$ thick and has a high initial impedance of $\geq 10^{11} \Omega\text{-cm}^2$ at 0.01 Hz. Samples not in the stated thickness range or below the initial impedance level were discarded. The choice of this clear resin as a coating for samples in field tests and LALTs allows the underpaint corrosion to be imaged with optical microscopy. It also enables interrogation of the underpaint environment by 3D optical microscopy and Raman microscopy, both of which penetrate the clear coating to interrogate the substrate.

2.4.2 Sample Preparation Procedure

In preparation for coating, the surface of each metal sample was ground with 120, 180, 240, 300, and 600 grit silicon carbide paper to remove any surface oxide, even out any imperfections and create a clean bare surface for the application of the coating. The samples were then blown with compressed air to remove any large debris from the grinding. The samples were washed with water and detergent and rinsed with Millipore water. After washing, the samples were immediately blown dry with compressed dry air. The epoxy resin was applied to the steel samples by draw down bar to a thickness of $30 \pm 5 \mu\text{m}$. The metal samples were cured for five days in lab air and then cured at 60°C for 24 hours. After curing, the samples were cut to $2.5 \times 2.5 \text{ cm}$ dimensions and then scribed by hand down the middle with a diamond scribe tool. Figure 2.1 illustrates a top down diagram of the coated and scribed sample, while Figure 2.2 shows the sample and scribe in cross-section.

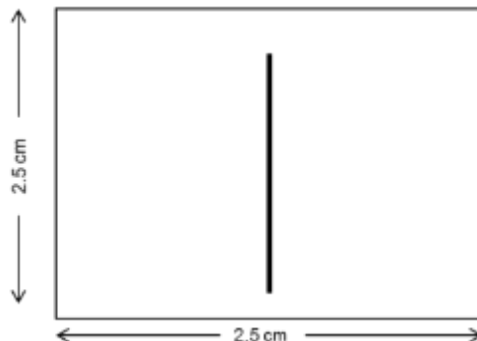


Figure 2.1 Schematic of coated and scribed 1018 steel sample.

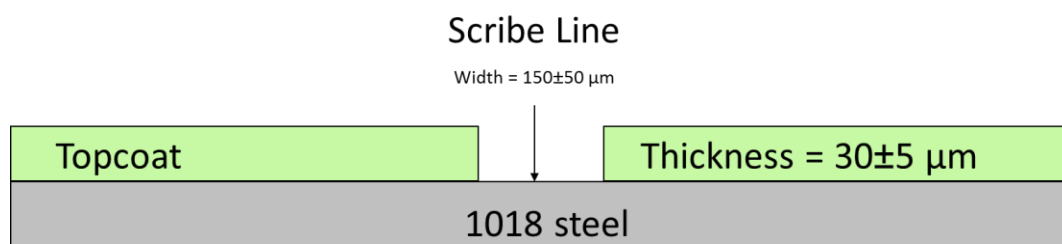


Figure 2.2 Schematic of Eponol coated and scribed 1018 steel sample. The substrate is roughly 1 mm thick and the Eponol topcoat is $30\pm5\ \mu\text{m}$. The scribe line is $150\pm50\ \mu\text{m}$ in width.

Epoxy resin films were also cast on inert polypropylene substrates. These substrates were exposed along with the bare and coated metal samples and were interrogated with FTIR after exposure.

2.4.3 High Level Surveillance Testing Methods

2.4.3.1 2D and 3D Digital Optical Microscopy

The bare and coated 1018 steel samples were imaged with a Hirox KH-7700 digital microscope. The samples were first imaged with a macro lens to get one image of the entire sample surface. The coated samples then had a 2D tiled image taken at 50x that extends the length of the scratch using the MXG-4050RZ lens. Higher resolution images (400x+) are taken at various interesting spots on the samples. The clear coating allows for visual imaging of the metal surface under the coating. The image analysis software ImageJ 1.44p released by the National Institutes of Health was employed to make quantitative measurements of scribe creep from 2D images of the scribe and surrounding scribe creep. Scribe creep lengths were measured from the scribe line perpendicularly to the edge of the scribe creep front. The measurements were done at 10 random locations along the scribe in both directions for a total of 20 measurements. These data were then used to determine an average scribe creep length.

The coated samples then have 3D tiled images taken at 350x that start at the scratch and run perpendicular out from the scratch using the MXG-10C lens with the OL 350 II lens attachment. Continuous 3D optical tiling was used to generate images that were 600 by 3000 μm in the x-y plane with full penetration of the clear epoxy resin coating. 3D images were used to generate line profiles of the corrosion product morphology across the scribe. These 3d tiled images are taken at the same place every time to monitor the progress of the corrosion from the scratch. The 3D images were processed using Mitiani Corporation 3DMeasurement software and with Mountains Map® Analysis Software 6.2 by Digital Surf.

2.4.3.2 Digital Image Analysis

The image analysis software ImageJ 1.44p released by the National Institutes of Health was employed to make quantitative measurements of scribe creep from 2D images of the scribe and surrounding scribe creep. Scribe creep lengths were measured from the scribe line perpendicularly to the edge of the scribe creep front underneath the clear coating. The measurements were done at 10 random locations along the scribe in both directions for a total of 20 measurements. These data were then used to determine an average scribe creep length.

2.4.3.3 X-Ray Diffraction (XRD)

X-Ray Diffraction (XRD) was performed using a PANalytical X'pert Pro MPD powder diffractometer with a Cu-K α source. All samples were scanned continuously from 10 to 120 degrees at a rate of 1 degree per minute. The data were analyzed using Highscore Plus 3.0c analysis software by PANalytical. Pure powders of individual iron oxides and hydroxides were characterized with XRD for comparison to XRD spectra of exposed samples. Standard powder samples were examined as received while exposed steel samples were examined with the oxide intact on the sample.

2.4.3.4 Raman Microscopy

Raman microscopy is a surface sensitive spectroscopy method that detects the molecular identity of corrosion products. It is used to determine the species that form on the surface of the samples that are either amorphous or in limited quantities that are undetectable by

XRD.³⁴ Raman microscopy was conducted using a Renishaw InVia Raman Microscope with a 200 mW, 785 nm laser with a fixed diffraction grating over a range of 200 to 1400 cm^{-1} . The laser power was 0.1% with a spot size of 50 square micrometers. Raman was performed on standard powders for comparison to experimental results. For exposed samples, Raman spectra were taken from varied locations over the surface of the sample, with care taken to perform scans on all different types of colors and morphologies seen. The data were processed using KnowItAll® Informatics System 2013 software by Bio-Rad Laboratories Inc.

2.4.3.5 Fourier Transform Infrared Spectroscopy (FTIR)

Fourier Transform Infrared Microscopy detects molecular bonds and was used to monitor degradation of the coating over time. Eponol films cast on inert polypropylene substrates were exposed, and, after exposure, the films were removed and analyzed. The polypropylene substrate on which the Epoxy resin coating was cast was inert, and thus has no effect on the degradation of the coating. This isolated the effects of the environment from the effects of underpaint corrosion on degradation of the coating. Degradation of the coating was observed by comparing the results of an unexposed coating to exposed coatings.

Films were exposed in all standard and non-standard LALT environments as well as at KSC and BRD. FTIR analysis was run on Eponol films that had been cast on inert polypropylene substrates and then exposed. For samples analyzed at UVa, the films were removed from the substrate after exposure and placed into a ScienceTech benchtop FTIR spectrometer

and analyzed. For samples analyzed at USM, coatings were left on the substrate and spectra were taken from three different locations on the Eponol film by securing them to the Smart iTR attachment. The spectra were obtained using a Nicolet 6700 FTIR from Thermo Scientific running Omnic software, in 4000-650 cm^{-1} range. The spectrophotometer was operated in transmission mode. The spectra were recorded at a resolution of 2 cm^{-1} and 32 scans were run per location.

2.4.3.6 Electrochemical Impedance Spectroscopy

Electrochemical Impedance Spectroscopy was used to measure the change in the electrical properties of the coating over time. EIS was performed at locations near to and far from the scribe. This was done to more accurately determine the rate at which the scribe creep front moved away from the scribe and to determine the effects of the scribe and ESFs on the electrical characteristics of the coating.

The testing was done on a Princeton Applied Research Versastat 4 using the VersaStudio software. A five minute OCP test was run before EIS. A typical EIS scan was acquired in sine mode from 100 kHz to 0.01 Hz with 6 points per decade. Coated panels were scanned with an AC amplitude of 60 mV. The tests were run in a flat cell containing 50 mM sodium sulfate solution with ambient aeration at 25°C. The area of the sample tested was a circle with an area of 1 cm^2 . The reference electrode used was a saturated calomel reference electrode was used as the reference electrode. Samples were used as the working electrode, and a platinum mesh was used as the counter electrode. The EIS data were processed using Z-View 3.3d analysis software by Scribner Associates Inc.

2.4.3.7 Mass Loss Test Procedure

Mass loss samples were all weighed before exposure on a Denver Instrument Company M-220D scale with a resolution of 0.01mg. The back samples were covered in electroplating tape, and then the edges were coated with stop-off lacquer before exposure. After exposure, the tape and lacquer were removed and the samples placed in a hydrochloric acid solution until all visible corrosion products had been removed according to the ASTM G 1-03.³⁵ The samples were then removed, rinsed, dried and weighed. Mass loss samples were not returned to the exposure chambers after testing.

2.4.4 **Sample Exposure Conditions**

2.4.4.1 LALT Exposure Conditions

The suite of LALT exposure chambers included a QUV™ cyclic condensation (CC/UV) chamber and a salt fog chamber. The salt fog chamber was modified to include UV lights ($\lambda=340$ nm).¹² The QUV™ allows the use of elevated temperatures, humidity and condensation cycling, as well as UV exposure in LALTs. These chambers can be used to perform standard LALTs like ASTM B-117 and ASTM D-5894, and also allow for modified versions of standard LALTs. Coated and bare steel samples were exposed in ASTM B-117,¹⁴ ASTM G-85 Annex 3,³⁶ ASTM G-85 Annex 5,³⁶ ASTM D-4587³⁷ and ASTM D-5894³⁸ standardized tests. (The UV irradiation in the ASTM D-4587 and ASTM D-5894 were found to be far too harsh on the coating substrate system. No data from the ASTM D-4587 will be presented. Limited data from the ASTM D-5894 will be shown as an example of the damage

seen.) Samples were also exposed in one non-standard test, a modified ASTM G-85 Annex 5 that included UV light. For this non-standard LALT, all exposure conditions were identical to the ASTM G-85 Annex 5 except for the addition of UV light (wavelength of 340 nm at 0.5 W/m²) for 12 hours per day. The exposure conditions can be found in Table 2.1. Coated and bare steel samples were removed from the exposure chambers and tested with the suite of characterization techniques at 0, 1, 3, 5, 10, and 15 days. After testing, the samples were immediately returned to the exposure chambers. After 15 days of exposure were completed, the samples were stored in a desiccator.

Table 2.1 List of all LALTs used in this study.

Standard LALT	Conditions and Notes	Cl ⁻	UV	Cycling
ASTM B-117	Standard practice for operating salt spray (fog) apparatus. 5% NaCl solution, continuous spray. ¹⁴ ASTM B-117 SW used ASTM synthetic sea water solution in place of the 5% NaCl solution. ToW 75-100%	✓		
ASTM G-85 A3	Seawater acidified test, cyclic. Solution is 42 g of synthetic sea salt and 10 mL glacial acetic acid per liter of solution. $2.8 \leq \text{pH} \leq 3.0$. Test cycle is 0.5 hours spray of this solution followed by 1.5 hours soak at or above 98% RH. ³⁶	✓		✓
ASTM G-85 A5	Dilute electrolyte cyclic fog dry test. Test consists of two step cycles of 1 hour spray at room temperature and 1 hour dry off at 35°C. Solution of 0.05% sodium chloride and 0.35% ammonium sulfate. ³⁶	✓		✓
ASTM D-4587	Standard practice for fluorescent UV-condensation exposures of paint and related coatings. 4 hours of UV (340 nm) at 0.89 W/m ² at 60°C followed by 4 hours of condensation (dark) at 50°C. ³⁷ Condensation comes from the heating of water in a tray below the samples.		✓	✓
ASTM D-5894	Standard practice for cyclic salt fog/UV exposure of painted metal (alternating exposures in a fog/dry cabinet and a UV/condensation cabinet). A combination of ASTM G-85 Annex 5 and ASTM D-4587 Cycle 2. One week of ASTM D-4587 (4 hours of UV (340 nm) at 0.89 W/m ² at 60°C followed by 4 hours of condensation (dark) at 50°C.) followed by one week of ASTM G-85 Annex 5. ³⁸	✓	✓	✓
Modified ASTM G-85 Annex 5	Dilute electrolyte cyclic fog dry test. Test consists of two step cycles of 1 hour spray at room temperature and 1 hour dry off at 35°C. Solution of 0.05% sodium chloride and 0.35% ammonium sulfate. ³⁶ Addition of UV light (340 nm, 0.5 W/m ²) for 12 hours per day.	✓	✓	✓

2.4.4.2 Field Exposure Conditions

Coated and bare 1018 steel samples were prepared and deployed at two sites, Kennedy Space Center in Titusville, Florida, and Charlottesville, Virginia. Kennedy Space Center (KSC) is a severe marine site with exposure racks 100 feet from the high tide line. The Charlottesville (BRD) site is a suburban/rural site on land near a local golf course. Samples

were returned from the sites every two weeks for three months for both sites. A full list of exposure locations and ESF data can be found in Table 2.2.

Table 2.2 Environmental severity factors for field sites.

Site Location	Mean Temp °C	Mean RH (%)	Mean O ₃ Concentration (ppb)	Mean UV (W/m ²)	Mean Cl- deposition rate (mg/m ² /day)
Charlottesville, VA	15.6	64.6	47*	-	1.08
Kennedy Space Center, FL	23.6	77.2	75.3*	0.6	640

Note: “-” indicates that the data is not available. “*” indicates that the data were taken from nearby NOAA site.

2.4.4.3 Full Immersion Test Conditions

Coated and bare 1018 steel samples were also exposed in Full Immersion Tests (FIT). The samples were secured to an electrochemical flatcell and immersed in a 0.05 M solution of sodium sulfate with ambient aeration. The samples were held potentiostatically for 15 days and were removed and characterized at 0, 1, 3, 5, 10, and 15 days. FITs were performed at potentiostatic holds of -1 V vs. saturated calomel electrode (SCE) and at open circuit potential (OCP) in 0.3 wt% NaCl (0.05 M NaCl). Additionally, FIT at OCP was also run with 5% NaCl solution (0.91 M), equivalent to the solution used in ASTM B-117.¹⁴

2.5 **Results**

2.5.1 **Mass Loss of Uncoated Steel**

Mass loss versus time is reported in Figure 2.3. In all cases, mass loss increases with time, but the rate of increase slows over the time of exposure. In the case of LALTs, the rate appears to slow by 10 days. In the case of KSC, the rate begins to plateau at 6 weeks. In the case of field exposures, the marine atmospheric site at KSC indicates a higher mass loss than the rural environment at BRD. Concerning LALTs, ASTM G-85 Annex 3 has the greatest mass loss over time, followed by ASTM G-85 Annex 5 with and without UV and ASTM B-117. In the case of the FITs, the OCP in 0.3 wt% NaCl exposure has a greater mass loss than the -1 V vs. SCE potentiostatic polarization in 0.3 wt% NaCl. OCP in 5 wt% NaCl experienced greater mass loss than either of the FITs in 0.3 wt% NaCl.

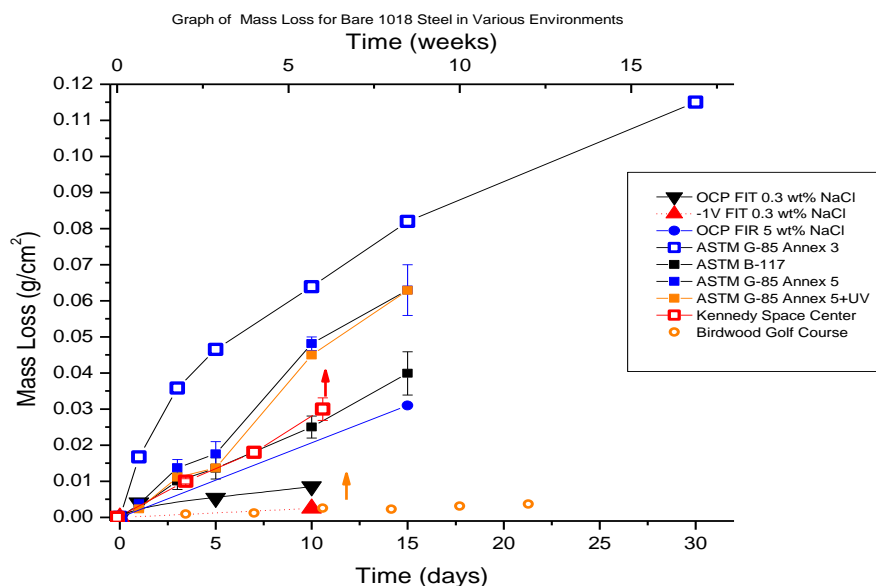


Figure 2.3 Graph of mass loss versus exposure time for bare 1018 steel in various environments. Error bars represent standard error for environments with multiple exposures.

ASTM B-117 through 15 days appears to be most similar to KSC through 16 weeks, followed by ASTM G-85 Annex 5. There is virtually no difference between ASTM G-85 Annex 5 with UV and without UV in terms of mass loss of bare steel.

2.5.2 Corrosion Product Analysis

2.5.2.1 X-Ray Diffraction

XRD was used to determine the identity of corrosion products that formed on bare samples. The assumption is that this is also representative of corrosion products at the scribe. Figure 2.4 shows the spectra for all field, LALTs and standard powders. FIT at -1 V is not included because XRD did not detect anything besides the steel substrate. The spectra show that the

corrosion products most seen in KSC are iron oxide hydroxide FeOOH in α and γ phases. The same products are found in the ASTM G-85 Annex 5 with and without UV. In contrast, the corrosion product found on samples exposed in ASTM B-117 is iron(II, III) oxide (Fe_3O_4). The FIT at OCP produces iron(II, III) oxide (Fe_3O_4) and appears to be similar to ASTM B-117 (OCP at 0.3 wt% and 5% NaCl produced identical spectra, so one representative exposure is shown). ASTM G-85 Annex 5 with and without UV appear to correlate more closely with KSC than did ASTM B-117. Samples exposed at BRD showed one large iron peak with many peaks corresponding to γ - FeOOH . The results are summarized in Table 2.4; the species detected with XRD are marked with an X.

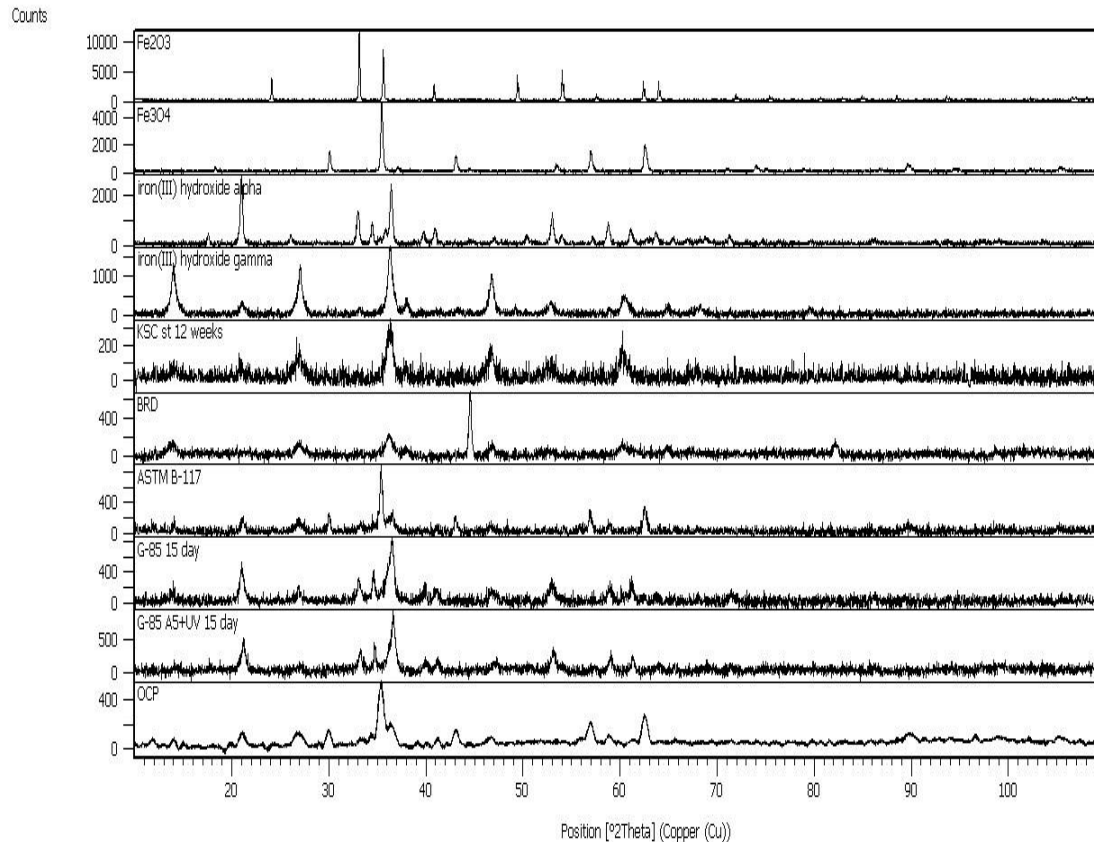


Figure 2.4 XRD spectra for all standard LALTs, field sites and standard powders for iron based corrosion products. No results are shown for FIT at -1 V because only iron peaks were detected.

Because of the difficulty in identifying every species from the XRD spectra, XRD was also performed on 50/50 mixtures of standard corrosion product powders to better understand the effects that certain corrosion products may have on each other (Figure 2.5 and 2.6). When iron (II) oxide and iron (III) oxide are mixed, all of the individual peaks are still visible (Figure 2.6). However, when iron (III) hydroxide α -phase is mixed with iron (III) hydroxide γ -phase certain peaks disappear (Figure 2.5). This may explain the spectrum seen for samples exposed at KSC.

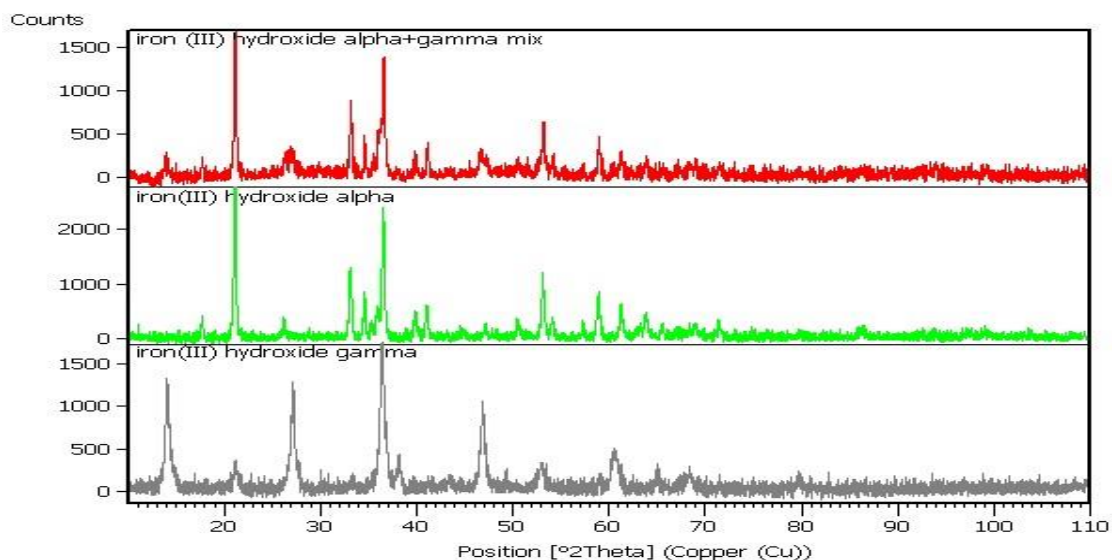


Figure 2.5 XRD spectra of standard powders individually (iron III hydroxide α and γ phase) compared to a 50/50 by weight mix of the two powders. Iron III hydroxide γ phase peaks at 9, 28 and 47 degrees appear to be greatly reduced in intensity in the mix relative to the pure powder.

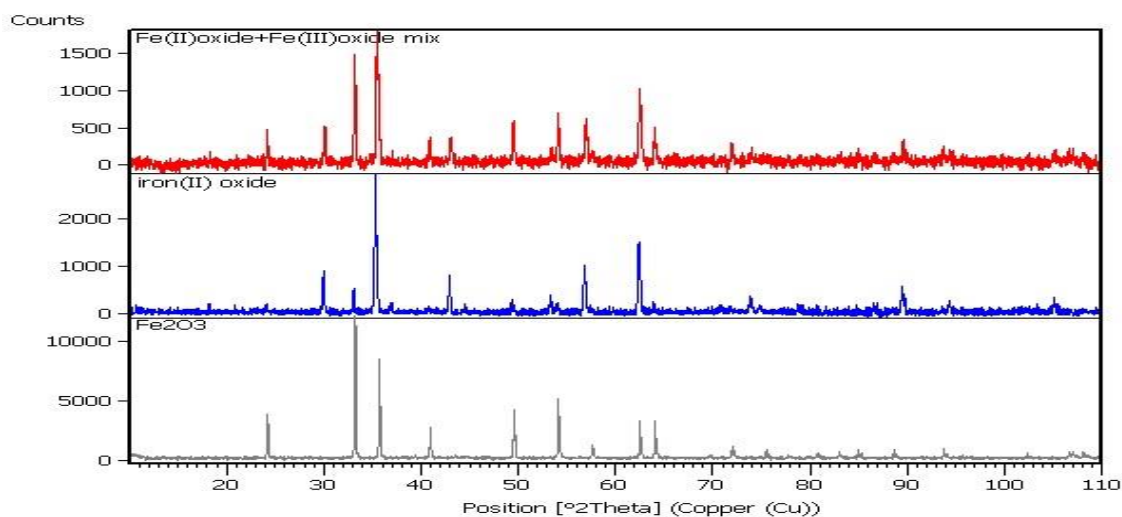


Figure 2.6 XRD spectra of standard powders individually (iron (II) oxide and iron (III) oxide) compared to a 50/50 by volume mix of the two powders.

2.5.2.2 Raman Spectroscopy

Figure 2.7 shows the Raman spectra for the standard powders. Figure 2.8 shows the spectra for KSC where β and γ phase FeOOH were detected. For BRD only γ -FeOOH was detected (Figure 2.9). Figure 2.10 shows the Raman spectra for samples expose in ASTM B-117 where FeOOH α and γ phases were detected. Raman spectra for samples exposed in ASTM G-85 Annex 5 with and without UV are shown in Figure 2.11 and Figure 2.12, respectively. FeOOH α and γ phases were detected on samples exposed to both of these tests. Figure 2.13 shows that FeOOH γ phase and iron (II,III) oxide were detected with Raman on samples exposed to FIT at OCP (the spectra are representative of both 0.3 wt% and 5% NaCl exposures). In the case of KSC, FeOOH γ was detected with both XRD and Raman while FeOOH α phase was detected only with XRD and FeOOH β phase was detected only with Raman. For ASTM B-117, iron(II,III) oxide was detected only with XRD while FeOOH α and β phases were detected only with XRD. α and γ phases of FeOOH were detected both with XRD and Raman for ASTM G-85 Annex 5 with and without UV. For FIT at OCP FeOOH γ phase was detected with Raman and iron (II,III) oxide was detected with both Raman and XRD. The results are summarized in Table 2.4; the species detected with Raman are marked with an R.

Experimental results were also compared with published data; the wavenumbers of the peaks of each species are given in Table 2.3. The results of this study are compared with an in-depth study conducted by Oh et al.,³⁹ and with published results from other sources.⁴⁰⁻⁴⁴

The results are summarized in Table 2.4; the species detected with Raman are marked with an R.

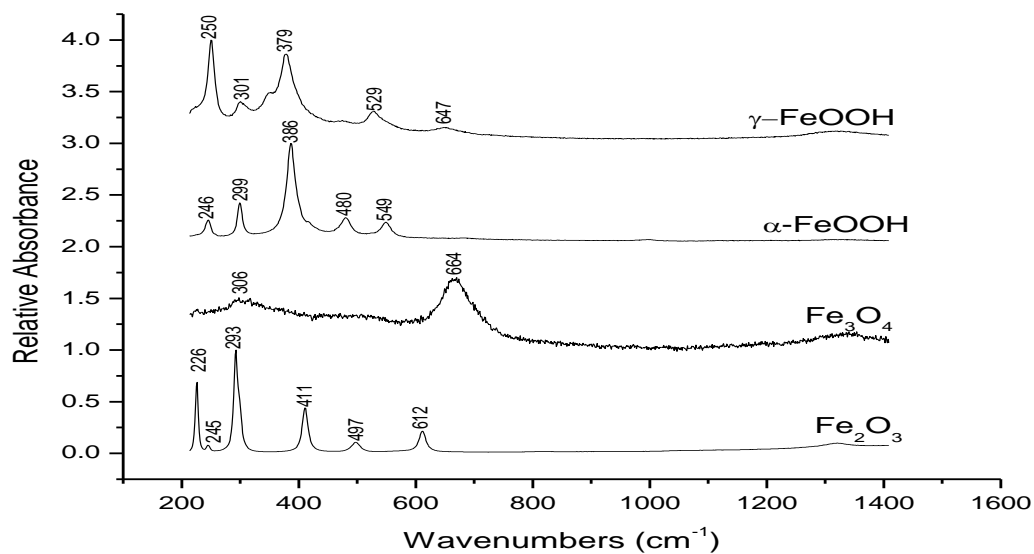


Figure 2.7 Experimental Raman spectra for standard powders.

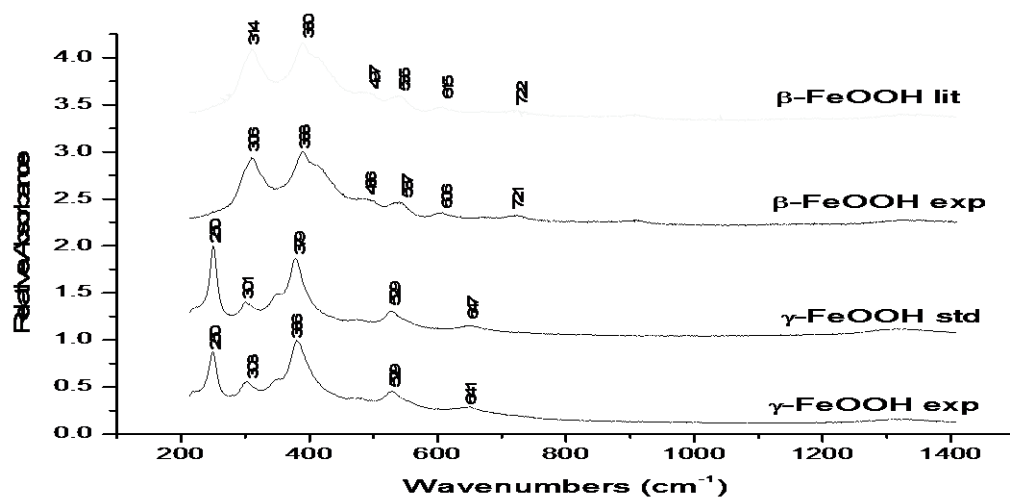


Figure 2.8 Raman spectra for bare 1018 steel exposed at KSC for 6 weeks. “exp” indicates experimental spectra, “std” indicates standard powder spectra, “lit” indicates spectra from literature.

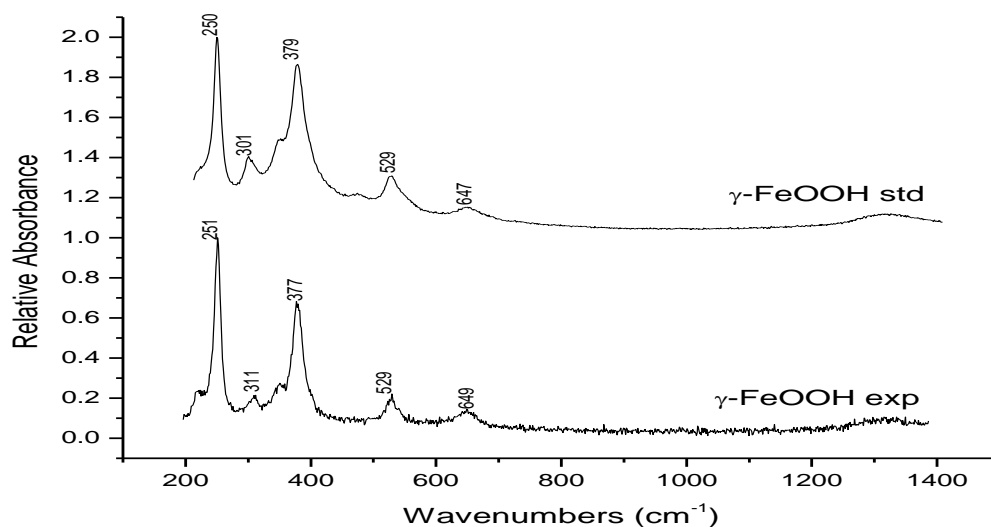


Figure 2.9 Raman spectra for bare 1018 steel exposed at BRD for 9 months. “exp” indicates experimental spectra, “std” indicates standard powder spectra.

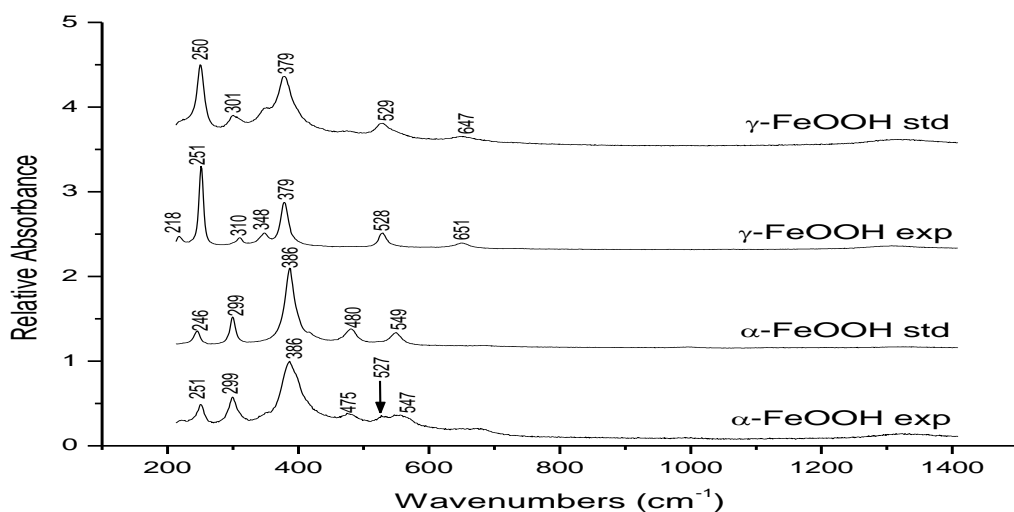


Figure 2.10 Raman spectra for bare 1018 steel exposed in ASTM B-117 for 15 days. "exp" indicates experimental spectra, "std" indicates standard powder spectra.

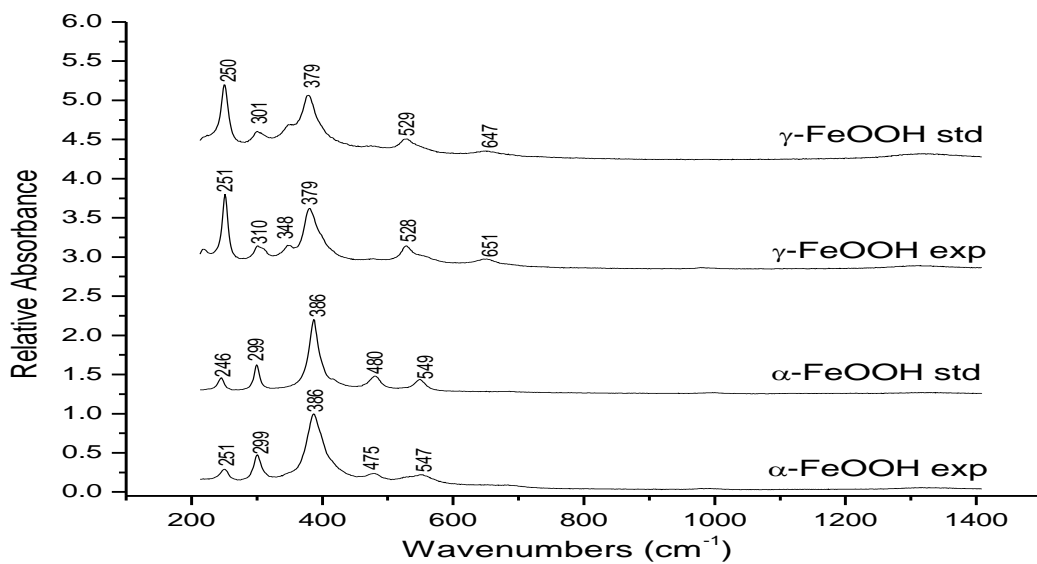


Figure 2.11 Raman spectra for bare 1018 steel samples exposed in ASTM G-85 Annex 5 for 15 days. "exp" indicates experimental spectra, "std" indicates standard powder spectra.

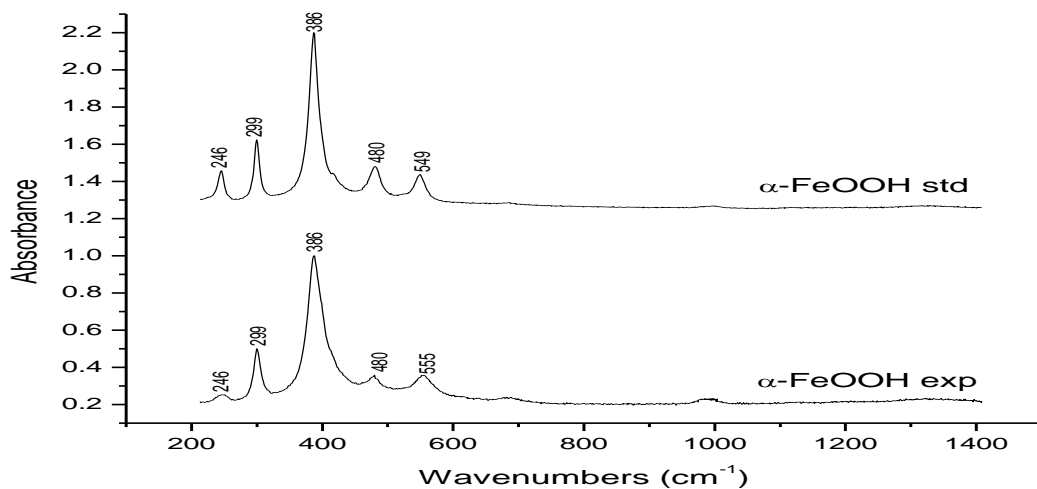


Figure 2.12 Raman spectrum for bare 1018 steel exposed in ASTM G-85 Annex 5+UV for 15 days. “exp” indicates experimental spectra, “std” indicates standard powder spectra.

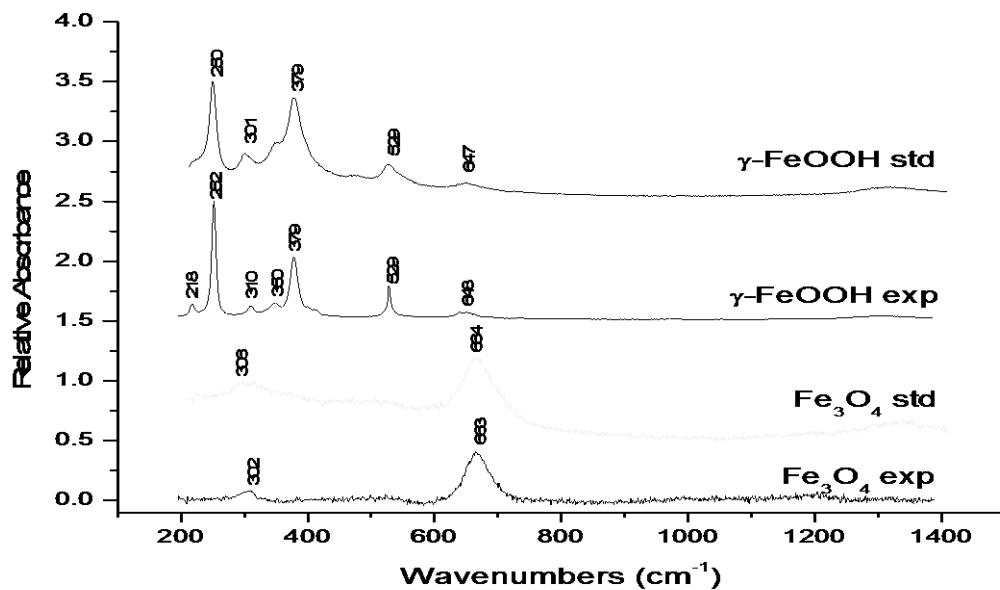


Figure 2.13 Raman Spectra for bare 1018 steel exposed in FIT at OCP for 15 days. “exp” indicates experimental spectra, “std” indicates standard powder spectra.

Table 2.3 Table of Raman peaks of iron corrosion products.

Oxide	Wavenumbers (cm ⁻¹)*	Wavenumbers (cm ⁻¹)**	Wavenumbers (cm ⁻¹ ***	Wavenumbers (cm ⁻¹)†
α- FeOOH	205, 247, 300, 386, 418, 481, 549	245, 300, 390, 420, 480, 550, 685	256, 299, 386, 480, 549	246, 251, 299, 386, 475, 480, 527, 547, 555
β- FeOOH	314, 380, 549, 722	310, 386, 497, 538, 723	N/A	311, 388, 486, 537, 607, 721
γ- FeOOH	219, 252, 311, 349, 379, 528, 648	255, 380, 528, 654, 1054, 1307	250, 300, 379, 529, 647	218, 251, 301, 310, 379, 528, 651
α- Fe ₂ O ₃	226, 245, 292, 411, 497, 612	227, 245, 293, 298, 414, 501, 612	226, 245, 293, 410, 497, 612	N/A
Fe ₃ O ₄	532, 667	616, 663	306, 664	N/A

*From Townsend et al.⁴⁰ ** From other literature sources.⁴¹⁻⁴⁶ ***Experimental results from standard powders. †Experimental results for exposed samples.

Table 2.4 Table of corrosion products found with XRD and Raman. X indicates that the species was found with XRD, and R indicates that it was found with Raman.

Exposure	Iron (II,III) oxide Fe_3O_4	Iron (III) oxide Fe_2O_3	Iron (III) Oxide- Hydroxide Alpha Phase $\alpha\text{-FeOOH}$	Iron (III) Oxide- Hydroxide Beta Phase $\beta\text{-FeOOH}$	Iron (III) Oxide- Hydroxide Gamma phase $\gamma\text{-FeOOH}$
KSC	-	-	X	R	X,R
BRD	-	-	-	-	X
B-117	X	-	R	-	R
G-85 A3	-	-	-	-	X
G-85 A5	-	-	X,R	-	X,R
G-85 A5 + UV	-	-	X,R	-	X,R
OCP	X,R	-	-	-	R

2.5.3 Scribe Creep Behavior

Figure 2.14 shows the progression of scribe creep over time for KSC. Scribe creep progresses irregularly from the scribe with some semi-circular fingers of corrosion damage or filiform-like filaments at the leading edges for weeks 2 and 4. There is also discoloration due to underpaint corrosion ahead of the heavily corroded region. Small spots of corrosion can be seen away from the scribe creep front at 2 and 4 weeks. By week 6 the KSC sample is so corroded that it becomes impossible to differentiate between scribe creep and underpaint corrosion initiated at random defects far away from the scratch.

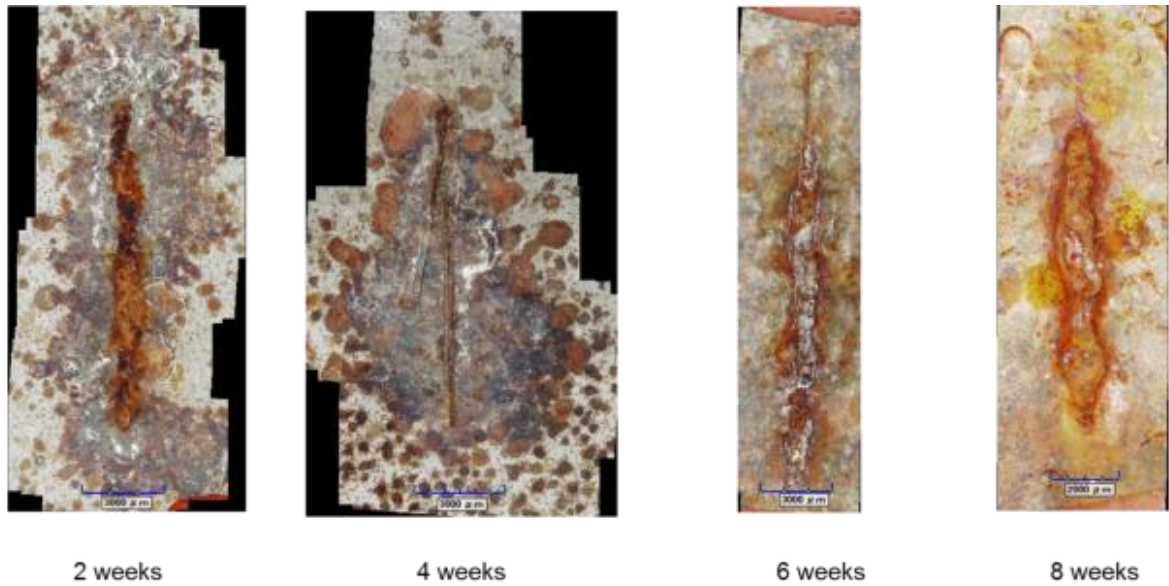


Figure 2.14 Optical images of the progression of scribe creep for Eponol coated steel exposed at KSC as a function of exposure time. Scale bars show 3000 μm .

Figure 2.15 shows scribe creep progression for BRD. Scribe creep occurs slowly, and even by week 6, there are still some parts of the scribe where scribe creep has not begun. There are many spots where corrosion has initiated that appear near to and far from the scribe. The scribe creep front appears to advance slowly until it comes to one of the small damage spots where the spot is incorporated into the scribe creep front. The creep front then advances slowly until it comes to a damage spot. This results in a very irregular scribe creep length along the scribe.

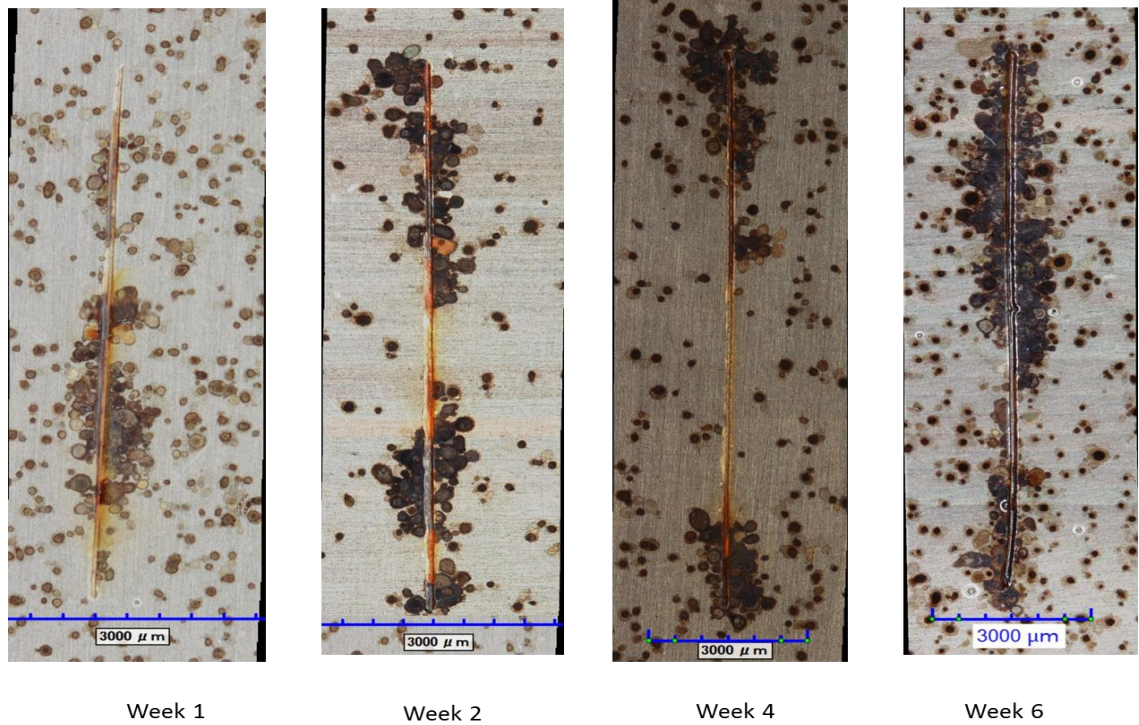


Figure 2.15 Optical images of the progression of scribe creep for Eponol coated steel exposed at BRD as a function of exposure time. Scale bars show 3000 μm .

In ASTM B-117, there is very little corrosion at the scribe at day 1, but there is some discoloration that extends about 3000 micrometers away from the scribe (Figure 2.16). This discolored area is then filled with corrosion product by day 3 and corrosion can be seen at positions away from the scribe. Figure 2.16 shows that corrosion proceeds quickly between day 1 and day 3. However, by day 10 the sample is too corroded to make any meaningful scribe creep measurements.

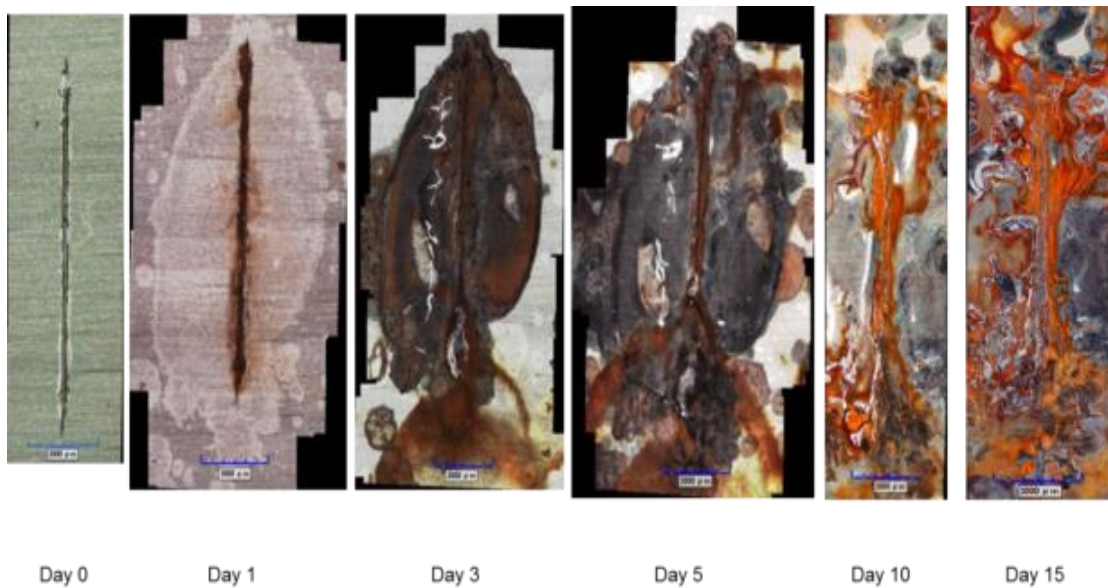


Figure 2.16 Optical images of the progression of scribe creep for Eponol coated steel exposed in ASTM B-117 as a function of exposure time. Scale bars show 3000 μm .

In ASTM G-85 Annex 5 scribe creep appears to progress at a steady rate with many filiform-like filaments extending from the scribe (Figure 2.17). Little to no corrosion appears to begin at locations away from the scribe, such as defect sites. ASTM G-85 Annex 5 has a faster progression of scribe creep compared with ASTM G-85 Annex 5 with UV (Figure 2.18).

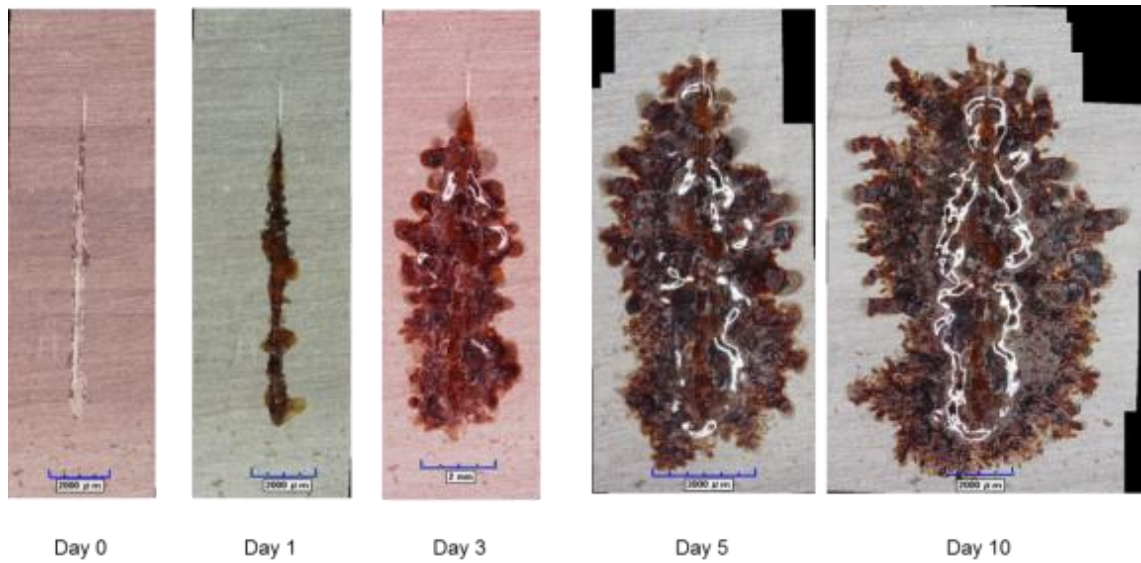


Figure 2.17 Optical images of the progression of scribe creep for Eponol coated steel exposed in ASTM G-85 Annex 5 as a function of exposure time. Scale bars show 3000 μm .

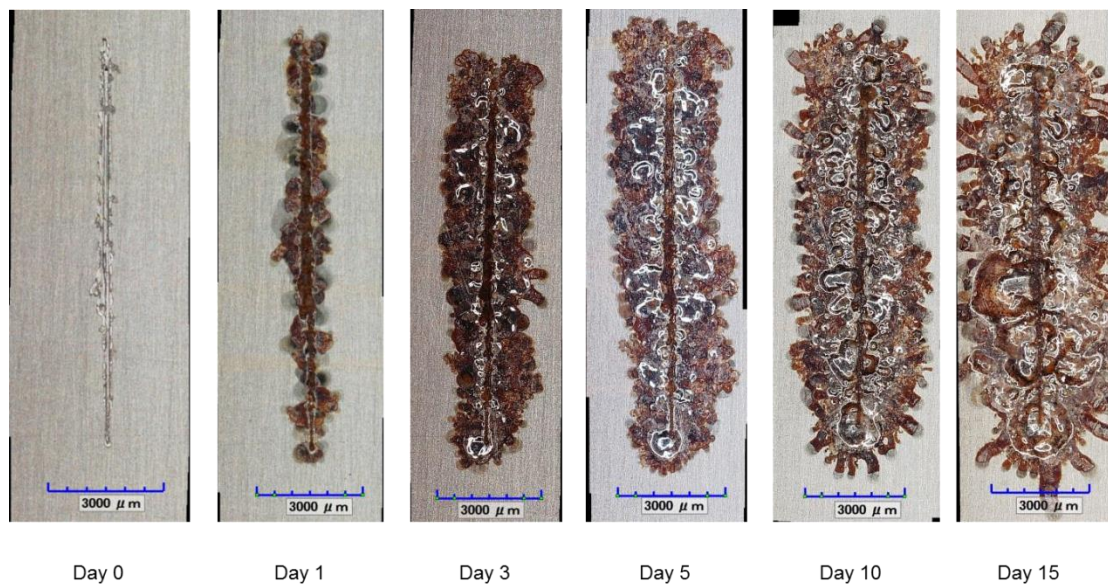


Figure 2.18 Optical images of the progression of scribe creep for Eponol coated steel exposed in ASTM G-85 Annex 5+UV as a function of exposure time. Scale bars show 3000 μm .

ASTM G-85 Annex 3 showed distinctly different behavior. Figure 2.19 shows discoloring around the scribe and at spots away from the scribe by day 1. By day 3, corrosion has

progressed significantly from the scribe until by day 5 it became difficult to distinguish scribe creep from corrosion initiated at defects away from the scribe. By day 10 the entire surface of the sample had corroded.

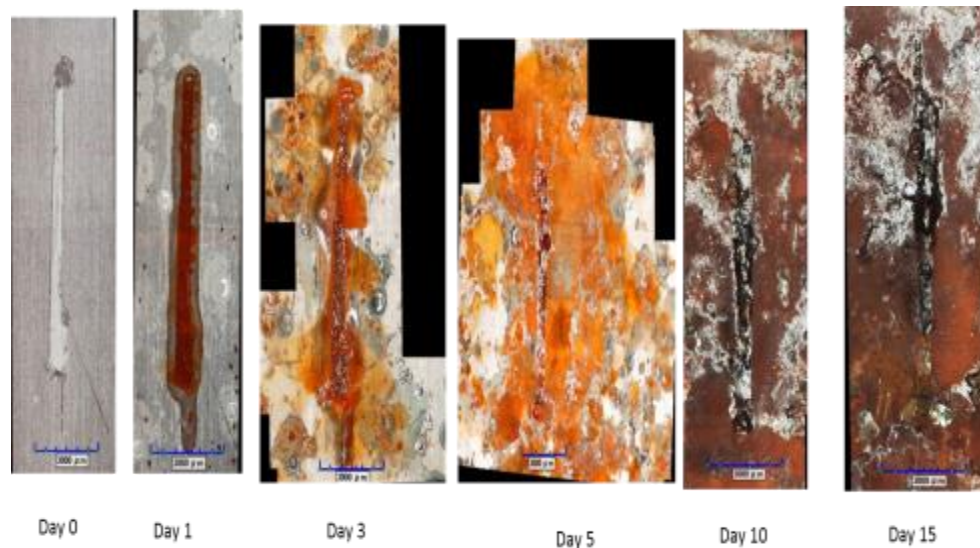


Figure 2.19 Optical images of the progression of scribe creep for Eponol coated steel exposed in ASTM G-85 Annex 3 as a function of exposure time. Scale bars show 3000 μm .

Images of the FITs are given for -1 V (Figure 2.20), OCP in 0.3 wt% NaCl (Figure 2.21) and OCP in 5% NaCl (Figure 2.22). It can be seen from Figure 2.20 that there is little scribe creep occurring over the duration of the test. There is discoloration in the scribe itself after one day and the discoloration progresses away from the scribe slightly over 15 days. Figure 2.21 shows corrosion building up in the scribe and moving out away from the scribe over time. By day 15 scribe creep can be seen to have progressed away from the scribe in all directions. OCP in 5% NaCl behaves in a similar manner as OCP in 0.3 wt% NaCl but progresses at an increased rate (Figure 2.22). The coating around the scribe appears to behave similarly to ASTM B-117 although the damage occurs more quickly and is much

more extensive in the ASTM B-117. Scribe creep progresses most quickly for OCP in 5% NaCl, then OCP in 0.3 wt% NaCl. However it is much slower for -1 V in 0.3 wt% NaCl.



Figure 2.20 Optical images of the progression of scribe creep for Eponol coated steel exposed in full immersion test in 0.3 wt% NaCl solution held at -1 V vs. SCE as a function of exposure time. Scale bars show 3000 μm.

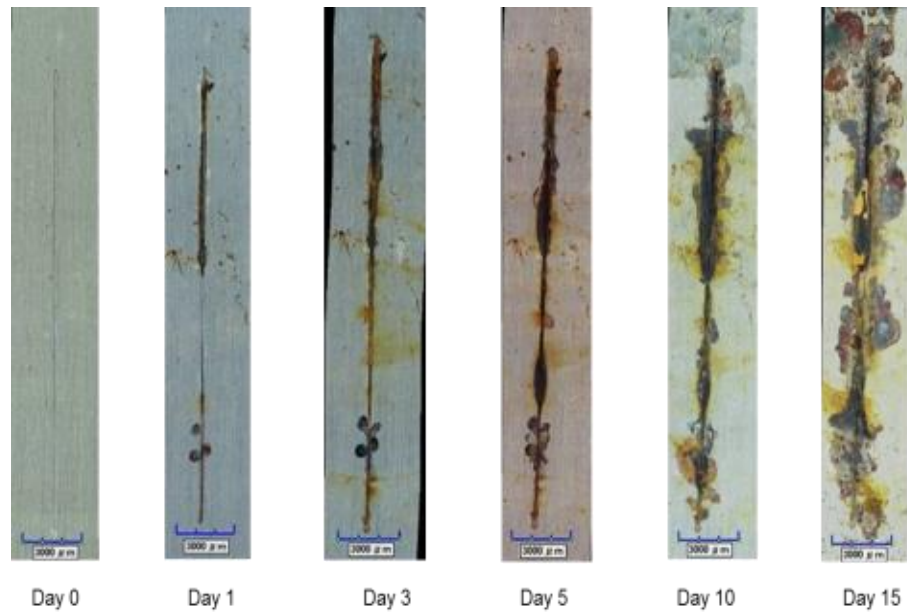


Figure 2.21 Optical images of the progression of scribe creep for Eponol coated steel exposed in full immersion test in 0.3 wt% NaCl solution held at OCP as a function of exposure time. Scale bars show 3000 μm .

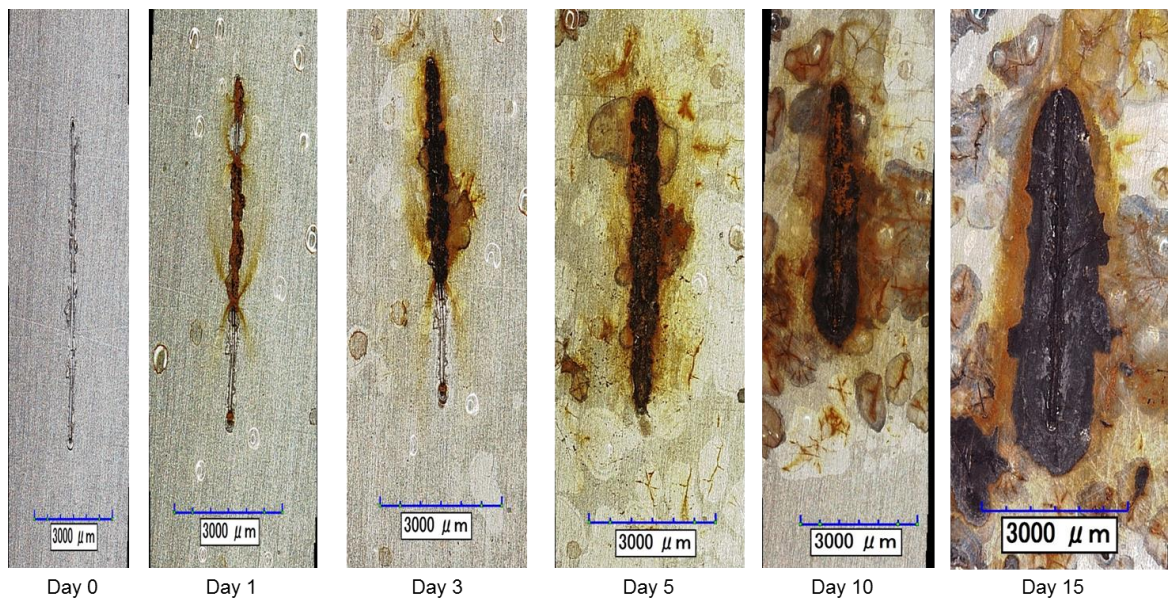


Figure 2.22 Optical images of the progression of scribe creep for Eponol coated steel exposed in full immersion test in 5% NaCl solution held at OCP as a function of exposure time. Scale bars show 3000 μm .

Images for the ASTM D-5894 are given in Figure 2.23. At 0.5 cycles (7 days in cyclic condensation and UV) there does not appear to be much corrosion at the scribe itself. However, there are many small dark spots all over the coated area of the sample that are indicative of damage to the coating. The spots are somewhat similar to the spots seen at BRD (Figure 2.15).

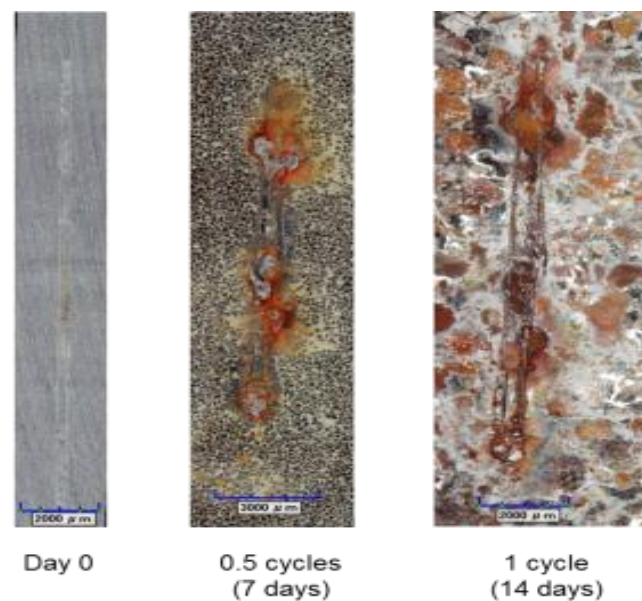


Figure 2.23 Optical images of the progression of scribe creep for Eponol coated steel exposed in ASTM D-5894 as a function of exposure time. Scale bars show 3000 μm .

The visual images of the scribe also allowed for scribe creep rate to be quantified and compared across exposures. Figure 2.24 shows the average scribe creep lengths for various exposure times summarized in one plot. The trends for scribe creep length are similar to trends for mass loss in that length increased more slowly over time. Moreover, the lengths observed at KSC at 6 weeks are similar to those in LALT after 15 days. Finally, lengths in full immersion are less than LALT or field.

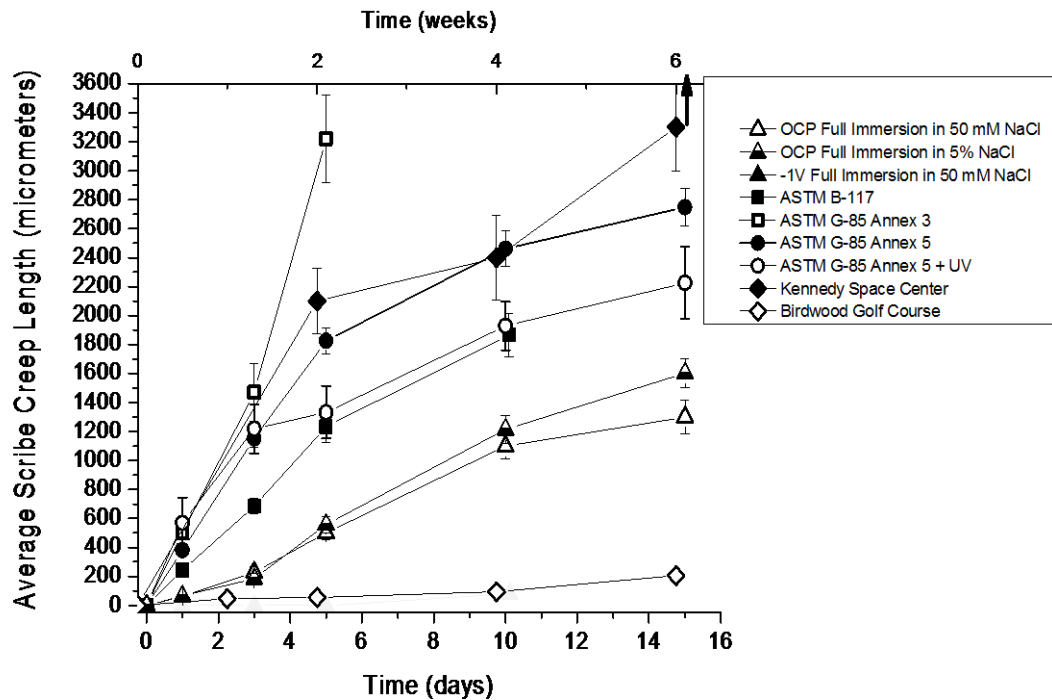


Figure 2.24 Plot of average scribe creep length vs. time for coated 1018 steel exposed to various LALT, field and full immersion environments. Error bars show standard error.

Higher level visual inspection was also done by taking 3D optical images of the scribe at specific locations, extracting the profile data and observing the change over time. Figure 2.26 shows line profiles of the scribe over time for KSC. It can be seen from visual inspection that corrosion product fills in the scribe and then begins to grow both upward and outward from the scribe; the outward growth wedging underneath the coating.

Samples exposed at BRD show some corrosion at the scribe and at spots near to and far from the scribe (Figure 2.27 and 2.28). The 3D images for ASTM B-117 are shown in Figure 2.29 and the line profiles in Figure 2.30. In contrast to KSC, corrosion products grow and build at the edges of the scribe but never fully fill the scribe. For ASTM G-85 Annex 5,

Figure 2.31 shows the 3D images and Figure 2.32 shows the line profiles for ASTM G-85 Annex 5. Over time, the corrosion product grows to fill the scribe and pushes outward under the coating in a manner similar to KSC. Therefore, ASTM G-85 Annex 5 appears to correlate better with KSC than ASTM B-117. Figure 2.33 shows the 3D images for ASTM G-85 Annex 5+UV and Figure 2.34 shows the line profiles. It can be seen that the corrosion product filled the scribe and grows outward similar to ASTM G-85 Annex 5 without UV. Figure 2.37 shows the 3D images for FIT at -1 V vs. SCE and Figure 2.38 shows the line profiles. It can be seen that little if any corrosion product buildup occurs in the scribe. Figure 2.39 shows the 3D images and Figure 2.40 shows profiles for FIT OCP in 50mM NaCl. It can be seen that corrosion product builds up in the scribe but doesn't quite fill the scribe completely. Corrosion product also spreads out away from the scribe underneath the coating. The 3D images (Figure 2.41) and line profiles (Figure 2.42) for OCP in 5% NaCl show that corrosion extends away from the scribe quickly and builds up at the edge of the scribe but never fills in the scribe itself.

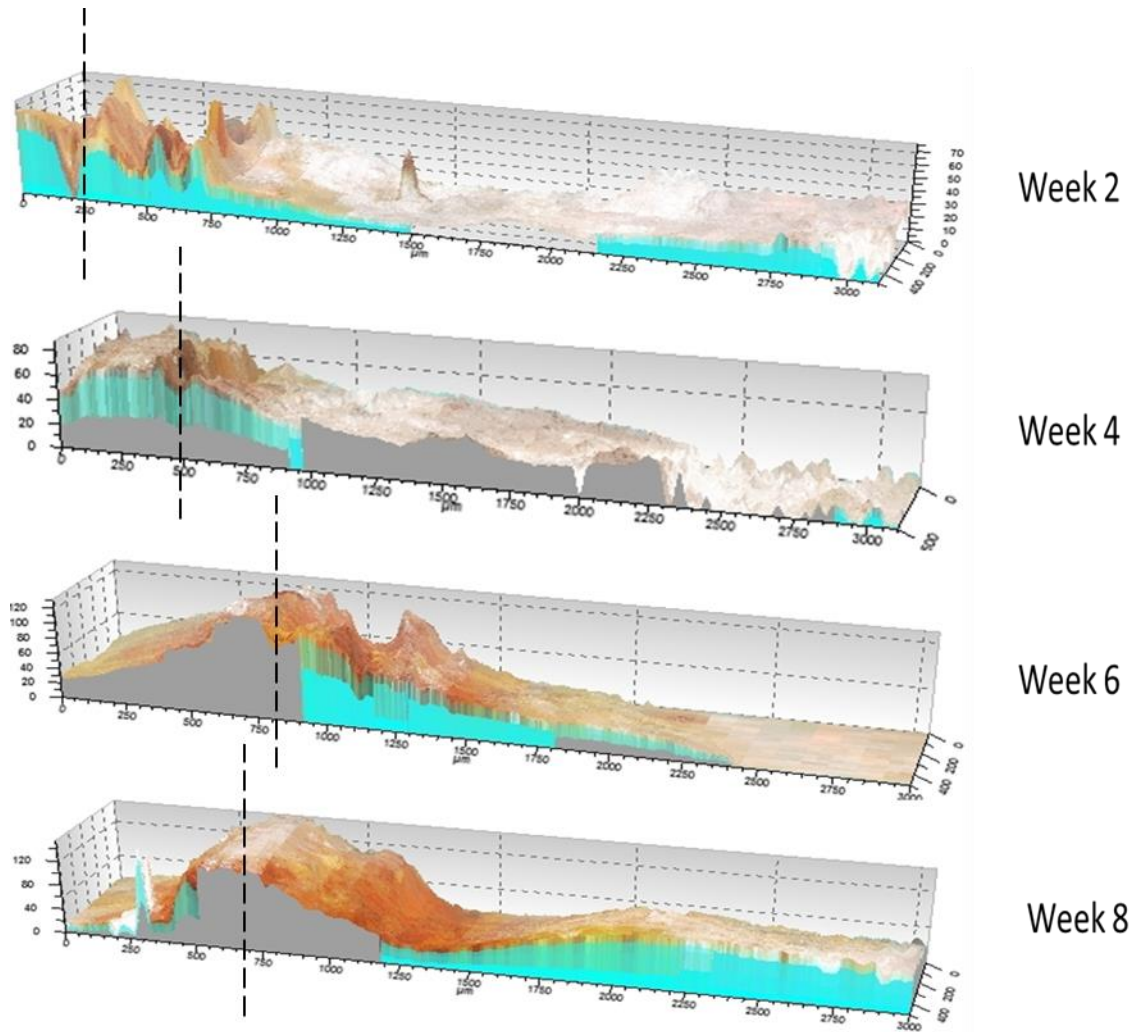


Figure 2.25 3D images of the scribe on epoxy resin coated 1018 steel exposed at KSC for 8 weeks. The units of the images are micrometers. Dashed lines show the location of the scribe.

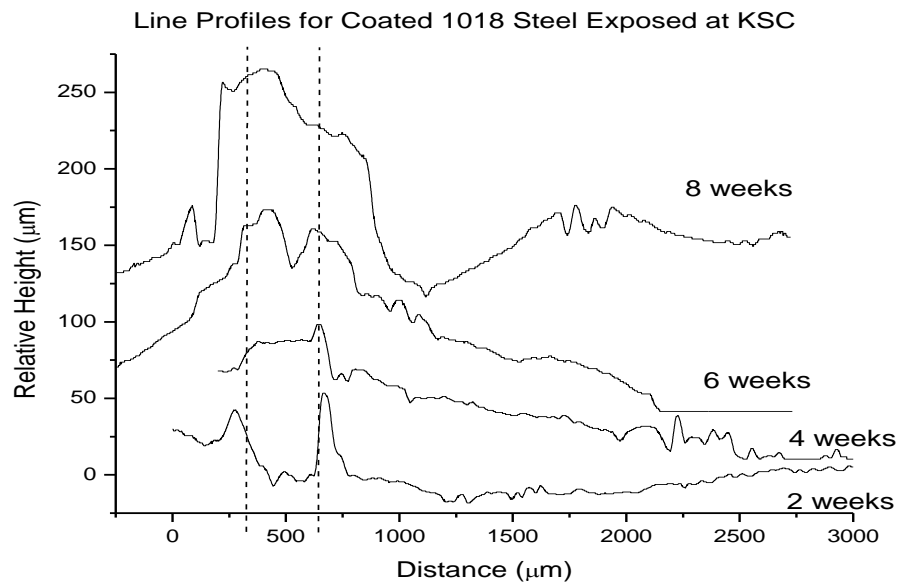


Figure 2.26 Selected line profiles for Eponol coated steel exposed at KSC. Vertical offset for data from each day reported is 50 μm. Dashed lines indicate original scribe location.

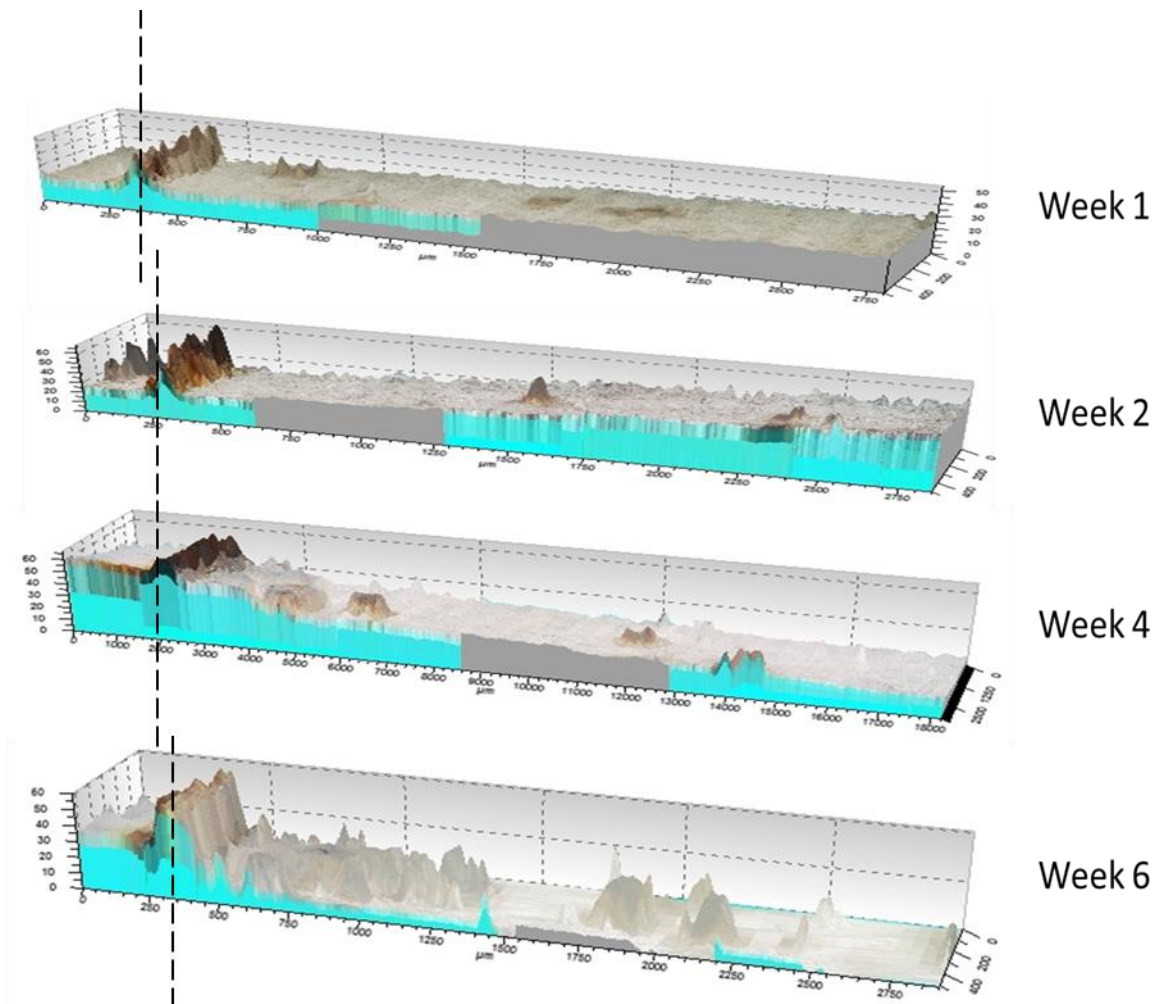


Figure 2.27 3D images of the scribe on epoxy resin coated 1018 steel exposed at BRD for 8 weeks. The units of the images are micrometers. Dashed lines show the location of the scribe.

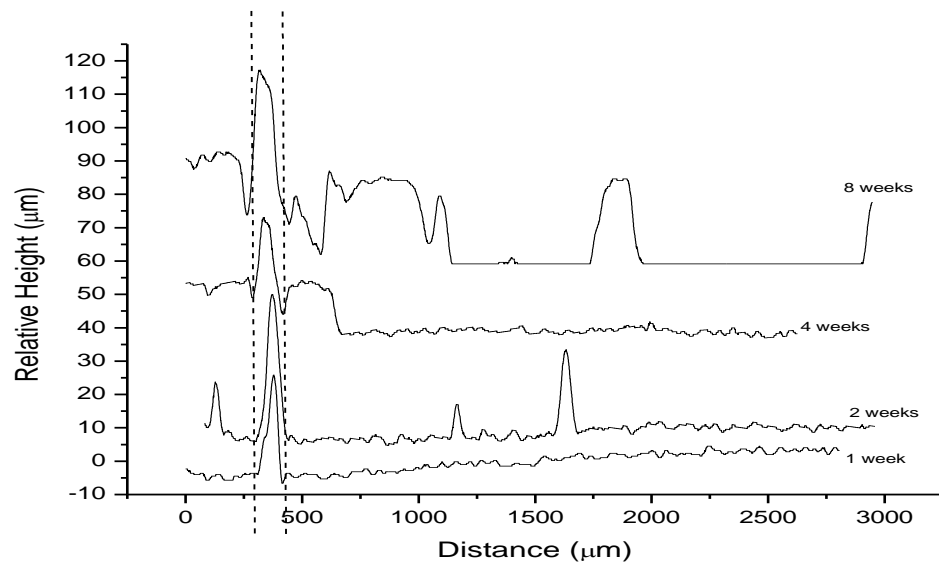


Figure 2.28 Selected line profiles for Eponol coated steel exposed at BRD. Vertical offset for data from each day reported is 30 μm . Dashed lines indicate original scribe location.

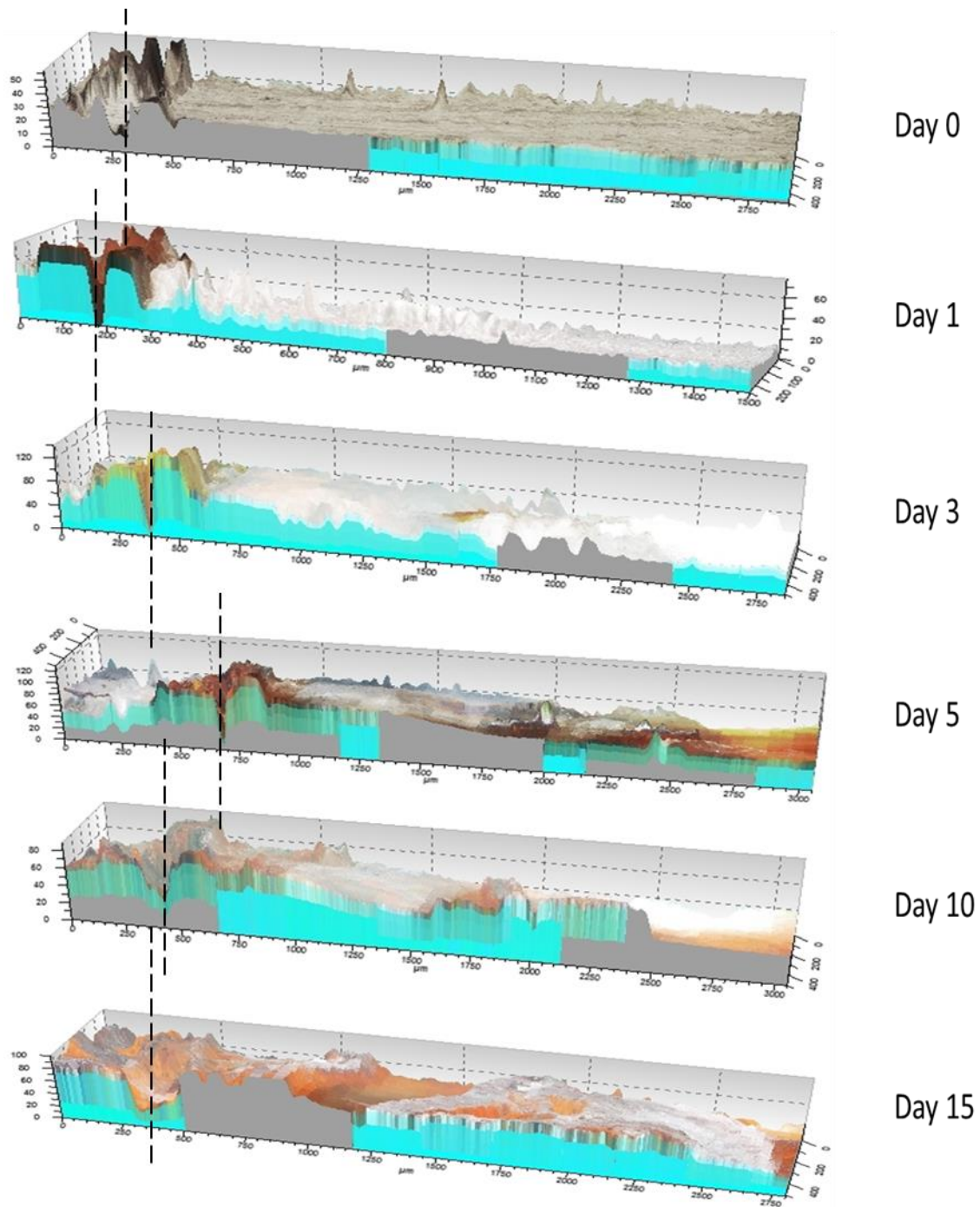


Figure 2.29 3D images of the scribe on epoxy resin coated 1018 steel exposed to ASTM B-117 for 15 days. The units of the images are micrometers. Dashed lines show the location of the scribe.

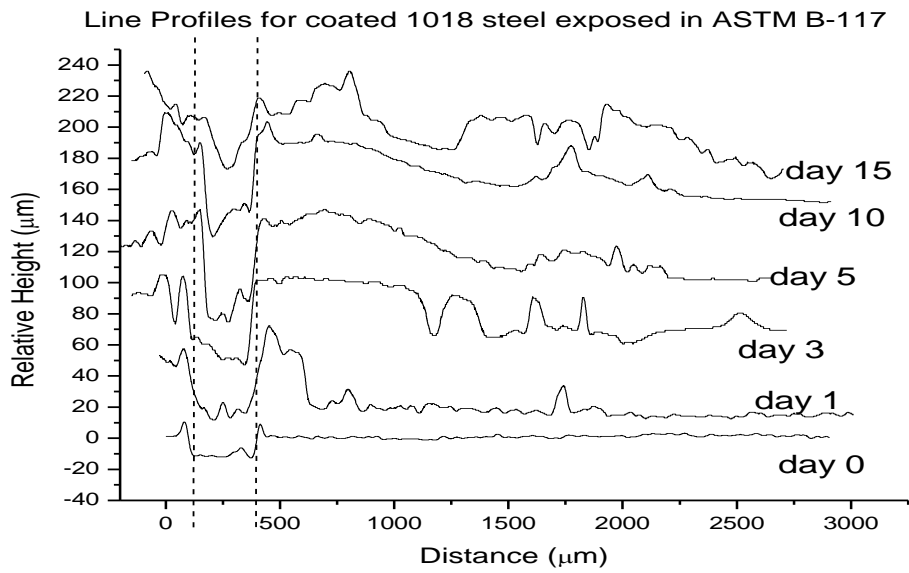


Figure 2.30 Selected line profiles for Eponol coated steel exposed in ASTM B-117. Vertical offset for data from each day reported is 40 μm . Dashed lines indicate original scribe location.

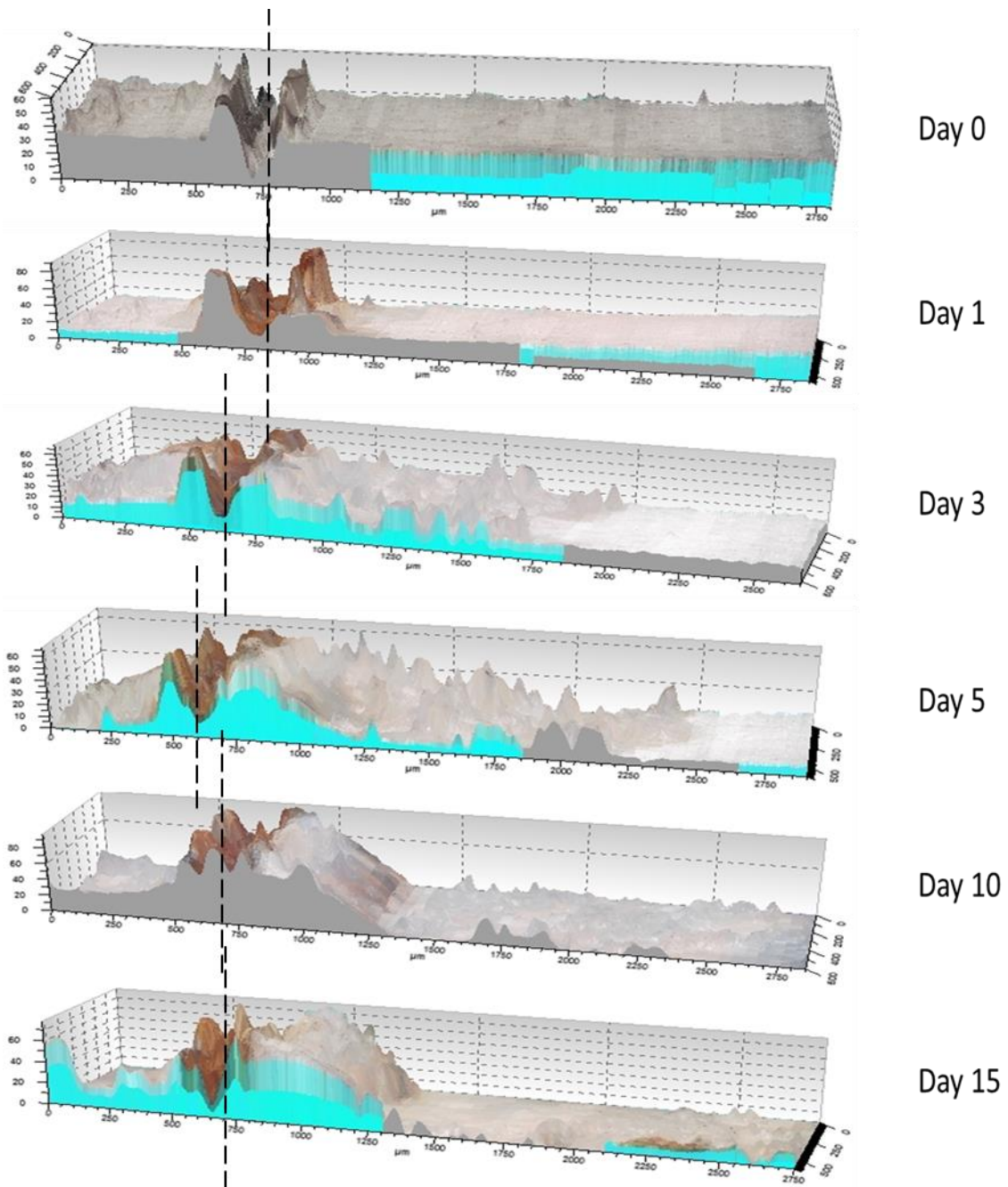


Figure 2.31 3D images of the scribe on epoxy resin coated 1018 steel exposed to ASTM G-85 Annex 5 for 15 days. The units of the images are micrometers. Dashed lines show the location of the scribe.

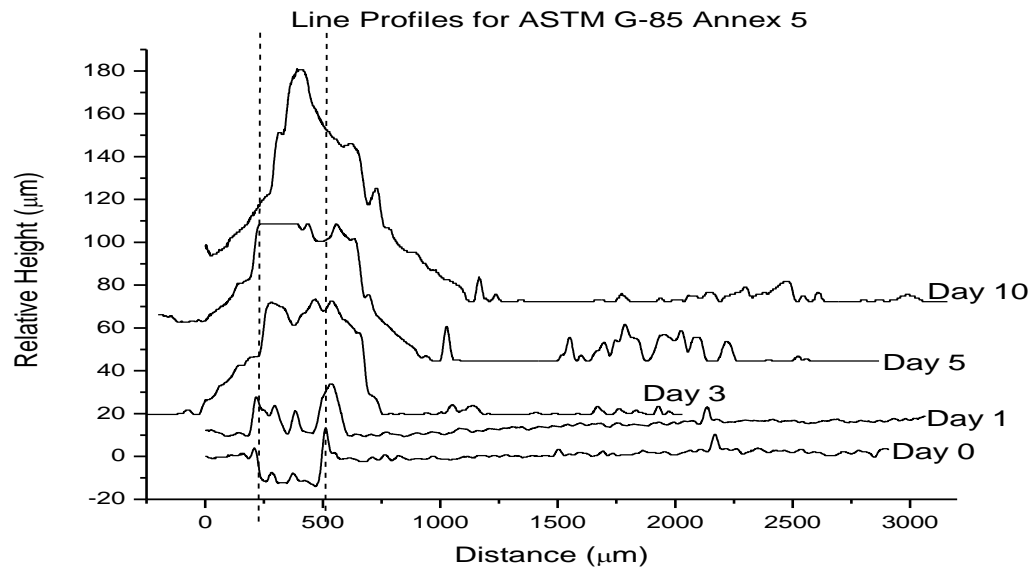


Figure 2.32 Selected line profiles for Eponol coated steel exposed in ASTM G-85 Annex 5. Vertical offset for data from each day reported is 20 μm . Dashed lines indicate original scribe location.

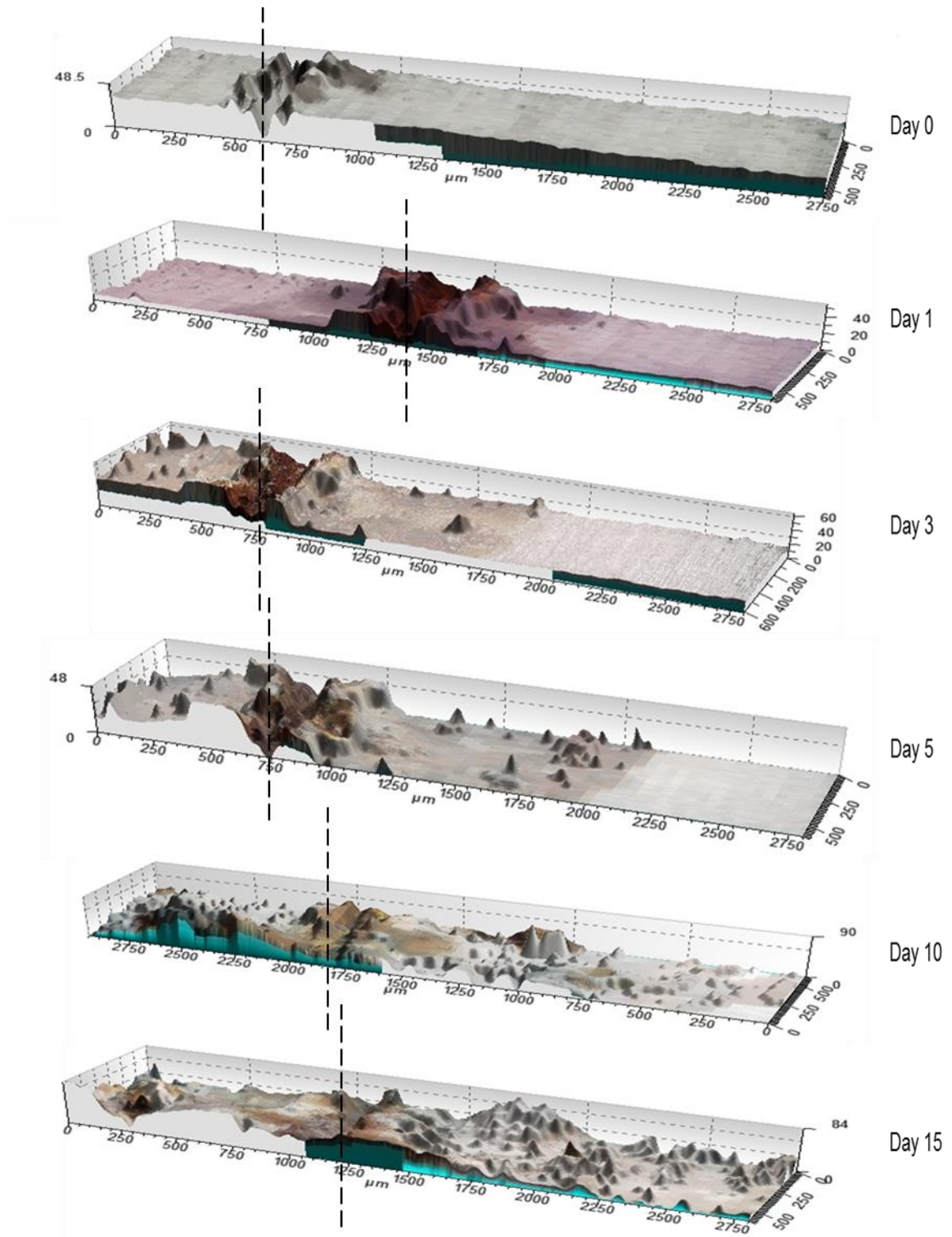


Figure 2.33 3D images of the scribe on epoxy resin coated 1018 steel exposed to ASTM G-85 Annex 5+UV for 15 days. The units of the images are micrometers. Dashed lines show the location of the scribe.

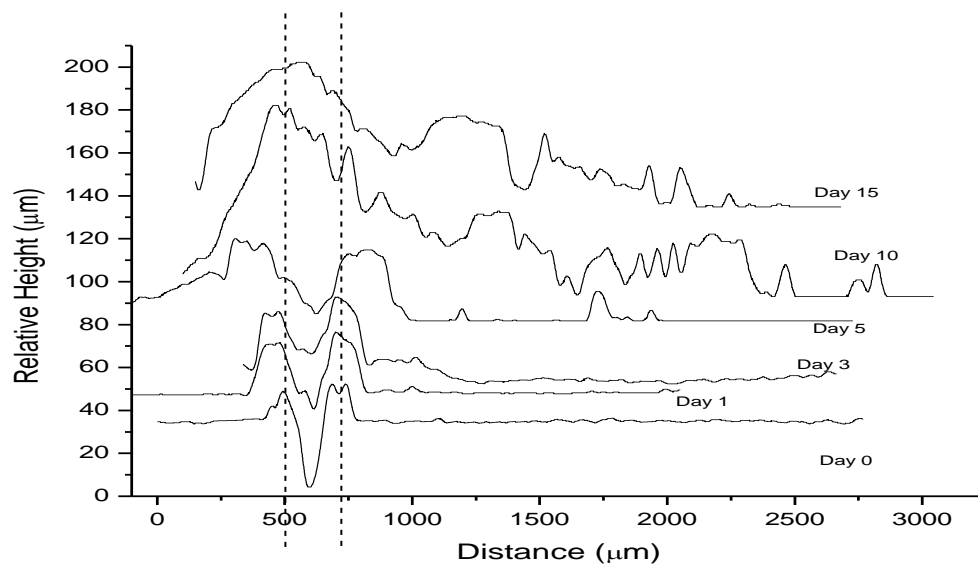


Figure 2.34 Selected line profiles for Eponol coated steel exposed in ASTM G-85 Annex 5+UV. Vertical offset for data from each day reported is 20 μm. Dashed lines indicate original scribe location.

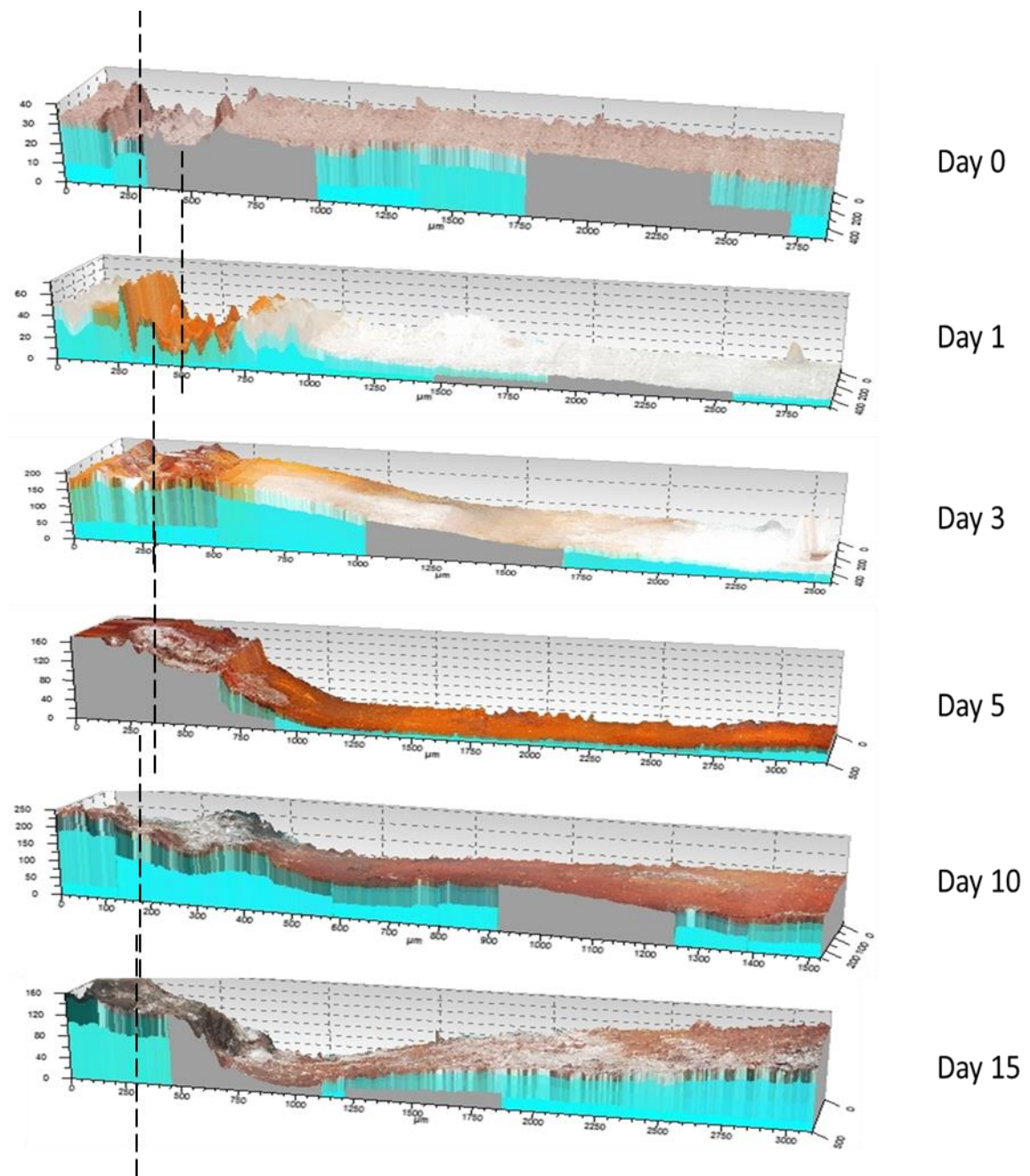


Figure 2.35 3D images of the scribe on epoxy resin coated 1018 steel exposed to ASTM G-85 Annex 3 for 15 days. The units of the images are micrometers. Dashed lines show the location of the scribe.

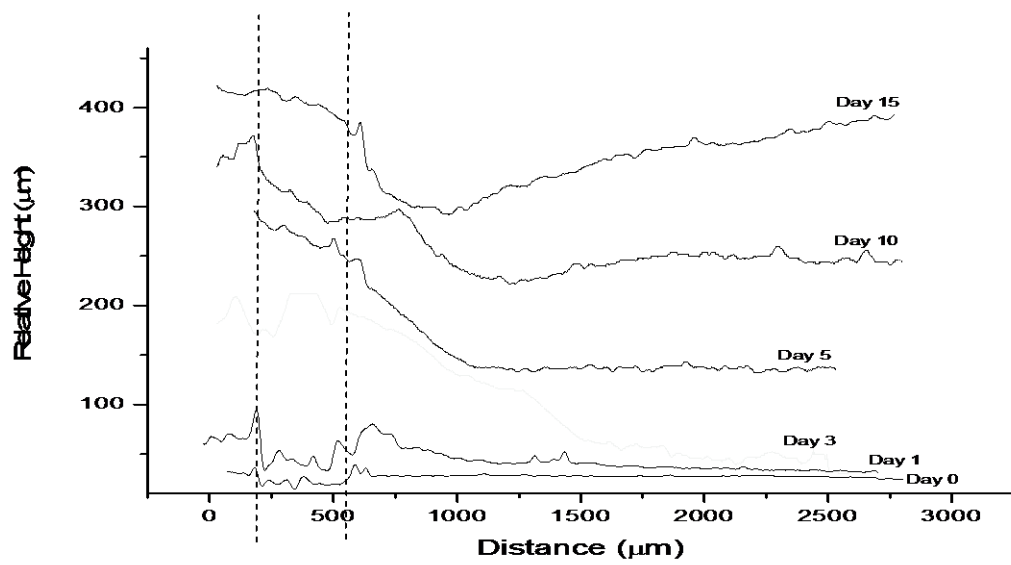


Figure 2.36 Selected line profiles for Eponol coated steel exposed in ASTM G-85 Annex 3. Vertical offset for data from each day reported is 60 μm . Dashed lines indicate original scribe location.

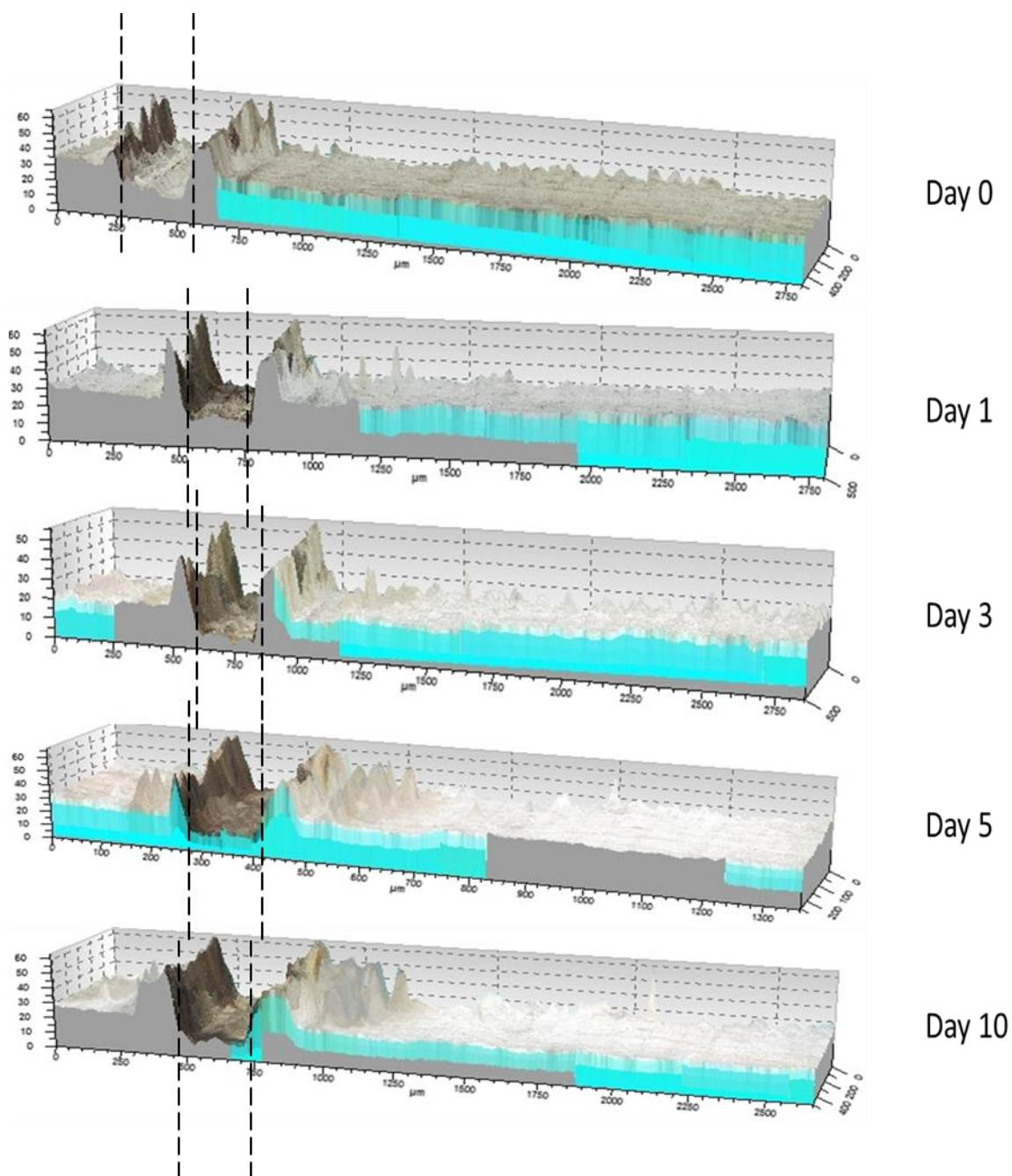


Figure 2.37 3D images of the scribe on epoxy resin coated 1018 steel exposed in full immersion in aerated 0.3 wt% NaCl solution at 25°C held at -1 V vs. SCE as a function of exposure time. The units of the images are micrometers. Dashed lines show the location of the scribe.

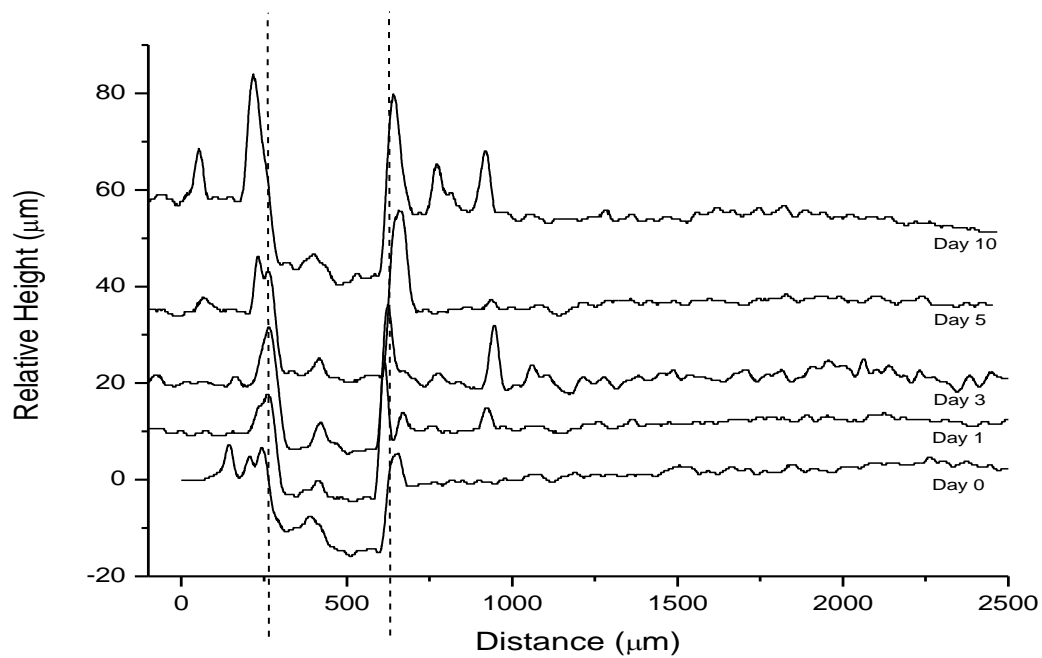


Figure 2.38 Selected line profiles for Eponol coated steel exposed in full immersion test in 0.3 wt% NaCl solution held at -1 V vs. SCE. Vertical offset for data from each day reported is 10 μm . Dashed lines indicate original scribe location.

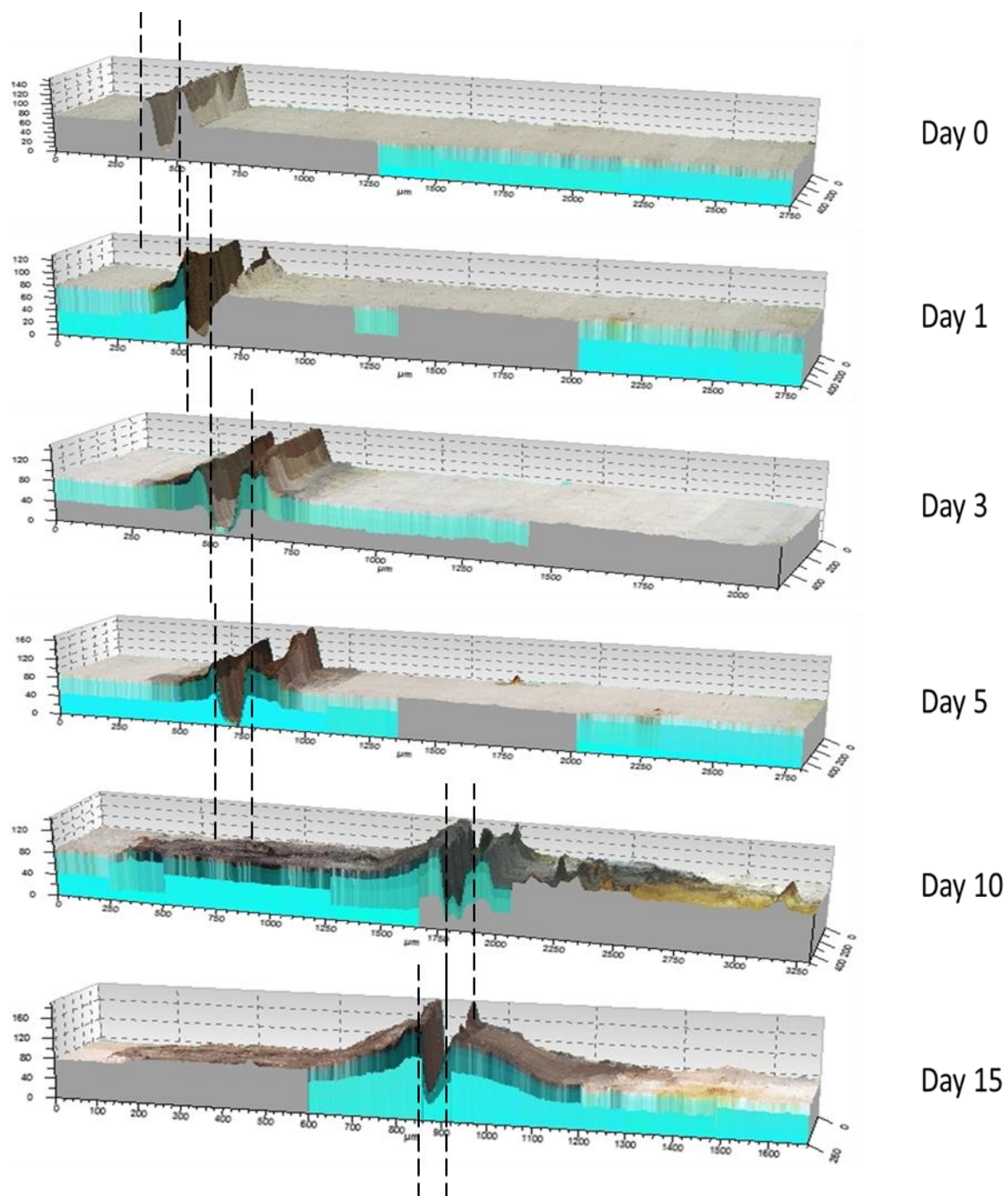


Figure 2.39 3D images of the scribe on epoxy resin coated 1018 steel exposed in full immersion in aerated 0.3 wt% NaCl solution at 25°C held at OCP as a function of exposure time. The units of the images are micrometers. Dashed lines show the location of the scribe.

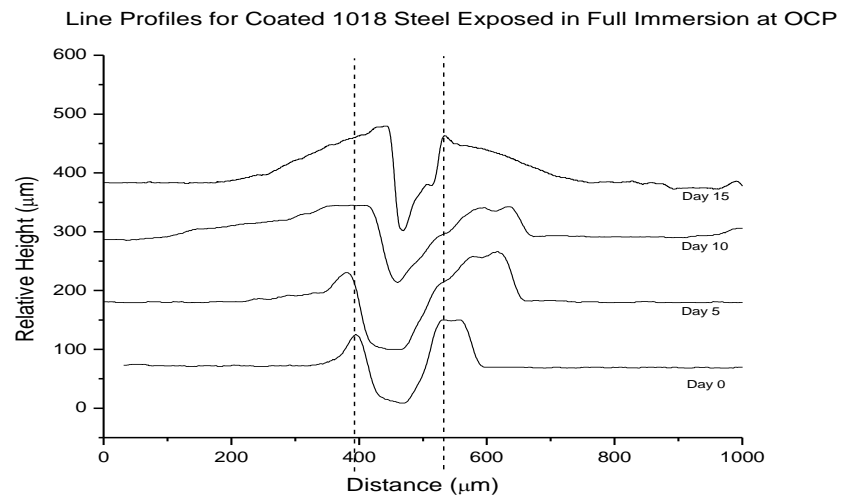


Figure 2.40 Selected line profiles for Eponol coated steel exposed in full immersion test in 0.3 wt% NaCl solution held at OCP. Vertical offset for data from each day reported is 100 μm. Dashed lines indicate original scribe location.

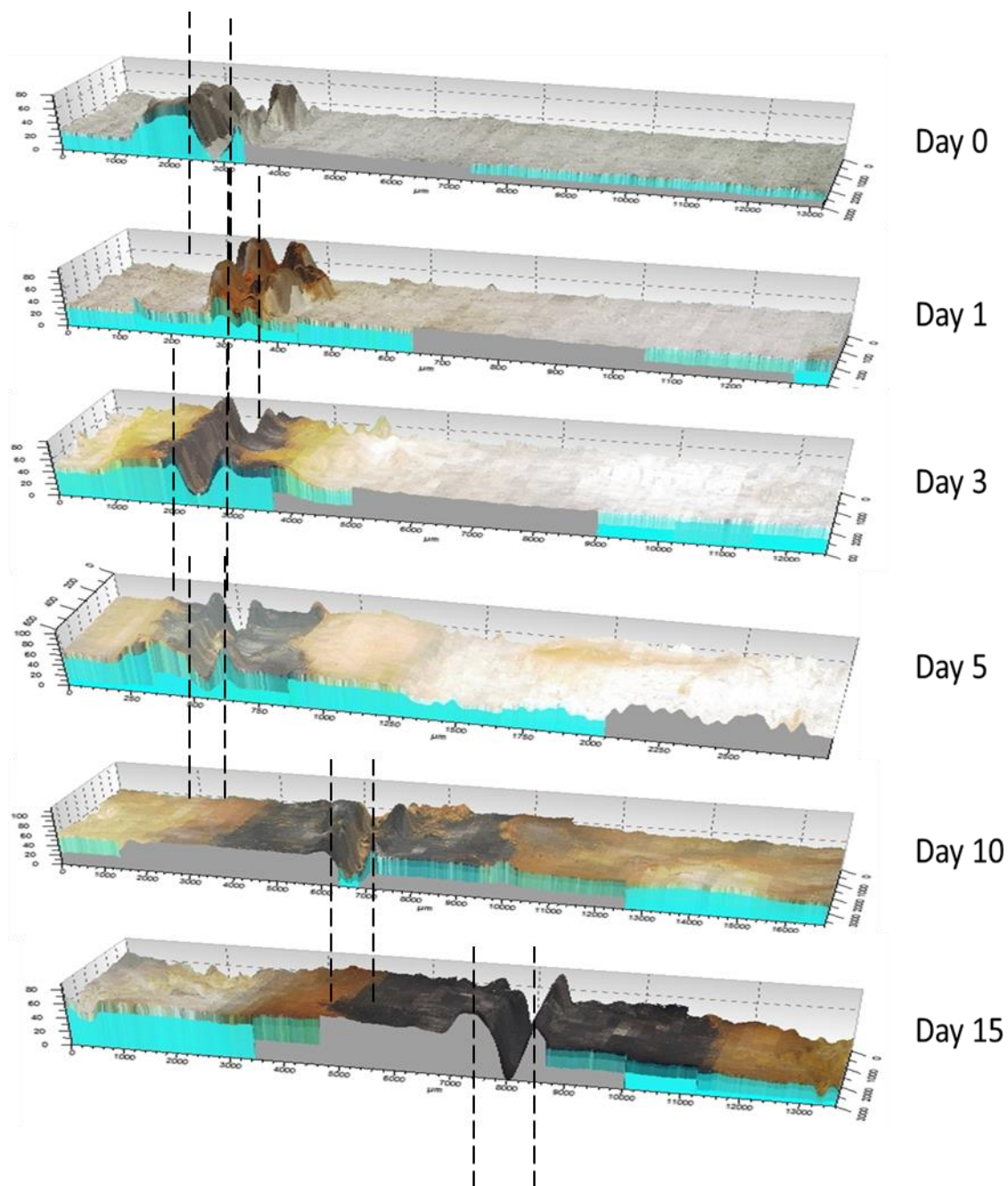


Figure 2.41 3D images of the scribe on epoxy resin coated 1018 steel exposed in full immersion in aerated 5% NaCl solution at 25°C held at OCP as a function of exposure time. The units of the images are micrometers. Dashed lines show the location of the scribe.

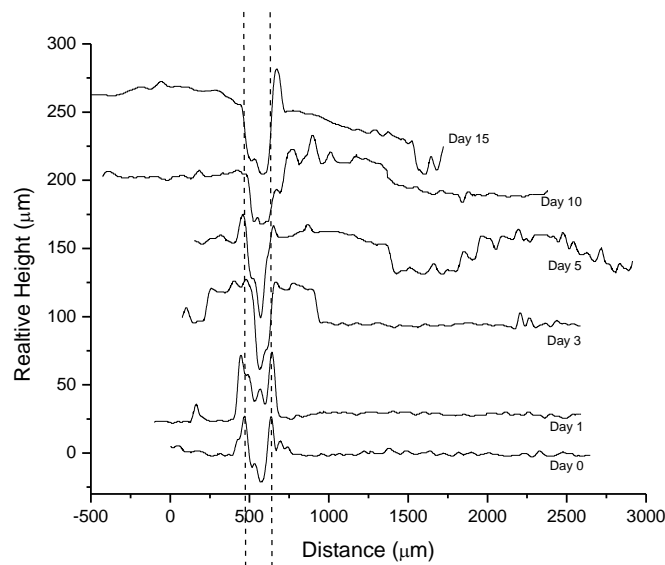


Figure 2.42 Selected line profiles for Eponol coated steel exposed in full immersion test in 5% NaCl solution held at OCP. Vertical offset for data from each day reported is 100 μm . Dashed lines indicate original scribe location.

Mass loss results across exposures were also compared to scribe creep results to determine if any correlation between the two exists. It was found that there is a strong positive correlation between mass loss values and scribe creep length values as discussed in Section 2.6.2 ($r^2=0.9012$; see Figure 2.56 and 2.57). This suggests that scribe creep susceptibility of an epoxy resin coated steel without surface treatments could be estimated from readily available mass loss data. This issue is addressed further in the discussion section.

2.5.4 Coating Analysis

2.5.4.1 Electrochemical Impedance Spectroscopy

It is well known that EIS can be used to characterize the sum of the Ohmic (solution) resistance (R_s), the coating resistance (R_{coat}), and the polarization resistance (R_p) for typical organic coated specimens.⁴⁷⁻⁵⁰ The complex impedance ($|Z|$) is taken at 0.01 Hz for a typical coating with an interrogation area of 1 cm². Therefore $Z_{0.01}$ can be used to monitor the coating resistance during exposure and provides a measure of $R_{coat} + R_p + R_s$. The EIS data is shown from Figure 2.43 to 2.51 in the Bode magnitude format. Normalized EIS data for all exposures can be seen in Figure 2.52 and 2.53. The EIS data indicate that the electrical properties of the coating on samples exposed at KSC decreased with time of exposure more quickly near the scribe but also decreased substantially far from the scribe. (Figure 2.52 and 2.53). For BRD, coating properties degrade slowly far from the scribe and only slightly faster near to the scribe (Figure 2.52 and 2.53). Coating properties for ASTM G-85 Annex 3 corrode quickly both near to and far from the scribe (Figure 2.52 and 2.53). Coating properties for the ASTM B-117 degrade quickly both near and far from the scribe (Figure 2.52 and 2.53). Coating properties in the ASTM G-85 Annex 5 also degrade quickly near to the scribe similar to KSC, but unlike KSC and ASTM B-117, barely change at all far from the scribe (Figure 2.52 and 2.53). This may be an effect of the 0.05% concentration of NaCl in ASTM G-85 Annex 5 vs. 5% in ASTM B-117. However, coating properties in the ASTM G-85 Annex 5+UV also degrade quickly near the scribe, and degrade far from the scribe after day 5 of the test (Figure 2.52 and 2.53), similar to KSC. Changes in EIS data that occur over six weeks at KSC occur in 15 days in ASTM G-85 Annex 5+UV.

FIT -1 V vs. SCE samples (Figure 2.52 and 2.53) showed little change in the electrical properties of the coating over time, both near to and far from the scribe. FIT OCP samples in 0.3 wt% NaCl (Figure 2.52 and 2.53) showed some degradation of the coating properties over time, but the degradation is not as severe as the coating degradation seen for KSC, ASTM B-117 and ASTM G-85 Annex 5+UV both near to and far from the scribe. FIT OCP samples in 5% NaCl degraded quickly near to the scribe. FIT OCP in 5% NaCl (Figure 2.52 and 2.53) showed fairly rapid decrease in electrical properties near to the scribe while far from the scribe the properties remained high until day 15.

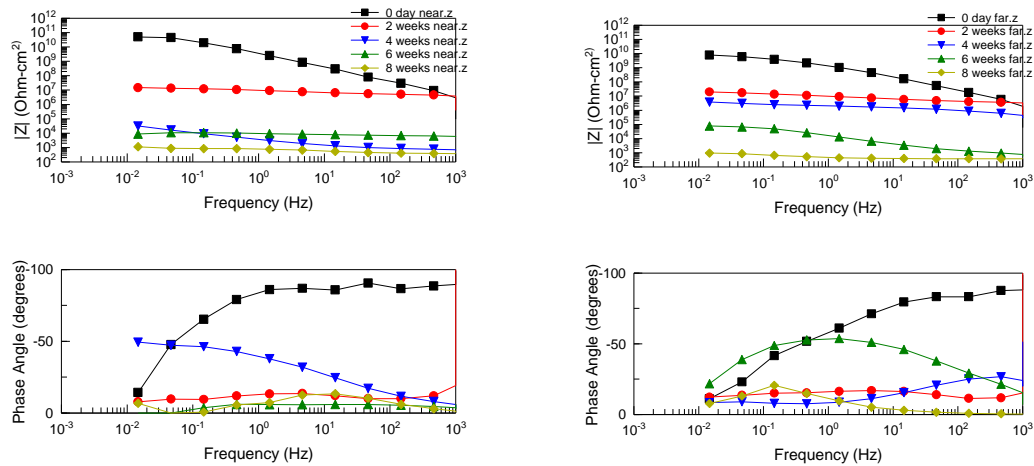


Figure 2.43 Raw EIS data from samples exposed at KSC. Data were taken from the near location (left) and far location (right).

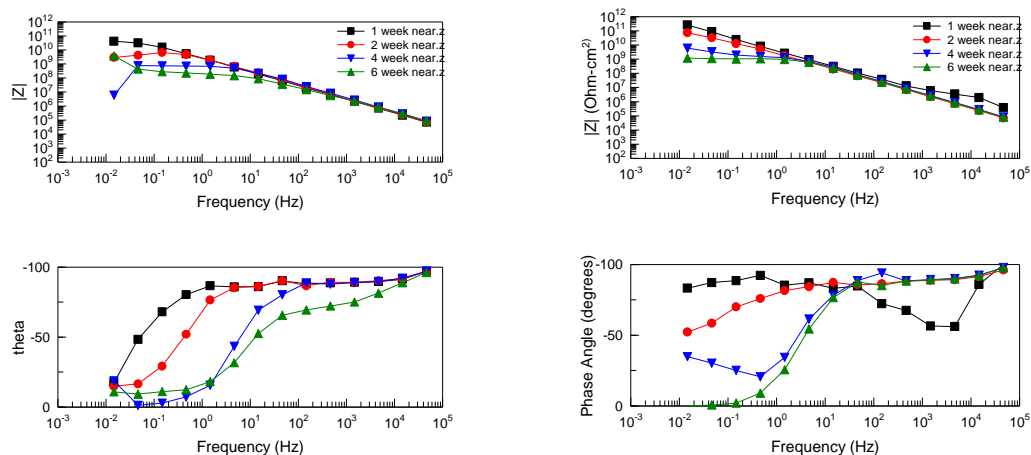


Figure 2.44 Raw EIS data for samples exposed at BRD. Data were taken from the near location (left) and far location (right).

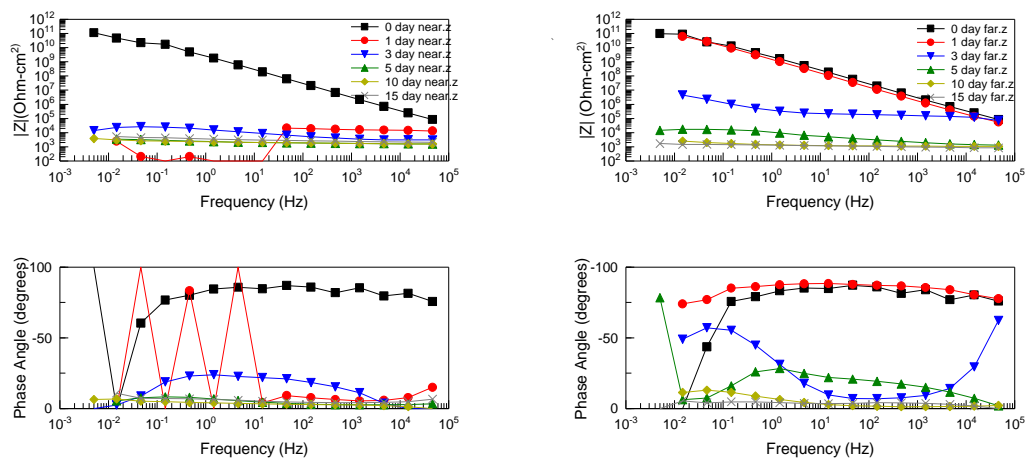


Figure 2.45 Raw EIS data from samples exposed in ASTM B-117. Data were taken from the near location (left) and far location (right).

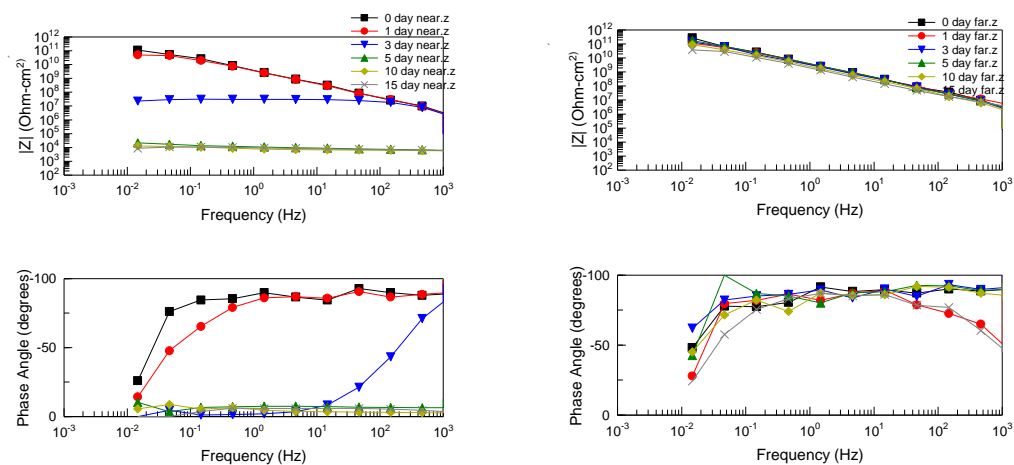


Figure 2.46 Raw EIS data from exposed in ASTM G-85 Annex 5. Data were taken from the near location (left) and far location (right).

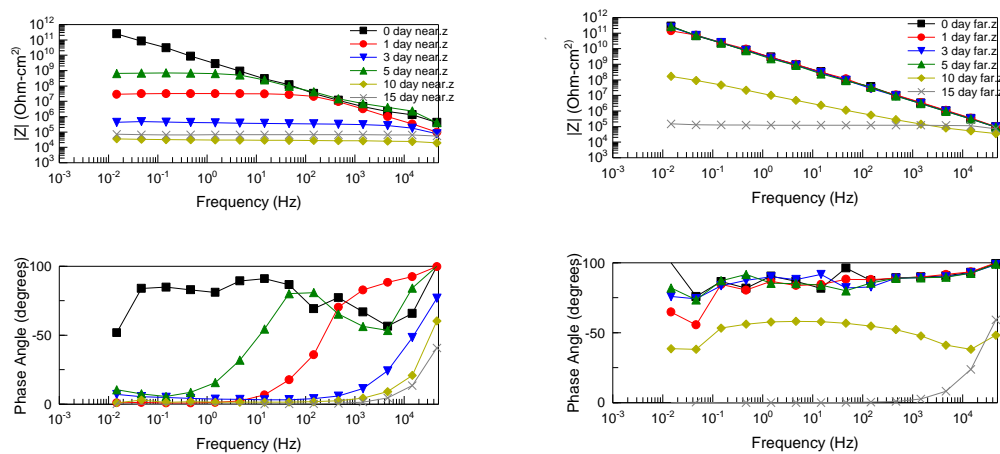


Figure 2.47 Raw EIS data from samples exposed in ASTM G-85 Annex 5+UV. Data were taken from the near location (left) and far location (right).

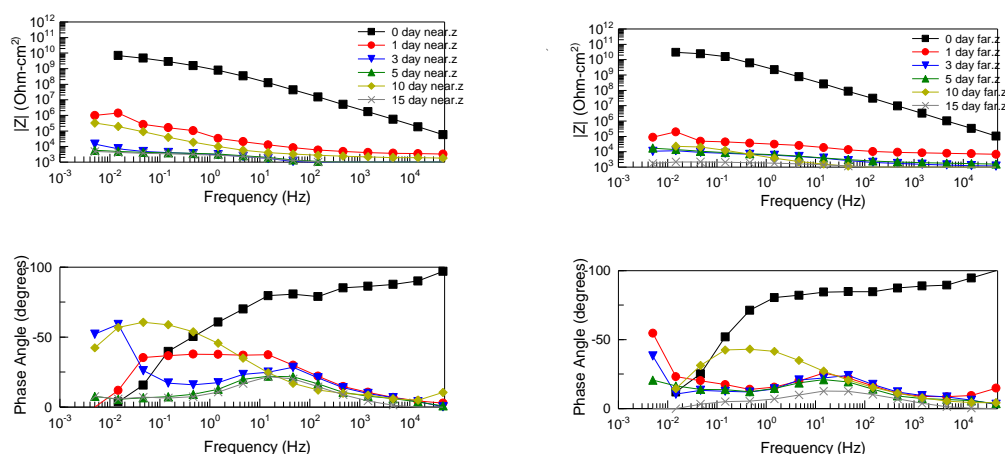


Figure 2.48 Raw EIS data from samples exposed in ASTM G-85 Annex 3. Data were taken from the near location (left) and far location (right).

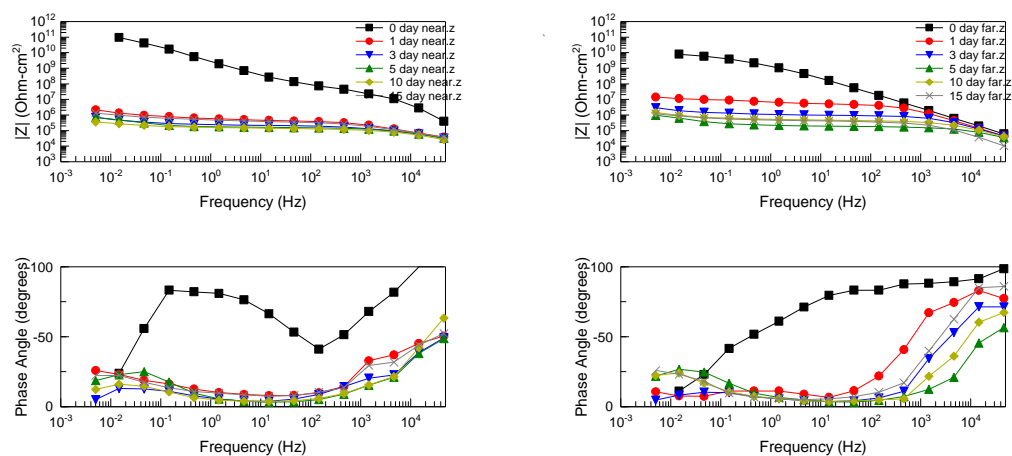


Figure 2.49 Raw EIS data from samples exposed in full immersion at OCP in aerated 0.3 wt% NaCl solution at 25°C. Data were taken from the near location (left) and far location (right).

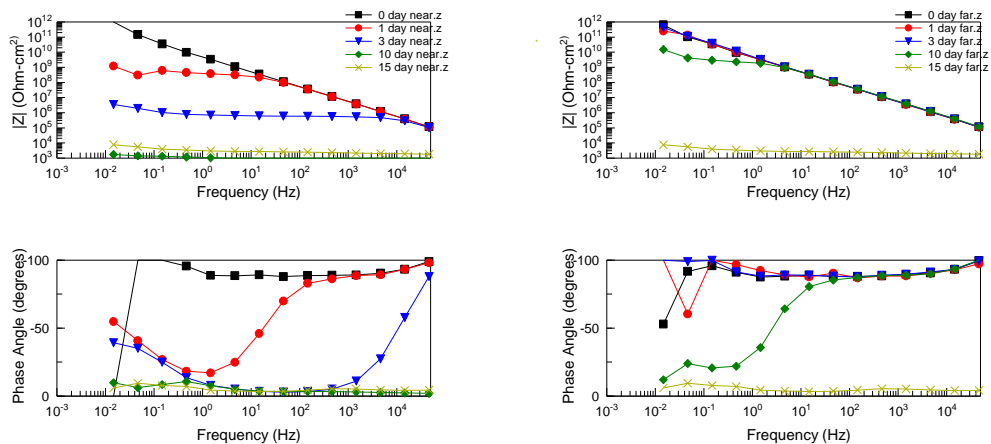


Figure 2.50 Raw EIS data from samples exposed in full immersion at OCP in aerated 5% NaCl solution at 25°C. Data were taken from the near location (left) and far location (right).

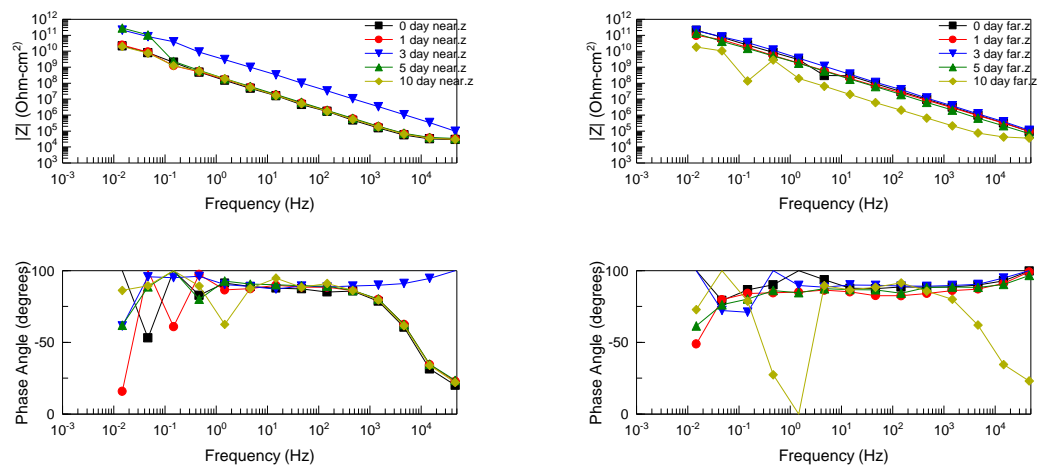


Figure 2.51 Raw EIS data from samples exposed in full immersion at -1 V vs. SCE in aerated 0.3 wt% NaCl solution at 25°C. Data were taken from the near location (left) and far location (right).

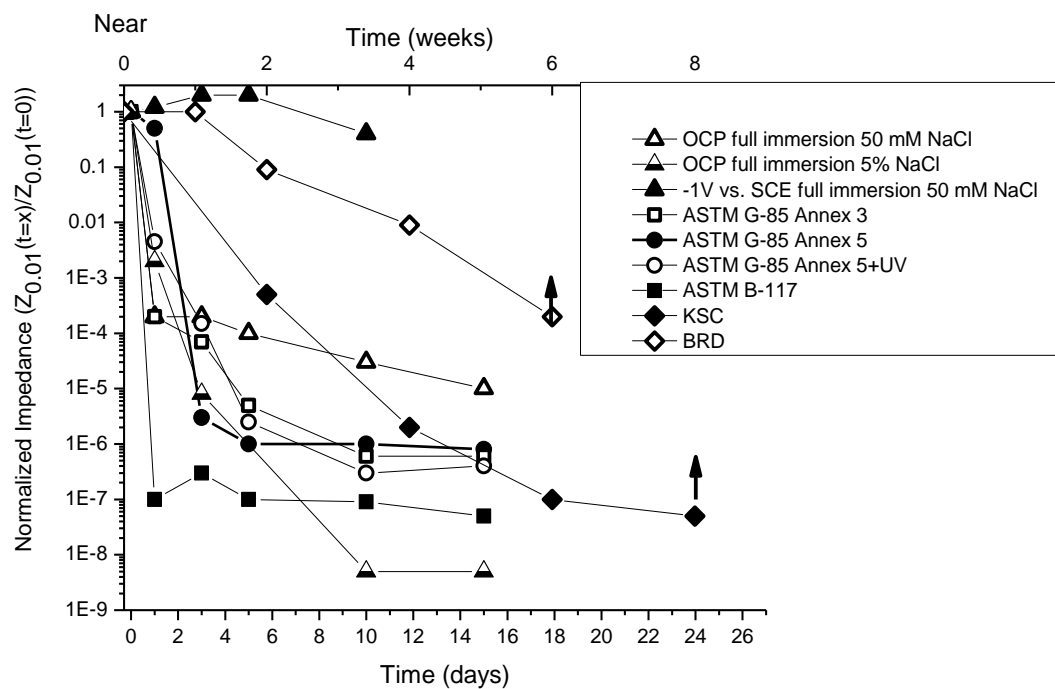


Figure 2.52 Normalized low frequency impedance values over time for Eponol coated steel samples exposed in various standard LALTs. EIS readings taken at near location. Normalization was $|Z_{0.01}|(\text{day})/|Z_{0.01}|(\text{initial})$ for all days of the test. Time for KSC and BRD are shown on the top axis.

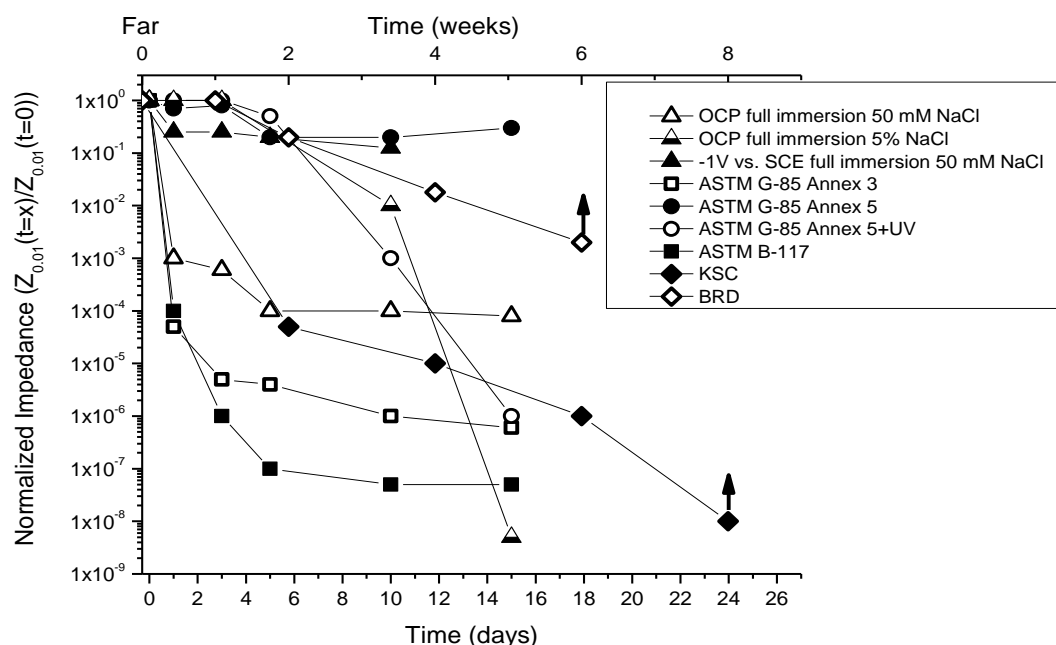


Figure 2.53 Normalized low frequency impedance values over time for Eponol coated steel samples exposed in various standard LALTs. EIS readings taken at far location. Normalization was $|Z_{0.01}|(\text{day})/|Z_{0.01}|(\text{initial})$ for all days of the test.

2.5.4.2 Fourier Transform Infrared Spectroscopy

FTIR was performed on 30 μm thick Eponol coatings on polypropylene substrates exposed to ASTM B-117, ASTM G-85 Annex 3 (Figure 2.54) and KSC (Figure 2.55). The polypropylene substrate on which the Eponol coating is cast is inert, and thus has no effect on the degradation of the coating. This isolates the effects of the environment from the effects of underpaint corrosion on degradation of the coating. Degradation of the coating was observed by comparing the results of an unexposed coating to exposed coatings. The results, shown in Figure 2.54, show that there is no degradation of the epoxy resin coating after 15 days of exposure in ASTM B-117 or ASTM G-85 Annex 5. In contrast, Figure 2.55

shows ASTM B-117 as well as ASTM G-85 Annex 5 with and without UV, and two samples exposed at KSC for 2 and 5 months; degradation of the coating of the KSC and ASTM G-85 Annex 5+UV samples can be seen. The decrease in intensity of the 2963 and 2920 cm^{-1} peaks show degradation of CH, CH_2 , and CH_3 bonds in the coating.⁵¹⁻⁵⁵ The appearance and increase of a peak at 1717 cm^{-1} is caused by the formation of carbonyls and aldehydes which are products of degradation of the aliphatic carbon bonds in the coating.⁵¹⁻⁵⁵ The broadening of the peak at 3362 cm^{-1} and the appearance of a shoulder at 1609 cm^{-1} indicate an increase in OH bonds due to an increase in water molecules in the coating.⁵¹⁻⁵⁵

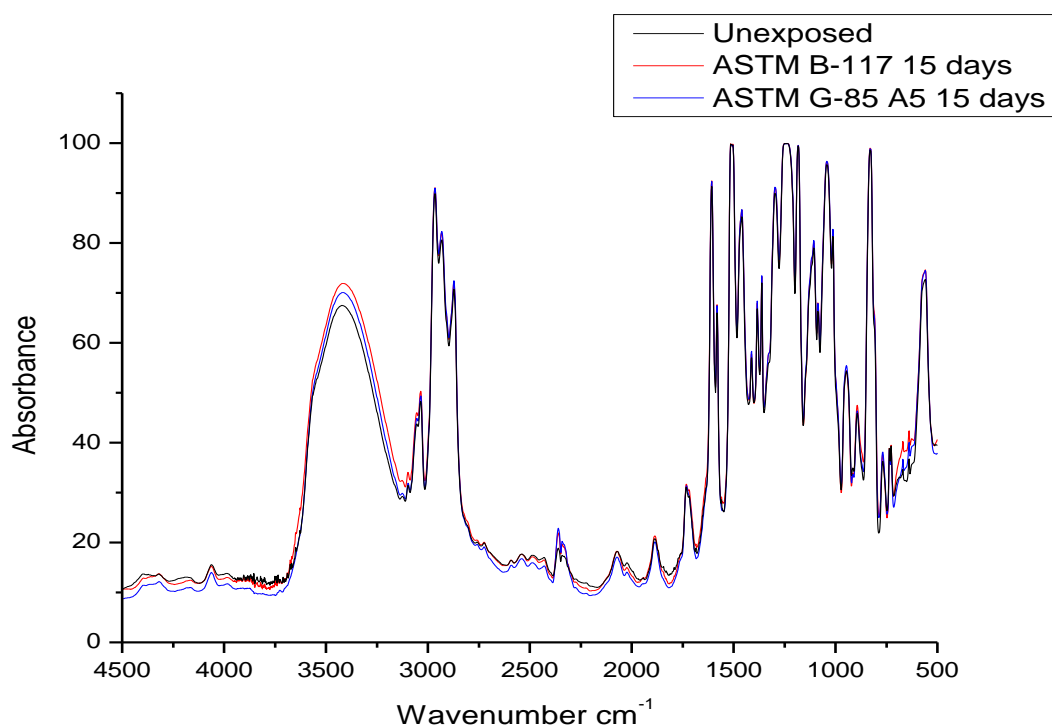


Figure 2.54 FTIR spectra of Eponol films exposed in ASTM B-117 and G-85 A5 for 15 days. Data taken at UVa.

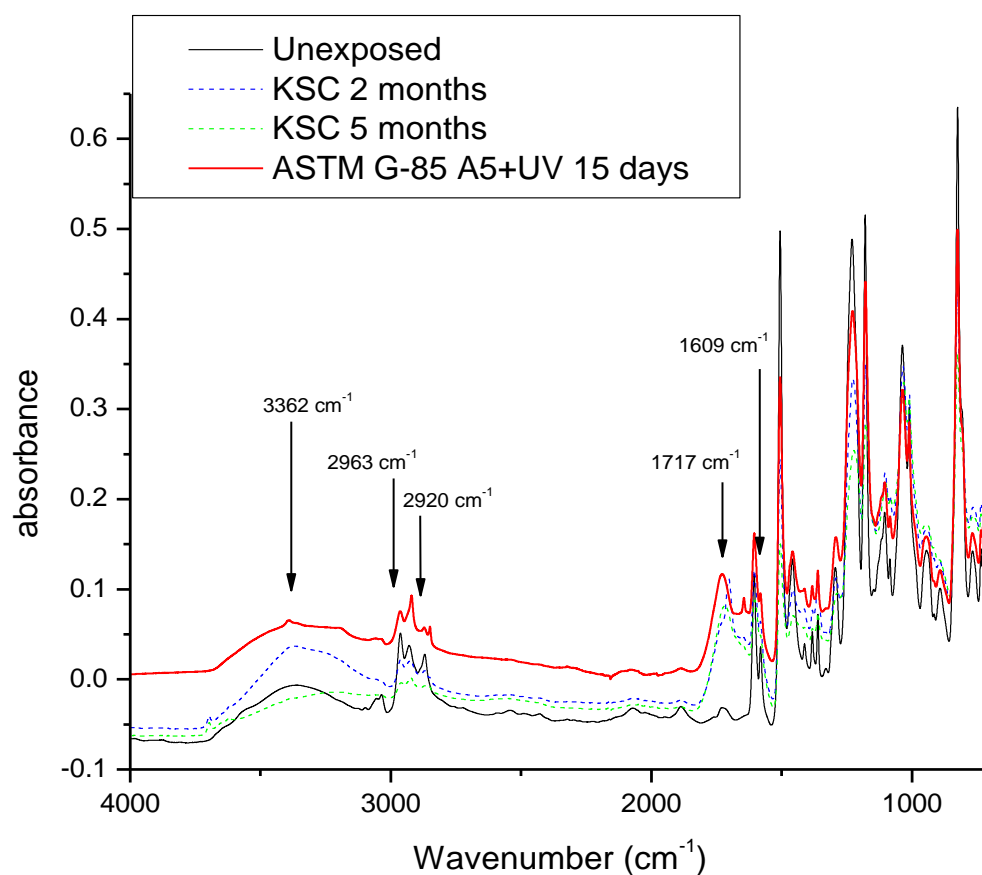


Figure 2.55 FTIR spectra of Eponol films exposed in various conditions. Data taken at USM.

2.6 Discussion

2.6.1 Environmental Severity Factors

2.6.1.1 Chloride Ions

It has been well established that chloride is a promoter of corrosion of steel, and that increasing levels of chloride generally increase the rate of corrosion.^{21-23, 56-59} With respect

to polymer coatings, however, there is little literature on the effects of chloride ions and degradation of the polymer. One previous study showed that sodium ions (from NaCl) degrade polybutadiene coatings by either ion exchange reactions in the coating or by breaking the bonds at the polymer/metal interface.⁶⁰ However, when the polymer was exposed to BaCl₂ the same effects were not seen, ruling out the Cl⁻ ions as the cause of the coating degradation.⁶⁰ In this study, Figure 2.54 shows that when the high molecular weight epoxy resin is exposed to environments with high chloride ion levels (such as the ASTM B-117) no degradation is detected with FTIR. Together, these results suggest that chloride is very corrosive to the steel substrate, but has little, if any, effect on the epoxy resin coating.

With regards to scribe creep, the effect of chloride is more difficult to determine. Figure 2.24 shows that ASTM G-85 Annex 5 has more scribe creep over time than does the ASTM B-117 which has a greater concentration of chloride in the fog solution (0.05% for ASTM G-85 Annex 5 to 5% for ASTM B-117). However, scribe creep could only be measured for 10 days for ASTM B-117 due to the extensive corrosion occurring at locations away from the scribe. Additionally, ASTM G-85 Annex 5+UV appears to have the same scribe creep rate as does the ASTM B-117 even though they have different chloride levels. Regarding FITs, less severe scribe creep was seen in 0.3 wt% NaCl compared with 5% NaCl. At this time, the overall effect of chloride concentration on scribe creep of epoxy resin coated steel is unclear.

2.6.1.2 UV Radiation

UV irradiation has been previously shown to damage many polymer coatings in general,⁸ and specifically bisphenol-A based polymers like the epoxy resin used in this study.⁵³ In current experiments, Figure 2.55 shows that exposure to UV causes degradation of the epoxy resin. In contrast, bare steel exposed to ASTM G-85 Annex 5 with or without UV did not experience a significant difference in mass loss (Figure 2.3). Together, these results suggest that, unlike chloride which affects the substrate but not the coating, UV has a considerable impact on the UV susceptible epoxy coating without affecting the corrosion rate of the substrate. Previous studies have observed instances where UV light affects the corrosion rate of bare steel by creating electron-hole pairs in the metal oxide surface which gives the oxide a positive or negative charge.⁶¹⁻⁶⁴ However, these studies samples were exposed high levels of intense and prolonged UV (3 to 5 months) in an effort to understand the behavior of metals in a water sanitization process.⁶¹⁻⁶⁴ In contrast, the conditions used in current experiments were selected to mimic natural weathering in natural conditions experienced by bare steel. In this work, UV irradiation was found to damage the coating without noticeable effect on the corrosion rate of the steel substrate.

For scribe creep, the effect of UV is unclear. Figure 2.24 indicates that scribe creep length is greater for ASTM G-85 Annex 5 without UV than with UV. UV damage to the polymer coating (Figure 2.55) suggests that an increased scribe creep length for coated steel exposed to UV. At this time, it is not understood why UV would reduce scribe creep length and more research is needed to verify this result.

2.6.1.3 Wet/Dry Cycling

The effect of wet/dry cycling has been shown to increase corrosion rate of bare iron, both during dryout and during rewetting.^{32, 65-67} Figure 2.3 shows that ASTM G-85 Annex 5 with and without UV show increased mass loss over time with respect to ASTM B-117.

Moreover, the mass loss test of bare steel immersed in 0.3 wt% NaCl exhibits mass loss rates of an order of magnitude lower than those seen in ASTM B-117. This supports the literature that cycling accelerates the corrosion rate of bare steel.^{32, 65-67} Figure 2.54 shows that wet/dry cycling has no direct effect on coating degradation, as both ASTM B-117 (non-cyclic) and ASTM G-85 Annex 5 (cyclic) show no damage to the coating.

Figure 2.24 shows the subtle effect of cycling on scribe creep length. ASTM G-85 Annex 5 has a greater scribe creep length than does ASTM B-117. However, the ASTM G-85 Annex 5+UV has similar scribe creep length to ASTM B-117. The reasons for this are unclear and more investigation is warranted.

2.6.2 **Correlation of Mass Loss with Scribe Creep**

Although the measurement of mass loss rates is a well-established practice for determining the severity of environments for atmospheric corrosion,^{20, 23} the measurement of the rate of scribe creep has not been used similarly. In order to understand the relationship between scribe creep rates and environmental severity, the rates must be determined and then compared to a well-known measure of environmental corrosivity (e.g. mass loss). In order to determine how mass loss rates relate to scribe creep rates, the data for each were

plotted. A positive correlation (Figure 2.56) and similar rank order from least to most severe was found (Figure 2.57). Examination of Figure 2.57 shows that, in general, experimental conditions that produce the greatest mass loss also produce the greatest scribe creep. KSC appears to produce a higher ratio of scribe creep length to mass loss than do LALTs. The possible reasons for this are not immediately clear. However, together the data suggest that using published mass loss rates could potentially be used to estimate ranking in severity of scribe creep as a function of atmospheric ESFs.

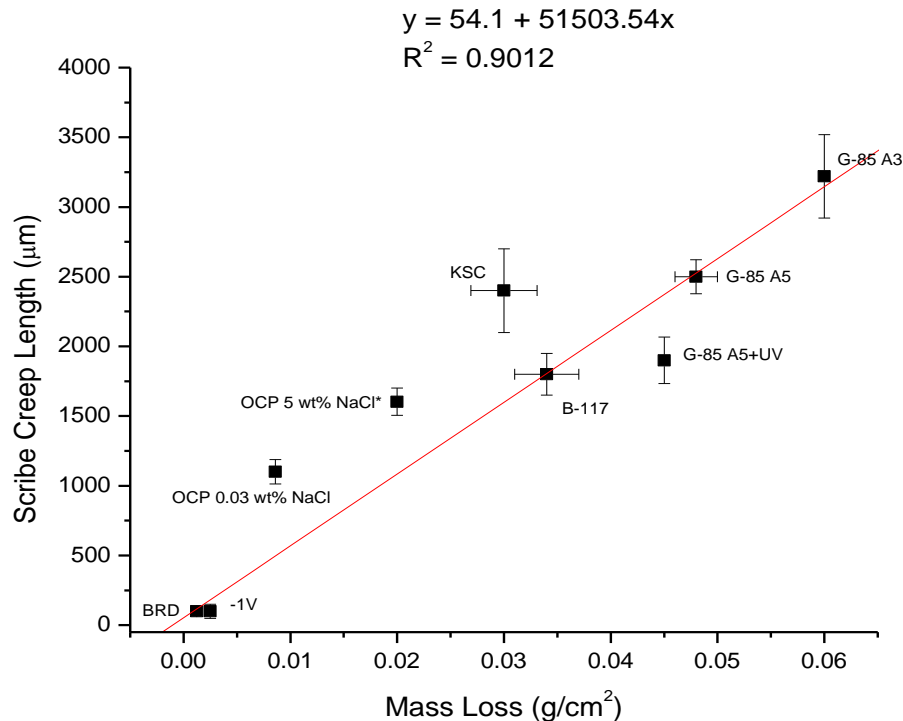


Figure 2.56 Correlation chart showing a positive correlation between mass loss and scribe creep. Exposure conditions are labeled. Equation for fit line and R^2 value are given. Error bars represent standard error. Values for KSC are at 6 weeks, while values for LALTs are at 10 days. *interpolated value.

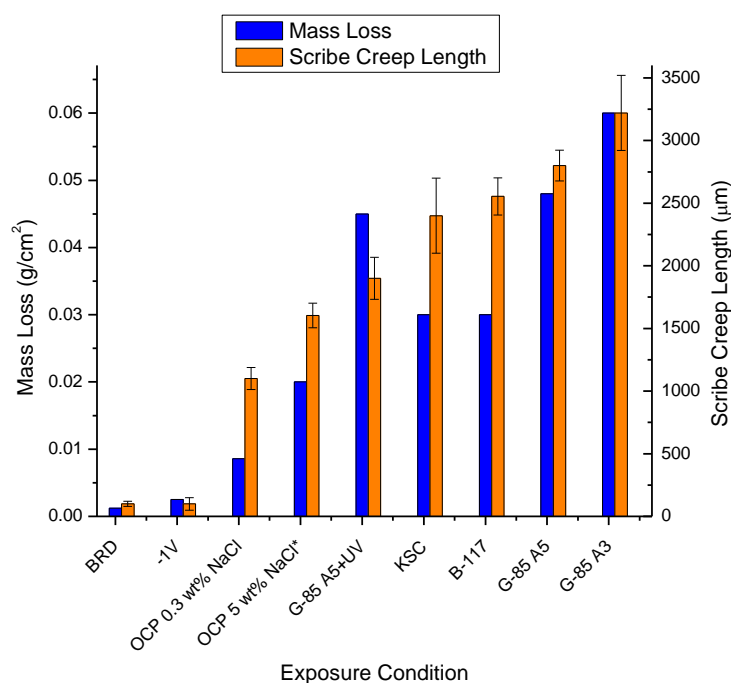


Figure 2.57 Bar graph showing positive correlation and similarity of rank order between mass loss and scribe creep for 1018 steel after 10 days of exposure in various environments. Values for KSC are at 6 weeks, while values for LALTs are at 10 days. *interpolated value.

2.6.3 Corrosion Product Analysis

Samples exposed in atmospheric conditions or in LALTs with cycling formed α -FeOOH and γ -FeOOH in amounts detectable by both XRD and Raman spectroscopy (Table 2.4). For samples exposed at BRD, γ -FeOOH was detected both with XRD and Raman microscopy (Table 2.4 and Figure 2.9). The Raman data support the XRD data and agree with literature showing iron oxide hydroxides to be the main products formed in atmospheric exposures.^{17, 18, 21, 40} Samples exposed in ASTM G-85 A5 with and without UV show α - and γ -phase FeOOH with both XRD and Raman. However, for samples exposed at KSC, no α -FeOOH was detected with Raman, but was detected with XRD. This would imply that there is a top layer

of γ -FeOOH with an inner layer of α -FeOOH in field exposed samples. β -FeOOH was only found in the rust of species exposed at KSC, and literature supports the formation of β -FeOOH in marine atmospheric environments.^{17, 32} Other work suggests that the species formed depends not only upon the exposure environment, but on the type of steel itself (i.e. weathering steel vs. mild steel).^{18, 68, 69}

Iron (II,III) oxide (Fe_3O_4) was detected on samples exposed in ASTM B-117 with XRD but not with Raman spectroscopy (Figure 2.4). Both α - and γ -phases of FeOOH were detected with Raman on the surface of samples exposed in ASTM B-117 (Figure 2.10) but were not detected with XRD. For FeOOH species, Raman light has a penetration depth of roughly 0.5λ , where λ is the wavelength of light used.⁴² The laser used in this study has a λ equal to 785 nm giving a penetration depth of roughly 392.5 nm. XRD has a penetration depth of roughly 15 micrometers for pure iron.⁷⁰ Detecting FeOOH α and γ phases on samples exposed in ASTM B-117 with Raman but not with XRD suggests that these species exist as thin layers on the surface of the corrosion products, a conclusion that is supported in the literature.⁶⁹ It has been shown that during the final stages of drying, Iron (II,III) oxide (Fe_3O_4) is oxidized to γ -FeOOH.³² Therefore, it may be that the FeOOH species formed when the sample dried after completing exposure to the ASTM B-117, and not during test exposure.

Similar to ASTM B-117, γ -FeOOH was detected on the surface of samples exposed to FIT at OCP in both 0.3 wt% and 5% NaCl. Iron (II,III) oxides were detected with both XRD and Raman. Unlike ASTM B-117, γ -FeOOH did not cover the entire surface and α -FeOOH was not detected. However, because XRD detected iron (II,III) oxides and not γ -FeOOH, it

appears that, like ASTM B-117, FIT at OCP at both 0.3 wt% and 5% NaCl produced bulk iron (II,III) oxides with γ -FeOOH forming on the top and that the γ -FeOOH formed when the samples dried out after testing and not during the test.

In terms of corrosion products formed during exposure, ASTM G-85 Annex 5 with and without UV correlated the best with KSC of all the LALTs tested (Table 2.4). Species found in all three exposures were FeOOH α and γ phases. Additionally, β -FeOOH was detected on samples exposed at KSC. In contrast, other LALTs tested did not compare as well with field exposures. For ASTM G-85 Annex 3, only γ -FeOOH was detected. ASTM B-117 was the only sample in which Fe_3O_4 was detected. FeOOH α and γ phases were found only with Raman on samples exposed in ASTM B-117, showing that those species exist only on the surface and not in the bulk in quantities detectable by XRD.

It should be noted that due to the limitations of XRD (cannot detect amorphous corrosion products) and Raman (penetration depth of roughly 400 nm) discussed at the beginning of this section, there could be corrosion products that were not detected. The table of corrosion products found in Table 2.4 is by no means meant to be an exhaustive list of all corrosion products that might have formed.

2.6.4 Scribe Creep Behavior of Coated Steel

Inspection of the visual images of scribe creep over time for KSC, ASTM G-85 Annex 5 and ASTM G-85 Annex 5+UV (Figure 2.14, 2.17, and 2.18) shows that scribe creep appears to

progress in a similar manner: filiform-like growth can be seen around the edges of the advancing scribe creep front with scribe creep appearing to progress monotonically right behind the filiform-like growth. From the line profile data across the scribe (Figure 2.26 , 2.32, and 2.34), it can be seen that for both KSC and ASTM G-85 Annex 5 with and without UV, corrosion products build up at the scribe until the scribe is filled. Corrosion product then grows outward underneath the coating, wedging the coating up away from the surface of the sample. ASTM B-117, in contrast, appears to have a shorter scribe creep length over time than either KSC or ASTM G-85 Annex 5 (Figure 2.24). Additionally, visual images show that there is a large discolored area that appears under the coating around the scribe after only one day, and by day 3 the area is completely covered with corrosion products (Figure 2.16). Line profile data show that the scribe itself never completely fills in with corrosion products for ASTM B-117, as it does in both KSC and ASTM G-85 Annex 5 (Figure 2.30). The ASTM B-117 line profile data appears to show a more uniform growth underneath the coating. This could be indicative of a different scribe creep process in ASTM B-117 compared to that of ASTM G-85 Annex 5 and KSC.

From the line profiles for coated steel exposed in FIT at -1 V (Figure 2.38), it can be seen that there is no discernable buildup of corrosion products in the scribe or corrosion product wedging away from the scribe. Figure 2.40 shows that corrosion products build up in the scribe and begin to wedge underneath the coating for coated steel exposed in FIT at OCP in both 0.3 wt% and 5% NaCl. However, the scribes never completely fill and the wedging is of limited extent. The scribe creep mechanism for FIT at -1 V does not appear similar to KSC. The scribe creep mechanism for FIT at OCP in 5% NaCl appears to be similar to ASTM B-117, but progresses more slowly.

2.6.5 Coating Degradation During Exposure

EIS data can be used to determine the electrically and electrochemically active defect area of the coating and give an indication of the coating quality from the perspective of coating pore resistance.⁴⁷ Figure 2.52 and 2.53 show the normalized change in impedance at 0.01 Hz over time and allow for direct comparison of changes in coating properties. While KSC, ASTM B-117 and ASTM G-85 Annex 5 with and without UV showed similar coating properties near to the scribe (Figure 2.52), there were definite differences far from the scribe (Figure 2.53). KSC showed some damage, ASTM B-117 showed definite damage, and ASTM G-85 Annex 5 showed no damage far from the scribe. ASTM G-85 Annex 5+UV appears to behave the most similarly to KSC in terms of coating degradation far from the scribe (Figure 2.53).

FTIR data show that ASTM B-117 and ASTM G-85 Annex 5 have no direct effect on the molecular bonding in the coating (Figure 2.54). However, the coating was damaged by the environment at KSC. Only ASTM G-85+UV shows similar damage to the coating seen on field exposed samples with FTIR (Figure 2.55). These results point to UV being an important ESF to include in any LALT used to compare the corrosion of organically coated samples to field sites with significant UV exposure (i.e., field sites in locations with high solar radiation or upper atmosphere environments where heightened UV levels occur).

ASTM B-117 appeared to be too severe for this system. Visually, damage was seen to occur quickly and in many places across the coated sample (Figure 2.16). EIS results also show

coating damage occurring quickly both near to and far from the scribe for coated samples exposed in ASTM B-117, which is not seen in any other exposure (Figure 2.52 and 2.53). Since the FTIR data have shown that the ASTM B-117 does not damage the coating specifically (Figure 2.54), it follows that the damage to the coating is a result of interactions of the test environment with the substrate. Why then is ASTM B-117 so aggressive to this system? It has been shown that some ESFs (i.e., chloride) are severe with respect to substrate corrosion, while being benign with respect to the coating.^{8, 51, 71, 72} It has also been shown that increasing the level of chloride ions increases the corrosion rate of bare steel.^{22, 23, 58} The high chloride content (5% NaCl) of the solution may cause aggressive corrosion at any and all coating defects causing the entire scribe and surface to be corroded after just 10 days of exposure. It bears repeating that in no cases were samples exposed in the ASTM B-117 found to be similar to samples exposed at KSC. The coating was not damaged by the environment in ASTM B-117 as it was at KSC because of the lack of UV in ASTM B-117. The EIS parameters of the coating degraded quickly near and far from the scribe for samples exposed in ASTM B-117 but did not degrade as quickly far from the scribe for samples exposed at KSC. The corrosion products found also differed in both species and amount.

2.6.6 Anodic Wedging vs. Cathodic Delamination as a Main Factor in Scribe Creep

Full immersion tests run on both bare and coated samples held at OCP showed expected behavior in terms of mass loss (Figure 2.3), scribe creep (Figure 2.24) and coating damage as measured with EIS (Figure 2.52 and 2.53). However, samples held -1V vs. SCE behaved very differently. -1V vs. SCE is a very cathodic potential and should allow only cathodic

reactions to take place at and around the scribe where there is minimal IR drop. This notion is supported by the high value of $Z_{0.01}$ (Figure 2.52 and 2.53). Mass loss (Figure 2.3) and scribe creep data (Figure 2.24) indicate very little corrosion during the exposure.

Additionally, EIS data show that there is no measureable drop in $Z_{0.01}$ near to or far from the scribe (Figure 2.52 and 2.53). These results suggest, but do not prove, that cathodic disbondment caused by cathodic reactions under the coating is not the dominant factor controlling scribe creep in this system.

It may be that cathodic delamination is dominant in consistently wet conditions like ASTM B-117 while anodic wedging plays a bigger role in cyclic wet/dry conditions where more voluminous corrosion products are formed.^{32, 69} For instance, if corrosion in the scribe led to a cathodic reaction rate underneath the coating which exceeded the rate of FIT at -1 V vs. SCE, it would be possible that cathodic disbondment could still be a dominant scribe creep mechanism with respect to -1 V vs. SCE. However, an important point is that corrosion products formed in cyclic conditions are often less dense than those formed in continuously wet conditions (i.e. the densities for iron oxide hydroxides are 3.55 g/cm³ for Akaganeite (β -FeOOH), 3.8 g/cm³ for Goethite (α -FeOOH), and 3.85 g/cm³ for Lepidrocite (γ -FeOOH))⁷³. The densities for species found in continuously wet conditions (5.26 g/cm³ for Hematite (α -Fe₂O₃), 5.1 g/cm³ for Maghemite (γ -Fe₂O₃) and 5.18 g/cm³ for Magnetite (Fe₃O₄)) are much higher than the hydroxides found in atmospheric and cyclic LALT conditions.⁷³ The more voluminous corrosion products found in cyclic conditions may cause more physical stress on the coating as they grow, increasing the role of anodic wedging during scribe creep.

Line profile data (Figure 2.26 and 2.32) show what appears to be anodic corrosion product growth and wedging on samples exposed at KSC and in ASTM G-85 Annex 5. In order to determine the importance of anodic wedging in the scribe creep of field samples, potentiostatic FITs were performed. Samples held at -1 V vs. SCE showed no signs of coating damage or cathodic disbondment as measured with EIS after 10 days, which is seen in the lack of change in the low frequency impedance results (Figure 2.52 and 2.53). In contrast, when samples were held at OCP in 0.3 wt% and 5% NaCl, allowing for both anodic and cathodic processes, coating damage is seen (Figure 2.52 and 2.53).

2.6.7 LALTs that Simulate Field Tests

The processes that make up underpaint corrosion and scribe creep for the Eponol coated steel system in a cyclic wet/dry environment are shown in Figure 2.58.⁵⁶ When there are no ESFs present that strongly attack the coating (i.e., UV), underpaint corrosion is dominated by anodic corrosion product wedging at the scribe and supporting cathodic reactions that may generate hydroxyl ions. This can occur both at the scribe and at any unintentional defects. This suggests that the primary mechanisms to reproduce during LALTs on coated and scribe steel is anodic corrosion product wedging with matched corrosion product identity that enables growth below the coating. Therefore, ESFs which match the corrosion type and form similar corrosion products are important. In contrast, when ESFs that attack the coating are present, coating defects can also be created by the ESF by degradation of the organic coating itself. These defects allow for underpaint corrosion to begin away from the scribe which further damages the coating. LALTs, such as ASTM B-117, that do not incorporate an ESF that attacks the coating specifically, and those that produce very severe

metal corrosion, do not demonstrate the type of coating degradation seen in field exposures. These results emphasize the importance of incorporating ESFs that attack the coating for improved lab/field correlation as well as those that produce similar corrosion and similar corrosion products at the scribe.

Schematic of Underpaint Corrosion Mechanisms on Coated 1018 Steel

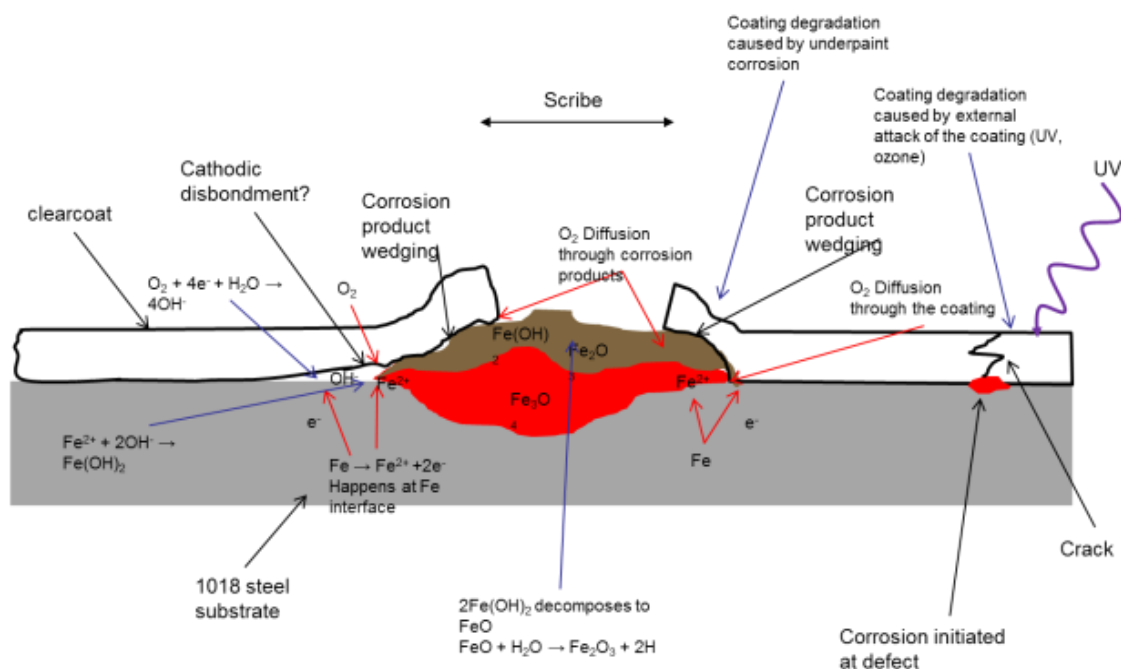


Figure 2.58 Schematic of underpaint corrosion and scribe creep processes on Eponol coated 1018 steel. Diagram adapted from.⁵⁶

2.7 Conclusions

Scribe creep lengths were found to correlate with mass loss on ultra-high molecular weight epoxy resin (Eponol) coated 1018 steel (UNS G10180) for field, LALTs, and FITs.

Concerning field exposures and FITs, FIT at -1 V vs. SCE did not behave similarly to KSC field exposures. FIT at OCP also did not mimic field results.

Overall, it has been shown that ASTM G-85 Annex 5 correlated well with KSC in terms of scribe creep rate, scribe creep corrosion morphology, and corrosion mechanism, but not in coating degradation as observed with EIS and FTIR. However, the addition of UV to ASTM G-85 Annex 5 produced better correlation with KSC with regards to coating degradation. ASTM G-85 Annex 5+UV correlated the best with KSC of any LALT tested. In contrast, ASTM B-117 was shown to correlate poorly with KSC because of the very aggressive substrate degradation and non-aggressive polymer degradation aspects of the ASTM B-117. FITs also correlated poorly with KSC. The incorporation of UV and wet/dry cycling in the LALTs served as the major determinants of successful correlation with field exposures.

Due to the benign nature of the BRD site, there was not enough scribe creep or mass loss over the exposure time to be able to draw any conclusions about correlation between BRD and LALTs.

The effects of ESFs on mass loss of bare steel are understood fairly well. However, the effects of ESFs on scribe creep behavior appear to be very complex. Systematic isolation and evaluation of the effects of ESFs, individually and in combinations, on scribe creep length of coated steel is still needed to more accurately determine how scribe creep is affected by the environment.

2.8 **References**

1. R.M. Fischer, W.D. Ketola and W.P. Murray, *Inherent variability in accelerated weathering devices*. Progress in Organic Coatings, 1991. **19**(2): p. 165-179.
2. E.L. Montgomery, L.M. Calle, J.C. Curran and M.R. Kolody, *Timescale Correlation between Marine Atmospheric Exposure and Accelerated Corrosion Testing*. 2011: p. 15.
3. C.A. Matzdorf and C.W. Nickerson. *Assesment of Accelerated Tests Compared to Beachfront Test and Proposed Evaluation Method*. in *DoD Corrosion Conference*. 2009.
4. B. Boelen, B. Schmitz, J. Defourny and F. Blekkenhorst, *A literature survey on the development of an accelerated laboratory test method for atmospheric corrosion of precoated steel products*. Corrosion Science, 1993. **34**(11): p. 1923-1931.
5. K. Johnson and E. Marsh, *A Study of Relationships Between Design of Precoated Steel Cladding and its Environmental Behaviour in Service*. 1987, British Steel Corporation: Brussels.
6. O. Guseva, S. Brunner and P. Richner, *Service life prediction for aircraft coatings*. Polymer Degradation and Stability, 2003. **82**.
7. S. Brunner, P. Richner, U. Muller and O. Guseva, *Accelerated weathering device for service life prediction for organic coatings*. Polymer Testing, 2005. **24**(1): p. 25-31.
8. J. Mallegol, M. Poelman and M.G. Olivier, *Influence of UV weathering on corrosion resistance of prepainted steel*. Progress in Organic Coatings, 2008. **61**(2-4): p. 126-135.
9. B.S. Skerry and C.H. Simpson, *Corrosion and Weathering of Paints for Atmospheric Corrosion Control*. Corrosion, 1993. **49**(8).
10. H.E. Townsend, *Behavior of Painted Steel and Aluminum Sheet in Laboratory Automotive Corrosion Tests*. CORROSION, 1996. **52**(1): p. 66-71.
11. H.E. Townsend. *Development of Laboratory Corrosion Tests by the Automotive and Steel Industries of North America*. in *Proceedings of The 4th International Conference on Zinc and Zinc-Alloy Coated Steel Sheet*. 1998.
12. Y. Wan, E. Neiser and R.G. Kelly, *Modification of ASTM Standard B117 Salt Spray Corrosion Test for Improved Correlation to Field Measurements*, in *DoD Corrosion Conference*. 2011: Palm Springs, Ca.
13. A. King and J.R. Scully, *Corrosion Protection of 2024-T351 by a Mg-Rich Primer: Discrepancies Between Field Versus Laboratory Exposures*, in *NACE 2010*. 2011: San Antonio Tx.
14. ASTM Standard B117 2007a, "Standard Practice for Operating Salt Spray (Fog) Apparatus," ASTM International, West Conshohocken, PA, 2007, DOI: 10.1520/B0117-11, www.astm.org
15. ASTM Standard D1654, 2008, "Standard Test Method for Evaluation of Painted or Coated Specimens Subjected to Corrosive Environments," ASTM International, West Conshohocken, PA, 2008, DOI: 10.1520/D1654-08, www.astm.org
16. H.E. Townsend, *Thirty-Year Atmospheric Corrosion Performance of 55% Aluminum-Zinc Alloy-Coated Sheet Steel*. Materials Performance, 1996. **35**(4): p. 30-36.

17. D. de la Fuente, I. Díaz, J. Simancas, B. Chico and M. Morcillo, *Long-term atmospheric corrosion of mild steel*. Corrosion Science, 2011. **53**(2): p. 604-617.
18. M. Yamashita, H. Miyuki, Y. Matsuda, H. Nagano and T. Misawa, *The long term growth of the protective rust layer formed on weathering steel by atmospheric corrosion during a quarter of a century*. Corrosion Science, 1994. **36**(2): p. 283-299.
19. H.E. Townsend and J.C. Zoccola, *Eight-Year Atmospheric Corrosion Performance of Weathering Steel in Industrial, Rural, and Marine Environments*, in *Atmospheric Corrosion of Metals*, ASTM STP 767, S.W. Dean and E.C. Rhea, Editors. 1982, American Society for Testing and Materials: Philadelphia.
20. M. Tullmin and P.R. Roberge, *Atmospheric Corrosion*, in *Uhlig's Corrosion Handbook*, R.W. Revie, Editor. 2000, John Wiley & Sons.
21. I. Matsushima, *Carbon Steel—Atmospheric Corrosion*, in *Uhlig's Corrosion Handbook*. 2011, John Wiley & Sons, Inc. p. 579-588.
22. S. Feliu, M. Morcillo and B. Chico, *Effect of distance from sea on atmospheric corrosion rate*. Corrosion, 1999. **55**(9): p. 883-891.
23. C. Leygraf and T.E. Graedel, *Atmospheric Corrosion*. 2000: John Wiley & Sons.
24. W.H.J. Vernon, *A laboratory study of the atmospheric corrosion of metals. Part II.-Iron: the primary oxide film. Part III.-The secondary product or rust (influence of sulphur dioxide, carbon dioxide, and suspended particles on the rusting of iron)*. Transactions of the Faraday Society, 1935. **31**: p. 1668-1700.
25. C.C. Lin and C.X. Wang, *Correlation between accelerated corrosion tests and atmospheric corrosion tests on steel*. Journal of Applied Electrochemistry, 2005. **35**(9): p. 837-843.
26. ASTM Standard D523 2008, "Standard Test Method for Specular Gloss," ASTM International, West Conshohocken, PA, 2008, DOI: 10.1520/D0523-08 www.astm.org
27. ASTM Standard D714 02-2009, "Standard Test Method of Evaluating Degree of Blistering of Paints," ASTM International, West Conshohocken, PA, 2009, DOI: 10.1520/D0714-02R09, www.astm.org
28. ASTM Standard D610, 2008, "Standard Practice for Evaluating Degree of Rusting on Painted Steel Surfaces," ASTM International, West Conshohocken, PA, 2008, DOI: 10.1520/D0610-08 www.astm.org
29. F. Deflorian, L. Fedrizzi and P.L. Bonora, *INFLUENCE OF THE PHOTO-OXIDATIVE DEGRADATION ON THE WATER BARRIER AND CORROSION PROTECTION PROPERTIES OF POLYESTER PAINTS* Corrosion Science, 1996. **38**(10): p. 1697-1708.
30. N. LeBozec and D. Thierry, *Influence of climatic factors in cyclic accelerated corrosion test towards the development of a reliable and repeatable accelerated corrosion test for the automotive industry*. Materials and Corrosion-Werkstoffe Und Korrosion, 2010. **61**(10): p. 845-851.
31. R.A. Dickie, *Paint adhesion, corrosion protection, and interfacial chemistry*. Progress in Organic Coatings, 1994. **25**(1): p. 3-22.
32. D.S. Dunn, M.B. Bogart, C.S. Brossia and G.A. Cragnolino, *Corrosion of Iron Under Alternating Wet and Dry Conditions*. Corrosion, 2000. **56**(5): p. 470-481.
33. 2014 [cited 2014 Jan. 27]; Available from: <http://www.miller-stephenson.com/products/?DepartmentId=54>.
34. F. Adar, *Depth Resolution of the Raman Microscope: Optical Limitations and Sample Characteristics*. Spectroscopy, 2010. **25**(3): p. 16-23.

35. ASTM Standard G 1 2003, "Standard Practice for Preparing, Cleaning and Evaluating Corrosion Test Specimens," ASTM International, West Conshohocken, PA, 2003, DOI: 10.1520/G0001-03R11, www.astm.org
36. ASTM Standard G-85, 2011, "Standard Practice for Modified Salt Spray Testing," ASTM International, West Conshohocken, PA, 2002, DOI: 10.1520/G0085-11, www.astm.org
37. ASTM Standard D4587, 2011, "Standard Practice for Fluorescent UV-Condensation Exposures of Paint and Related Coatings," ASTM International, West Conshohocken, PA, 2011, DOI: 10.1520/D4587-11, www.astm.org
38. ASTM Standard D5894, 2001, "Standard Practice for Cyclic Salt Fog/UV Exposure of Painted Metal, (Alternating Exposures in a Fog/Dry Cabinet and a UV/Condensation Cabinet)," ASTM International, West Conshohocken, PA, 2010, DOI: 10.1520/D5894-10, www.astm.org
39. S.J. Oh, D.C. Cook and H.E. Townsend, *Atmospheric corrosion of different steels in marine, rural and industrial environments*. Corrosion Science, 1999. **41**(9): p. 1687-1702.
40. S. Oh, D.C. Cook and H.E. Townsend, *Characterization of Iron Oxides Commonly Formed as Corrosion Products on Steel*. Hyperfine Interactions, 1998. **112**(1): p. 59-66.
41. T. Ohtsuka, *Raman Spectra of Passive Films of Iron in Neutral Borate Solution*. Materials Transactions, JIM, 1996. **37**(1): p. 67-69.
42. J. Dünnwald and A. Otto, *An investigation of phase transitions in rust layers using raman spectroscopy*. Corrosion Science, 1989. **29**(9): p. 1167-1176.
43. D.L.A. deFaria, S.V. Silva and M.T. deOliveira, *Raman microspectroscopy of some iron oxides and oxyhydroxides*. Journal of Raman Spectroscopy, 1997. **28**(11): p. 873-878.
44. C.T. Lee, M.S. Odziemkowski and D.W. Shoesmith, *An in situ Raman-electrochemical investigation of carbon steel corrosion in Na₂CO₃/NaHCO₃, Na₂SO₄, and NaCl solutions*. Journal of the Electrochemical Society, 2006. **153**(2): p. B33-B41.
45. F. Dubois, C. Mendibide, T. Pagnier, F. Perrard and C. Duret, *Raman mapping of corrosion products formed onto spring steels during salt spray experiments. A correlation between the scale composition and the corrosion resistance*. Corrosion Science, 2008. **50**(12): p. 3401-3409.
46. T. Ohtsuka, K. Kubo and N. Sato, *Raman Spectroscopy of Thin Corrosion Films on Iron at 100 to 150 C in Air*. Corrosion, 1986. **42**(8): p. 476-481.
47. H.P. Hack and J.R. Scully, *Defect Area Determination of Organic Coated Steels in Seawater Using the Breakpoint Frequency Method*. Journal of the Electrochemical Society, 1991. **138**(1): p. 33-40.
48. J.R. Scully, *Electrochemical Tests*, in *Corrosion Tests and Standards: Application and Interpretation*, H.P. Hack, Editor. 2005, ASTM. p. 107-117.
49. J.N. Murray and H.P. Hack, *Long-Term Testing of Epoxy-Coated Steel in ASTM Seawater Using Electrochemical Impedance Spectroscopy*. Corrosion, 1991. **47**(6): p. 480-489.
50. J.N. Murray and H.P. Hack, *Testing Organic Architectural Coatings in ASTM Synthetic Seawater Immersion Conditions Using EIS*. Corrosion, 1992. **48**(8): p. 671-685.
51. P. Musto, G. Ragosta, M. Abbate and G. Scarinzi, *Photo-oxidation of high performance epoxy networks: Correlation between the molecular mechanisms of degradation and the viscoelastic and mechanical response*. Macromolecules, 2008. **41**(15): p. 5729-5743.

52. C. Konecki, *RE: UVa-Southern Miss ATR-FTIR 8-23-12.pptx*. 2012.
53. M. Diepens and P. Gijsman, *Photodegradation of bisphenol A polycarbonate*. Polymer Degradation and Stability, 2007. **92**(3): p. 397-406.
54. N. Nagai, H. Okumura, T. Imai and I. Nishiyama, *Depth profile analysis of the photochemical degradation of polycarbonate by infrared spectroscopy*. Polymer Degradation and Stability, 2003. **81**(3): p. 491-496.
55. A. Rivaton, B. Mailhot, J. Soulestin, H. Varghese and J.L. Gardette, *Comparison of the photochemical and thermal degradation of bisphenol-A polycarbonate and trimethylcyclohexane-polycarbonate*. Polymer Degradation and Stability, 2002. **75**(1): p. 17-33.
56. D.A. Jones, *Principles and Prevention of Corrosion*. 2nd ed. 1996: Prentice Hall.
57. I.S. Cole, *Mechanism of Atmospheric Corrosion in Tropical Environments*, in *Marine Corrosion in Tropical Environments*, ASTM STP 1399, S.W. Dean and J.B. Bushman, Editors. 2000, American Society for Testing and Materials: West Conshohocken, PA.
58. E. McCafferty, *Introduction to Corrosion Science*. 2010, New York: Springer.
59. L. Veleza and R.D. Kane, *Atmospheric Corrosion in Corrosion: Fundamentals, Testing and Protection*, Various, Editor. 2003, ASM International: Materials Park, OH. p. 196-209.
60. H. Leidheiser, R.D. Granata and R. Turoscy, *Technical Note: Alkali Metal Ions as Aggressive Agents to Polymeric Corrosion Protective Coatings*. Corrosion, 1987. **43**(5): p. 296-297.
61. P. Schmuki and H. Böhni, *Illumination effects on the stability of the passive film on iron*. Electrochimica Acta, 1995. **40**(6): p. 775-783.
62. D.F. Heaney and D.D. Macdonald, *On the Photoinhibition of Passivity Breakdown on Iron in Chloride-Containing Solutions*. Journal of the Electrochemical Society, 1999. **146**(5): p. 1773-1776.
63. H.R. Riazi, I. Danaee and M. Peykari, *Influence of ultraviolet light irradiation on the corrosion behavior of carbon steel AISI 1015*. Metals and Materials International, 2013. **19**(2): p. 217-224.
64. T.D. Burleigh, C. Ruhe and J. Forsyth, *Photo-Corrosion of Different Metals during Long-Term Exposure to Ultraviolet Light*. Corrosion, 2003. **59**(9): p. 774-779.
65. M. Stratmann, *The investigation of the corrosion properties of metals, covered with adsorbed electrolyte layers—A new experimental technique*. Corrosion Science, 1987. **27**(8): p. 869-872.
66. M. Stratmann and H. Streckel, *On the atmospheric corrosion of metals which are covered with thin electrolyte layers—II. Experimental results*. Corrosion Science, 1990. **30**(6-7): p. 697-714.
67. N.D. Tomashov, *Development of the Electrochemical Theory of Metallic Corrosion*. Corrosion, 1964. **20**(1): p. 7t-14t.
68. A. Raman and B. Kuban, *Infrared Spectroscopic Analysis of Phase Transformation Processes in Rust Layers Formed on Weathering Steels in Bridge Spans*. Corrosion, 1988. **44**(7): p. 483-488.
69. S. Nasrazadani and A. Raman, *Formation and Transformation of Magnetite (Fe₃O₄) on Steel Surfaces under Continuous and Cyclic Water Fog Testing*. Corrosion, 1993. **49**(4): p. 294-300.
70. V. Thomsen, D. Schatzlein and D. Mercuro, *Attenuation of X-Rays by Matter*. Spectroscopy, 2005. **20**(9): p. 22-25.

71. F. Delor-Jestin, D. Drouin, P.Y. Cheval and J. Lacoste, *Thermal and photochemical ageing of epoxy resin – Influence of curing agents*. Polymer Degradation and Stability, 2006. **91**(6): p. 1247-1255.
72. J. Pospíšil, J. Pilar, N.C. Billingham, A. Marek, Z. Horák and S. Nespurek, *Factors affecting accelerated testing of polymer photostability*. Polymer Degradation and Stability, 2006. **91**(3): p. 417-422.
73. W.L. Roberts, G.R.J. Rapp and J. Weber, *Encyclopedia of Minerals*. 1974, New York: Litton Educational Publishing.

3 Chapter 3 – Isolation and Systematic Analysis of Corrosion Factors in LALTs

3.1 Summary of Chapter 3

Chapter 2 demonstrated that the effects of ESFs on the scribe creep of ultra-high molecular weight epoxy resin coated steel are a complex function of ESFs. In order to gain a better understanding of the effects of ESFs on the coating/substrate system, a Fractional Factorial Design of Experiment (FFA) was employed to probe the effects of ESFs. The environmental variables explored were temperature, % relative humidity, chloride, UV and wet/dry cycling. The effects of ESFs (singularly and in combination) were examined through the creation of a LALT test matrix using controlled ESFs in lab exposures. In the FFA matrix selected ESFs were systematically varied at high and low levels across a series of experiments. Corrosion, scribe creep, and coating degradation of ultra-high molecular weight epoxy resin (Poly(Bisphenol A-co-epichlorohydrin) glycidyl end-capped ($C_{18}H_{22}O_3$) $n \bullet C_{22}H_{26}O_4$; CAS No. 25036-25-3, trade name Eponol) coated AISI 1018 steel (UNS# G10180; 0.15% C, 0.7% Mn, Fe; wt. %) were investigated. To accurately discern the effects of ESFs on mass loss, scribe creep, and coating degradation, a suite of high-level surveillance methods capable of interrogating both coating and substrate degradation was used. These methods included electrochemical impedance spectroscopy (EIS), X-ray diffraction (XRD), 3D optical microscopy, Raman microscopy and Fourier Transform Infrared Spectroscopy (FTIR). Mass loss samples were exposed concurrently with coated and scribed samples.

Results show mass loss was lowest for FFA1 and FFA2, involving low temperature and low cycling, and greatest for FFA4 and FFA6, involving high temperature and high cycling. Additionally, iron oxide hydroxides (FeOOH) were the main corrosion products formed in FFA exposures. Scribe creep results showed that FFA1, FFA2, FFA3 and FFA5 presented similar scribe creep lengths while FFA4 and FFA6 presented distinctly greater scribe creep lengths compared to the other FFAs. Scribe creep and mass loss were shown to have a positive correlation in all cases. Scribe creep lengths at 15 days were similar for FFA1, FFA2, FFA3 and FFA5. However, scribe creep lengths at 15 days for FFA4 and FFA6 were significantly higher compared to the other FFAs. FFA4 and FFA6 were the only exposures with high levels of both temperature and cycling. Possible reasons for the noted effects of the combination of high temperature and high cycling rate are discussed. Finally, high levels of UV were shown to promote coating degradation far from the scribe but were not found to be a strong factor in scribe creep.

3.2 **Background**

3.2.1 **Isolation of Corrosion Factors**

Chapter 2 showed that the effects of ESFs (specifically chloride, wet/dry cycling, and UV) on the mass loss of bare steel were fairly straightforward.¹⁻¹¹ Chloride and wet/dry cycling were both shown to significantly affect the corrosion of bare steel, while UV showed no discernable effect on mass loss. The effects of ESFs on scribe creep of a coating/substrate system, however, were more difficult to elucidate. First, although chloride and wet/dry cycling had a pronounced effect on the corrosion of bare steel, they were not observed to specifically affect the isolated degradation of the polymer coating of coated steel. Second,

although UV was found to degrade the coating, it did not have a discernable effect on the rate of scribe creep.

The effects of ESFs on scribe creep of coated steel may have been obfuscated due to fixed, but not judiciously selected, levels of ESFs across the standard LALTs used in Chapter 2. Although industry standard LALTs include differing levels of ESFs, these ESFs are not necessarily selected and implemented in a systematic way (see Table 3.1). As discussed in Chapter 1, there is a general lack of systematic variation and evaluation of the effects of individual corrosion drivers in the lab or field. ESFs are often combined at relatively high levels, producing a LALT that is more severe than the field environment. Such combinations may confound the impact of individual drivers on degradation of the coating, substrate and the coating/substrate system. Overall, the relationships between ESFs and corrosive mechanisms such as corrosion product wedging, underpaint corrosion and scribe creep are poorly understood.

Table 3.1 ESF levels for selected LALTs and field sties.

Exposure	Mean Temp °C	Mean RH (%)	Mean UV (W/m ²)	Mean Cl-impingement rate (g/cm ² /day)	Cycling (cycles per day)
Kennedy Space Center, FL	23.6	77.2	0.6	6.4x10 ⁻⁵	1
ASTM B-117	35	100	0	0.0145	0
ASTM G-85 Annex 5	29.5	60	0	7.23x10 ⁻⁵	6

Therefore, the current chapter attempts to more accurately determine the impact of ESFs on degradation of the coating/substrate system by isolating and systematically varying selected ESFs across scribe creep experiments. Individual corrosion drivers were varied in a controlled manner in a series of customized LALTs. The variables explored were temperature, % relative humidity, chloride, UV and wet/dry cycling. In order to isolate the effect of each ESF, experiments were designed that allowed for the manipulation of one or more factors while other factors remained unchanged. Additionally, these factors were varied (i.e., tested at a high or low level) broadly enough to detect the changes that they caused in scribe creep. Justification for the levels chosen is given in Section 3.2.3. Lastly, use of a fractional factorial experimental design enabled these test objectives to be completed within reasonable constraints of time and resources.

3.2.2 ESF Level Selection

In order for the factorial design to successfully elucidate the effects of individual ESFs, the levels for each variable had to be carefully selected. It was important that there be enough separation between the levels that the effects of each variable could be detected.

Appropriate levels were selected using a two-fold approach. First, visual inspection of the samples revealed that the ASTM B-117 produced significant corrosion across the surface of the coated samples, rather than corrosion originating from the scribe (Figure 2.16). This pattern was uncharacteristic of the KSC field samples and samples tested in the other LALT (ASTM G-85 A3 and G-85 A5) (Figure 2.14 and 2.17). By comparing variable levels set in the LALT standards, it was determined that the ASTM B-117's elevated chloride level (0.346 g/cm²/day, based on the continuous spray of 5% NaCl solution) was the mostly likely cause

of the irregular corrosion pattern (this determination will be addressed in the discussion section of this chapter). In contrast, the ASTM G-85 had a lower chloride level (7.23×10^{-5} g/cm²/day) and the irregular corrosion pattern was not seen. Based on these relative levels of chloride in the standard LALTs, it was decided that 1) the high level should be above the level for ASTM G-85 Annex 5, but well below the ASTM B-117 level and 2) that the low level should be below the value for KSC. Therefore, in the fractional factorial experimental design, chloride levels were held at either 2.3×10^{-4} g/cm²/day (high) or 2.3×10^{-5} g/cm²/day (low). For comparison, the International Organization for Standardization (ISO) rankings (ISO 9223) for chloride are shown in Table 3.2.¹² The chloride deposition rate and relative ISO classification for ASTM B-117, KSC and the high and low levels for the FFAs are given in Table 3.3.

Table 3.2 Table of International Organization for Standardization (ISO) rankings (ISO 9223) for chloride levels.¹²

Chloride ISO Table	
Class	Rate mg/m ² /day
S0	<3
S1	3-60
S2	61-300
S3	>300

Table 3.3 Chloride deposition rates and ISO classifications for various exposures.

Chloride Ranking		
Test	Rate mg/m ² /day	Class
ASTM B-117	144900	S3
ASTM G-85	723	S3
KSC	640	S3
FFA High	2275	S3
FFA Low	227.5	S2

Linear regression analysis was next performed on existing data from the LALT exposures performed in Chapter 2. Performing linear regression on mass loss data from bare steel was beneficial for many reasons: primarily, 1) the factors that affect mass loss were already known and documented,¹ 2) a model for atmospheric exposure of weathering steel was already known,¹ 3) it could provide a basis from which to determine the levels for scribe creep given the correlation seen between scribe creep and mass loss (Figure 2.57), and, 4) if the regression for mass loss proved valid, it would demonstrate the validity of the foundation for building a scribe creep model (Chapter 4). Linear regression analysis of the standard LALT exposures from Chapter 2 (ASTM B-117, ASTM G-85 Annex 5, ASTM G-85 Annex 3) produced the following equation for mass loss:

$$ML = 19.9(t^{1/2}) + 0.934[Cl^-] - 0.33RH - 2.95(pH) + 2.4(cycling) \quad 3.1$$

where ML is mass loss in mg/cm², t is time in days, [Cl⁻] is chloride concentration in g/L, RH is mean % relative humidity, and cycling is the number of cycles per day. This equation was constructed before the decision was made to measure chloride impingement rate, the chosen measurement method was in g/L of solution used in the standard LALT. This is the only situation in which the impingement rate is not used.

Equation 3.1 was plotted using the same environmental parameters used in the standard LALTs (ASTM B-117, G-85 A3 and G-85 A5, shown in Table 3.4). Figure 3.1 shows good agreement between the mass loss data from the standard LALTs (presented in Chapter 2) and the predictions from Equation 3.1. Linear regression of the data shows that there was a masking effect of temperature and chloride. This means that the effects of temperature could not be isolated very well from the effects of chloride alone because they were at held relative levels for each LALT that did not lend themselves to sorting out this issue. In the standard LALTs, when temperature was high, so was chloride level, and when temperature was low, so was chloride. For this reason, temperature was included in the equation for mass loss in standard LALTs. Equation 3.1 is valid only in the temperature range of 25-40°C. Therefore, these temperatures were chosen as the high and low levels for the FFA exposures.

Table 3.4 Table of ESF parameters in standard LALTs. These values were used with Equation 3.1 to determine the model predicted curves in Figure 3.1.

LALT	Cl ⁻ (g/L)	%RH	pH	cycling
ASTM B-117	32.5	100	6.5-7.2	0
ASTM G-85 A3	19.77	98	2.8-3.0	12
ASTM G-85 A5	0.03	70	5.0-5.4	12

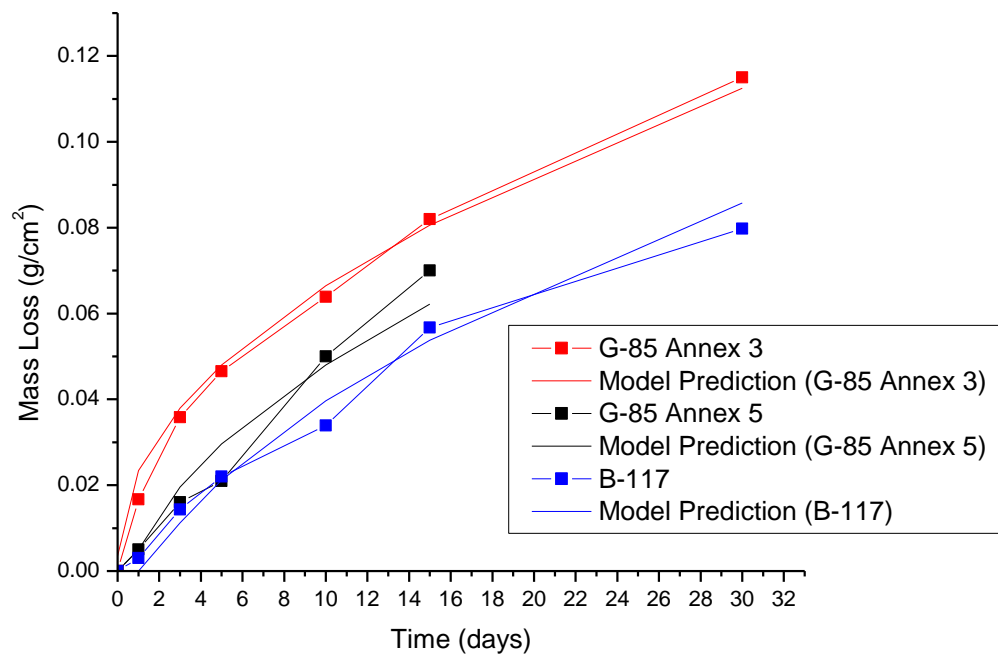


Figure 3.1 Mass loss data for standard LALTs plotted against Equation 3.1. Each curve for Equation 3.1 uses the same environmental parameters as the standard LALT (listed in Table 3.4) it is plotted against. Results demonstrate strong agreement between the model and the LALTs.

The pH of the ASTM G-85 Annex 3 was shown to cause extreme degradation of the substrate, so using a pH of that level was ruled out. It was decided that the two levels

chosen for pH would coincide with the pH of the ASTM B-117 for the high and the pH of the ASTM G-85 Annex 5 for the low (Table 3.4).

Based on the agreement between the model's predictions and actual LALT results, it was determined levels within those of the standard LALTs for cycling and mean % RH could be used in the fractional factorial experimental design. %RH levels were chosen at 70 for the low (equivalent to the ASTM G-85 Annex 5) and 85 for the high. The numbers of wet/dry cycles had to be chosen taking into account the desired levels of mean %RH and making sure that changing the number of cycles did not change the overall amount of time that samples spent in each stage (spray, dwell and dryout). The relative humidity during dryout is 20% and the relative humidity during the spray stage is assumed to be 100%. These considerations dictated that 4 cycles per day was the high level and 1 cycle per day was the low level.

UV levels in the ASTM G-85 Annex 5+UV (0.5 W/m² for 6 hours) caused easily detectable damage to the polymer coating as measured with FTIR, as discussed in Chapter 2. Levels were chosen that were lower than the level used in the ASTM G-85 Annex 5+UV in order to determine whether UV was a factor in scribe creep. Therefore, UV levels of 0.28 W/m² for four hours for the high level and 0.16 W/m² for four hours for the low level were chosen.

Table 3.5 The selected levels of variables for the fractional factorial design of experiment.

	Mean Temperature (°C)	Ozone (ppb)	Mean %RH	Cl ⁻ (g/cm ² /day)	pH	UV (W/m ²)	Cycling (# per day)
High	40	500	85	2.3×10^{-4}	7	0.28	4
Low	25	8	70	2.3×10^{-5}	5.5	0.16	1

A change, however, in the functionality of lab equipment during the fall of 2013 resulted in a necessary modification of the factorial experimental design. Due to the difficulty of measuring pH on a corroding metal surface, pH was removed from the remaining experiments. Statistical analysis of the data obtained up to October 2013 indicated that ozone had no detectable effect on mass loss, or scribe creep, of the steel samples. Figure 3.2 shows the mass loss of bare steel for the first four conditions in the fractional factorial design test matrix (Table 3.7). FFA1 through 3 were run prior to the equipment failures in the fall of 2013, and FFA4 was run once the equipment was back online. The mass loss results were affected by temperature more than any other single variable. Additionally, it was found that ozone did not produce any detectable change in the polymer coating when coated polypropylene samples were exposed to 500 ppb ozone for 15 days (Figure 3.3). For these reasons, ozone was also removed from the set of variables for the remaining factorial experiments (Table 3.5).

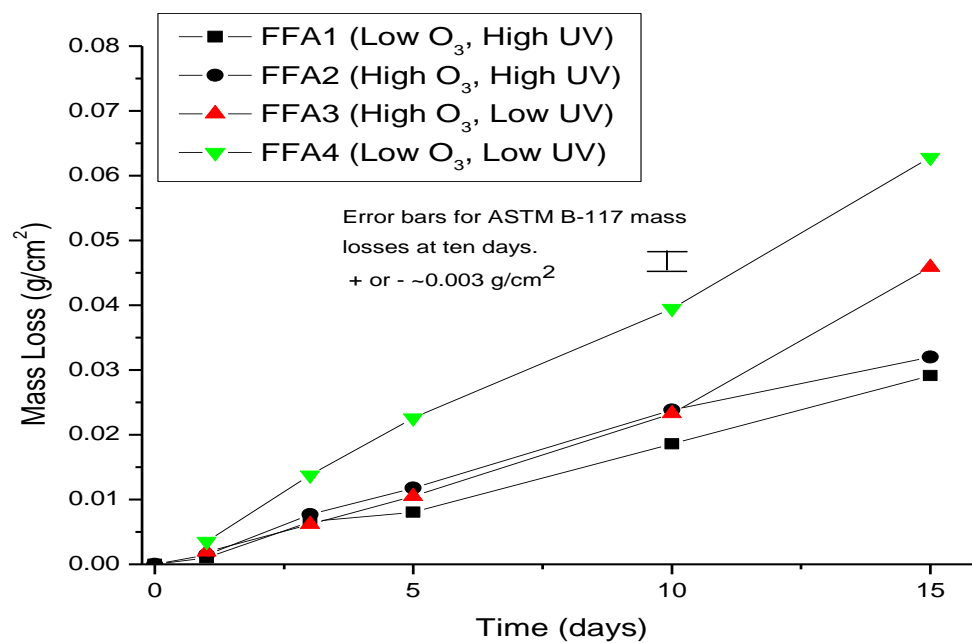


Figure 3.2 Mass loss of bare steel for the first four conditions in the fractional factorial test matrix.

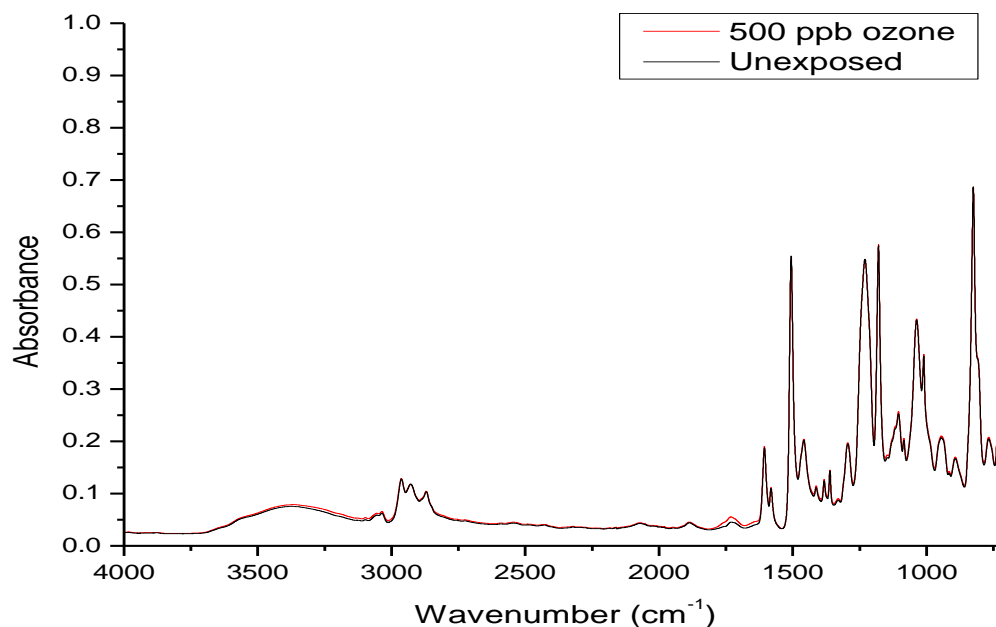


Figure 3.3 FTIR spectra for Eponol coated polypropylene samples unexposed and exposed in 500 ppb ozone for 15 days.

3.2.3 Theory of Factorial Design

In classical experimentation, a testable hypothesis is developed and an experiment is run to test the hypothesis. Sometimes one variable is systematically varied while the others are held constant. The data obtained by the experiment are used to modify the original hypothesis and new experiments are then designed and conducted.¹³ This iterative process is continued until the desired result is achieved. This type of experimentation relies heavily on an experimenter's prior knowledge and is often time consuming, especially if there are multiple variables to be studied.¹³ However, factorial experimental designs enable efficient investigation of multiple variables by selecting a fixed number of levels for each variable

and performing experiments to test all possible combinations.¹³ For example, to test the effects of three additives to a lubricating agent at two different levels (i.e., high/low amount of the additive) would require eight experiments (see Table 3.6).

Table 3.6 Factorial design test matrix for testing three variables in eight experiments.

Run	Variable 1	Variable 2	Variable 3
1	-	-	-
2	+	-	-
3	-	+	-
4	+	+	-
5	-	-	+
6	+	-	+
7	-	+	+
8	+	+	+

The benefits of factorial experimental designs include: 1) relatively limited number of experiments to generate significant data, 2) the ability to detect major trends that can be used to direct and refine further experimentation, and 3) all possible effects, including effects caused by the interaction of multiple factors, can be determined.¹³

Originally, seven ESFs (temperature, chloride, cycling, ozone, pH, mean %RH and UV) were selected and studied. To test all possible combinations of factors with seven variables at two levels would require 128 individual experiments. This is known as a 2^7 factorial design

where 7 variables are tested at two levels. 128 experiments would be needed to determine all of the effects caused by interactions between three, four or more variables. However, many of these higher order interactions generally have a negligible effect on the overall trends of the data, and thus can be disregarded¹³ (this is analogous to ignoring higher order terms in a Taylor series expansion). By taking a specific fraction of the experiments, the main effects can be determined without the time and resources required to perform a full factorial design. Such a design is called a fractional factorial design. In fractional factorial design, $n-1$ variables can be tested at two levels using n experiments.¹³ Performing eight experiments for seven variables at two levels is known as a 2^{7-4} fractional factorial design and is a fairly common experimental design choice.¹³ In this type of experimental setup, a high and low level for each variable is chosen and then the experimental test matrix is designed so that each variable “experiences” every other variable at a high and low level.

There is a tradeoff when one performs a fraction of a full factorial test matrix, such that savings in time and resources must be balanced with a possible reduction in resolution of the effects of these variables.¹³ Resolution in this sense is the ability to detect all main effects and higher order interactions between individual ESFs. Statistical experimental resolution is not very different from resolution in microscopy. For example, an optical microscope could be used to interrogate the surface of a sample to identify locations of interest before interrogation with SEM. Similarly, in statistical analysis, a fractional factorial design can be implemented before a full factorial design of experiment to detect significant trends or patterns in the data. The fractional factorial design used in this study is of resolution (III), meaning that main effects (those caused by individual environmental factors) can be determined, but they may be confounded by two factor interactions.¹³

Higher order interactions between three or more factors are not discernable. In this study, a 2^{7-4} fractional factorial design of experiment was conducted. Eight experiments investigating the effects of 7 ESFs on scribe creep were to be conducted. However, as discussed in Section 3.2.2, the number of variables was reduced to five (temperature, UV, chloride, cycling, and %RH).

3.3 **Objective**

The objective of this experimental design is to systematically develop an understanding the effects of isolated individual and combined environmental severity factors (ESF) on mass loss, underpaint corrosion sensed by scribe creep and polymer coating degradation. The ESFs examined were temperature, ozone, UV, pH, % relative humidity, chloride and cycling.

3.4 **Experimental Methods**

3.4.1 **Materials**

Organic coated and scribed AISI 1018 steel (UNS# G10180; 0.15% C, 0.7% Mn, Fe; wt. %) was used as a model coating system. A clear epoxy resin (Poly(Bisphenol A-co-epichlorohydrin) glycidyl end-capped ($C_{18}H_{22}O_3$) $_n$ • $C_{22}H_{26}O_4$; Trade name Eponol) was used. The chosen epoxy resin is a high molecular weight resin used primarily as a constituent of paint coatings.¹⁴ The coating was applied to be 30 ± 5 μ m thick and had a high initial impedance of $\geq 10^{11}$ Ω -cm² at 0.01 Hz. Samples not in the stated thickness range or below the initial impedance level were discarded. The choice of this clear resin as a coating for samples in LALTs allowed the underpaint corrosion to be imaged with optical microscopy.

It also enabled interrogation of the underpaint environment by 3D optical microscopy and Raman microscopy, both of which penetrate the clear coating to interrogate the substrate.

Epoxy resin films were also cast on inert polypropylene substrates. These substrates were exposed along with the bare and coated metal samples and were interrogated with FTIR after exposure.

3.4.2 Sample Preparation

In preparation for coating, the surface of each metal sample was ground with 120, 180, 240, 300, and 600 grit silicon carbide paper to remove any surface oxide, even out any imperfections and create a clean bare surface for the application of the coating. The samples were then blown with compressed air to remove any large debris from the grinding. The samples were washed with water and detergent and rinsed with Millipore water. After washing, the samples were immediately blown dry with compressed dry air. The epoxy resin was applied to the steel samples by draw down bar to a thickness of 30 ± 5 μm . The metal samples were cured for five days in lab air and then cured at 60°C for 24 hours. After curing, the samples were cut to 2.5 x 2.5 cm dimensions and then scribed by hand down the middle with a diamond scribe tool. Figure 1.20 (Chapter 1) illustrates a top down diagram of the coated and scribed sample, while Figure 1.21 (Chapter 1) shows the sample and scribe in cross-section.

3.4.3 High-Level Surveillance Testing Methods

3.4.3.1 2D and 3D Digital Optical Microscopy

The bare and coated 1018 steel samples were imaged with a Hirox KH-7700 digital microscope. The samples were first imaged with a macro lens to get one image of the entire sample surface. The coated samples then had a 2D tiled image taken at 50x that extends the length of the scratch using the MXG-4050RZ lens. Higher resolution images (400x+) are taken at various interesting spots on the samples. The clear coating allows for visual imaging of the metal surface under the coating. The image analysis software ImageJ 1.44p released by the National Institutes of Health was employed to make quantitative measurements of scribe creep from 2D images of the scribe and surrounding scribe creep. Scribe creep lengths were measured from the scribe line perpendicularly to the edge of the scribe creep front. The measurements were done at 10 random locations along the scribe in both directions for a total of 20 measurements. These data were then used to determine an average scribe creep length.

The coated samples then have 3D tiled images taken at 350x that start at the scratch and run perpendicular out from the scratch using the MXG-10C lens with the OL 350 II lens attachment. Continuous 3D optical tiling was used to generate images that were 600 by 3000 μm (bounds set by the magnification of the lens) in the x-y plane with full penetration of the clear epoxy resin coating. 3D images were used to generate line profiles of the corrosion product morphology across the scribe. These 3d tiled images are taken at the same place every time to monitor the progress of the corrosion from the scratch. The 3D

images were processed using Mitiani Corporation 3DMeasurement software and with Mountains Map® Analysis Software 6.2 by Digital Surf

3.4.3.2 Digital Image Analysis

The image analysis software ImageJ 1.44p released by the National Institutes of Health was employed to make quantitative measurements of scribe creep from 2D images of the scribe and surrounding scribe creep area. Scribe creep lengths were measured from the scribe line perpendicularly to the edge of the scribe creep front. The measurements were done at 10 random locations along the scribe in both directions for a total of 20 measurements. These data were then used to determine an average scribe creep length. Error bars reported for scribe creep length represent standard error, which is the standard deviation divided by the square root of the sample size.

3.4.3.3 Electrochemical Impedance Spectroscopy

Electrochemical Impedance Spectroscopy was used to measure the change in the electrical properties of the coating over time. EIS was performed at locations near to and far from the scribe. This was done to more accurately determine the rate at which the scribe creep front moved away from the scribe and to determine the effects of the scribe and ESFs on the electrical characteristics of the coating.

The testing was done on a Princeton Applied Research Versastat 4 using the VersaStudio software. A five minute OCP test was run before EIS. A typical EIS scan was acquired in sine mode from 100 kHz to 0.01 Hz with 6 points per decade. Coated panels were scanned with

an AC amplitude of 60 mV. The tests were run in a flat cell containing 50 mM sodium sulfate solution with ambient aeration at 25°C. The area of the sample tested was a circle with an area of 1cm². The reference electrode used was a saturated calomel reference electrode was used as the reference electrode. Samples were used as the working electrode, and a platinum mesh was used as the counter electrode. The EIS data were processed using Z-View 3.3d analysis software by Scribner Associates Inc.

3.4.3.4 Fourier Transform Infrared Spectroscopy (FTIR)

Fourier Transform Infrared Spectroscopy was performed at the University of Southern Mississippi and was used to monitor degradation of the coating over time. Films were left on the substrate and spectra were taken from three different locations on the epoxy resin film by securing them to the Smart iTR attachment. The spectra were obtained using a Nicolet 6700 FTIR from Thermo Scientific running Omnic software, in 650-4000 cm⁻¹ range. The spectrophotometer was operated in transmission mode. The spectra were recorded at a resolution of 2 cm⁻¹ and 32 scans were run per location. The polypropylene substrate on which the Epoxy resin coating was cast was inert, and thus had no effect on the degradation of the coating. This isolated the effects of the environment from the effects of underpaint corrosion on degradation of the coating. Degradation of the coating was observed by comparing the results of an unexposed coating to exposed coatings. Films were exposed in all factorial experiments.

3.4.3.5 Raman Microscopy

Raman microscopy is a surface sensitive spectroscopy method that detects the molecular identity of corrosion products. It is used to determine the species that form on the surface of the samples that are either amorphous or in limited quantities that are undetectable by XRD.¹⁵ Raman microscopy was conducted using a Renishaw InVia Raman Microscope with a 200 mW, 785 nm laser with a fixed diffraction grating over a range of 200 to 1400 cm^{-1} . The laser power was 0.1% with a spot size of 50 μm . Raman was performed on standard powders for comparison to experimental results. For exposed samples, Raman spectra were taken from at least ten varied locations over the surface of the sample, with care taken to perform scans on all different types of colors and morphologies seen.

3.4.3.6 X-Ray Diffraction (XRD)

X-Ray Diffraction (XRD) was performed using a PANalytical X'pert Pro MPD powder diffractometer with a $\text{Cu-K}\alpha$ source. All samples were scanned continuously from 10 to 120 degrees at a rate of 1 degree per minute. The data were analyzed using Highscore Plus 3.0c analysis software by PANalytical. Pure powders of individual iron oxides and hydroxides were characterized with XRD for comparison to XRD spectra of exposed samples. Standard powder samples were examined as received while exposed steel samples were examined with the oxide intact on the sample.

3.4.3.7 Mass Loss Test Procedure

Mass loss samples were all weighed before exposure on a Denver Instrument Company M-220D scale with a resolution of 0.01mg. The back samples were covered in electroplating tape, and then the edges were coated with stop-off lacquer before exposure. After exposure, the tape and lacquer were removed and the samples placed in a hydrochloric acid solution until all visible corrosion products had been removed according to the ASTM G 1-03.¹⁶ The samples were then removed, rinsed, dried and weighed. Mass loss samples were not returned to the exposure chambers after testing. Error bars reported for mass loss represent standard error, which is the standard deviation divided by the square root of the sample size.

3.4.4 **Sample Exposure Conditions**

3.4.4.1 Experimental Setup

Temperature, ozone, mean % RH, chloride, pH, UV and cycling were chosen as variables for this study. The way a variable is measured is important for understanding how the levels chosen for the fractional factorial experimental design compare with real world exposures. Most variables were measured in a straightforward way (e.g., temperature, wet/dry cycling, ozone, %RH and UV were all measured by sensors designed to detect those factors). Other factors, however, were not as straightforward.

Chloride ion deposition rate in the field is often measured with a wet chloride candle. A wet chloride candle is a long wick of gauze with one end threaded through a rubber stopper into a bottle of a glycerol/water solution. The other end is exposed to the atmosphere. Chloride

ions in the air come in contact with the wick and are wicked into the solution in the bottle.¹⁷ After a set period of time, the chloride concentration in the solution is measured and a chloride deposition rate is determined. However, there are several major shortcomings with this method. First, the difference in geometry and materials between a flat metal panel and a strip of gauze can cause differences in the deposition rate measured by the candle and the actual deposition rate on the sample surface. Second, the amount of chloride measured by the chloride candle over time is not the amount that may stick to the surface of the sample. Precipitation events can remove chloride from the surface of the sample and these events would not remove the wicked chloride from the candle solution. Therefore, to establish a chloride deposition rate by chloride candle is misleading in that the actual amount of chloride on the sample surface is never known. This creates problems in comparing the amount of chloride in a LALT solution to a chloride deposition "rate." In order to make comparison more straightforward, a different measure has been proposed: a chloride impingement rate. The impingement rate is the amount of chloride that contacts the surface of the sample per unit time. The impingement rate makes no assumption about deposition, runoff, or the length of time that chloride stays on the surface of the sample. A chloride candle measures all chloride that impinges upon the wick. In a controlled LALT, the rate of chloride impingement on the surface of the sample can be calculated using the amount of solution that impinges on the. For the 2.5 by 2.5 cm samples used in this study held at 60° from horizontal in the ASTM B-117, the impingement rate is 0.34668 g Cl⁻/cm² per day.

The pH of a solution is straightforward to measure. However, the pH of a solution on a corroding metal surface is much more complex. An aqueous solution exposed to air on the

surface of a sample will become acidic due to carbon dioxide being absorbed and converted to carbonic acid.¹ At normal atmospheric concentrations, pure water exposed to air will equilibrate at pH 5.7.¹ Additionally, aerosol particles in the atmosphere can introduce sulfate or nitrate species that can also affect the pH of the water layer on the surface of a metal sample. Despite the complex nature of measuring the pH of a water layer on a corroding metal surface, pH is important due to its well-known effects on the corrosion of steel.^{1, 2, 18, 19} Because of its importance, pH was originally tracked in these experiments by measuring the pH of the salt solution that was put into the exposure chamber. The pH was adjusted by HCl and NaOH.

For this study, the originally chosen variables have been arranged in a test matrix presented in Table 3.7.

Table 3.7 Test matrix for fractional factorial experiments in this study.

Run	Temperature	Ozone	Mean %RH	Cl ⁻	pH	UV	Cycling
1	-	-	+	-	-	-	-
2	-	+	-	+	+	-	-
3	+	+	+	+	-	+	-
4	+	-	-	-	+	+	-
5	+	-	-	+	-	-	+
6	+	+	+	-	+	-	+
7	-	+	-	-	-	+	+
8	-	-	+	+	+	+	+

3.4.4.2 Variable Level Selection

Appropriate testing levels for the ESFs examined using factorial design were selected using a two-fold approach. First, visual inspection was employed to evaluate corrosion produced by the variable levels set in the B-117, G85 A3, and G85 A5 standards. Second, linear regression analysis of the mass loss data (presented in Chapter 2) for these tests and the KSC field site was performed. This analysis was used to develop an expression for mass loss for the Eponol/1018 steel system. The variables tracked were time in days, mean temperature, mean %RH, chloride concentration in grams per liter of solution, pH, UV in terms of intensity multiplied by the number of hours per day, and cycling in terms of the number of cycles per day. The data were analyzed using R statistical software.²⁰ A consultant was employed to help the author learn and perform statistical analysis of the data.

The levels of the selected ESFs were adjusted in the following manner: mean chloride impingement rate was adjusted by changing the concentration of chloride ions in the solution. The pH of the solution was brought to the desired level by using acetic acid and sodium hydroxide. Mean %RH was adjusted during the dwell stage of the test setup. The fog chamber spray stage has 100% RH and the dry out stage, using lab air, has 20% RH, which is below the NaCl deliquescence point of 75% RH.²¹ The %RH of the dwell stage was therefore adjusted by performing a dryout for four minutes between the fog and the dwell stage to reach the desired mean %RH over the length of the dwell stage. The change in %RH over the course of a day can be seen in Figure 3.4. The temperature was controlled and adjusted by the salt fog cabinet. The UV light intensity was adjusted by placing the

samples at specific locations within the chamber where the UV intensity had been measured. A timer for the UV lights was installed to control the irradiation time.

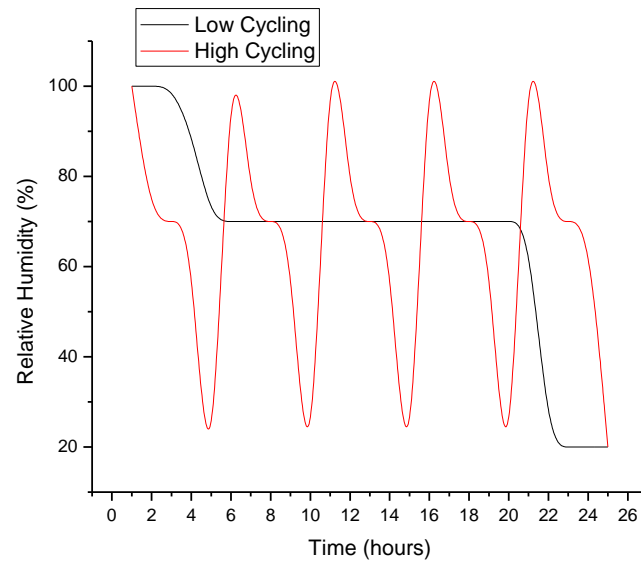


Figure 3.4 Chart of relative humidity during one day for high and low cycling for a mean relative humidity of 70%.

The modified salt spray cabinet has three operation modes: spray (also called fog) where the solution is sprayed on the samples; dwell, where the cabinet is kept at a specific relative humidity and temperature; and dry out, where lab air is blown through the cabinet to dry out the moisture on the samples. Therefore, the test setup used in these experiments could only incorporate these three modes. For the current experiments, the test cycle consisted of three stages: four hours of spray, sixteen hours of dwell and four hours of dry out. To incorporate cycling into the test, the test setup was changed to one hour spray, four hours dwell and one hour dry out repeated four times in 24 hours. All experiments thus had the same total time spent in each stage.

3.4.4.3 Modification of Original Experimental Setup

There is no one lab exposure device that can control and cycle humidity, UV, solution fog rate, temperature, pH and gas concentration. Therefore, a salt fog chamber was modified to include UV lights and an inlet port for gases,²² allowing for the combination of all ESFs thought to affect scribe creep. Due to unforeseen circumstances, the lab space in which this work was conducted was rendered unusable from October through December of 2013. Additionally, the modified exposure chambers were made inoperable and had to be replaced. Due to time constraints, new chambers could not be modified with UV lights and gas inlets. It was decided that a modification to the remaining experiments and conditions was necessary. Ozone and pH were removed from the remaining experiments. With the removal of pH and ozone from the test matrix, the fractional factorial design changed from seven variables to five variables. This new matrix is given in Table 3.8. Note that once again, each variable “experiences” every other variable at both high and low levels. Variable levels did not change from the values given in Table 3.5.

Table 3.8 Revised test matrix for fractional factorial experiments in this study.

Run	Temperature	Mean %RH	Cl ⁻	UV	Cycling
FFA1	-	+	-	+	-
FFA2	-	-	+	+	-
FFA3	+	+	+	-	-
FFA4	+	-	-	-	+
FFA5	-	-	+	-	+
FFA6	+	+	-	+	+

Table 3.9 Revised table of variable levels for fractional factorial experiments.

	Mean Temperature (°C)	Mean %RH	Cl ⁻ (g/cm ² /day)	UV (W/m ²)	Cycling (# per day)
High	40	85	2.3x10 ⁻⁴	0.28	4
Low	25	70	2.3x10 ⁻⁵	0.16	1

3.4.4.4 Diagnostic Tests

Two diagnostic tests were also performed on coated steel samples. The diagnostic tests sought to examine whether scribe creep was controlled by corrosion reactions at the scribe or a combination of reactions at both the head and the scribe, such as the oxygen reduction reaction (ORR) through the coating ahead of the scribe creep front and cathodic delamination. In the first, a coated and scribed steel sample was exposed in FFA6 for 3 days. It was removed, imaged with the optical microscope and stored in a desiccator

overnight. The next morning it was coated with a 5 μm film Au-Pd film by sputter coating as an oxygen permeation barrier over the intact coating and imaged again with the optical microscope. The scribe itself was masked so that it was not coated enabling corrosion reactions and corrosion product accumulation to proceed at the scribe. The sample was then returned to the FFA exposure for 10 days. It was then removed and imaged a last time with the optical microscope. This sample is referred to as the metal cover test.

The second diagnostic test was cathodic polarization to examine the rate of the ORR on intact coated samples exposed in all FFA exposures. The coated samples were unscribed. At 0, 10 and 15 days, the following test sequence was performed: 5 minute OCP, EIS, cathodic polarization from -1.1 V to -0.3 V, 1 hour OCP, EIS, cathodic polarization from -1.1 V to -0.3 V, 24 hour OCP, EIS, cathodic polarization from -1.1 V to -0.3 V. The electrochemical tests were performed in a flatcell in 50 mM sodium sulfate in ambient aeration at room temperature.

3.5 **Results**

3.5.1 **Mass Loss of Bare Steel**

Mass loss versus time is reported in Figure 3.5 for FFA1 through FFA6. In all cases, mass loss increases with time, but the rate of increase varies for different exposures. Mass loss is roughly linear with time FFA1 and FFA2 showed the least amount of mass loss over time. FFA3 and FFA5 show similar amounts of mass loss, while FFA4 and FFA6 show the greatest amount of mass loss. FFA1 and FFA2 have low levels of temperature and cycling. FFA3 has high temperature and low cycling while FFA5 has high cycling and low temperature. FFA4

and FFA6 both have high temperature and high cycling. These differences will be addressed in the discussion section.

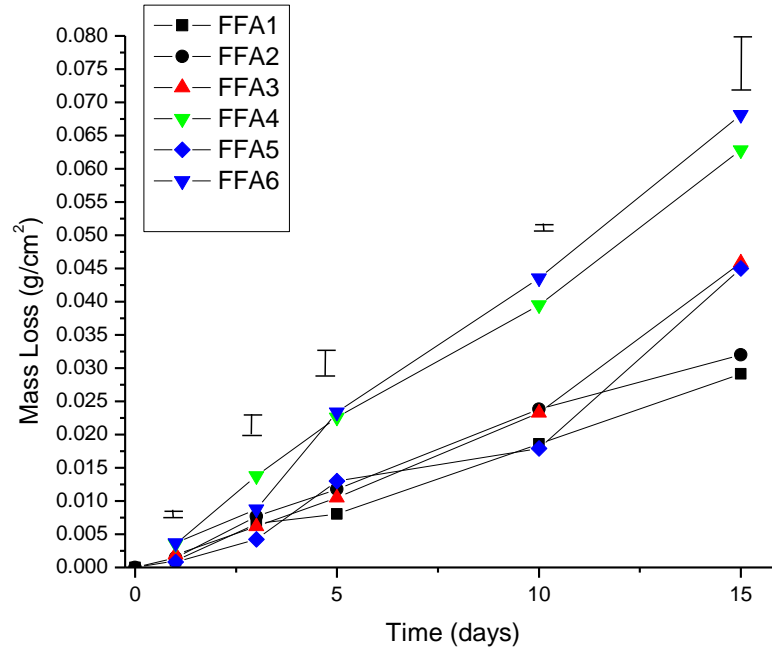


Figure 3.5 Graph of mass loss versus time for bare 1018 steel exposed in various FFA environments (Table 3.9). The error bars shown above the data are the standard error from mass loss results for ASTM G-85 Annex 5.

3.5.2 Corrosion Product Analysis

3.5.2.1 X-Ray Diffraction

XRD was used to determine the identity of corrosion products that formed on bare samples exposed in FFA1 through FFA6. The assumption is that this is also representative of corrosion products at the scribe. Figure 3.6 shows the XRD spectra for all FFA experiments compared with the standard powders. FFA1 shows BCC iron peaks at 44.7 and 65.1

degrees. Other peaks may indicate possible iron oxide hydroxides (FeOOH). FFA2 and FFA3 may show peaks for gamma phase iron oxide hydroxide (γ -FeOOH). FFA4 and FFA6 appear to show peaks for both alpha and gamma phase iron oxide hydroxide. FFA5 is difficult to interpret, but may show peaks for gamma phase iron oxide hydroxide.

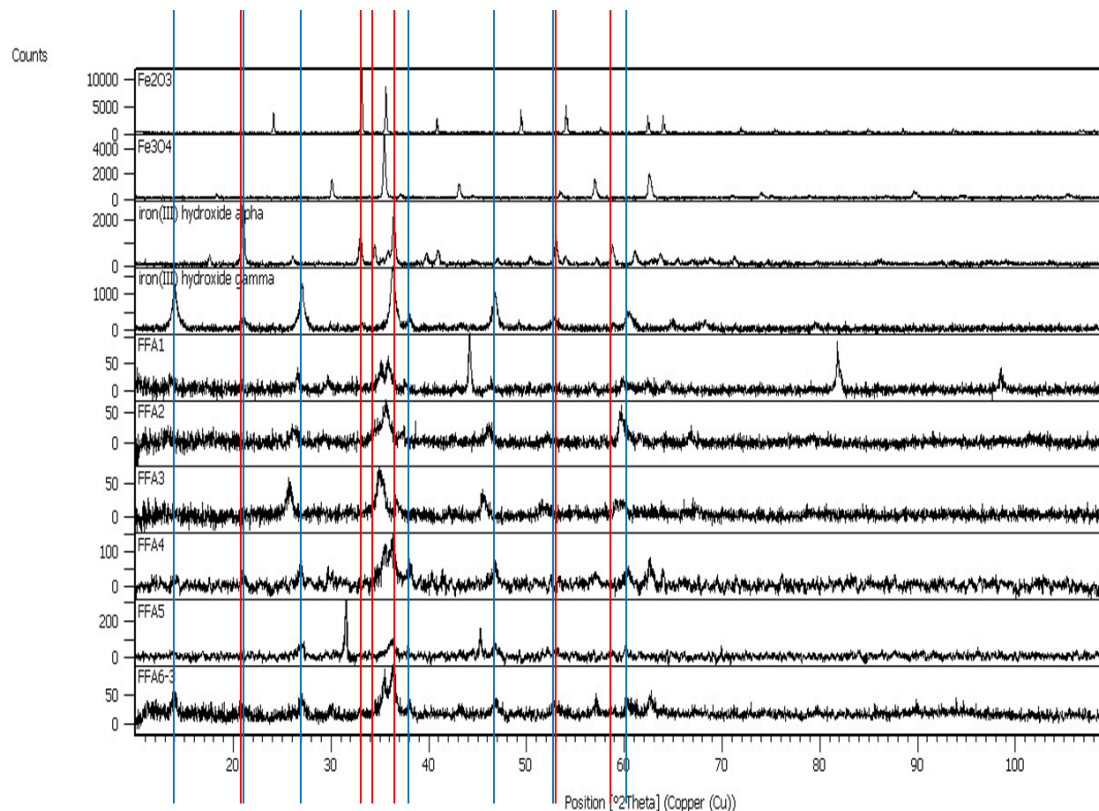


Figure 3.6 XRD spectra for standard powders and all FFA experiments. Vertical lines indicate peaks for α -FeOOH (blue) and γ -FeOOH (red).

3.5.2.2 Raman Spectroscopy of Corrosion Products on Bare Steel

Figure 3.7 shows the Raman spectra for standard powders. Figure 3.8 shows the spectra for FFA1 indicating the detection of γ -FeOOH. The spectra for FFA2 (Figure 3.9) show α -

FeOOH, β -FeOOH and Fe₂O₃. FFA3 spectra are given in Figure 3.10 and indicate detection of γ -FeOOH, β -FeOOH and an as yet unidentified species. Figure 3.11 shows the spectra for FFA4 indicating the detection of γ -FeOOH. Figure 3.12 shows that γ -FeOOH and β -FeOOH were detected for FFA5. Figure 3.13 shows the spectra for FFA6 indicating the detection of γ -FeOOH. The γ -FeOOH species was detected in every exposure except for FFA2. FFA2 was also the only exposure in which Fe₂O₃ was detected. β -FeOOH was detected on samples exposed in FFA2, FFA3 and FFA5. Results are summarized in Table 3.10; the species detected with Raman are marked with an R.

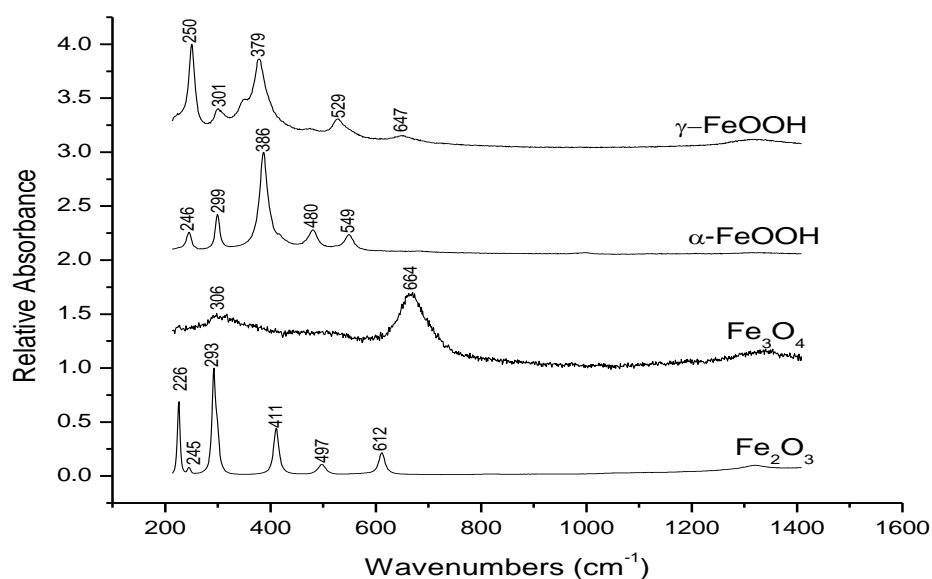


Figure 3.7 Experimental Raman spectra for standard powders.

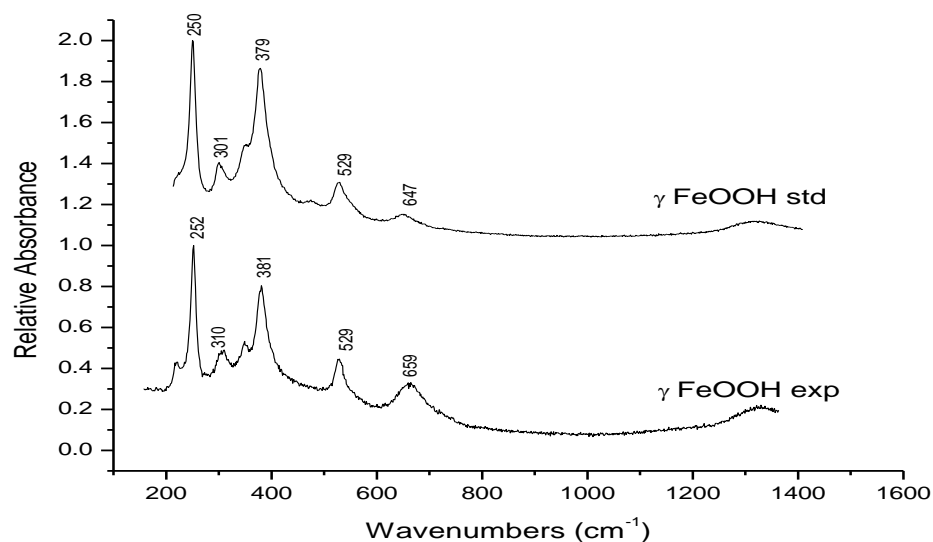


Figure 3.8 Raman spectra for bare 1018 steel exposed in FFA1 for 15 days. “exp” indicates experimental spectra from this study, “std” indicates standard powder spectra from this study. Conditions: T(-), %RH(+), Cl(-), UV(+), Cycling(-).

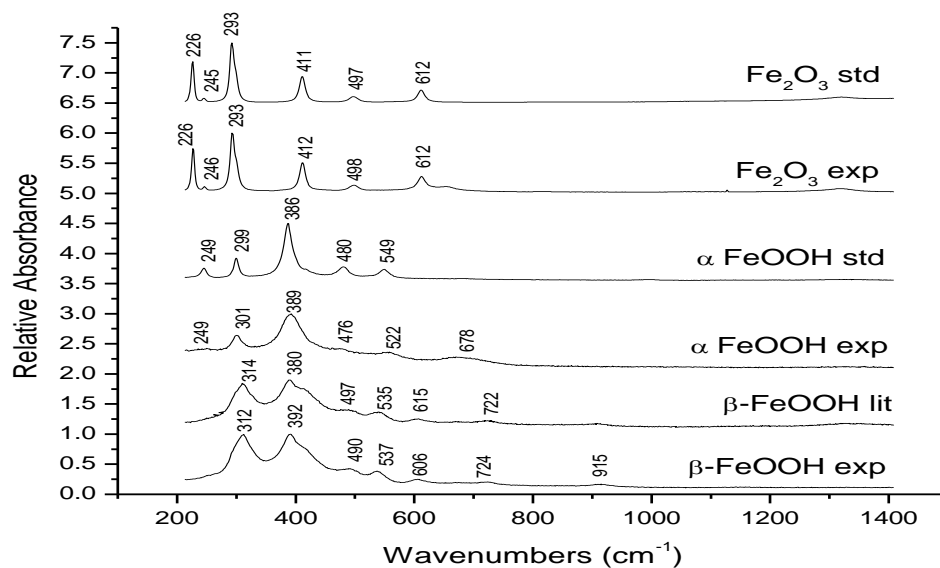


Figure 3.9 Raman spectra for bare 1018 steel exposed in FFA2 for 15 days. “exp” indicates experimental spectra from this study, “std” indicates standard powder spectra from this study, “lit” indicates spectra from literature. Conditions: T(-), %RH(-), Cl(+), UV(+), Cycling(-).

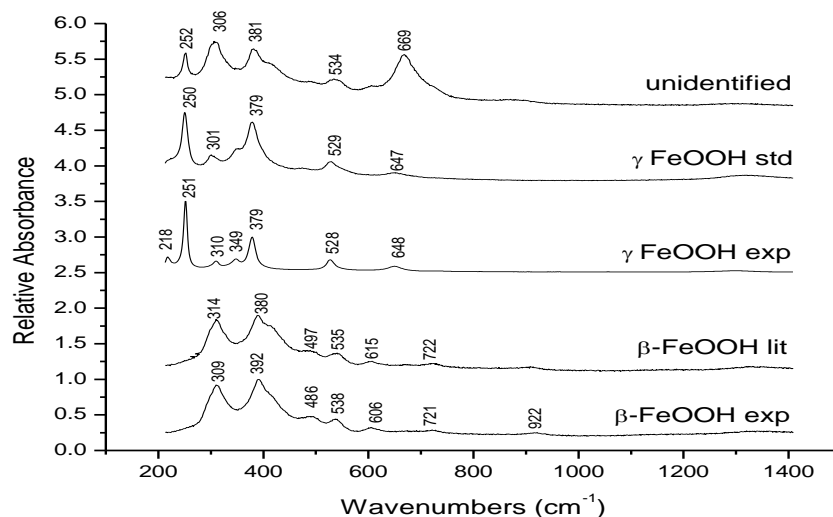


Figure 3.10 Raman spectra for bare steel exposed in FFA3 for 15 days. “exp” indicates experimental spectra from this study, “std” indicates standard powder spectra from this study, “lit” indicates spectra from literature. Conditions: T(+), %RH(+), Cl(+), UV(-), Cycling(-).

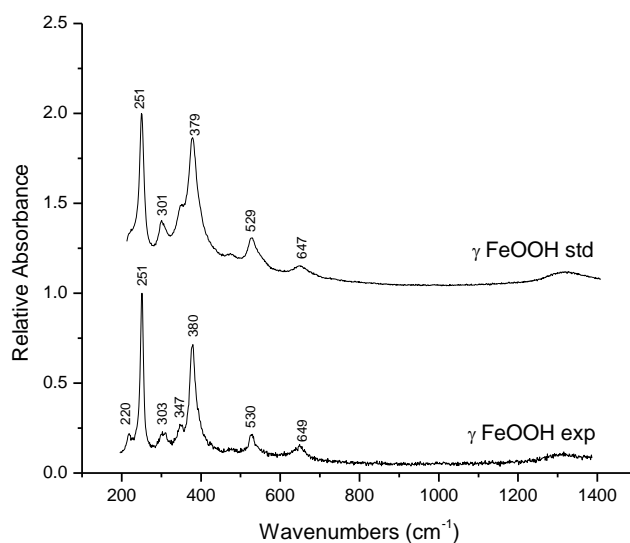


Figure 3.11 Raman spectra bare steel exposed in FFA4 for 15 days. “exp” indicates experimental spectra from this study, “std” indicates standard powder spectra from this study. Conditions: T(+), %RH(-), Cl(+), UV(-), Cycling(+).

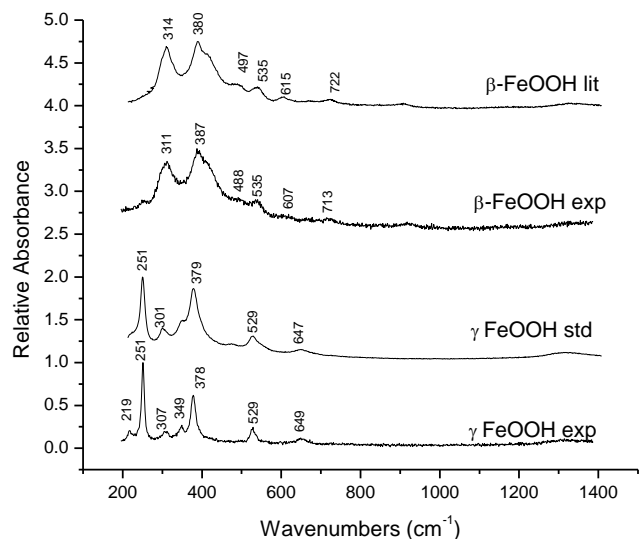


Figure 3.12 Raman spectra bare steel exposed in FFA5 for 15 days. “exp” indicates experimental spectra from this study, “std” indicates standard powder spectra from this study, “lit” indicates spectra from literature. T(-), %RH(-), Cl(+), UV(-), Cycling(+).

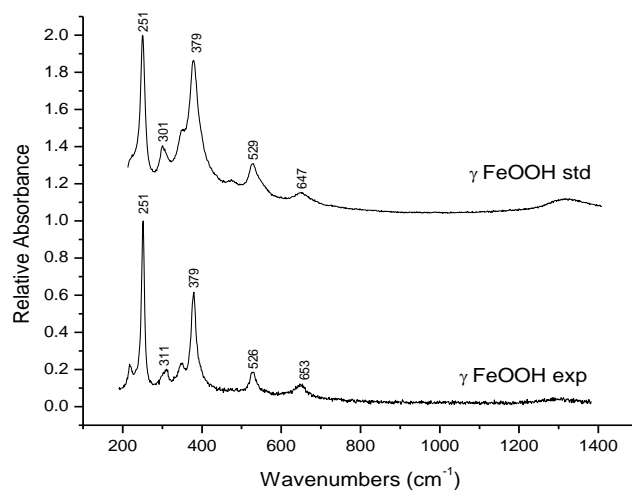


Figure 3.13 Raman spectra bare steel exposed in FFA6 for 15 days. “exp” indicates experimental spectra from this study, “std” indicates standard powder spectra from this study. Conditions: T(+), %RH(+), Cl(-), UV(+), Cycling(+).

Table 3.10 Table of iron oxide species found on bare steel with XRD and Raman spectroscopy compared to KSC, ASTM B-117 and ASTM G-85 Annex 5. (X) indicates species found with XRD, (R) indicates species found with Raman, and (-) indicates that the species was not detected.

Exposure	Iron (II,III) oxide Fe_3O_4	Iron (III) oxide Fe_2O_3	Iron (III) Oxide- Hydroxide Alpha Phase $\alpha\text{-FeOOH}$	Iron (III) Oxide- Hydroxide Beta Phase $\beta\text{-FeOOH}$	Iron (III) Oxide- Hydroxide Gamma phase $\gamma\text{-FeOOH}$
FFA1	-	-	X	R	X,R
FFA2	-	R	R	R	X
FFA3	-	-	-	R	X,R
FFA4	-	-	-	-	X,R
FFA5	-	-	-	R	R
FFA6	-	-	-	-	X,R
KSC ¹	-	-	X	R	X,R
B-117 ²	X	-	R	-	R
G-85 A5 ³	-	-	X,R	-	X,R

1. Kennedy Space Center

2. ASTM B-117

3. ASTM G-85 Annex 5

3.5.3 Scribe Creep Behavior

Figure 3.14 shows the progression of scribe creep over time for FFA1. Scribe creep progresses with many small lobes associated with underpaint corrosion that grow away from the scribe. As these lobes grow outward (day 3 and 5) they also appear to sometimes coalesce with one another along the length of the scribe creating a slightly more uniform scribe creep front by day 10 and day 15. There is also damage to the intact coating away from the scribe that appears as time progresses and is particularly noticeable by days 10 and 15.

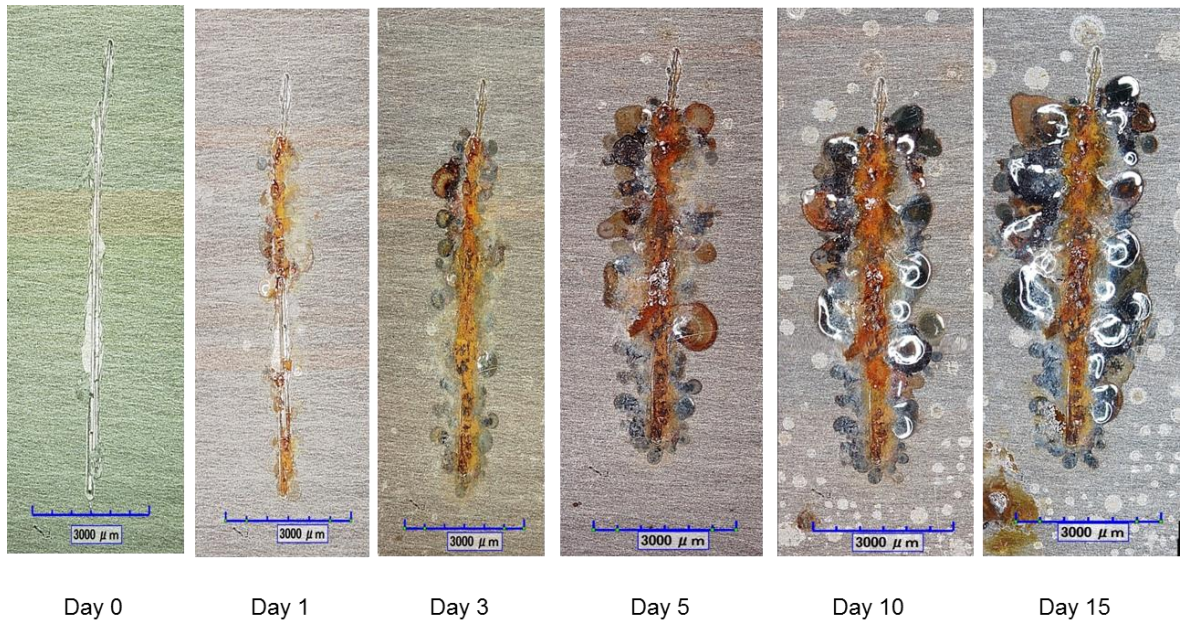


Figure 3.14 Optical images of the progression of scribe creep for Eponol coated steel exposed in FFA1 for 15 days. Conditions: T(-), %RH(+), Cl(-), UV(+), Cycling(-).

Images of scribe creep for FFA2 are shown in Figure 3.15. The lobe shape of the scribe creep front is relatively large and the lobes are fewer in number compared to FFA1. The

scribe creep progresses relatively slowly. Noticeably less damage occurs away from the scribe over time as time progresses compared to FFA1.

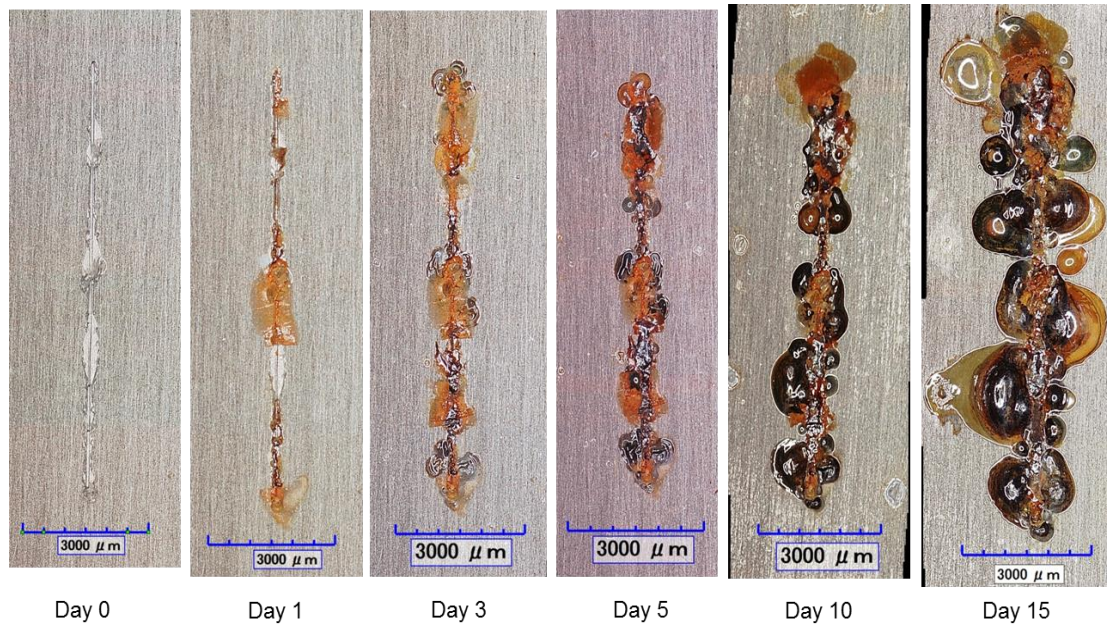


Figure 3.15 Optical images of the progression of scribe creep for Eponol coated steel exposed in FFA2 for 15 days. Conditions: T(-), %RH(-), Cl(+), UV(+), Cycling(-).

Figure 3.16 shows optical images of the scribe creep for FFA3. Scribe creep appears to progress slowly through three days. At five days many large lobes of discoloration appear along the scribe. Through days 10 and 15, scribe creep appears to mainly progress from the lobes formed at day 5. The lobes appear to progress under the coating with minimal lifting of the coating. Noticeably less damage occurs away from the scribe over time as time progresses compared to FFA1.

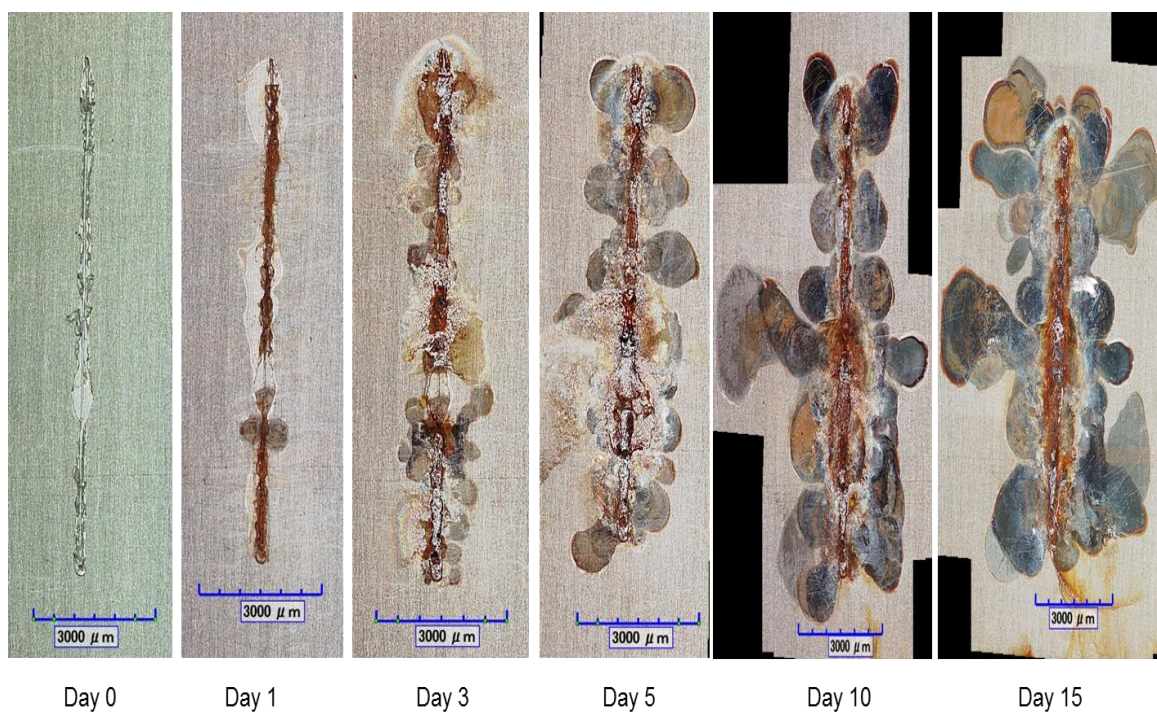


Figure 3.16 Optical images of the progression of scribe creep for Eponol coated steel exposed in FFA3 for 15 days. Conditions: T(+), %RH(+), Cl(+), UV(-), Cycling(-).

Figure 3.17 shows the progression of scribe creep in FFA4. Scribe creep appears to progress relatively quickly. The coating appears to be lifted at the scribe creep front, but in a few places discoloration has spread under the coating with minimal lifting.

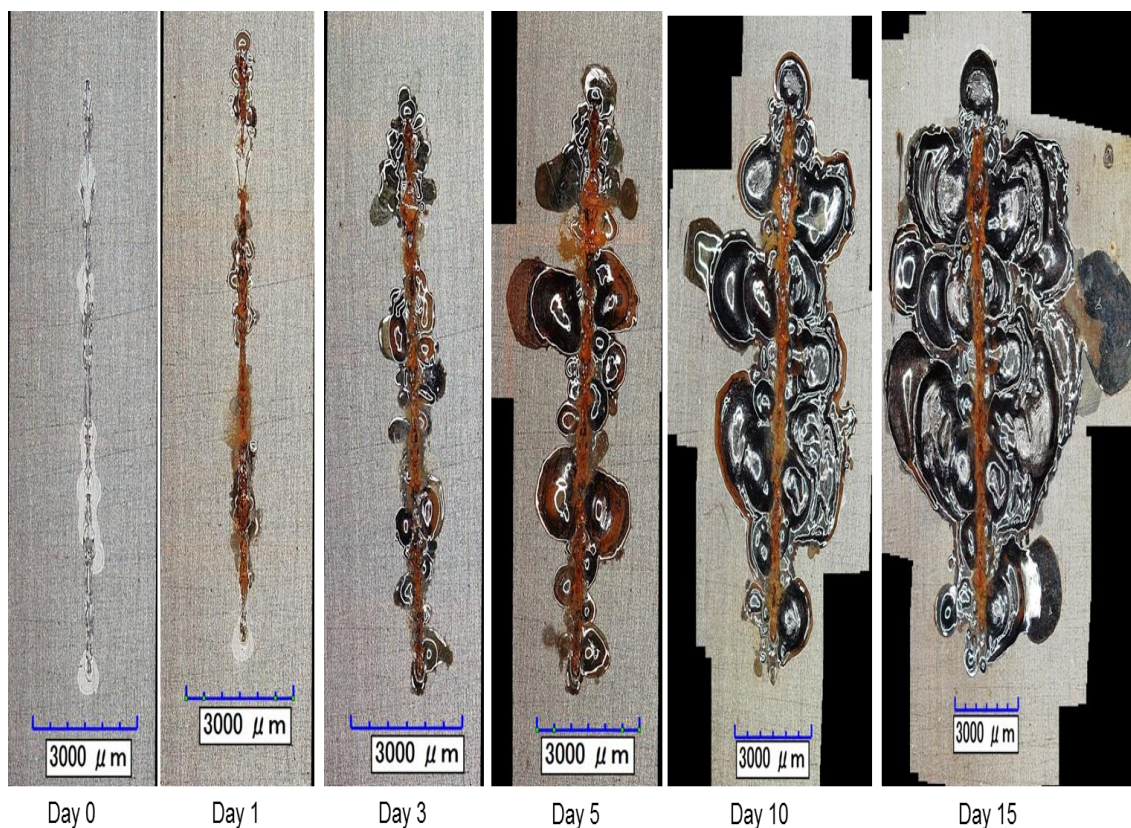


Figure 3.17 Optical images of the progression of scribe creep for Eponol coated steel exposed in FFA4 for 15 days. Conditions: T(+), %RH(-), Cl(+), UV(-), Cycling(+).

Scribe creep progression for FFA5 is shown in Figure 3.18. Scribe creep progresses quickly through days three and five. This progression appears to be mostly discoloration under the coating with minimal lifting of the coating itself. Scribe creep does not appear to progress quickly at day 10 and day 15.

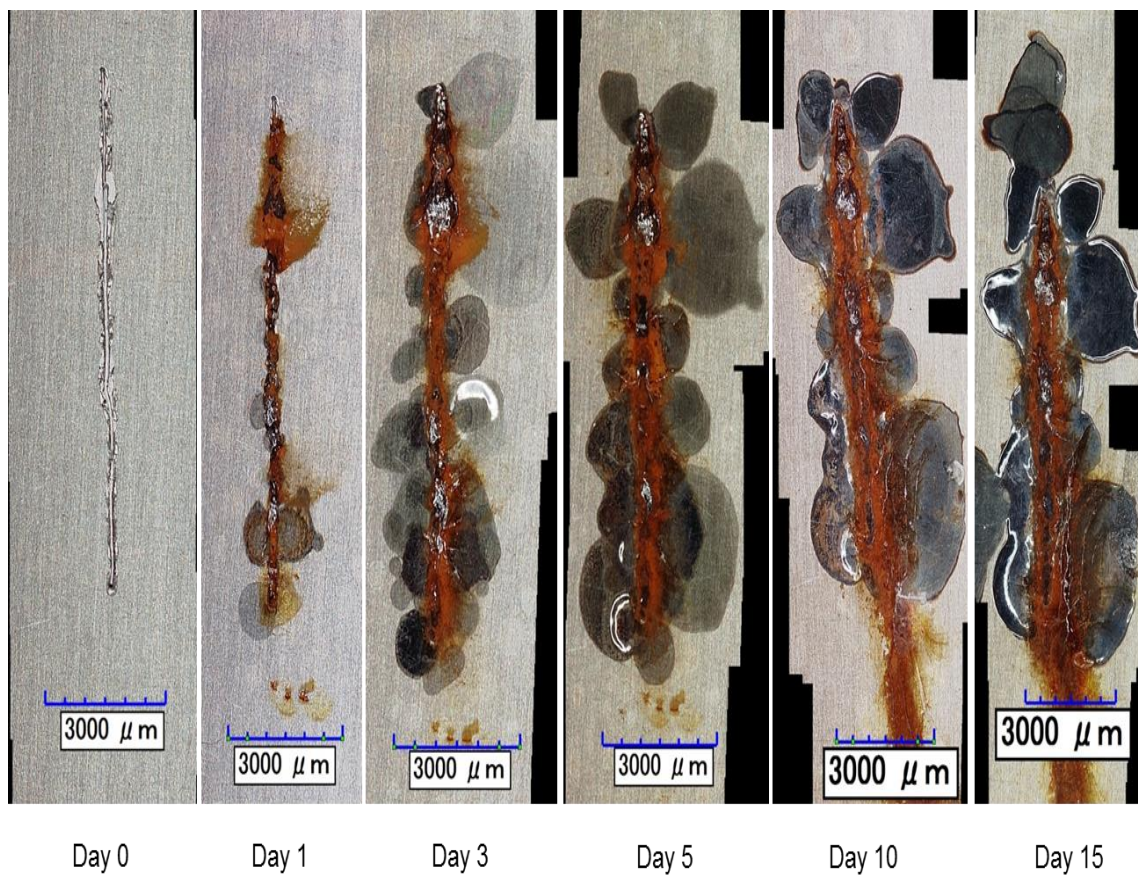


Figure 3.18 Optical images of the progression of scribe creep for Eponol coated steel exposed in FFA5 for 15 days. Conditions: T(-), %RH(-), Cl(+), UV(-), Cycling(+).

For FFA6, scribe creep progresses quickly and fairly uniformly from the scribe (Figure 3.19). Some damage can be seen away from the scribe creep front by day 5 and increases though days 10 and 15.

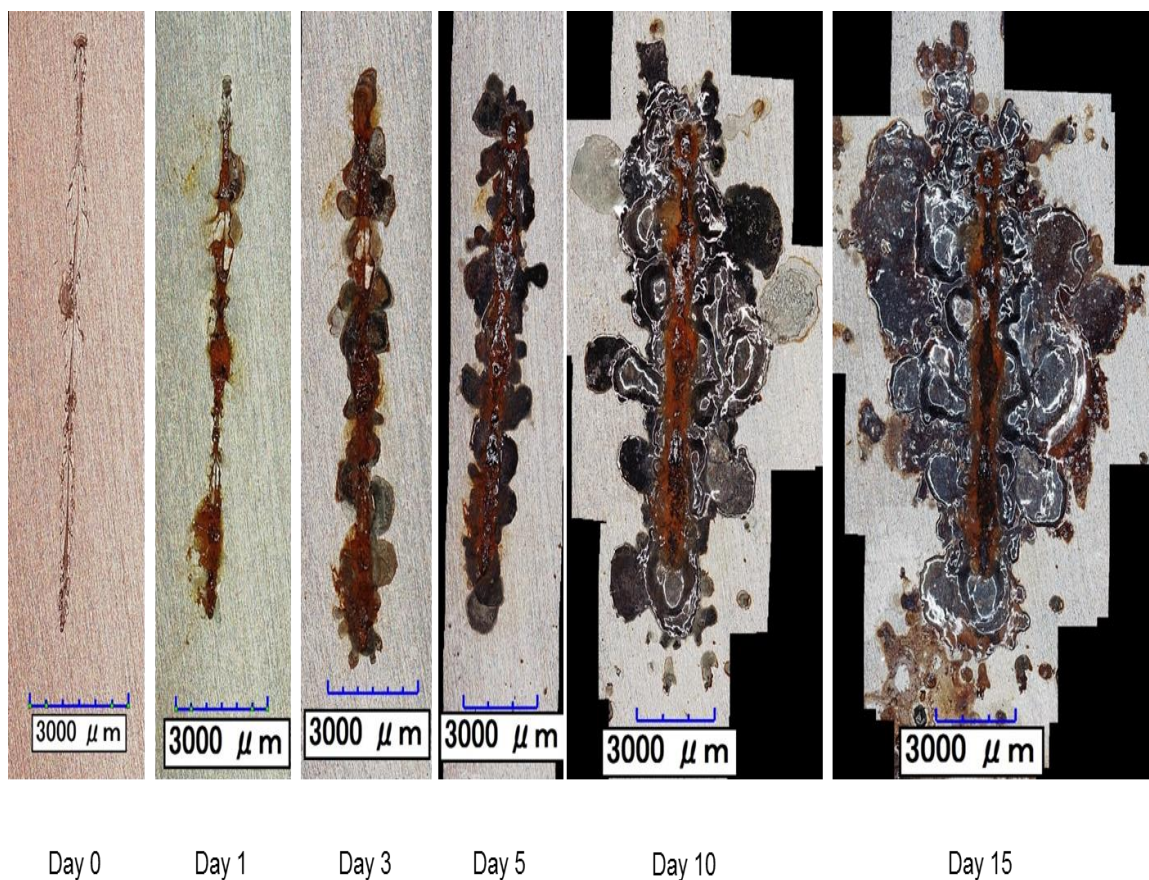


Figure 3.19 Optical images of the progression of scribe creep for Eponol coated steel exposed in FFA6 for 15 days. Conditions: T(+), %RH(+), Cl(-), UV(+), Cycling(+).

Images of the Eponol coated sample that was covered with a film of Au-Pd are shown in Figure 3.20 after exposure in FFA6. Day 3a is the sample before it was covered with an Au-Pd film and Day 3b is after it was covered. The Au-Pd film was intended to provide a barrier to oxygen ingress ahead of the scribe creep front. Only corrosion reactions and reactants from the scribe can enable corrosion product formulation. The scribe was masked so that it was not covered with the metal film. After 3 days of exposure to FFA6, scribe creep has begun to move outward from the scribe. At day 10, scribe creep has continued outward from the scribe.

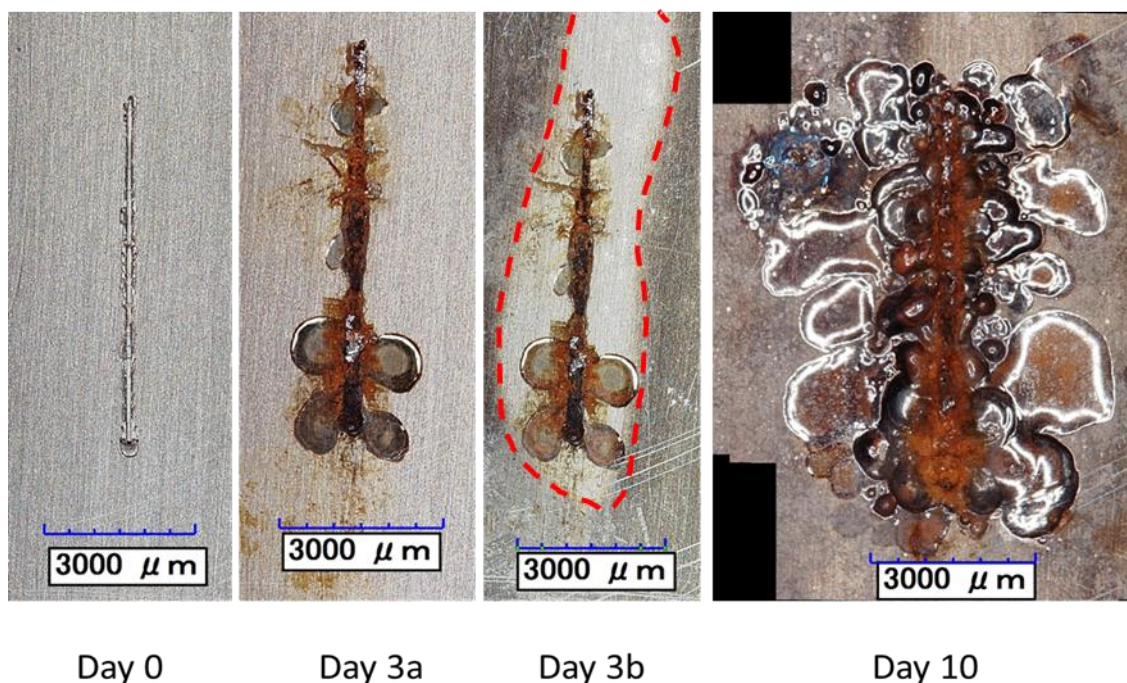


Figure 3.20 Images of Eponol coated 1018 steel. Sample was exposed for three days in FFA6 and then coated with gold-palladium over the polymer coating. Dotted lines mark where the boundary where the Au-Pd film was deposited.

The visual images of the scribe allowed for scribe creep rate to be quantified and compared across exposures. Multiple samples were run in FFA5 and FFA6 for replication purposes. These replicates are shown in Figure 3.21 and indicate the level of reproducibility for replicate experiments. Figure 3.22 shows the scribe creep lengths for all samples exposed in FFA tests. The multiple samples for FFA5 and FFA6 have been averaged to give one general line for each exposure. Figure 3.22 shows that FFA1, FFA2, FFA3 and FFA5 have similar trends for scribe creep length. FFA4 and FFA6 are noticeably different from the other exposures, but are similar to each other. The metal cover test sample that was exposed for 10 days in FFA6 has a similar scribe creep length to other samples exposed in FFA6

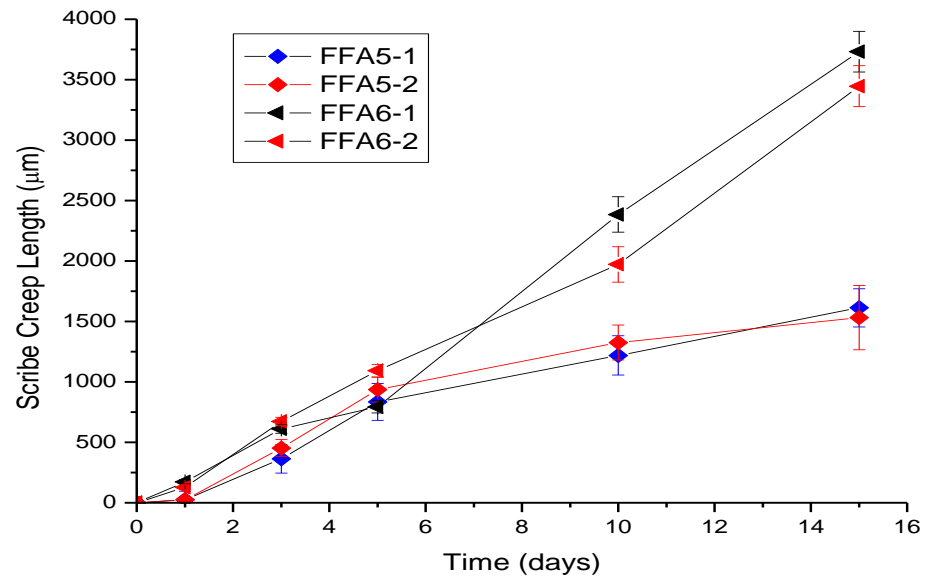


Figure 3.21 Graph of scribe creep for coated 1018 steel replicate samples exposed in FFA5 and FFA6. Error bars show standard error.

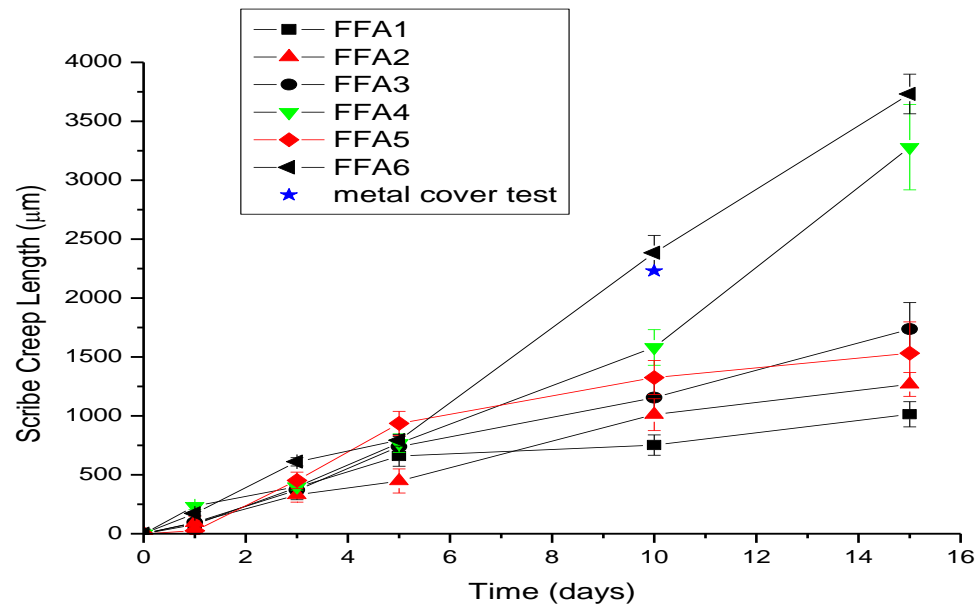


Figure 3.22 Graph of average scribe creep length versus time for 1018 steel samples exposed in FFA environments. The metal test was under FFA6 exposure conditions. Error bars show standard error.

Higher level visual inspection was also done by taking 3D optical images of the scribe at specific locations, extracting the profile data and observing the change over time. Figure 3.23 and 3.21 show the 3D images and line profiles for FFA1. It can be seen from visual inspection that corrosion product fills in the scribe and moves outward from the scribe, wedging underneath the coating. Figure 3.25 and 3.26 show 3D images and line profiles for FFA2. FFA2 behaves similarly to FFA1 with corrosion product filling up the scribe and wedging underneath the coating. 3D images and line profiles for FFA3 are shown in Figure 3.27 and 3.28. For FFA3, the scribe does not fill with corrosion product until day ten and discoloration can be seen spreading under the coating in the 3D images. Figure 3.29 and Figure 3.30 show the 3D images and line profiles for FFA4. The scribe fills quickly with corrosion product and wedges underneath the coating. For FFA5, Figure 3.31 and 3.32

show the 3D images and line profiles. The scribe fills with corrosion product and wedging occurs slowly underneath the coating. Figure 3.33 and 3.34 show the 3D images and line profiles for FFA6. The scribe quickly fills with corrosion product and pushes out underneath the coating.

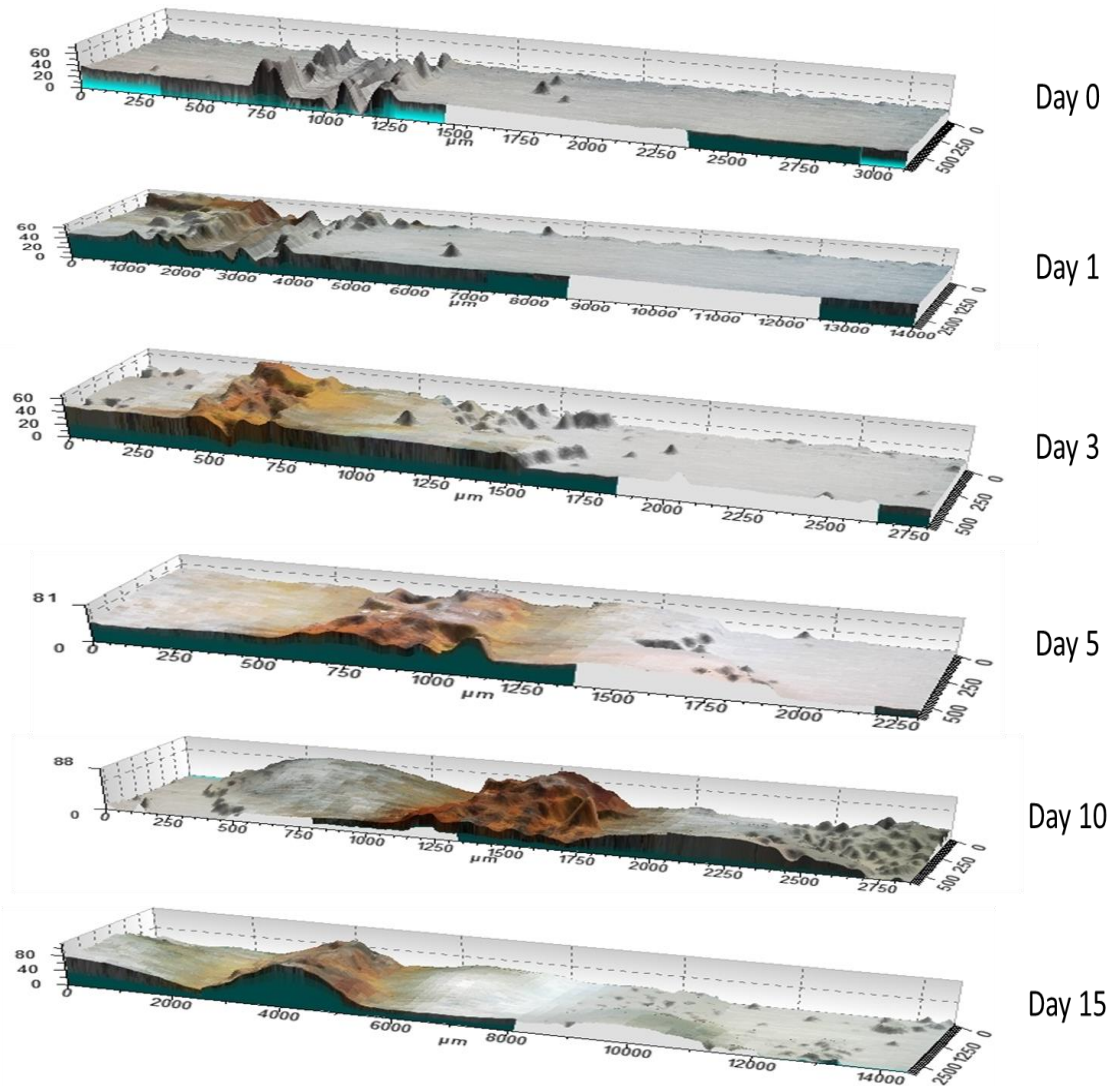


Figure 3.23 3D images of the scribe on epoxy resin coated 1018 steel exposed in FFA1 for 15 weeks. The units of the images are micrometers.

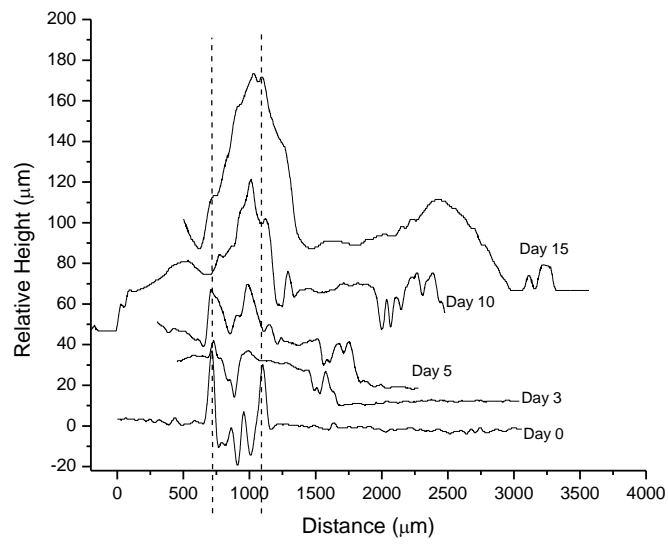


Figure 3.24 Selected line profiles for Eponol coated steel exposed at FFA1 Vertical offset for data from each day reported is 20 μm. Dashed lines indicate original scribe location.

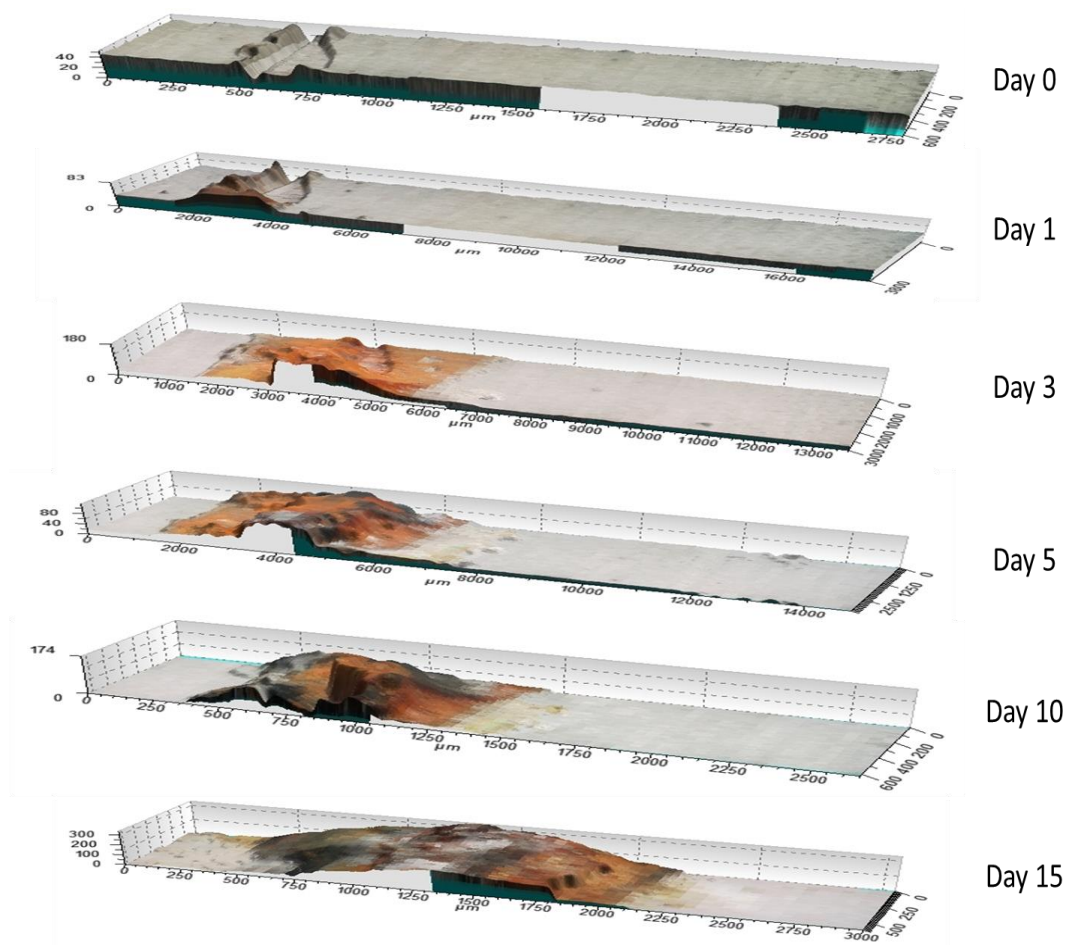


Figure 3.25 3D images of the scribe on epoxy resin coated 1018 steel exposed in FFA2 for 15 weeks. The units of the images are micrometers.

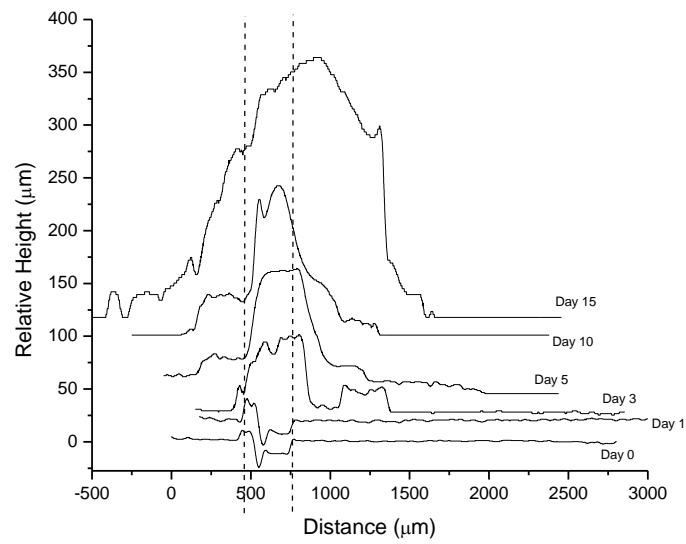


Figure 3.26 Selected line profiles for Eponol coated steel exposed at FFA2 Vertical offset for data from each day reported is 30 μm. Dashed lines indicate original scribe location.

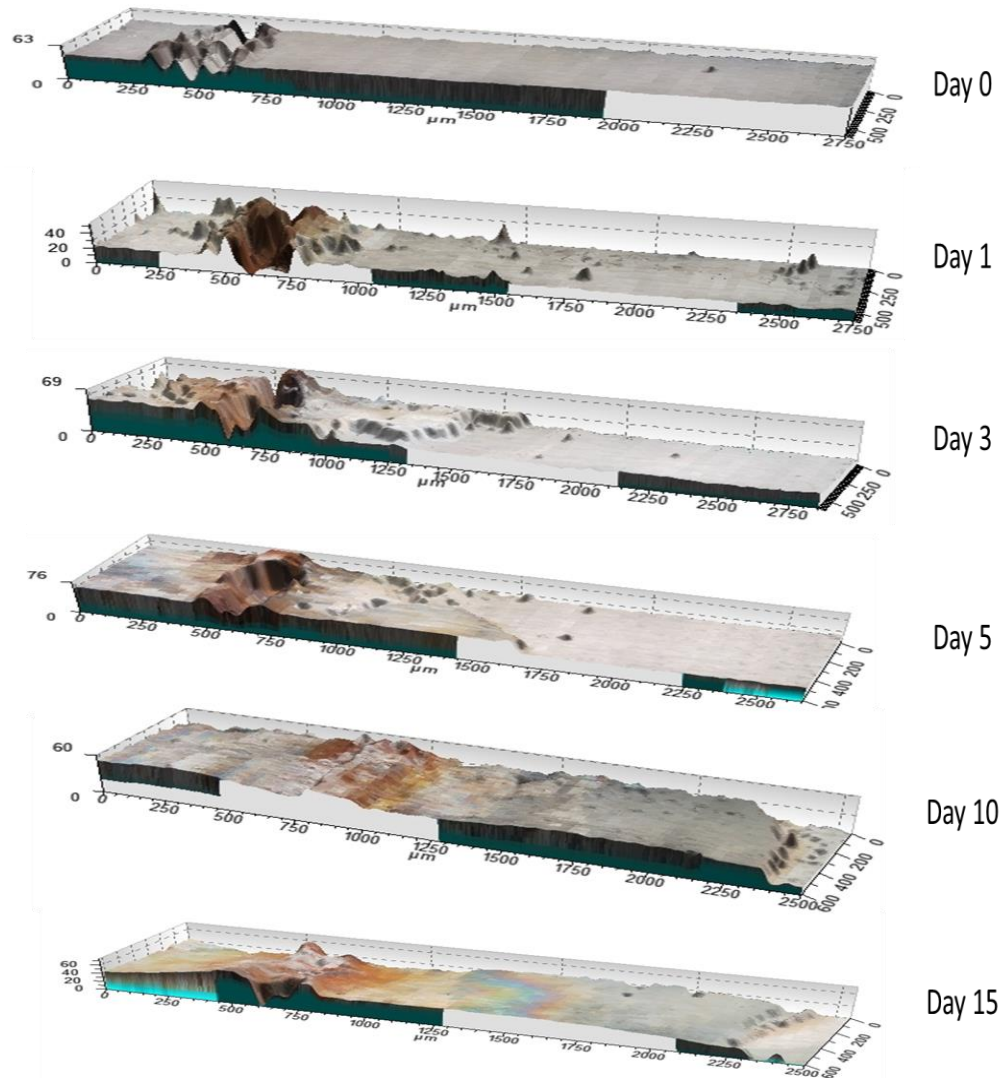


Figure 3.27 3D images of the scribe on epoxy resin coated 1018 steel exposed in FFA3 for 15 weeks. The units of the images are micrometers.

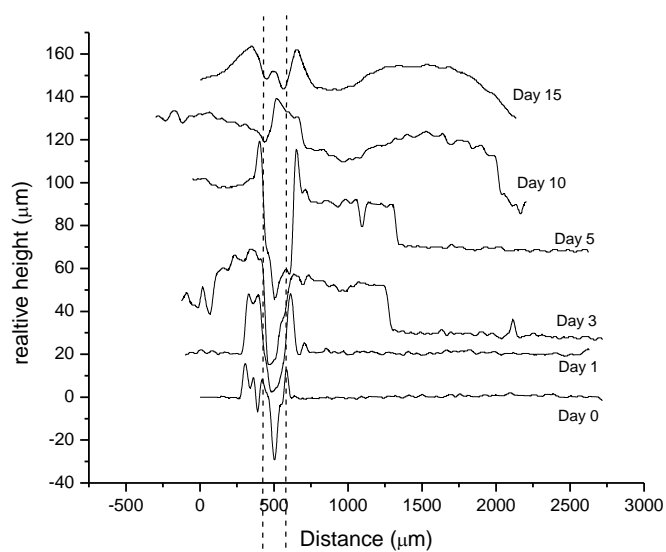


Figure 3.28 Selected line profiles for Eponol coated steel exposed at FFA3 Vertical offset for data from each day reported is 20 μm . Dashed lines indicate original scribe location.

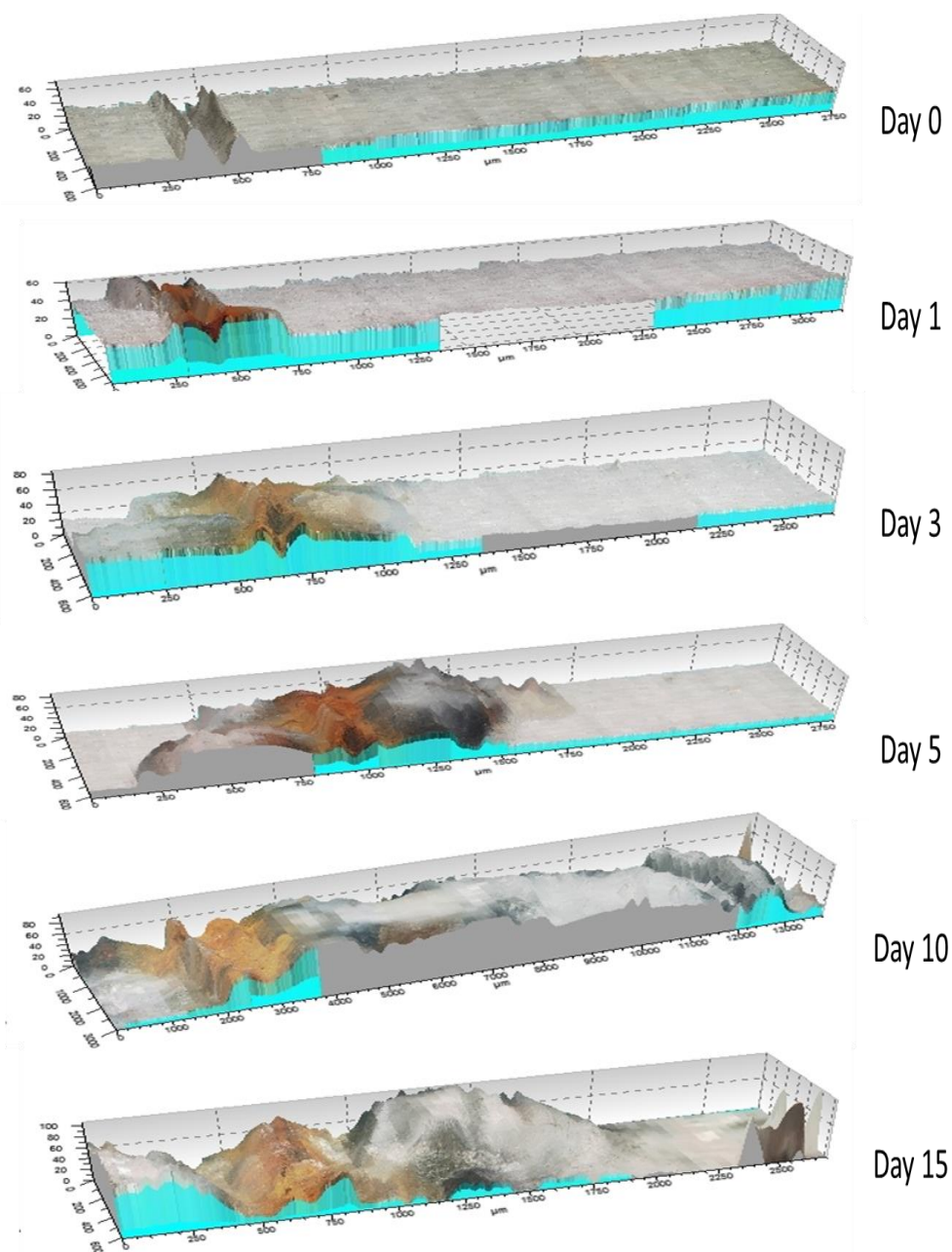


Figure 3.29 3D images of the scribe on epoxy resin coated 1018 steel exposed in FFA4 for 15 weeks. The units of the images are micrometers.

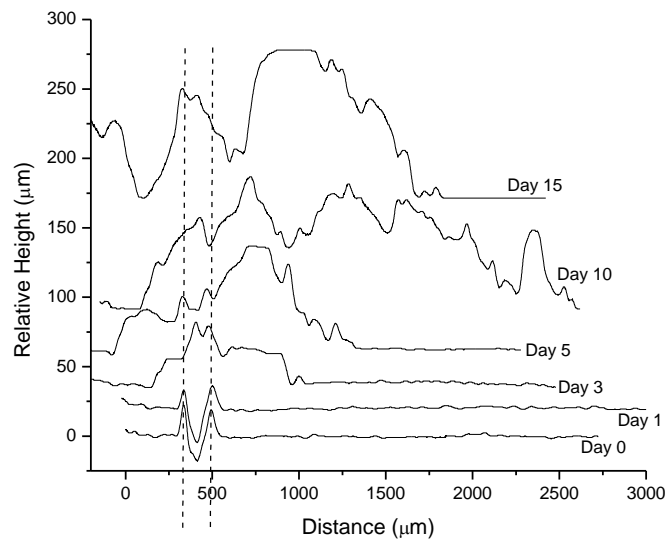


Figure 3.30 Selected line profiles for Eponol coated steel exposed at FFA4 Vertical offset for data from each day reported is 25 μm. Dashed lines indicate original scribe location.

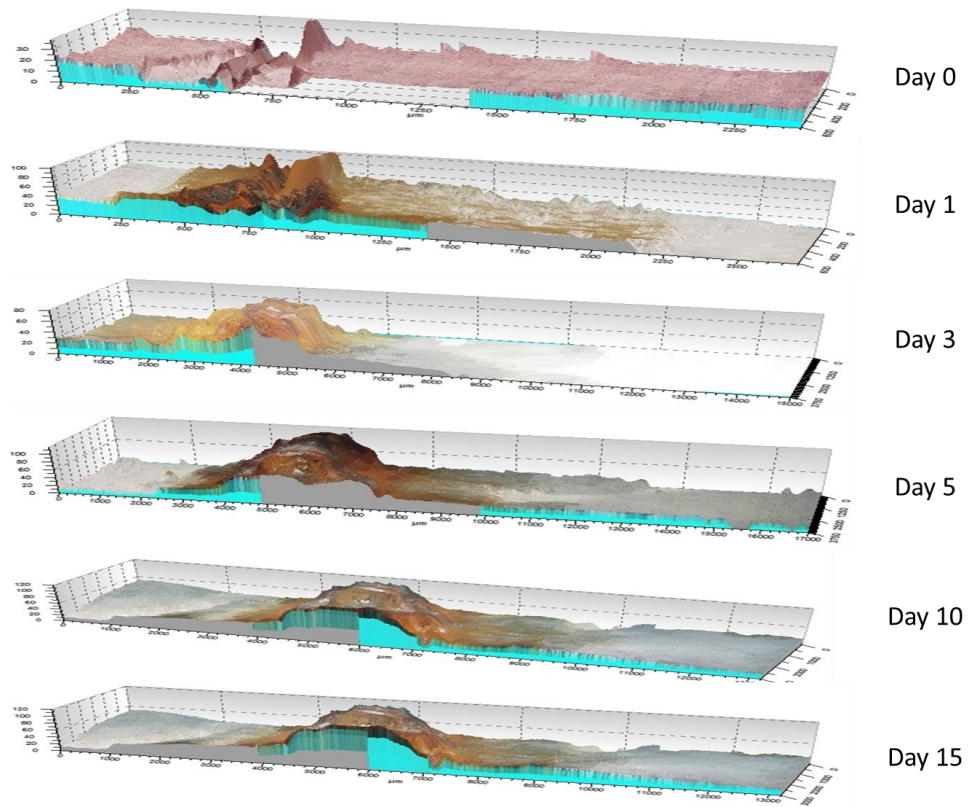


Figure 3.31 3D images of the scribe on epoxy resin coated 1018 steel exposed in FFA5 for 15 weeks. The units of the images are micrometers.

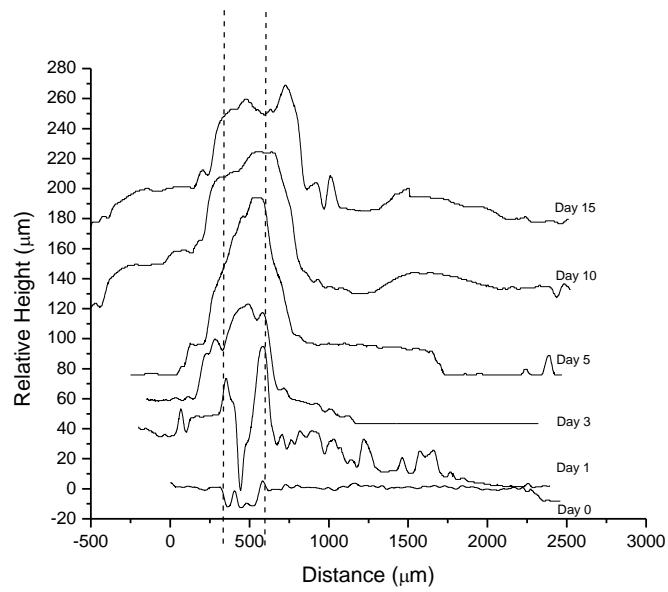


Figure 3.32 Selected line profiles for Eponol coated steel exposed at FFA5 Vertical offset for data from each day reported is 20 μm. Dashed lines indicate original scribe location.

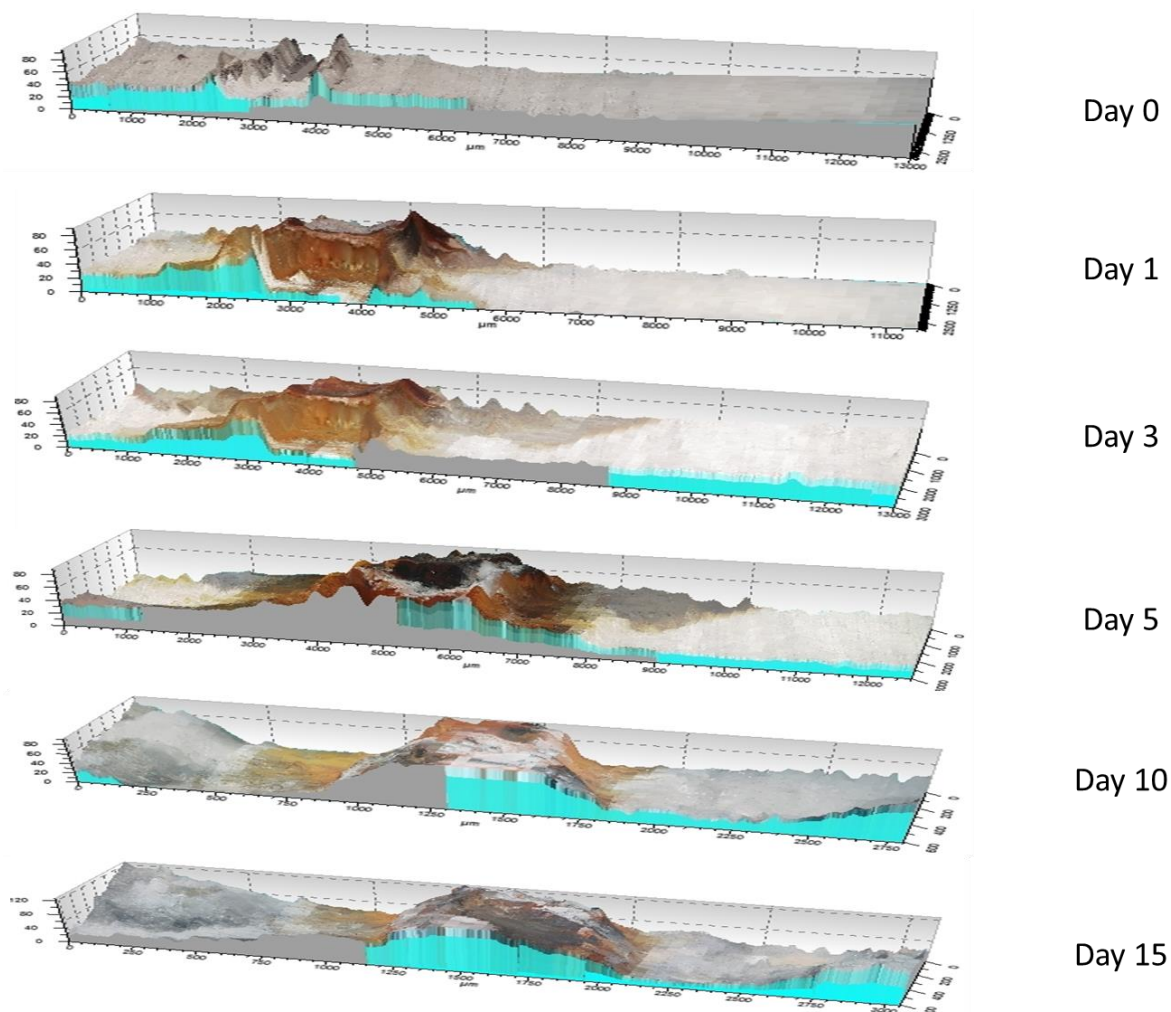


Figure 3.33 3D images of the scribe on epoxy resin coated 1018 steel exposed in FFA6 for 15 weeks. The units of the images are micrometers.

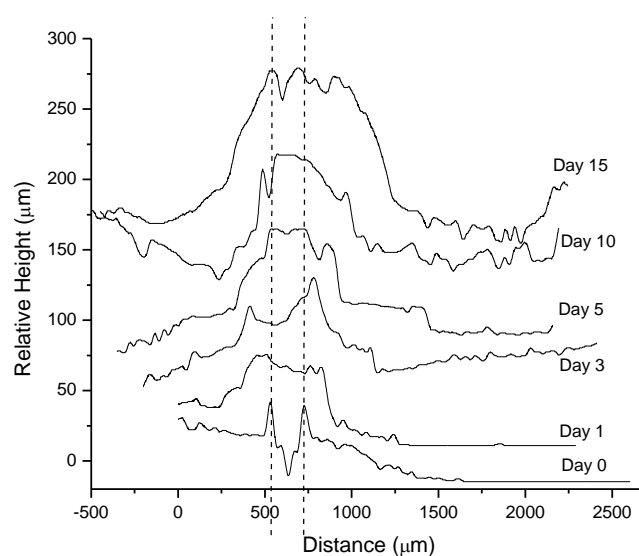


Figure 3.34 Selected line profiles for Eponol coated steel exposed at FFA6 Vertical offset for data from each day reported is 20 μm . Dashed lines indicate original scribe location.

3.5.4 Coating Analysis

3.5.4.1 Electrochemical Impedance Spectroscopy

As discussed in Chapter 2, it is well known that EIS can be used to characterize the sum of the Ohmic (solution) resistance (R_s), the coating resistance (R_{coat}), and the polarization resistance (R_p) for typical organic coated specimens.²³⁻²⁶ The complex impedance ($|Z|$) is taken at 0.01 Hz for a typical coating with an interrogation area of 1 cm^2 . Therefore $Z_{0.01}$ can be used to monitor the coating resistance during exposure and provides a measure of $R_{\text{coat}} + R_p + R_s$. The EIS data in the bode format can be seen in Figure 3.35 to Figure 3.40. The data have been normalized for all exposures. Graphs showing replicates from FFA5 and FFA6 are shown in Figure 3.41. These results show reasonable replication at short and long times

(1 day and 15 days). At intermediate times (5 days and 10 days), the results show scatter. Normalized EIS data for the near location are shown in Figure 3.42 and far location in Figure 3.43. Again, the results show good reproducibility at short and long times, but at intermediate times there is relatively greater scatter. The interpretation of the scatter is that coating breakdown with a large drop in $Z_{0.01}$ cannot occur at the same exact time and location in each replicate exposure. thus the scatter increases in these intermediate times. Coating properties near to the scribe decrease quickly for all exposures except FFA3 (Figure 3.42 and 3.44). Coating properties near to the scribe decrease most quickly for FFA4 and FFA6 (Figure 3.42 and 3.44). Far from the scribe, the coating properties decrease most quickly for FFA1, FFA2 and FFA6, but less quickly for FFA3, FFA4 and FFA5.

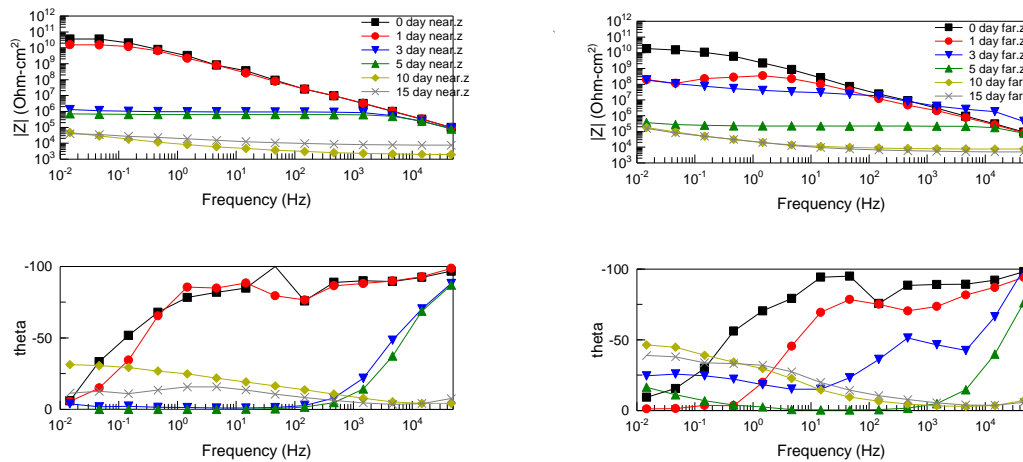


Figure 3.35 Raw EIS data from samples exposed in FFA1. Data were taken from the near location (left) and far location (right).

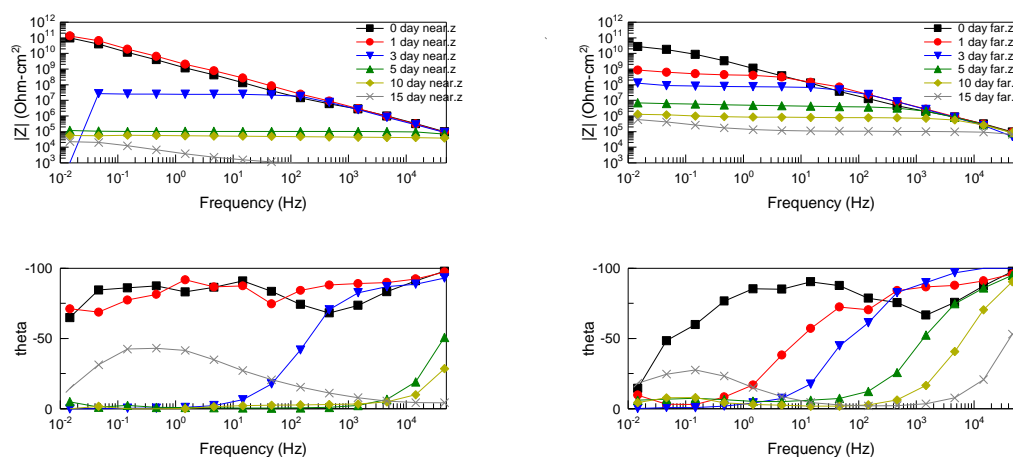


Figure 3.36 Raw EIS data from samples exposed in FFA2. Data were taken from the near location (left) and far location (right).

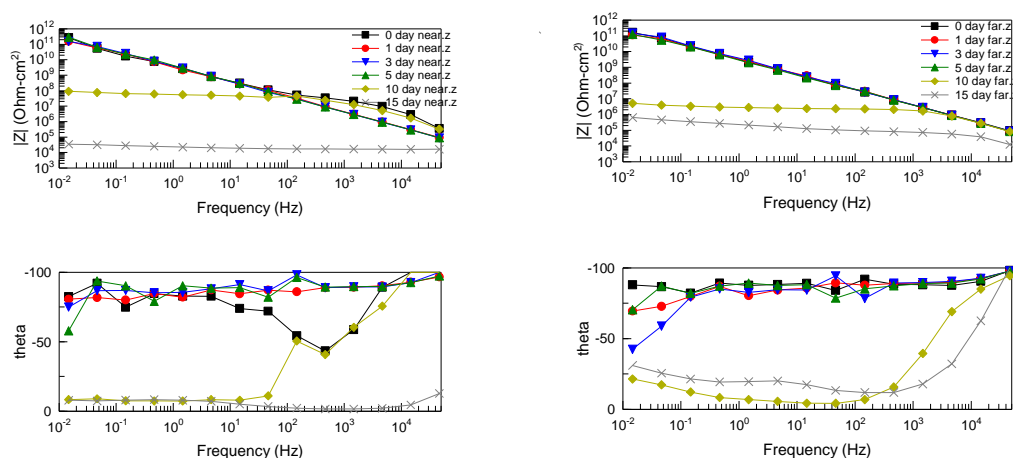


Figure 3.37 Raw EIS data from samples exposed in FFA3. Data were taken from the near location (left) and far location (right).

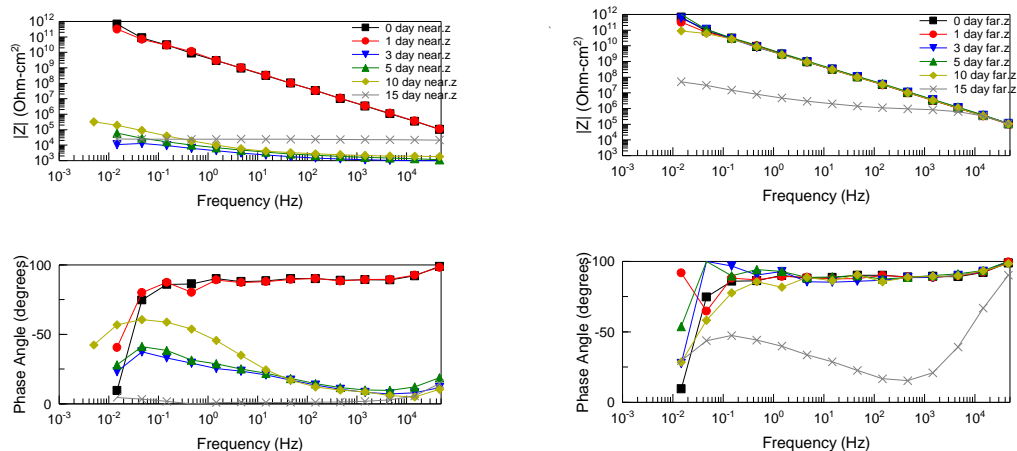


Figure 3.38 Raw EIS data from samples exposed in FFA4. Data were taken from the near location (left) and far location (right).

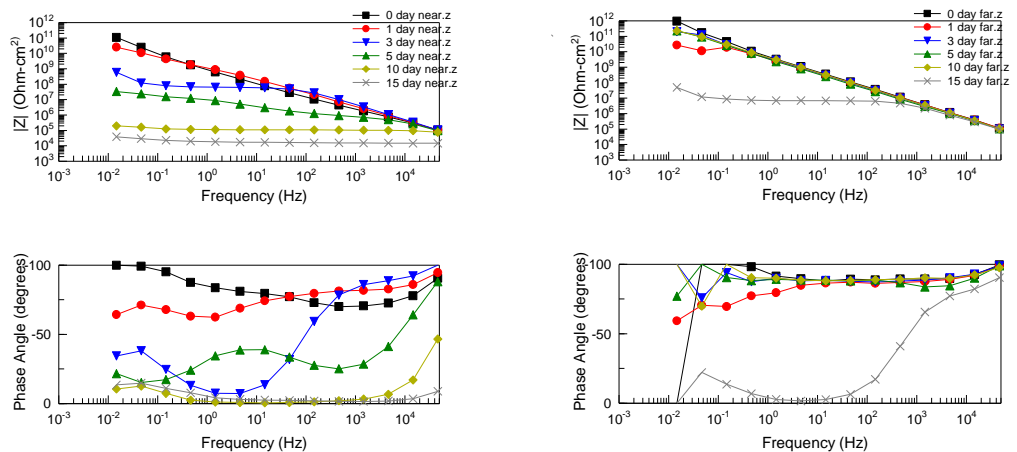


Figure 3.39 Raw EIS data from samples exposed in FFA5. Data were taken from the near location (left) and far location (right).

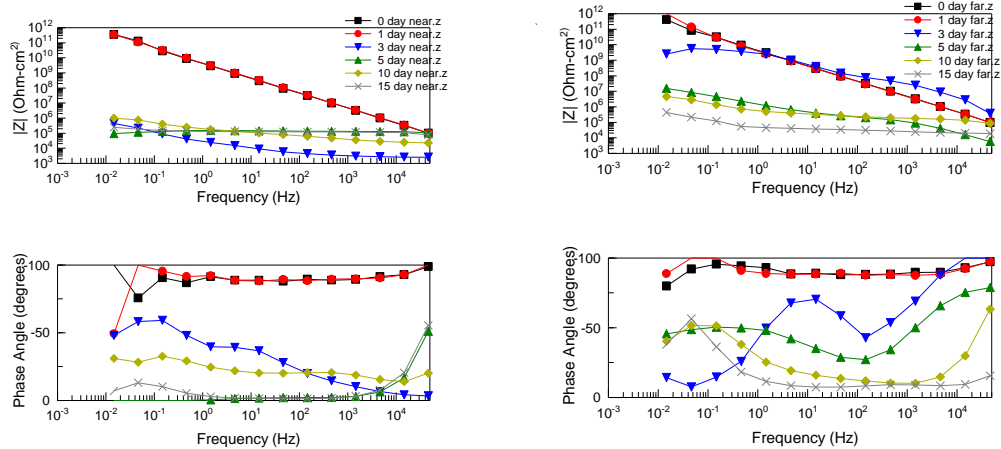


Figure 3.40 Raw EIS data from samples exposed in FFA6. Data were taken from the near location (left) and far location (right).

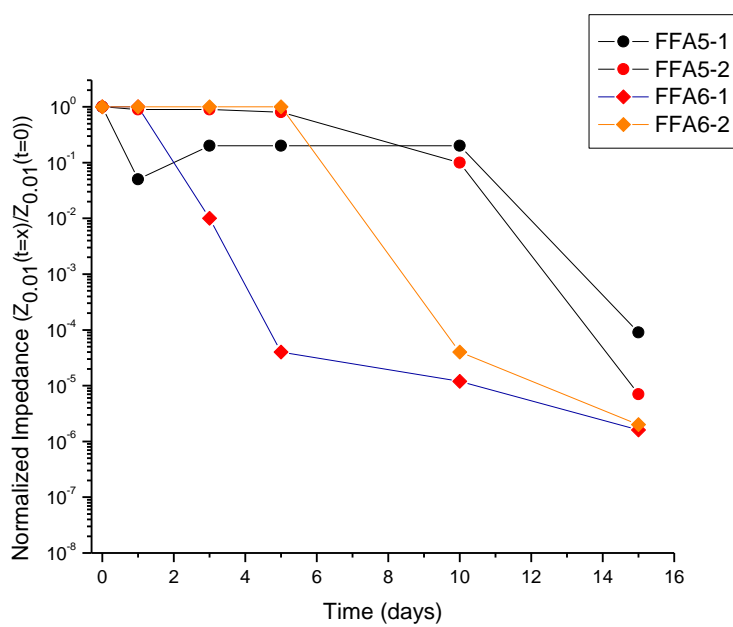
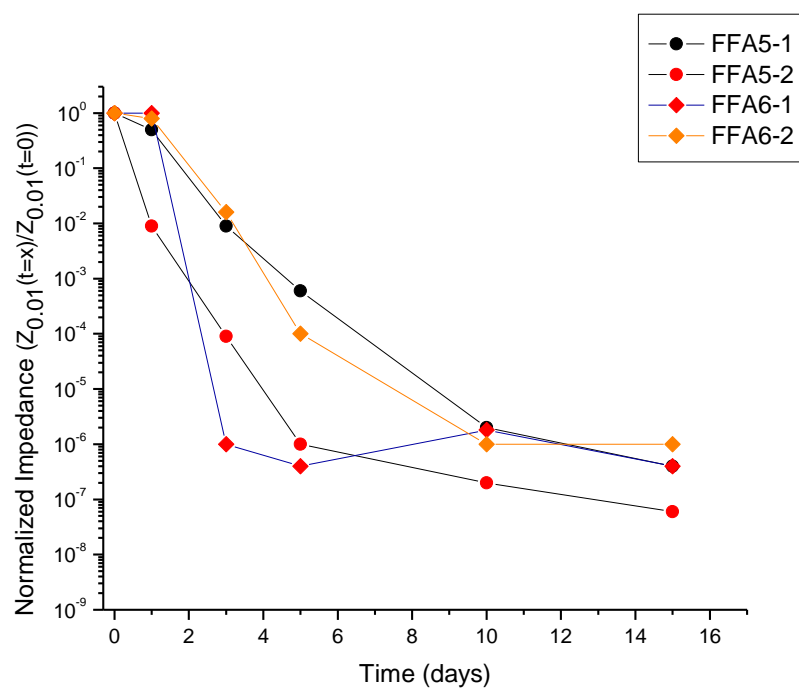


Figure 3.41 Normalized EIS data from samples exposed in FFA5 and FFA6. Data were taken from the near location (top) and far location (bottom).

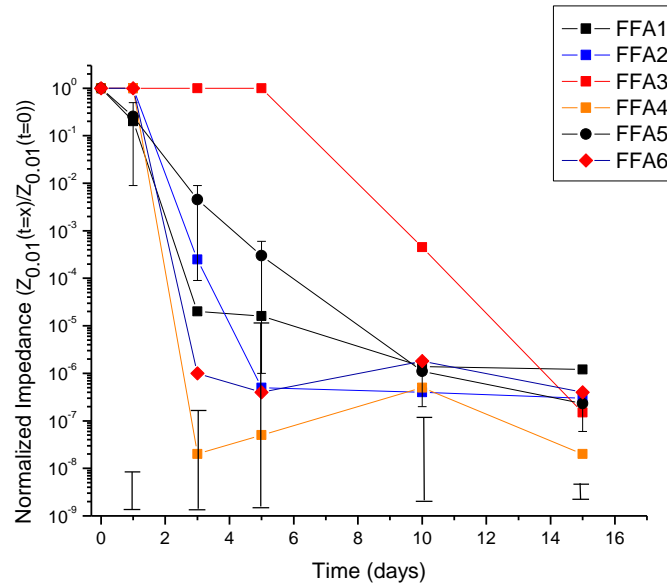


Figure 3.42 Normalized low frequency impedance values over time for Eponol coated steel samples exposed in FFAs. EIS readings taken at near location. Normalization was $|Z_{0.01}|(\text{day})/|Z_{0.01}|(\text{initial})$ for all days of the test. The error bars below the graph shows the error bars for four identical samples exposed to ASTM B-117 at each time indicated.

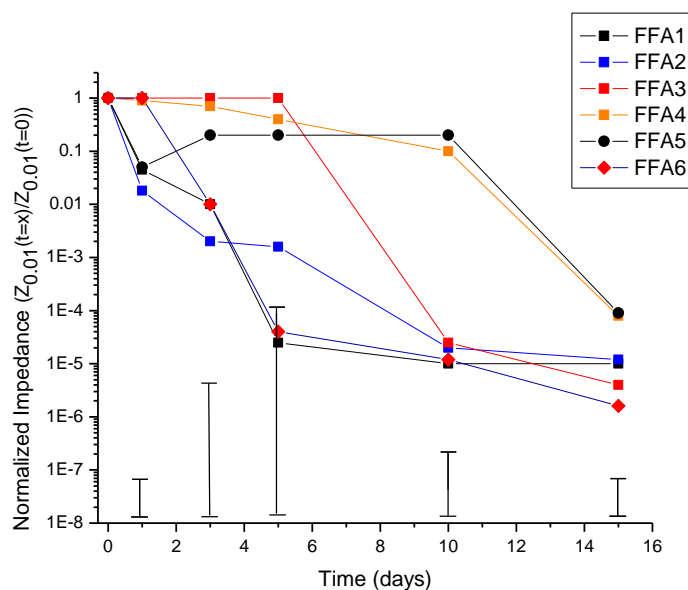


Figure 3.43 Normalized low frequency impedance values over time for Eponol coated steel samples exposed in FFAs. EIS readings taken at far location. Normalization was $|Z_{0.01}(\text{day})|/|Z_{0.01}(\text{initial})|$ for all days of the test. The error bars below the graph shows the error bars for four identical samples exposed to ASTM B-117 for each time indicated.

3.5.4.2 Fourier Transform Infrared Spectroscopy

FTIR was performed on 30 μm thick Eponol coatings on polypropylene substrates exposed to the FFAs (Figure 3.44 and 3.45). The polypropylene substrate on which the Eponol coating is cast is inert, and thus has no effect on the degradation of the coating. This isolates the effects of the environment from the effects of underpaint corrosion on degradation of the coating. Degradation of the coating was observed by comparing the results of an unexposed coating to exposed coatings. Figure 3.44 shows the full spectra for each FFA exposure. Figure 3.45 shows a section of the spectrum to show the differences between the exposures. The decrease in intensity of the 2963 and 2920 cm^{-1} peaks show degradation of

CH, CH₂, and CH₃ bonds in the coating.²⁷⁻³¹ The appearance and increase of a peak at 1717 cm⁻¹ is caused by the formation of carbonyls and aldehydes which are products of degradation of the aliphatic carbon bonds in the coating.²⁷⁻³¹ The broadening of the peak at 3362 cm⁻¹ and the appearance of a shoulder at 1609 cm⁻¹ indicate an increase in OH bonds due to an increase in water molecules in the coating.²⁷⁻³¹ Figure 3.45 shows an increase in the 1717 cm⁻¹ peak for FFA1, FFA2 and FFA6 compared to FFA3, FFA4 and FFA5.

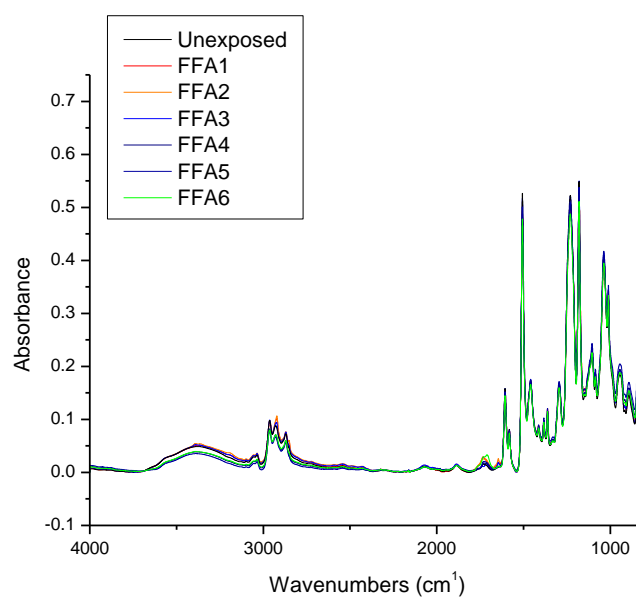


Figure 3.44 FTIR spectra of Eponol films exposed FFAs.

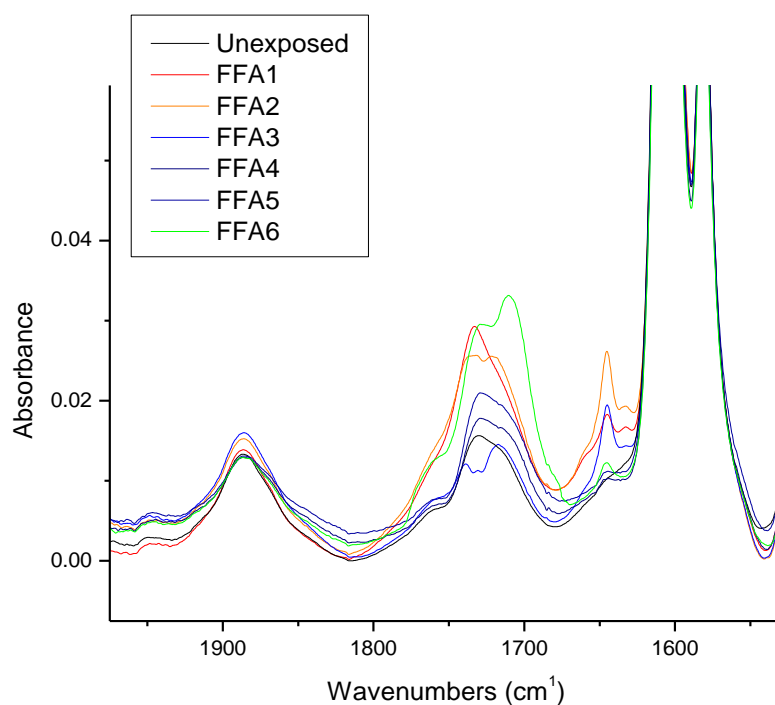


Figure 3.45 FTIR spectra of Eponol films exposed in FFAs. The graph has been rescaled to show the changes at the 1717 cm^{-1} peak.

3.5.4.3 Cathodic Polarization

Cathodic polarization results for Eponol coated steel exposed in all FFA exposures are given in Figure 3.46. The rate of ORR on steel under the coating is assessed. As the coating properties, as measured with EIS at $Z_{0.01}$, decrease, the cathodic current density associated with the ORR increases. This is a measure of the ability of the ORR to occur beneath the partially degraded coating. The low frequency impedance ($Z_{0.01}$) drops and cathodic current increases more quickly for FFA1, FFA2 and FFA6 (which have high UV) than for the other exposures.

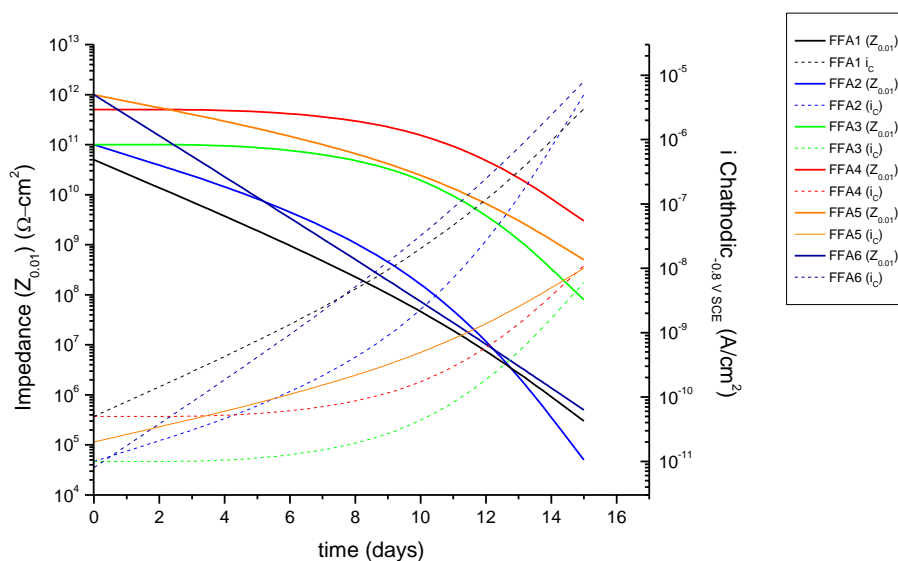


Figure 3.46 Graph of low frequency impedance ($Z_{0.01}$) and cathodic current density measured at -0.8 V vs. SCE over time for all FFA exposures.

3.6 Discussion

3.6.1 Corrosion Product Analysis

γ -FeOOH was detected for all exposures (Table 3.10). This would be expected because γ -FeOOH is commonly seen in atmospheric exposures of steel and in LALTs that include cycling.³²⁻³⁴ β -FeOOH was detected for FFA1, 2, 3 and 5 exposures (Table 3.10). As shown in Table 3.10, β -FeOOH was only detected on samples exposed at KSC and not in any of the standard LALTs. β -FeOOH is usually found on steel in marine atmospheric environments.^{32,}
³³ It is unclear at this time why β -FeOOH was detected on every FFA environment except for FFA4 and FFA6 which have the highest levels of temperature and cycling. Additionally, γ -FeOOH was the only species detected on FFA4 and FFA6. Again, the reasons behind this

are not clear at this time. FFA2 was the only exposure where Fe_2O_3 was detected. FFA2 is also the most benign of the FFA environments, with low temperature, cycling, and %RH.

It should be noted that due to the limitations of XRD (cannot detect amorphous corrosion products) and Raman (penetration depth of roughly 400 nm) discussed at the beginning of this section, there could be corrosion products that were not detected. The table of corrosion products found in Table 3.10 is by no means meant to be an exhaustive list of all corrosion products that might have formed.

3.6.2 Correlation of Mass Loss and Scribe Creep

The measurement of mass loss rates is a well-established practice for determining the severity of environments for atmospheric corrosion.^{1, 35} However, the measurement of the rate of scribe creep of organic coated steel has not been used similarly. In order to understand the relationship between scribe creep rates and environmental severity, the data for each were plotted. A positive correlation and similar rank order between mass loss and scribe creep after a given time were found for all FFA exposures (Figure 3.49 and Figure 3.50). Experimental conditions that caused the most mass loss also caused the most scribe creep on steel (Figure 3.49). These findings are consistent with the scribe creep and mass loss correlation found for the LALTs and field sites studied in Chapter 2 (Figure 2.57). Exposures that had low levels of temperature and cycling also showed the lowest mass loss (Figure 3.49). Exposures with either high levels of temperature or cycling (but not both) showed more mass loss than did exposures with low temperature and low cycling (Figure 3.49). Exposures with high levels of temperature and cycling also had the highest mass loss

values (Figure 3.49). This is consistent with previous work that shows that temperature and cycling are both factors that drive mass loss of bare steel.^{1, 2, 36-39} The positive correlation between scribe creep and mass loss is understood from the effects of temperature and cycling. Temperature increases the rate of corrosion reactions and also increases the corrosivity of other ESFs (see Section 1.4.1 for a detailed discussion on the effects of temperature on corrosion of steel).^{36, 40}

Corrosion rates of bare steel have been shown to increase during drying.³⁸ Stratmann et al showed that the corrosion is temporarily increased significantly, sometimes as much as an order of magnitude until the surface dries, when iron with 1 g/m² of SO₂ on the surface dries as the %RH drops from 95% to 40% (Figure 3.47).³⁸ Additionally, the equilibrium concentration of NaCl in droplets is known to increase as relative humidity decreases (Figure 3.48).⁴¹ This concentrates the NaCl solution and increases the corrosion rate of iron.^{1, 3} An increase in wet/dry cycles would therefore lead to an increase in mass loss of bare steel. Another important effect is that of cycling on the oxide. Cycling has been found to reduce the adhesion increase delamination of polymer coatings on mild steel.⁴² The corrosion product precipitates during the dry cycle, resulting voluminous corrosion product at the scribe creep front (Table 3.11).⁴² This corrosion product wedge exerts a mechanical stress on the coating increasing the delamination at the scribe creep front (see Section 1.4.7 for a more detailed discussion on the effects of wet/dry cycling on the corrosion of bare and coated steel).^{42, 43}

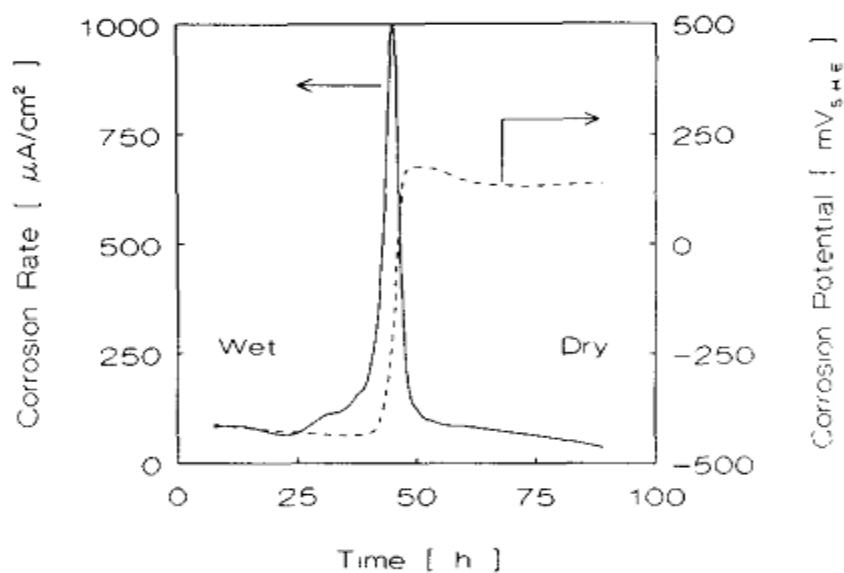


Figure 3.47 Plot of corrosion rate and corrosion potential over time for iron with 1 g/m^2 of SO_2 on the surface as the relative humidity drops from 95% to 40%. The solid line shows the corrosion rate and the dashed line shows the corrosion potential.³⁸

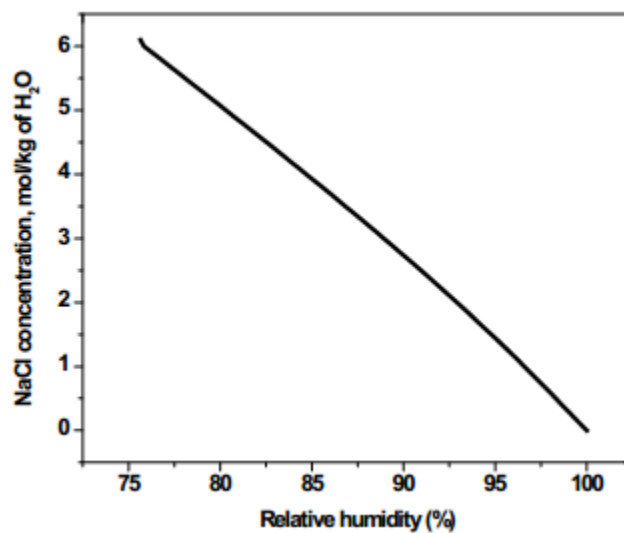


Figure 3.48 Thermodynamic equilibrium concentration of various saltwater solutions relative to the relative humidity in equilibrium at 25°C . Calculated by OLI.⁴¹

From Figure 3.49 and Figure 3.50 it can be seen that the ratio of scribe creep to mass loss is larger for FFA4 and FFA6 than for the other exposures. The values of the ratios are given in FFA4 and FFA6 show much higher ratios than do the other exposures. FFA4 and FFA6 are also the only exposures to have high levels of both temperature and cycling. Scribe creep length increases to a greater extent for FFA4 and FFA6 compared to the other exposures. With regards to mass loss, it would appear an increase in temperature or cycling produces a specific increase in mass loss (Figure 3.5). If both temperature and cycling are increased, the overall increase in mass loss appears to be an addition of the specific increase caused singly by temperature and cycling alone. For scribe creep, the same reasoning appears to hold until both temperature and cycling are increased. When both increase, the increase in scribe creep length appears to be greater than just the sum of the specific increases caused by temperature and cycling (Figure 3.22).

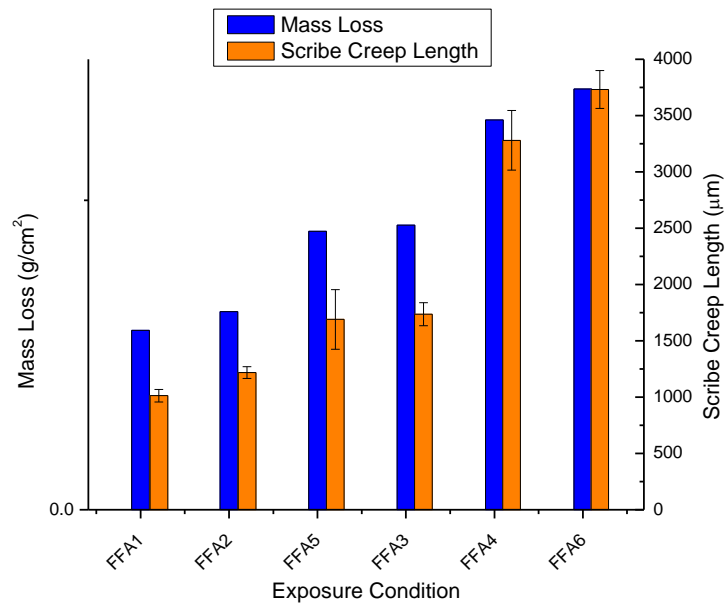


Figure 3.49 Bar chart showing the correlation between mass loss and scribe creep for all FFA exposures at 15 days. Error bars are standard error.

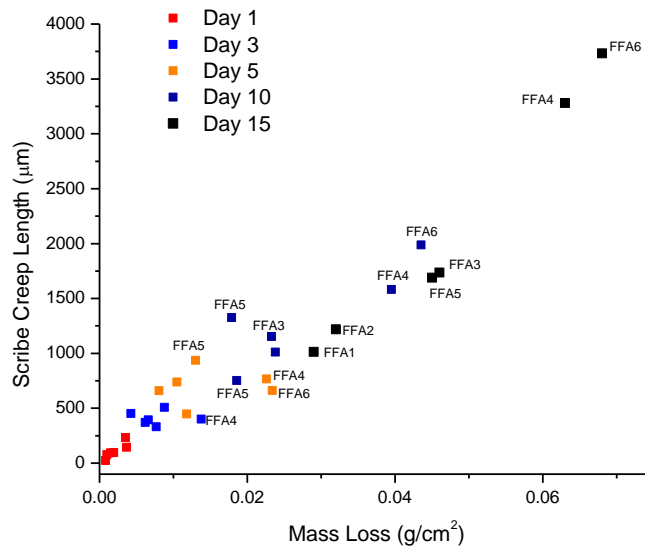


Figure 3.50 Correlation chart of mass loss with scribe creep for all FFA exposures.

Table 3.11 Calculated Piling-Bedworth ratios for iron oxides. The PB ratio is the ratio of the molar volume of the oxide to the molar volume of the metal.

Oxide	Piling-Bedworth Ratio
Hematite (Fe_2O_3)	2.1
Magnetite (Fe_3O_4)	2.14
Goethite ($\alpha\text{-FeOOH}$)	3.3
Akaganeite ($\beta\text{-FeOOH}$)	3.53
Lepidrocite ($\gamma\text{-FeOOH}$)	3.25

3.6.3 Scribe Creep Behavior of Coated Steel

Inspection of the visual images of scribe creep for all FFA exposures (Figure 3.14 through 3.19) shows that scribe creep appears to progress in a similar manner. The scribe creep front appears filiform-like, but lobes of scribe creep are bigger than would be seen in true filiform corrosion.^{2, 44} The lobes grow perpendicularly from the scribe, but also spread parallel to the scribe and join creating a broad scribe creep front. The lobes appear largest for FFA3, 4, 5 and 6 (Figure 3.14 - 3.19). Line profile data and 3D images for all exposures show that corrosion product fills the scribe and then begins to wedge underneath the scribe (Figure 3.23 - 3.34). Figure 3.22 shows scribe creep lengths over time for all exposures. It can be seen that FFA4 and FFA6 have distinctly greater scribe creep compared with the other exposures. Again, FFA4 and FFA6 are the only exposures with high levels of both cycling and temperature.

3.6.4 Coating Degradation

From EIS data for FFA exposures from the near location (Figure 3.42), it can be seen that coating properties sensed by EIS degrade quickly for all exposures except for FFA3. FFA4

and FFA5, which experience the fastest rate of increase of scribe creep length, show the fastest degradation of coating properties sensed by EIS near to the scribe. It appears that the degradation of coating properties near to the scribe is related, at least in part, to rate at which scribe creep length increases over time. The coating barrier properties sensed by EIS are affected. It is not understood at this time why FFA3 would behave differently from the other exposures.

EIS data from the far location (Figure 3.43) shows that coating properties degrade most quickly for FFA1, FFA2 and FFA6. UV is at high level for all of these exposure experiments and not for any of the others. The coating properties sensed by EIS do decrease for samples exposed with low UV (FFA3, FFA4, and FFA5), but not as quickly as those exposed to high UV. FTIR results also show more damage to the polymer film in exposures with higher UV levels (Figure 3.45). It appears that the rate of decrease of coating properties far from the scribe is dependent on the amount of UV radiation exposure of the sample, with higher UV causing a faster decrease in coating properties.

FTIR results (Figure 3.44 and 3.45) show that the exposures with higher UV (FFA1, FFA2, and FFA6) show more coating damage as detected with FTIR. The difference between high and low levels of UV irradiation does not create large differences in the damage as detected with FTIR when compared with the ASTM G-85 Annex 5+UV and KSC field site discussed in Chapter 2 (Figure 2.54 and 2.55). However, the UV damage induced drop in $Z_{0.01}$ at positions far from the scribe does not govern scribe creep.

3.6.5 Anodic Wedging vs. Cathodic Delamination as a Main Factor in Scribe Creep

Section 2.6.6 in Chapter 2 discussed the roles that anodic and cathodic corrosion mechanisms may play in scribe creep of polymer coated steel samples exposed to standard LALTs and field sites. It was hypothesized that scribe creep in exposures with no cycling such as ASTM B-117 and full immersion was driven more by cathodic reactions while exposures with cycling such as the ASTM G-85 Annex 5 (12 wet/dry cycles per day) were driven more by anodic reactions. Work by Frankel et al. also showed that wet/dry cycling increased de-adhesion of a polymer coating on steel due to lifting of the coating caused by oxide wedging.⁴² Images and line profiles of FFA3 (Figure 3.16 and 3.28) show that scribe creep proceeds underneath the coating with comparatively little physical lifting of the coating. FFA3 is the most similar to ASTM B-117 of any of the FFAs in terms ESF levels. Images and line profiles for FFA4 (Figure 3.17 and Figure 3.30) and FFA6 (Figure 3.19 and 3.34) show lifting of the coating up to the scribe creep front. FFA4 and FFA6 have high levels of temperature and cycling. FFA4 and FFA6 also have the greatest scribe creep length which supports the idea of anodic wedging playing a greater role in scribe creep as cycling increases.

The metal cover test samples showed no retardation effect on scribe creep of having a metal film put over the top of the polymer coating (Figure 3.20). The metal film would have reduced, if not stopped, oxygen diffusion through the polymer coating ahead of the scribe creep front as a result of the metal overlayer. Oxygen diffusion through the coating is an important part of cathodic delamination and scribe creep driven by cathodic delamination

ahead of the scribe creep front,^{2,3} yet the reduction of oxygen diffusion at that site did not reduce the scribe creep length (Figure 3.22).

Cathodic polarization tests of Eponol coated samples with an intact coating showed that when the coating properties, as measured with EIS, remained high, the cathodic current was low (Figure 3.46). This would suggest that the intact coating is a good barrier and does not support cathodic reactions occurring on the metal surface below the coating at positions ahead of the scribe creep front. However, as the coating properties degrade, the coating is a less effective barrier allowing cathodic reactions to be supported on the metal surface beneath the coating (Figure 3.46). Therefore, evidence for scribe creep dominated by cathodic delamination is not strong. Even assuming that scribe creep is entirely controlled by the local coupled cathodic delamination at the scribe creep front, it would appear that oxide wedging brought about by cycling “assists” the cathodic delamination by underpaint corrosion and physical lifting of the coating.

3.6.6 The Need for Statistical Analysis

Analysis of the samples exposed in the various FFA environments has shown distinct differences between FFA4 and FFA6 compared with the other environments. The scribe creep lengths at 15 days for FFA1, FFA2, FFA3 and FFA5 are similar. However, this does not hold true for FFA4 and FFA6 which show higher scribe creep lengths at day 15. Statistical analysis of the FFA data is needed to better understand the effects of the ESFs on the scribe creep of this coated steel system. Constructing an empirical statistical model of scribe creep and mass loss that can accurately reproduce the mass loss and scribe creep lengths for FFA

exposures would give valuable insight into the effects of ESFs on the coated steel system. Specifically, such a model could show the relative strength of each ESF on mass loss and scribe creep, as well as indicate and interactions between ESFs. This need and issue is addressed in Chapter 4.

3.7 **Conclusions**

It was shown that, in general, FFA exposures created similar corrosion products to those seen in the field (KSC) and in cyclic LALTs (ASTM G-85 A5). Additionally, line profiles for all exposures showed that corrosion products filled the scribe and wedged outward underneath the coating as exposure time increased.

Scribe creep and mass loss were found to have a positive correlation in custom LALTs that was similar to what was seen in Chapter 2 during comparison of standard LALT to field. Temperature and cycling increased scribe creep and mass loss. The effects of ESFs on mass loss are fairly straightforward, but the effects of ESFs on scribe creep are more complex. The scribe creep lengths at 15 days for all exposures with low temperature and low cycling or high temperature or high cycling, but not both, were similar. The scribe creep lengths at 15 days for exposures with both high temperature and high cycling were much higher. This was rationalized though the effects of temperature and cycling on steel corrosion rate, corrosion product accumulation, and, in turn, scribe creep. An essential part of this argument was evidence that supports a strong role for corrosion product wedging in scribe creep.

Characterization of the coating showed that the rate of decrease in coating barrier properties depended on the exposure of the sample to UV radiation. Coating barrier properties decreased more quickly for samples exposed to higher levels of UV radiation. This was supported by FTIR results. However, UV was not found to be a governing factor in scribe creep at intentional defects.

3.8 **References**

1. C. Leygraf and T.E. Graedel, *Atmospheric Corrosion*. 2000: John Wiley & Sons.
2. E. McCafferty, *Introduction to Corrosion Science*. 2010, New York: Springer.
3. D.A. Jones, *Principles and Prevention of Corrosion*. 2nd ed. 1996: Prentice Hall.
4. I.S. Cole, *Mechanism of Atmospheric Corrosion in Tropical Environments*, in *Marine Corrosion in Tropical Environments, ASTM STP 1399*, S.W. Dean and J.B. Bushman, Editors. 2000, American Society for Testing and Materials: West Conshohocken, PA.
5. S. Feliu, M. Morcillo and B. Chico, *Effect of distance from sea on atmospheric corrosion rate*. *Corrosion*, 1999. **55**(9): p. 883-891.
6. I. Matsushima, *Carbon Steel—Atmospheric Corrosion*, in *Uhlig's Corrosion Handbook*. 2011, John Wiley & Sons, Inc. p. 579-588.
7. L. Veleva and R.D. Kane, *Atmospheric Corrosion in Corrosion: Fundamentals, Testing and Protection*, Various, Editor. 2003, ASM International: Materials Park, OH. p. 196-209.
8. P. Schmuki and H. Böhni, *Illumination effects on the stability of the passive film on iron*. *Electrochimica Acta*, 1995. **40**(6): p. 775-783.
9. D.F. Heaney and D.D. Macdonald, *On the Photoinhibition of Passivity Breakdown on Iron in Chloride-Containing Solutions*. *Journal of the Electrochemical Society*, 1999. **146**(5): p. 1773-1776.

10. H.R. Riazi, I. Danaee and M. Peykari, *Influence of ultraviolet light irradiation on the corrosion behavior of carbon steel AISI 1015*. Metals and Materials International, 2013. **19**(2): p. 217-224.
11. T.D. Burleigh, C. Ruhe and J. Forsyth, *Photo-Corrosion of Different Metals during Long-Term Exposure to Ultraviolet Light*. Corrosion, 2003. **59**(9): p. 774-779.
12. ISO 9223:1992(F) *Corrosion of Metals and Alloys - Corrosivity of Atmospheres - Classification*. 1992, International Organization for Standardization.
13. G.E.P. Box, W.G. Hunter and J.S. Hunter, *Statistics for Experimenters*. 1976, New York: John Wiley and Sons.
14. 2014 [cited 2014 Jan. 27]; Available from: <http://www.miller-stephenson.com/products/?DepartmentId=54>.
15. F. Adar, *Depth Resolution of the Raman Microscope: Optical Limitations and Sample Characteristics*. Spectroscopy, 2010. **25**(3): p. 16-23.
16. ASTM Standard G 1 2003, "Standard Practice for Preparing, Cleaning and Evaluating Corrosion Test Specimens," ASTM International, West Conshohocken, PA, 2003, DOI: 10.1520/G0001-03R11, www.astm.org
17. ASTM Standard G140, 02, "Standard Test Method for Determining Atmospheric Chloride Deposition Rate by Wet Candle Method," ASTM International, West Conshohocken, PA, 2008, DOI: 10.1520/G0140-02R08, www.astm.org
18. A.A. Mikhailov, *Dose-Response Functions as Estimates of the Effect of Acid Precipitates on Materials*. Protection of Metals, 2001. **37**(4): p. 357-366.
19. J. Tidblad, V. Kucera, A. Mikhailov, J. Henriksen, K. Kreislova, T. Yates, B. Stöckle and M. Schreiner, *UN ECE ICP Materials: Dose-Response Functions on Dry and Wet Acid Deposition Effects After 8 Years of Exposure*. Water, Air, & Soil Pollution, 2001. **130**(1): p. 1457-1462.
20. R. Ihaka and R. Gentleman, *R: A Language for Data Analysis and Graphics*. 1996.
21. I.N. Tang and H.R. Munkelwitz, *Composition and temperature dependence of the deliquescence properties of hygroscopic aerosols*. Atmospheric Environment, Part A, 1993. **27A**(4).
22. Y. Wan, E. Neiser and R.G. Kelly, *Modification of ASTM Standard B117 Salt Spray Corrosion Test for Improved Correlation to Field Measurements*, in DoD Corrosion Conference. 2011: Palm Springs, Ca.
23. H.P. Hack and J.R. Scully, *Defect Area Determination of Organic Coated Steels in Seawater Using the Breakpoint Frequency Method*. Journal of the Electrochemical Society, 1991. **138**(1): p. 33-40.
24. J.R. Scully, *Electrochemical Tests*, in *Corrosion Tests and Standards: Application and Interpretation*, H.P. Hack, Editor. 2005, ASTM. p. 107-117.
25. J.N. Murray and H.P. Hack, *Long-Term Testing of Epoxy-Coated Steel in ASTM Seawater Using Electrochemical Impedance Spectroscopy*. Corrosion, 1991. **47**(6): p. 480-489.
26. J.N. Murray and H.P. Hack, *Testing Organic Architectural Coatings in ASTM Synthetic Seawater Immersion Conditions Using EIS*. Corrosion, 1992. **48**(8): p. 671-685.
27. P. Musto, G. Ragosta, M. Abbate and G. Scarinzi, *Photo-oxidation of high performance epoxy networks: Correlation between the molecular mechanisms of degradation and the viscoelastic and mechanical response*. Macromolecules, 2008. **41**(15): p. 5729-5743.
28. C. Konecki, *RE: UVa-Southern Miss ATR-FTIR 8-23-12.pptx*. 2012.

29. M. Diepens and P. Gijsman, *Photodegradation of bisphenol A polycarbonate*. Polymer Degradation and Stability, 2007. **92**(3): p. 397-406.
30. N. Nagai, H. Okumura, T. Imai and I. Nishiyama, *Depth profile analysis of the photochemical degradation of polycarbonate by infrared spectroscopy*. Polymer Degradation and Stability, 2003. **81**(3): p. 491-496.
31. A. Rivaton, B. Mailhot, J. Soulestin, H. Varghese and J.L. Gardette, *Comparison of the photochemical and thermal degradation of bisphenol-A polycarbonate and trimethylcyclohexane-polycarbonate*. Polymer Degradation and Stability, 2002. **75**(1): p. 17-33.
32. D. de la Fuente, I. Díaz, J. Simancas, B. Chico and M. Morcillo, *Long-term atmospheric corrosion of mild steel*. Corrosion Science, 2011. **53**(2): p. 604-617.
33. D.S. Dunn, M.B. Bogart, C.S. Brossia and G.A. Cragolino, *Corrosion of Iron Under Alternating Wet and Dry Conditions*. Corrosion, 2000. **56**(5): p. 470-481.
34. S. Nasrazadani and A. Raman, *Formation and Transformation of Magnetite (Fe₃O₄) on Steel Surfaces under Continuous and Cyclic Water Fog Testing*. Corrosion, 1993. **49**(4): p. 294-300.
35. M. Tullmin and P.R. Roberge, *Atmospheric Corrosion*, in *Uhlig's Corrosion Handbook*, R.W. Revie, Editor. 2000, John Wiley & Sons.
36. *Temperature Influence on Corrosion* [website] 2010 [cited 2014 May]; Available from: <http://events.nace.org/library/corrosion/Design/Temperature-effects.asp>.
37. M. Stratmann and H. Streckel, *On the atmospheric corrosion of metals which are covered with thin electrolyte layers—I. Verification of the experimental technique*. Corrosion Science, 1990. **30**(6-7): p. 681-696.
38. M. Stratmann and H. Streckel, *On the atmospheric corrosion of metals which are covered with thin electrolyte layers—II. Experimental results*. Corrosion Science, 1990. **30**(6-7): p. 697-714.
39. M. Stratmann, H. Streckel, K.T. Kim and S. Crockett, *On the atmospheric corrosion of metals which are covered with thin electrolyte layers-iii. the measurement of polarisation curves on metal surfaces which are covered by thin electrolyte layers*. Corrosion Science, 1990. **30**(6-7): p. 715-734.
40. P.J. Sereda, *Atmospheric factors affecting the corrosion of steel*. Industrial & Engineering Chemistry, 1960. **52**(2): p. 157-160.
41. M. Shedd, 2012, Modeling and Measurement of the Maximum Pit Size on Ferrous Alloys Exposed to Atmospheric Conditions. (Master's Thesis) University of Virginia, Charlottesville.
42. M. Kappes, G.S. Frankel and N. Sridhar, *Adhesion and adhesion degradation of a pressure sensitive tape on carbon steel*. Progress in Organic Coatings, 2010. **69**(1): p. 57-62.
43. R.A. Dickie, *Paint adhesion, corrosion protection, and interfacial chemistry*. Progress in Organic Coatings, 1994. **25**(1): p. 3-22.
44. D.E. Little, 2006, ROLE(S) OF PRETREATMENT, INHIBITORS, AND OTHER PROCESS STEPS THAT EFFECT SURFACE COMPOSITION ON THE UNDER-PAINT CORROSION OF AN Al-Cu-Mg ALLOY 2024-T3. University of Virginia, Charlottesville.

4 Chapter 4–Construction of an Empirical Scribe Creep Model as a Function of ESFs for Eponol Coated 1018 Steel

4.1 Summary of Chapter 4

In Chapter 3, Fractional Factorial Design of Experiment was employed to create an experimental matrix to examine the impact and relative importance of selected ESFs to mass loss and scribe creep of coated 1018 steel. From these experiments, temperature and cycling were identified as important ESFs that increase both mass loss and scribe creep. In this chapter, the data generated from the experiments run in Chapter 3 were analyzed so that empirical models for mass loss and scribe creep could be constructed. The scribe creep model is the first of its kind to relate ESFs to scribe creep on a painted and scribed surface. The models demonstrate the relative importance of individual and combined ESFs to mass loss and scribe creep, and also highlight possible second order interactions between ESFs.

The model constructed for mass loss showed very good agreement with experimental results not only for FFA exposures, but when compared to results for ASTM G-85 Annex 5 and KSC as well. Temperature was found to have the strongest effect on mass loss, followed by cycling, relative humidity, and chloride. UV was found to not have a statically significant effect on mass loss of bare steel. The model constructed for scribe creep also showed good agreement with experiment, but only for FFA1, 2, 3 and 5. In these FFAs, cycling was found to have the greatest effect followed by temperature. Other ESFs were found to have a lesser impact on the rate of scribe creep. Relative humidity had a much smaller effect than temperature or cycling. UV was also shown to have a negligible effect. Additionally, chloride

was shown to have no significantly different impacts on the rate of scribe creep when tested at either high or low levels.

The mass loss and scribe creep models constructed from the FFA data possess strong fidelity between predicted and observed results for most FFA exposures, as well as for scribe creep results from ASTM G-85 Annex 5 and KSC. However, FFA4 and FFA6 could not be modeled accurately. This is most likely due to an interaction between temperature and cycling that is only manifested when both ESFs are at the high levels established in the FFA experimental design. Additional investigation is needed to determine the existence and character of this possible second order interaction.

4.2 **Background**

4.2.1 **The Need for a Scribe Creep Model**

A number of expressions have been constructed to relate mass loss of bare steel to ESFs (Equation 1.1).¹⁻⁵ Measurements of the ESFs in field environments, such as those listed previously in Chapter 1, have been used to develop dose/response equations for mass loss for various uncoated metals.⁵ In these equations, mass loss has been used as a measure of severity of corrosive attack in the environment. One example for unsheltered weathering steel is given in Equation 4.1: where ML is mass loss in g/m², t is time in years, [SO₂] is the concentration of gas in µg/m³, RH is % relative humidity and T is temperature in degrees Celsius.⁵

$$\ln(ML) = 3.54 + 0.33 \ln(t) + 0.13 \ln[SO_2] + 0.020RH - 0.036 (T - 10) \quad 4.1$$

Table 1.3 in Chapter 2 lists many other empirical equations used to model mass loss in many different environments. Such equations are useful in predicting corrosion rates for various exposure locations.

Models have also been constructed for scribe creep on iron⁶ and aluminum.⁷ One model for aluminum is based on anodic and cathodic potentials and currents.⁸ It is a galvanic model of the reactions between the anodic region at the head of the filiform corrosion and the cathodic region at the tail.⁸ A time dependence of t^n , where $n < 1$, is shown to arise because the Ohmic resistance between the head and the tail grows with time.⁸ A model for iron showed a parabolic rate of delamination ($t^{1/2}$) that the authors attributed to underfilm cation migration control.⁶ The actual model had time as the only input and included a delamination rate constant term.⁶ A theoretical computer model for the delamination of polymer coatings on zinc in full immersion conditions simulated the porosity of the coating from the intact region through the scribe creep front, to the delaminated region.⁹ Other models for cathodic delamination of organic coatings have factors such as voltage and temperature, ion production rate, and applied and critical strain rates on the coating itself.⁹⁻¹¹ However, these models do not take into account key environmental factors such as wet/dry cycling, relative humidity or UV exposure. The author knows of no model to date that can relate ESFs to scribe creep on a painted and scribed surface. A model that could estimate scribe creep rate based on ESFs would be of great use to the corrosion community.

An empirical model for scribe creep could be useful in many ways. First, as shown in Chapter 2, ESFs have predictable and understood effects on the corrosion of bare steel. A model that could accurately predict scribe creep based on ESFs would give better insight into how the ESFs affect the coating/substrate system both singly and in combinations. Second, a model would give insight into the relative impact of ESFs on scribe creep and could indicate potential interactions between ESFs. Third, knowing how ESFs found in the field drive the degradation of the coating and substrate would aid in the construction of new, more accurate, LALTs that mimic field behavior to produce accelerated scribe creep and similar corrosion products. Lastly, a model of scribe creep for the epoxy resin coated steel system used in this study could serve as a stepping stone for creating models for real-world systems using commercial coating systems, pretreatments, and substrates. The construction of empirical models is often accomplished through statistical analysis.

4.2.2 Theory of Linear Regression

One of the most straight forward methods of creating a statistical model is linear regression. Linearity in this case has nothing to do with the straightness of the line that may be produced by the model; instead it refers to the parameters.¹² A model is linear if the parameters can be written in the form seen in Equation 4.2.¹² In this case, y is the response variable and x_n are the input variables.¹² The model does not need to be a straight line, as x_n can be raised to a power (x^3 for example).¹²

$$y = a + b_1x_1 + b_2x_2 + \cdots + b_nx_n \quad 4.2$$

4.2.2.1 Assumptions of Linear Regression

There are several assumptions of linear regression that must be met for the model to be valid. First, the model must behave linearly.¹³ This means that, as stated above, the model must be a linear combination of variables, i.e., y can be predicted by a series of input variables that are summed together. In general, any model equation that can be written in the form given in Equation 4.2 is considered linear.¹² Linearity can be tested using a plot of residual error, the difference between the observed and predicted value of y , versus predicted values of y .^{12, 13} The residual error, often called residuals, should be symmetrically distributed around 0.^{12, 13} A bowed or other non-symmetric pattern indicates that the data are nonlinearly related. Figure 4.1 shows two example graphs of linear and nonlinearly related data.

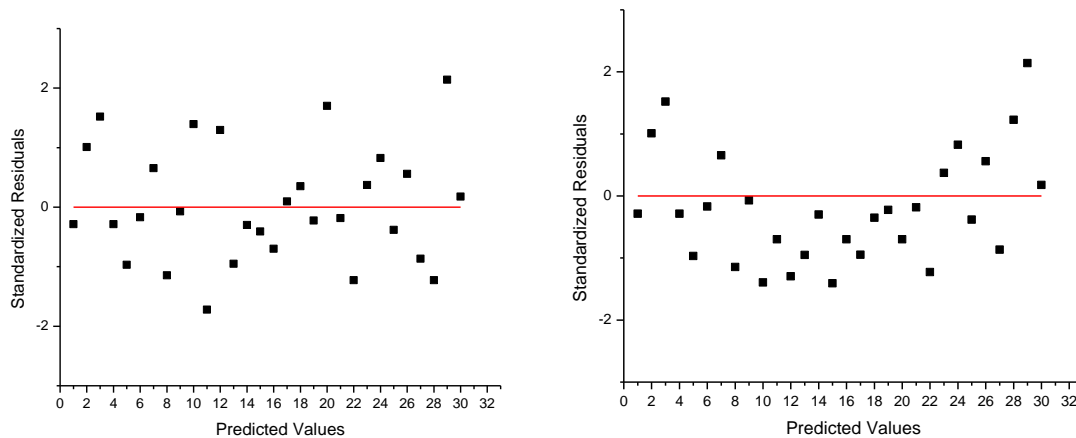


Figure 4.1 Example graphs of residual error versus predicted values to test for linearity. The left graph shows data that is linear. The right graph shows data that has a nonlinear relationship.

The second assumption is that the error of the response variable is independent.^{12, 13} This means that the value of the error of y_n is not dependent on the value of the error of y_{n-1} .^{12, 13} In other words, the error of one observation of y should not depend on the error of a previous observation of y . To test for independence of the errors, an autocorrelation plot is used.¹² The autocorrelation plot shows the degree to which each residual correlates with the residual before it (the first value has nothing before it to be correlated to so it is correlated with itself. Therefore the first value is always 1). If the error of the response variable is independent, then correlation values should fall within 95% confidence intervals shown in the plots. The time between observations is known as the lag and is the x axis for autocorrelation plots. In other words, lag=1 is the correlation between observations that are one time period apart (e.g. observation 1 and 2, observation 2 and 3, etc.). Lag 2 is observations that are two time periods apart, (observation 1 and 3, observation 2 and 4, etc.) and so on. Lag is the number of time periods between the variables that are being analyzed for correlation. Figure 4.2 shows example autocorrelation plots. The top plot shows correlated data while the bottom plot shows uncorrelated data.

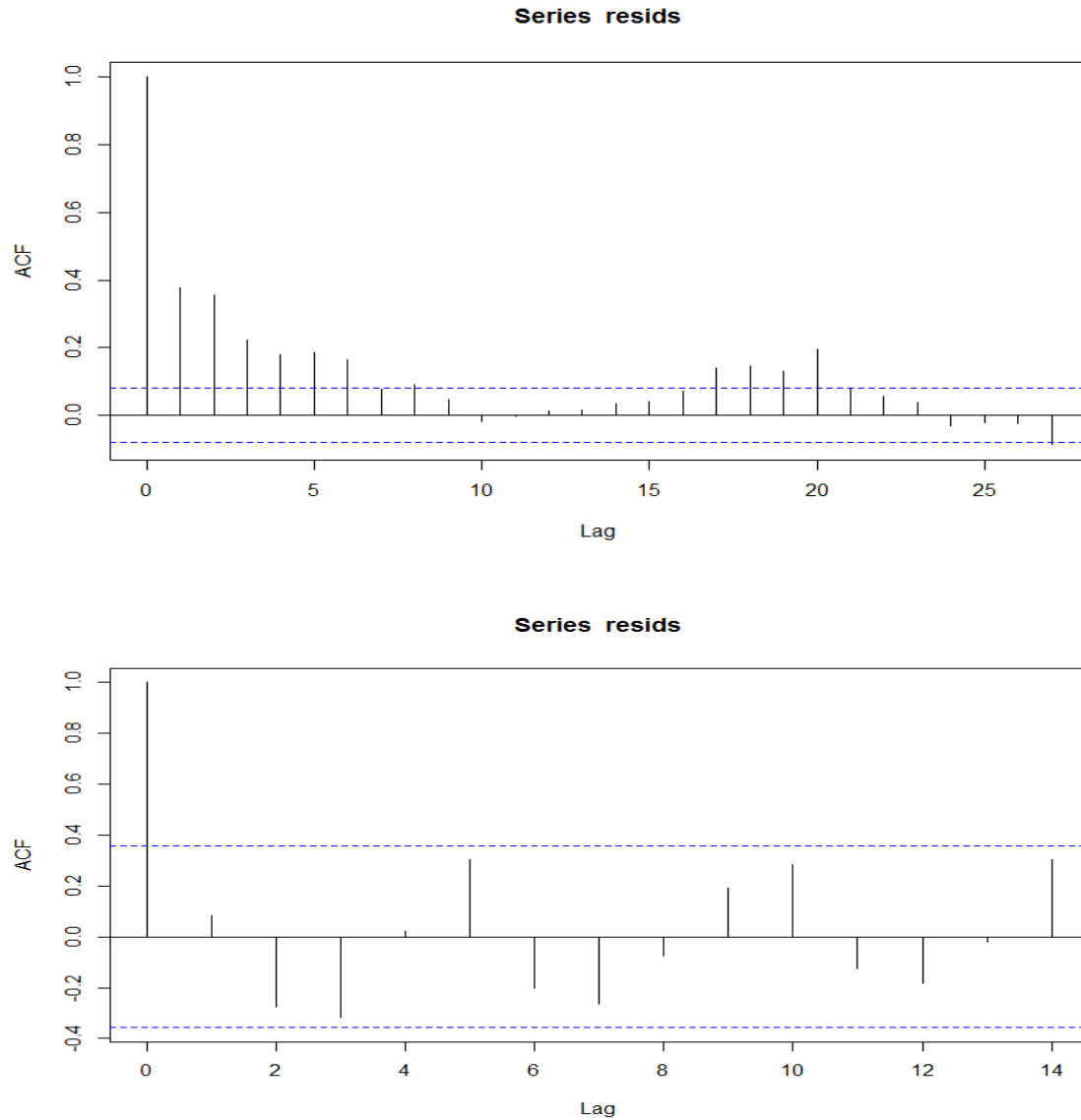


Figure 4.2 Example autocorrelation plots. The top plot shows correlated data while the bottom plot shows uncorrelated data.

The third assumption is homoscedasticity, meaning that the variance of the predicted variable does not change as the predicting variables change.^{12, 13} In other words, the variance does not change along the regression line on the model. This can be tested by

again looking at the plot of residuals versus predicted values of y .^{12, 13} Figure 4.3 shows example plots of residuals versus predicted values of y . The left plot shows homoscedastic data while the right shows heteroscedastic data.

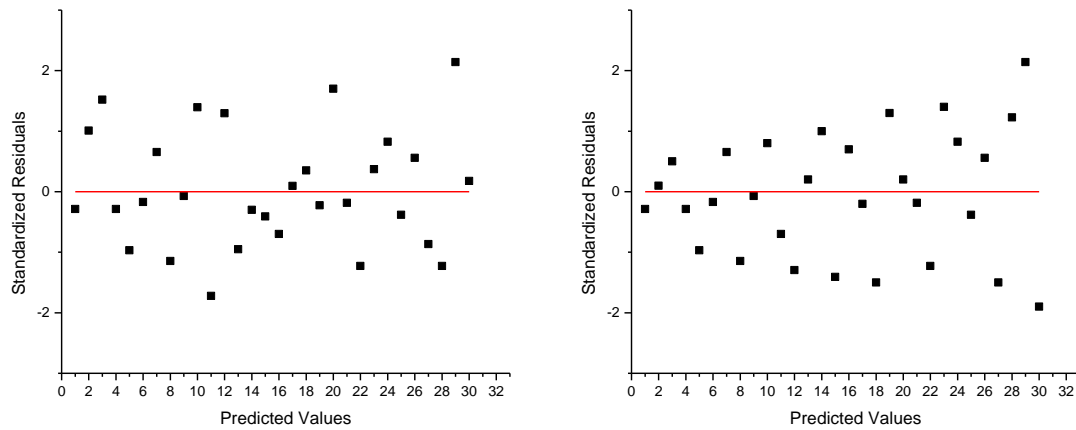


Figure 4.3 Example graphs of residuals vs. predicted values of y . The left graph shows homoscedastic data and the right graph shows heteroscedastic data.

The last assumption is that the residual error is normally distributed.^{12, 13} This assumption can be tested with a normal probability plot of the residuals.^{12, 13} A normal probability plot of the residuals plots the residuals versus the observed cumulative frequency.^{12, 13} In other words, the residuals are plotted against the expected values if the distribution were normal. If the residuals are normal, then the plot will be a straight line. Figure 4.4 shows examples of two normal probability plots. The top plot shows non-normal data while the bottom shows normal data.

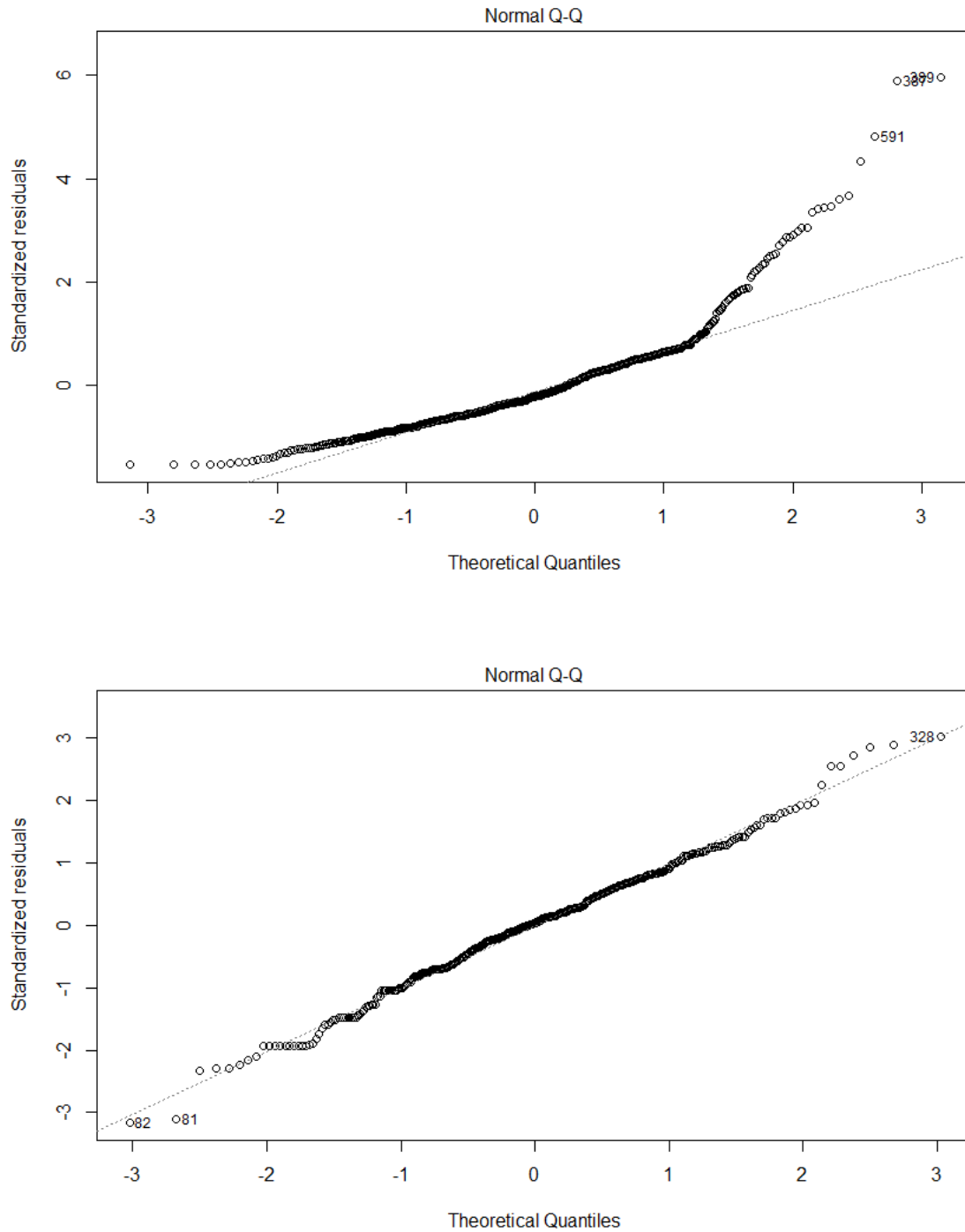


Figure 4.4 Example normal probability plots. The top plot shows non-normal data while the bottom shows normal data.

4.2.2.2 Transformations

If any of the assumptions of linear regression are violated, there are ways to transform the data so it can still be useful. For example, a conversion of length measurements from English units to metric would be a linear conversion. This transformation does not change the fundamental information in the data, but may make it easier to use. Other transforms include taking the log of y (dependent variable) or raising y to a power.¹²⁻¹⁴ However, the possible transformations that could be applied are infinite. Box and Cox developed a procedure to identify the most appropriate power to transform the data in order to make it normal.¹⁴ A complete analysis of the mathematics involved is beyond the scope of this work, but a complete description can be found in the 1964 paper by Box and Cox.¹⁴ The Box-Cox analysis determines the exponent of the transformation (λ for y^λ) by performing transformations across a range of values for λ and determining which value has the smallest standard deviation. The range of values for λ is technically infinite, but in practice, the values for λ fall between 3 and -3 (a value of 0 indicates that the natural log of y is the proper transform, while $\lambda \neq 0 \rightarrow y^\lambda$ is the proper transform).¹⁴ This is called a Box-Cox power transformation, and graphical example of such an analysis can be found in Figure 4.5. The x axis is the value for λ while the y axis is the log of the likelihood that the transformation will properly normalize the data. The dashed line across the top of the chart shows the region in which one can be 95% confident that the transformation will properly normalize the data. Of the three vertical dashed lines, the middle gives the predicted value of the exponent and left and right lines give the 95% confidence intervals on the predicted value. For this example the estimated value for λ is 0.34 with the edges of the confidence intervals at $\lambda = 0.23$ and $\lambda = 0.45$.

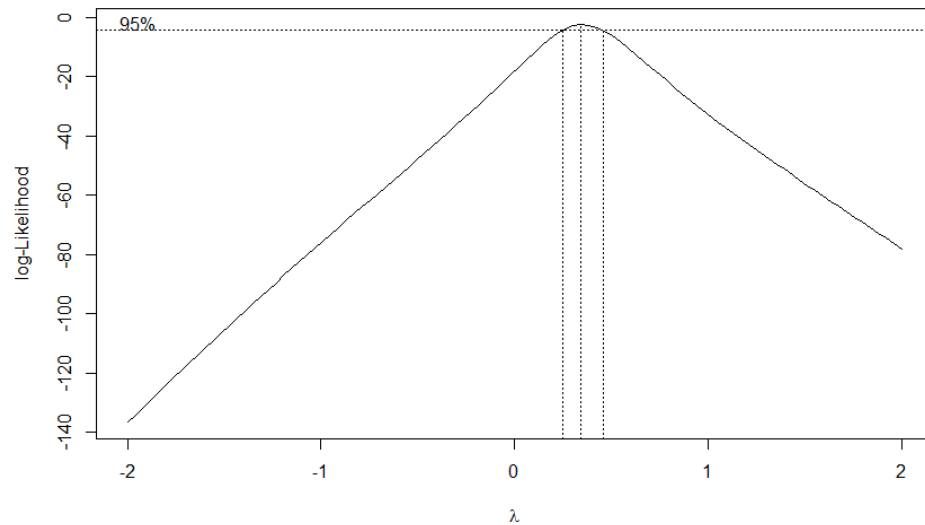


Figure 4.5 Box-Cox log likelihood plot for determining the exponent of a power transformation. λ is the value of the exponent for the transformation (y^λ). The estimated value of λ is 0.23-0.45.

A Box-Cox power transformation can only be used with data that is positive and greater than 0.¹⁴ Additionally, the analysis assumes normality, so a test for normality, like the normal probability plot in Figure 4.4, should be conducted on the transformed data. Lastly, when data is transformed, any analysis should be done within that transform, and only after analysis should the data be transformed back to its original state.^{12, 14}

4.3 **Objective**

The objective is to construct an empirical statistical model of scribe creep on Eponol coated 1018 steel that accepts ESF levels as inputs using the methods of statistical analysis described.

4.4 **Experimental Methods**

The data used to build the model came from the fractional factorial design of experiment performed in Chapter 3. The model outputs a predicted scribe creep length versus time as a function of five variables: temperature, UV intensity, chloride ion impingement rate, cycling and mean %RH. Linear regression and other statistical analyses were performed using R Statistical Software.¹⁵ Candidate models were tested to confirm that the assumptions of linear regression were met. Models that did meet the assumptions were graphed against the observed data. Visual inspection and R^2 values were used to determine goodness of fit.

4.5 **Results**

4.5.1 **Mass Loss Model Results**

Mass loss data were analyzed and a model constructed. The model is given in 4.3 where ML is the mass loss in g/cm^2 , T is temperature in Celsius, cycling is number of cycles per day, RH is percent relative humidity, Cl is the chloride impingement rate in $\text{g}/\text{cm}^2/\text{day}$, and t is time in days. The R^2 value for this model is 0.94. UV proved to not be statistically significant and is not included. The original data needed to be transformed as shown by the Box-Cox plot shown in Figure 4.6. The transform found to be appropriate was square root of mass loss ($\lambda=0.5$). The transformed data met the assumptions of linear regression. Figure 4.7 shows a plot of standardized residuals versus predicted values for transformed mass loss data that indicates the transformed data is linear and homoscedastic. Figure 4.8 shows an autocorrelation plot of the transformed FFA mass loss data that indicates that the

data is independent. Figure 4.9 shows a normal probability plot of the transformed FFA mass loss data that indicates that the errors are normally distributed.

$$ML^{1/2} = 0.002T + 0.0057(cycling) - 4 * 10^{-4}(RH) + 1.13(CL) + 0.058t^{1/2} - 0.0641 \quad 4.3$$

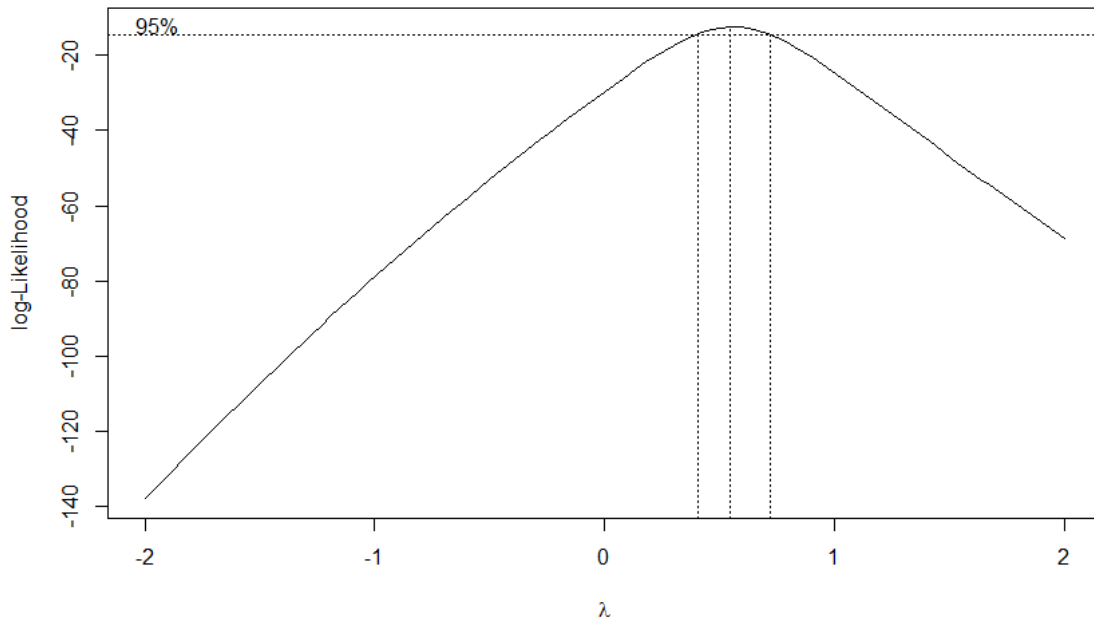


Figure 4.6 Box-Cox plot of FFA mass loss data showing the proper transform for the data is between $\lambda = 0.37$ and $\lambda = 0.71$. λ is the value of the exponent for the transformation (y^λ).

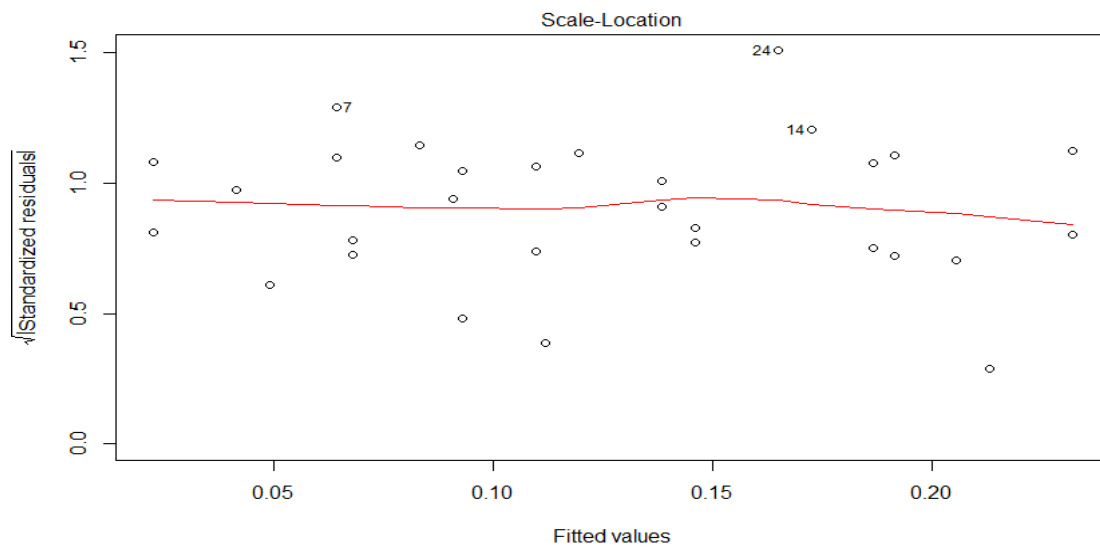


Figure 4.7 Plot of standardized residuals versus fitted values (values predicted by Equation 4.3, or $ML^{1/2}$) for transformed FFA mass loss data showing that the data is linear and homoscedastic.

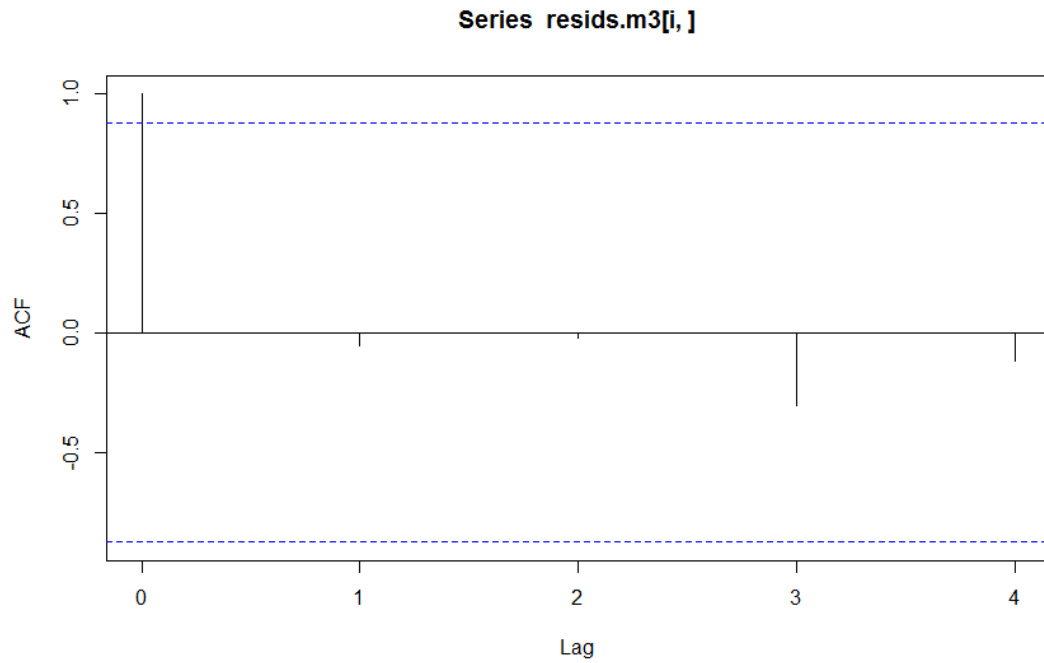


Figure 4.8 Autocorrelation plot of transformed FFA mass loss data showing that the data is independent. The x axis shows the lag, or time periods between the values that are being analyzed for correlation

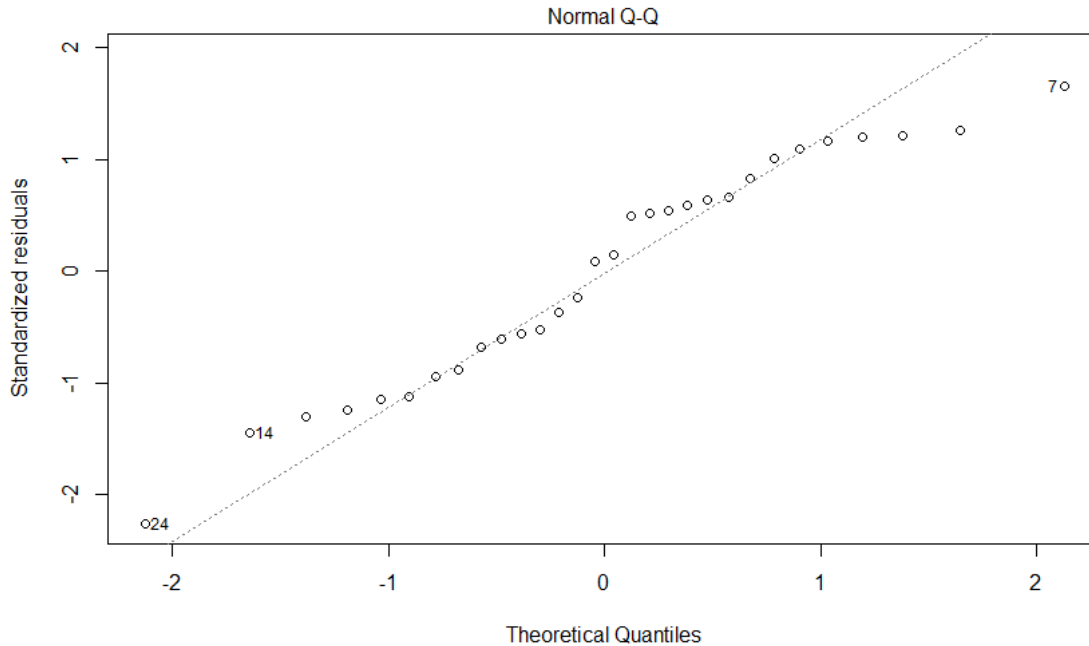


Figure 4.9 Normal probability plot for transformed FFA mass loss data showing that the errors are normal. The x axis is the theoretical values of the residuals if they are normal and the y axis is the actual values of the residuals.

The graphical representation of Equation 4.3 shows the predicted values of the model and the observed experimental results (Figure 4.10). Each exposure condition is graphed against the model using the same exposure parameters as the exposure condition it is graphed against (e.g., the ESF parameters for FFA1 are input into the model and the output is graphed against the experimental values for FFA1. See Table 3.9 for the experimental values). It can be seen by visual inspection of Figure 4.10 that the rank order of mass loss for the model matches the rank order of the experimental results except for FFA6 which the model ordered below FFA4. At day 15, the model predicts slightly higher values for FFA1 and FFA2 than the observed values, and slightly lower values for FFA4, FFA5 and FFA6 than observed. For FFA3, the model and observed values agree. It can be seen from Equation 4.3

that RH has a slight negative effect on the mass loss, while the other ESFs have a positive effect.

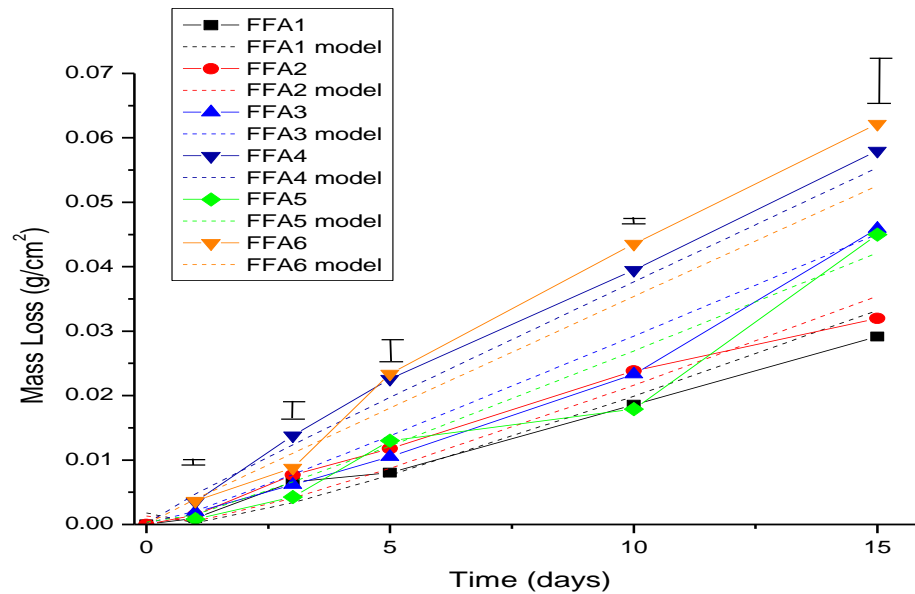


Figure 4.10 Graph of mass loss predicted by Equation 4.3 for bare 1018 steel compared with experimental results for 1018 steel in FFA exposures. The error bars shown above the data are from mass loss results for ASTM G-85 Annex 5.

The relative strength of each ESF has been shown visually in Figure 4.11 through Figure 4.14. For each figure the model baseline was calculated by choosing the mean values of each of the ESFs (Table 4.1), then each ESF was adjusted individually to its high and low values in the FFA test matrix to determine the sensitivity of mass loss to each individual ESF. These figures show that temperature had the largest effect on mass loss, followed by cycling, relative humidity and chloride.

Table 4.1 ESF levels for the model baseline. Baseline values are the mean values of the high and low levels.

	Temperature (°C)	%RH	Cl ⁻ (g/cm ² /day)	Cycling (# per day)
Baseline	32.5	77.5	1.04×10^{-4}	2
High	40	85	2.3×10^{-4}	4
Low	25	70	2.3×10^{-5}	1

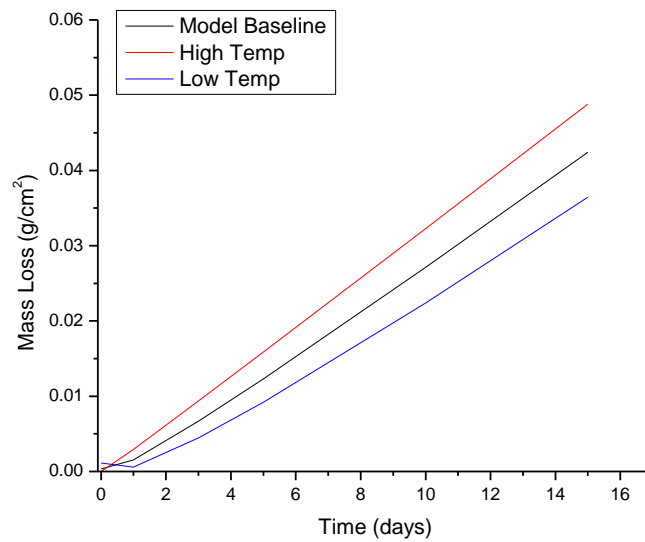


Figure 4.11 Graph showing the sensitivity of the model of mass loss of bare steel to temperature. High temperature is 40°C and low is 25°C. All other ESFs are at baseline values.

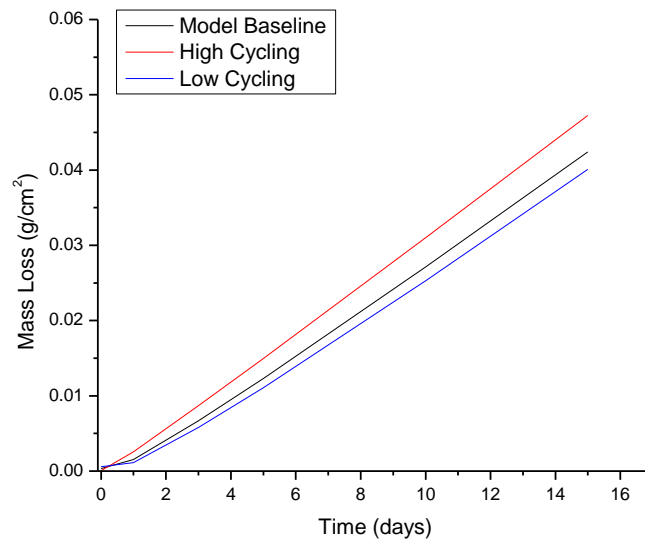


Figure 4.12 Graph showing the sensitivity of mass loss of bare steel to cycling. High cycling level is 4 wet/dry cycles per day and low is 1 cycle per day. All other ESFs are at baseline values.

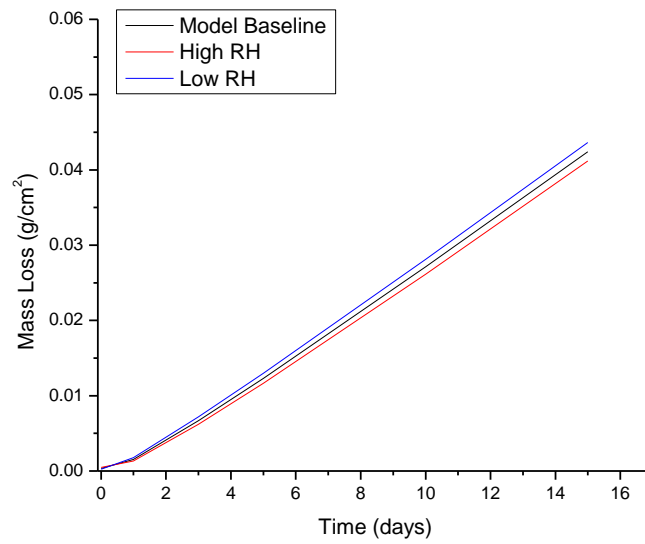


Figure 4.13 Graph showing the sensitivity of mass loss of bare steel to relative humidity. High relative humidity is 85% and low is 70%. All other ESFs are at baseline values.

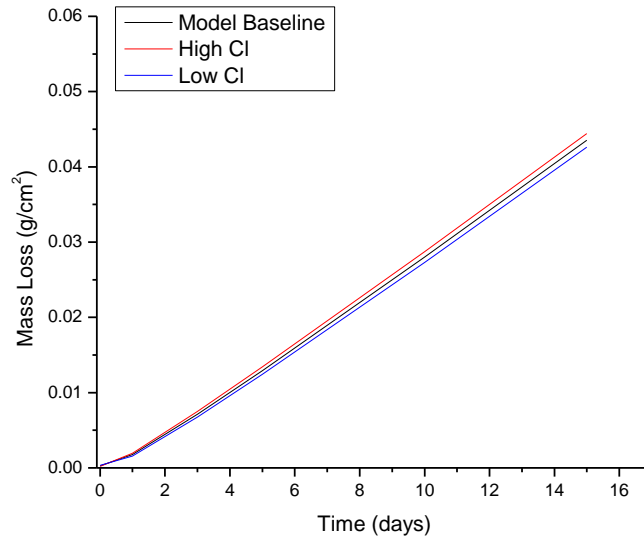


Figure 4.14 Graph showing the sensitivity of mass loss of bare steel to chloride. High chloride level is 2.3×10^{-4} g/cm²/day and the low level is 2.3×10^{-4} g/cm²/day. All other ESFs are at baseline values.

The mass loss model was also compared to experimental mass loss results for ASTM G-85 Annex 5 with and without UV and for mass loss results from KSC (Figure 4.15). The model prediction of mass loss over time shows good agreement with observed values for ASTM G-85 Annex 5. When the model was first plotted for KSC utilizing a $t^{1/2}$ time dependency, the predicted results were an order of magnitude higher than the observed results. However, when the exponent of time was modified from 0.5 to 0.35, which is just outside the 95% confidence interval, the model agreed much better with the observed results for KSC (Figure 4.15).

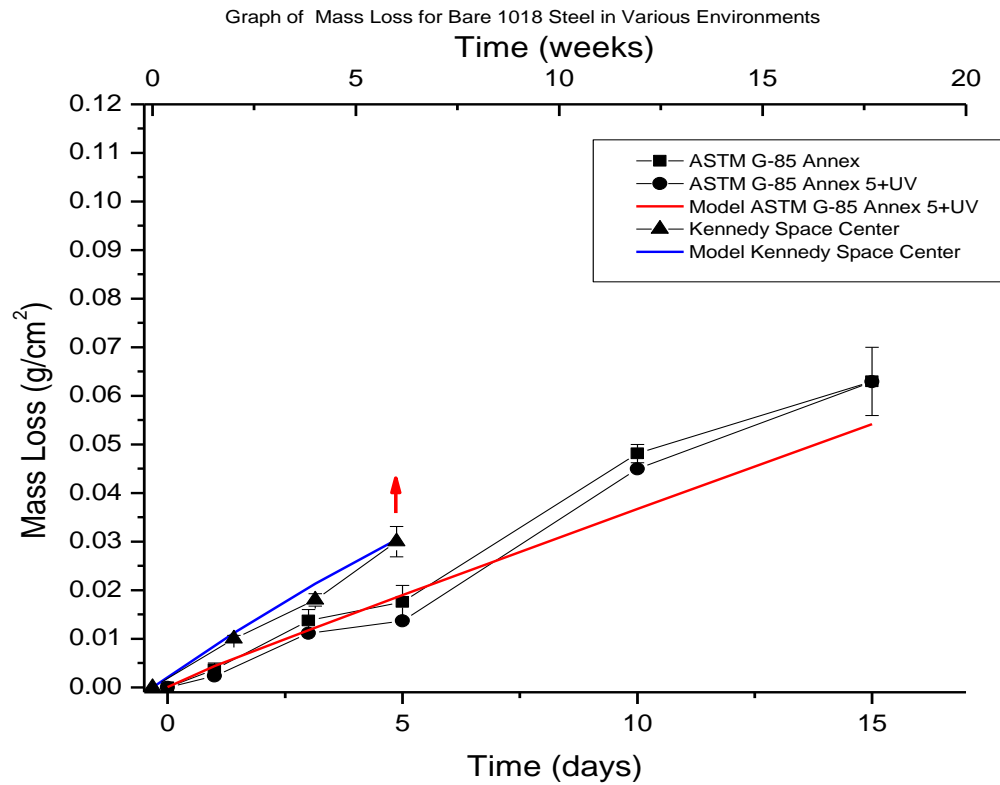


Figure 4.15 Graph of mass loss results for ASTM G-85 Annex 5 and KSC plotted against the model predictions for those exposures. The model inputs were the same ESF parameters as the exposure environments reported in Table 3.1. The model for ASTM G-85 Annex 5 used $t^{0.5}$ while the model for KSC used $t^{0.35}$.

4.5.2 Scribe Creep Model Results

The model for scribe creep is given in Equation 4.4 where SC is the scribe creep length in μm , T is temperature in Celsius, cycling is number of cycles per day, RH is percent relative humidity, Cl is the chloride impingement rate in $\text{g}/\text{cm}^2/\text{day}$, UV is the UV intensity in W/m^2 , and t is time in days.

$$SC^{1/2} = 0.225T + 3.75(Cycling) + 0.196RH + 0.4Cl + 0.016UV + 8.63t^{1/2} \quad 4.4$$

The R² value for this model is 0.75. It should be noted that this model is derived from data for FFA1, FFA2, FFA3 and FFA5. No model was able to accurately model scribe creep for all FFA exposures for reasons that will be addressed in the discussion section. A transformation was required to normalize the data as shown in the Box-Cox plot in Figure 4.16. The transform was square root of scribe creep ($\lambda=0.5$). The transformed data met the assumptions of linear regression. Figure 4.17 shows a plot of standardized residuals versus predicted values for transformed FFA1, 2, 3, and 5 scribe creep data indicating that the data are linear and homoscedastic. Figure 4.18 shows an autocorrelation plot for transformed FFA1, 2, 3, and 5 scribe creep data indicating that the errors are independent. Figure 4.19 shows a normal probability plot for transformed FFA1, 2, 3, and 5 scribe creep data indicating that the residuals are normally distributed.

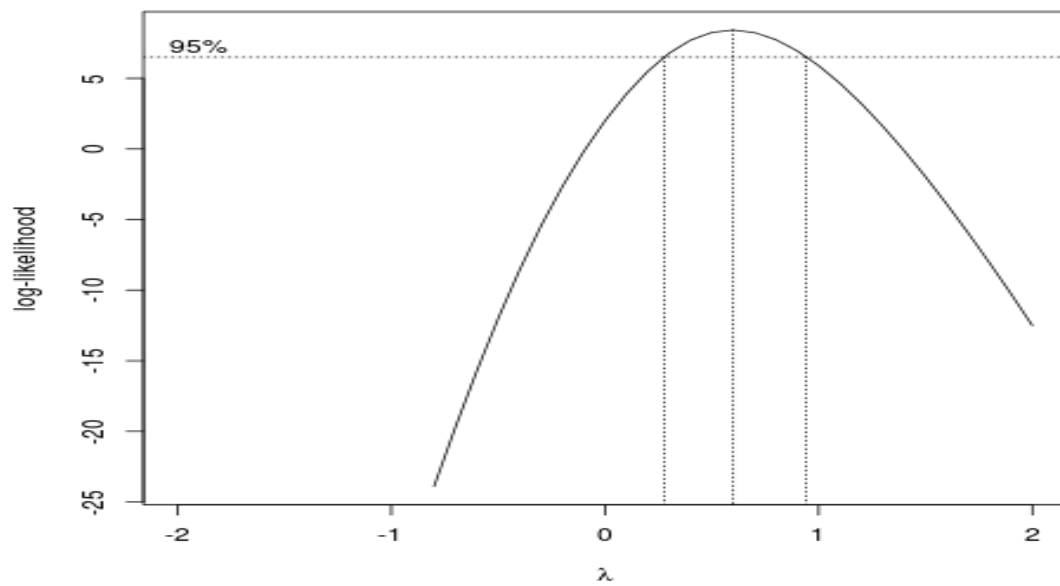


Figure 4.16 Box-Cox plot of FFA1, 2, 3, and 5 scribe creep data for Eponol coated steel indicating that the proper transform is between $\lambda = 0.35$ and $\lambda = 0.92$. λ is the value of the exponent for the transformation (y^λ).

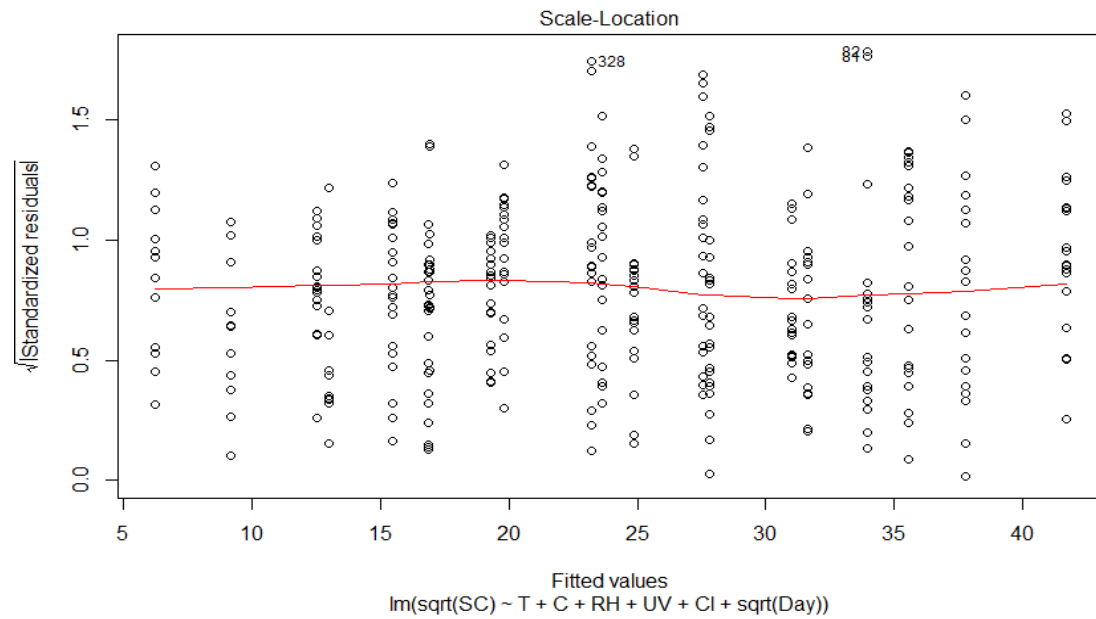


Figure 4.17 Graph of standardized residuals versus fitted values (the values predicted by Equation 4.4, or $SC^{1/2}$) for transformed FFA1, 2, 3, and 5 scribe creep data indicating that the residuals are linear and homoscedastic.

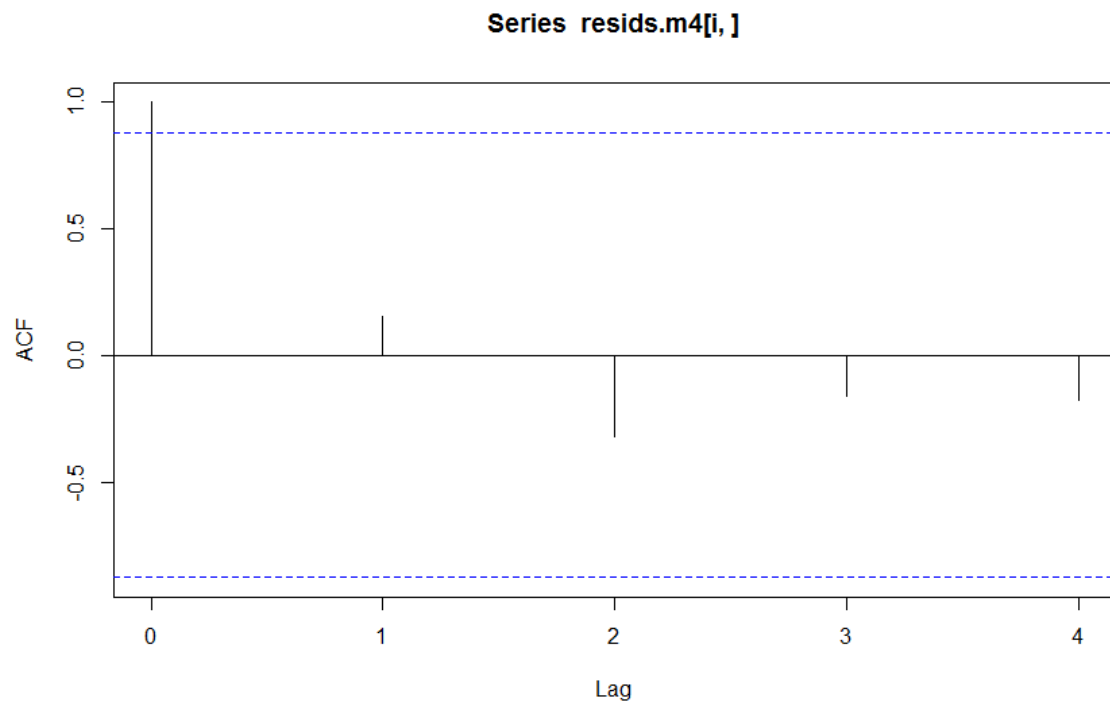


Figure 4.18 Autocorrelation plot of transformed FFA1, 2, 3, and 5 scribe creep data for coated steel showing that the errors are independent.

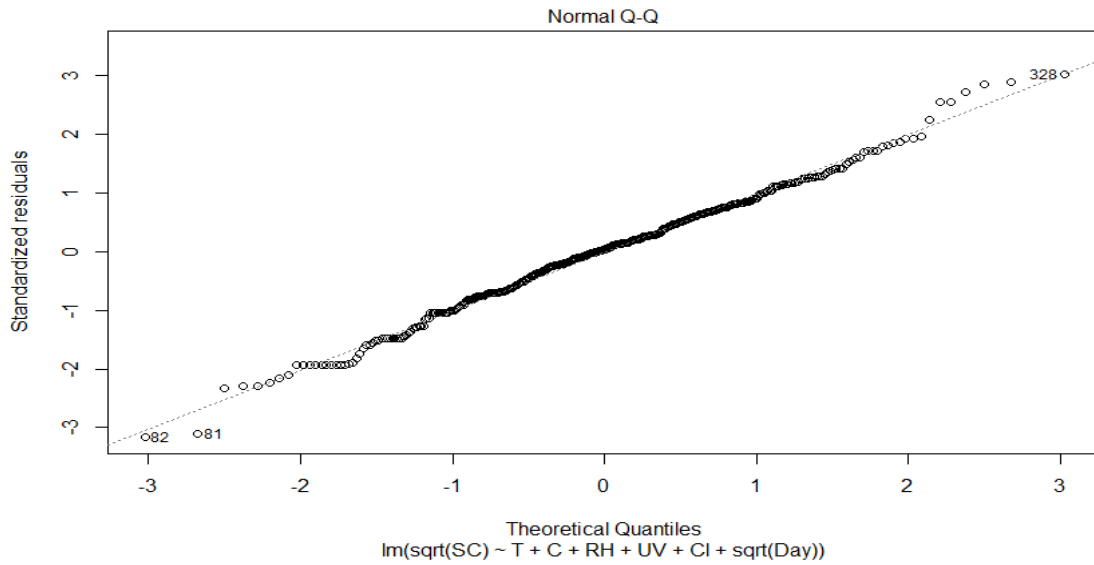


Figure 4.19 Normal probability plot of transformed FFA1, 2, 3, and 5 scribe creep data showing that the residuals are normally distributed.

A graphical representation of Equation 4.4 is given in Figure 4.20. Each exposure condition is graphed against the model using the same exposure parameters as the exposure condition it is graphed against summarized in Table 3.1. From visual inspection of Figure 4.20 it can be seen that at day 15 the model prediction for FFA1 is slightly higher than the observed value and slightly lower than the observed value for FFA2. The model prediction at day 15 for FFA3 is disparate from the observed value, however the model value for FFA5 and the observed value agree.

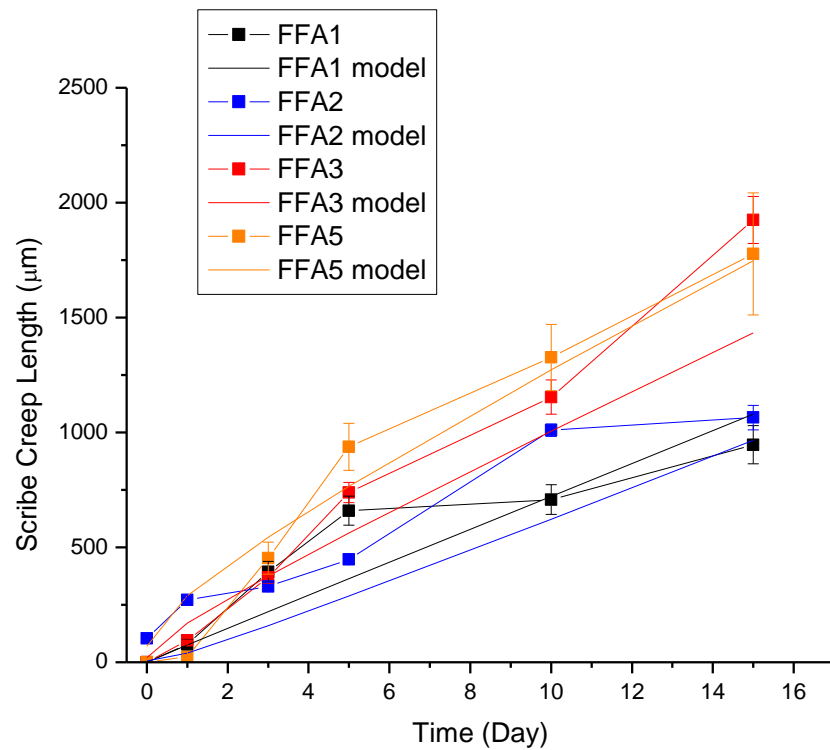


Figure 4.20 Graph of model values plotted against observed values of scribe creep for Eponol coated steel exposed to FFA1, 2, 3, and 5 test environments.

The sensitivity of the model to each ESF is shown in Figure 4.21 through 4.25

Similar to what was done for sensitivity tests for mass loss, the model baseline was

calculated by choosing the mean values of each of the ESFs (Table 4.2), then each ESF was

individually adjusted to its high and low values used in the FFA test matrix to determine the

sensitivity of mass loss to each ESF. The model is most sensitive to cycling followed by

temperature, relative humidity, UV and chloride.

Table 4.2 ESF levels for the scribe creep model baseline. Baseline values are the mean values of the high and low levels.

	Temperature (°C)	%RH	Cl ⁻ (g/cm ² /day)	UV (W/m ²)	Cycling (# per day)
Baseline	32.5	77.5	1.04x10 ⁻⁴	0.22	2
High	40	85	2.3x10 ⁻⁴	0.28	4
Low	25	70	2.3 x10 ⁻⁵	0.16	1

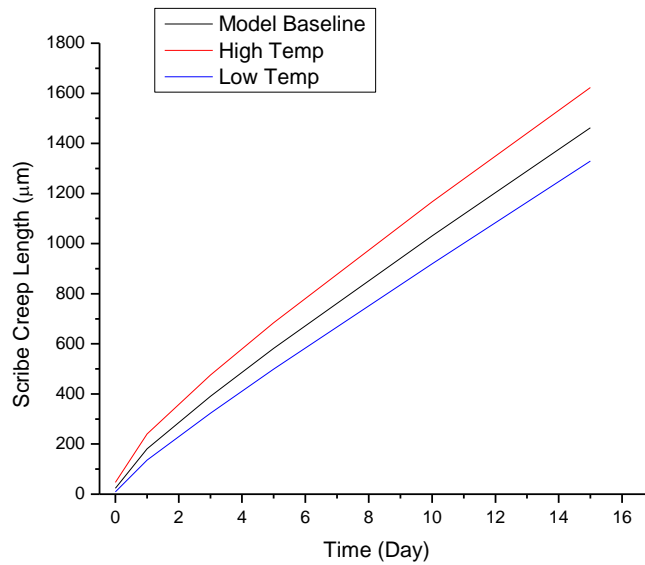


Figure 4.21 Graph showing the sensitivity of scribe creep of coated steel exposed in FFA1, 2, 3, and 5 to temperature. High temperature is 40°C and low is 25°C. All other ESFs are at baseline values.

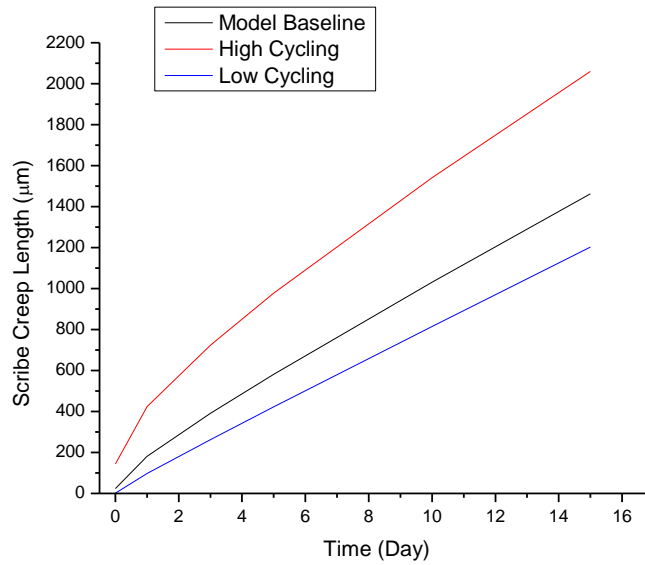


Figure 4.22 Graph showing the sensitivity of scribe creep of coated steel exposed in FFA1, 2, 3, and 5 to cycling. High cycling level is 4 wet/dry cycles per day and low is 1 cycle per day. All other ESFs are at baseline values.

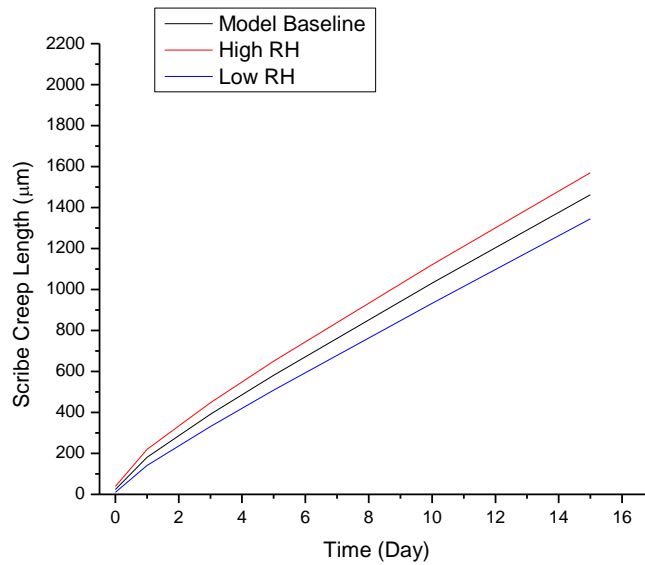


Figure 4.23 Graph showing the sensitivity of scribe creep of coated steel exposed in FFA1, 2, 3, and 5 to relative humidity. High relative humidity is 85% and low is 70%. All other ESFs are at baseline values.

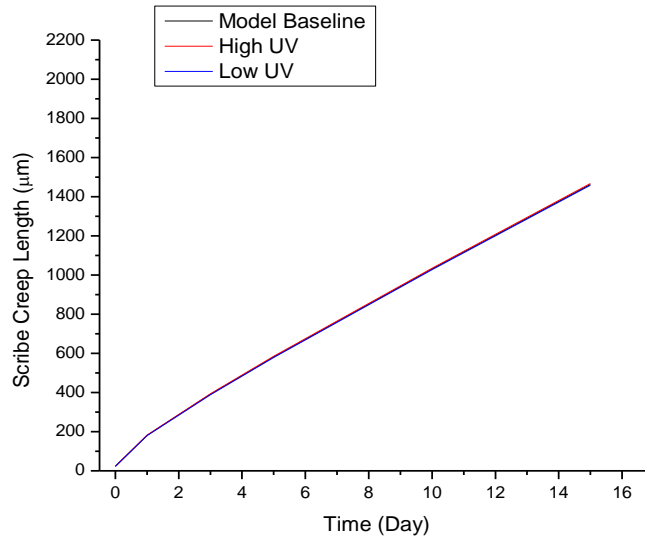


Figure 4.24 Graph showing the sensitivity of scribe creep of coated steel exposed in FFA1, 2, 3, and 5 to UV. High UV is 0.28 W/m^2 and low UV is 0.16 W/m^2 . All other ESFs are at baseline values.

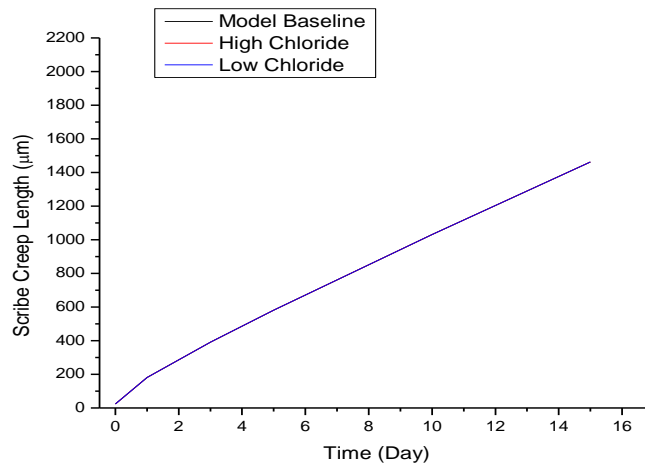


Figure 4.25 Graph showing the sensitivity of scribe creep of coated steel exposed in FFA1, 2, 3, and 5 to chloride. High chloride level is $2.3 \times 10^{-4} \text{ g/cm}^2/\text{day}$ and the low level is $2.3 \times 10^{-4} \text{ g/cm}^2/\text{day}$. All other ESFs are at baseline values.

The scribe creep model developed with data from the FFA exposures was also compared to the experimental data for ASTM G-85 Annex 5+UV and KSC (Figure 4.26) using the ESF levels in Table 3.1. It can be seen that the model results are in fairly good agreement with ASTM G-85 Annex 5+UV and KSC results.

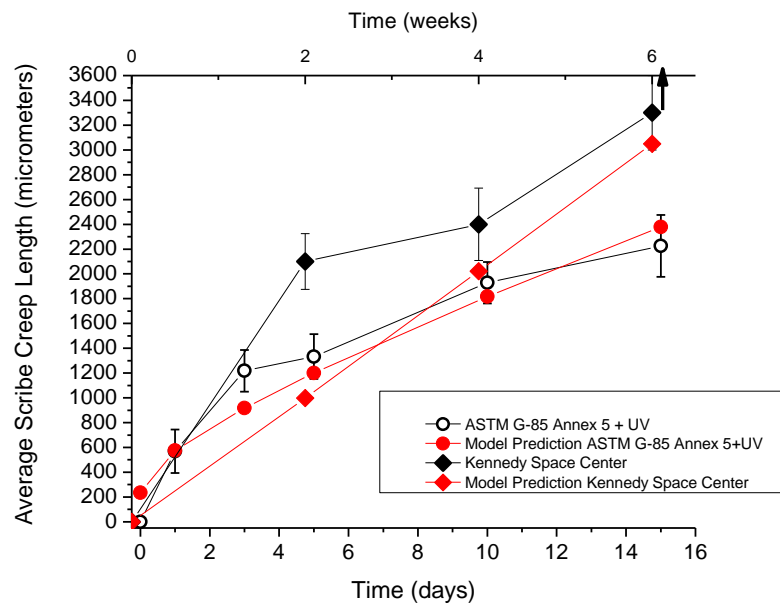


Figure 4.26 Graph of observed values of scribe creep plotted against predicted model values. The model inputs are the same ESF parameters present in exposures summarized in Table 3.1.

4.6 Discussion

4.6.1 Mass Loss Model

The model for mass loss appears to be able to capture the effects of ESFs on mass loss for all FFA environments. The prediction agrees well with experimental data as shown by Figure 4.10 and the R^2 value of the model (0.94). The model is valid within the ranges of the ESF

levels of the experiments, e.g., the model is valid from a temperature range of 25 to 40°C.

Concerning the relative strength or potency of the effects of ESFs on mass loss, the relatively strong effects of temperature and cycling appear to match with literature and with results from Chapter 2 (Figure 2.3) and Chapter 3 (Figure 3.5).^{5, 16-19} Moreover, the model showed some agreement with standard LALT and field results (Figure 4.15).

Relative humidity shows a slight negative effect on mass loss. This is consistent with the mass loss model made with data from the standard LALTs presented in Chapter 3 (Figure 3.1 and Equation 3.1). It is believed that this negative effect has to do with the effect of relative humidity on the concentration of NaCl in droplets on the surface of a metal. Figure 4.27 shows the equilibrium concentration of NaCl in water for various relative humidities. It can be seen that as %RH decreases, the concentration of NaCl in solution increases which in turn may further increase the corrosion rate.^{5, 19}

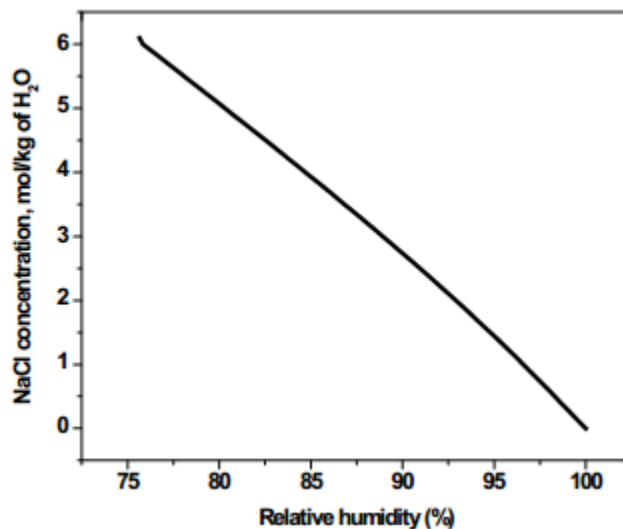


Figure 4.27 Thermodynamic equilibrium concentration of various saltwater solutions relative to the relative humidity in equilibrium at 25 °C. Calculated by OLI.²⁰

The effect of chloride itself on the mass loss of bare steel in FFA exposures appears to be slight (Figure 4.14). It is well known that chloride is a strong factor in the corrosion of bare steel.^{5, 19, 21-23} The lesser effect of chloride seen in the model is most likely due to the low level of chloride in the FFA exposures, especially when compared with the large differences in the high and low levels of temperature and cycling in the exposures.

The fact that the model results for ASTM G-85 Annex 5 with and without UV agree well with observed results (Figure 4.15) is likely due to the fact that the ESF parameters for ASTM G-85 Annex 5 with and without UV are within the ESF levels that were used in the FFA experiments. To make the model results for mass loss compare to KSC, the exponent on time had to be changed from 0.5 to 0.35 (e.g., $t^{0.5}$ became $t^{0.35}$). The original model predictions (with $t^{0.5}$) gave results that were higher than the observed results. This suggests that the 15 days was not enough time to accurately capture the time effect on the mass loss behavior that occurs in 6 weeks at KSC.

4.6.2 Scribe Creep Model

4.6.2.1 Effects of ESFs on Scribe Creep

The scribe creep model given in 4.4 for coated steel gives a good estimate of the scribe creep length over time for FFA1, 2, 3 and 5. This model is valid within the ESF ranges that were used in the experiments. The sensitivity tests show that cycling has the greatest effect on scribe creep of any ESF (Figure 4.22). This is consistent with findings of scribe creep in standard LALTs in Chapter 2. It was shown that ASTM G-85 Annex 5, which has 6 wet/dry

cycles per day, had greater scribe creep length over time than did ASTM B-117, despite the higher temperature and chloride level of the ASTM B-117 (Figure 2.24). Temperature had the next greatest effect on scribe creep, followed by relative humidity.

UV showed very little effect on scribe creep (Figure 4.24). In Chapter 2, it was shown that when UV was added to the standard ASTM G-85 Annex 5 test, scribe creep length was lower than for ASTM G-85 Annex 5 without UV (Figure 2.24). It is still unclear at this time why UV would cause a decrease in scribe creep length. UV was shown to be the most likely cause of a decrease in “intact” coating barrier properties far from the scribe for ASTM G-85 Annex 5+UV (Section 2.6.5) and for FFAs exposed to the high level of UV (FFA4, 5 and 6) (Section 3.6.4). UV was also shown in Chapter 3 not to be a governing factor in scribe creep (Section 3.6.4).

Chloride level had a nearly undetectable effect on scribe creep (Figure 4.25) at the levels tested. In Chapter 2, it was shown that ASTM G-85 Annex 5 produced a greater scribe creep length than did ASTM B-117 despite the fact that the concentration of chloride in the spray solution is two orders of magnitude greater for ASTM B-117 (Figure 2.24). It is worth noting that the effect of chloride was not statistically significant in the model, but was included for completeness. The model would not be significantly changed if the chloride term were not included. This, however, does not imply that chloride has no effect on scribe creep, just that there is no statistical difference in the levels chosen. Scribe creep appears to be relatively insensitive to chloride when the chloride level is low. It may be that chloride ions collect at the head of the scribe creep front and act like a catalyst to trigger corrosion similar to the effect of chloride on pitting.²⁴ As long as some chloride is present, it is

sufficient to affect scribe creep. Further post mortem analysis would be required to verify this speculation.

The model that only used data from FFA1, FFA2, FFA3, and FFA5 produced predictions for scribe creep for ASTM G-85 Annex 5+UV and KSC that matched well with observed values (Figure 4.26). The accurate prediction of the model for scribe creep on ASTM G-85 Annex 5+UV is likely due to the fact that the ESF levels in the ASTM G-85 Annex 5+UV are within the high and low ESF levels used in the FFA experiments. The agreement between model results and observed experimental results for KSC shows that the model accurately captures the effects of multiple ESFs on scribe creep. The model uses data from accelerated tests that are run to 15 days, yet was able to accurately predict scribe creep out to 6 weeks (42 days) for KSC. However, the model did not show very good agreement with KSC at 2 or 4 weeks. The model shows a nearly straight line while the observed results for KSC appear to show that scribe creep length does not increase as quickly at long time periods ($t > 2$ weeks) as it does at shorter time periods ($t < 2$ weeks). That this relationship was not accurately predicted by the model is most likely because 15 days is not enough time to properly capture the time effects.

4.6.2.2 Inability to Model Across all Exposures

The model presented in Equation 4.4 is only valid for FFA1, 2, 3 and 5 and not for FFA4 and 6. Despite numerous iterations of models, none were constructed that could accurately model FFA4 and 6 in addition to the other exposures. Models of FFA4 and 6 only were also inadequate because there was not enough variation in the ESF levels between the two

exposures. FFA4 and 6 are the only exposures that have high levels of both temperature and cycling. Even when FFA3 and 5, which have high levels of just one of temperature or cycling, were included, the model was still inadequate to describe those four exposures. This is believed to be caused by an interaction between temperature and cycling that is manifests itself only when both are at high levels. This hypothesis is supported by results of Chapter 3 that showed a significant increase in scribe creep for FFA4 and FFA6 over every other exposure that did not have both high temperature and high cycling (Figure 3.22). Possible scientific reasons for this effect were discussed in Section 3.6.5. It may be that temperature and cycling have a nonlinear relationship when both are high that cannot be captured by a linear model. More data is needed to investigate and elucidate the possible interaction between cycling and temperature.

4.7 **Conclusions**

An empirical model for mass loss was constructed that showed very good agreement with experimental data. Temperature had the strongest effect on mass loss followed by cycling, relative humidity, and chloride. UV was found to not have a statically significant effect on mass loss of bare steel.

An empirical model for scribe creep of Eponol coated steel showed good agreement with experiment, but only for FFA1, 2, 3 and 5, none of which have high levels of both temperature and cycling. For FFA1, 2, 3 and 5, cycling was found to have the greatest effect followed by temperature. Relative humidity had a much smaller effect than temperature or cycling. UV was shown to have a very small effect. It was also shown that there was no

statistical difference between the high and low chloride levels on scribe creep. It was proposed that the presence of chloride ions was sufficient to affect scribe creep.

It was found that FFA4 and FFA6 could not be modelled accurately. It is possible that there is an interaction between temperature and cycling that is only manifested in scribe creep when both ESFs are at the high levels established in the FFA experimental design. This hypothesis is supported by results from Chapter 3, but more investigation is needed to determine the existence, character and effect on scribe creep of the possible interaction.

The scribe creep model was able to accurately predict scribe creep for ASTM G-85 Annex 5. The model also predicted similar values of scribe creep to the observed values for KSC at 6 weeks, but not a 2 or 4 weeks.

4.8 **References**

1. A.U. Leuenberger-Minger, *Dose-response functions for weathering steel, copper and zinc obtained from a four year exposure programme in Switzerland*. Corrosion Science, 2002. **44**: p. 675-687.
2. A.A. Mikhailov, *Dose-Response Functions as Estimates of the Effect of Acid Precipitates on Materials*. Protection of Metals, 2001. **37**(4): p. 357-366.
3. J. Tidblad, V. Kucera, A. Mikhailov, J. Henriksen, K. Kreislova, T. Yates, B. Stöckle and M. Schreiner, *UN ECE ICP Materials: Dose-Response Functions on Dry and Wet Acid Deposition Effects After 8 Years of Exposure*. Water, Air, & Soil Pollution, 2001. **130**(1): p. 1457-1462.
4. J.F. Henriksen and A.A. Mikhailov, *Atmospheric Corrosion Tests of Metals in SO₂-Polluted Cold Atmosphere in Northern Norway and along Its Border with Russia*. Protection of Metals, 2002. **38**(6): p. 579-589.
5. C. Leygraf and T.E. Graedel, *Atmospheric Corrosion*. 2000: John Wiley & Sons.
6. G. Williams, A. Gabriel, A. Cook and H.N. McMurray, *Dopant Effects in Polyaniline Inhibition of Corrosion-Driven Organic Coating Cathodic Delamination on Iron*. Journal of the Electrochemical Society, 2006. **153**(10): p. B425-B433.
7. D.A. Little, M.A. Jakab and J.R. Scully, *Effect of surface pretreatment on the underpaint corrosion of AA2024-T3 at various temperatures*. Corrosion, 2006. **62**(4): p. 300-315.

8. D.E. Little, 2006, ROLE(S) OF PRETREATMENT, INHIBITORS, AND OTHER PROCESS STEPS THAT EFFECT SURFACE COMPOSITION ON THE UNDER-PAINT CORROSION OF AN Al-Cu-Mg ALLOY 2024-T3. University of Virginia, Charlottesville.
9. K.N. Allahar, M.E. Orazem and K. Ogle, *Mathematical model for cathodic delamination using a porosity-pH relationship*. Corrosion Science, 2007. **49**(9): p. 3638-3658.
10. R.F. Hamade, C.Y. Seif, F. Merhij and D.A. Dillard, *A Semi-empirical Model for the Cathodic Delamination of Elastomer-to-Metal Adhesive Joints*. Journal of Adhesion Science & Technology, 2008. **22**(7): p. 775-793.
11. R.F. Hamade, C.Y. Seif and D.A. Dillard, *Cathodic delamination of elastomer-to-metal adhesive joints: Experimental data and empirical modeling*. International Journal of Adhesion and Adhesives, 2007. **27**(2): p. 108-121.
12. G.E.P. Box, W.G. Hunter and J.S. Hunter, *Statistics for Experimenters*. 1976, New York: John Wiley and Sons.
13. D.C. Montgomery and G.C. Runger, *Applied Statistics and Probability for Engineers*. 3rd ed. 2006, New York: John Wiley and Sons, Inc.
14. G.E.P. Box and D.R. Cox, *An Analysis of Transformations*. Journal of the Royal Statistical Society. Series B, 1964. **26**: p. 211-252.
15. R. Ihaka and R. Gentleman, *R: A Language for Data Analysis and Graphics*. 1996.
16. M. Stratmann and H. Streckel, *On the atmospheric corrosion of metals which are covered with thin electrolyte layers—II. Experimental results*. Corrosion Science, 1990. **30**(6-7): p. 697-714.
17. M. Kappes, G.S. Frankel and N. Sridhar, *Adhesion and adhesion degradation of a pressure sensitive tape on carbon steel*. Progress in Organic Coatings, 2010. **69**(1): p. 57-62.
18. *Temperature Influence on Corrosion* [website] 2010 [cited 2014 May]; Available from: <http://events.nace.org/library/corrosion/Design/Temperature-effects.asp>.
19. E. McCafferty, *Introduction to Corrosion Science*. 2010, New York: Springer.
20. M. Shedd, 2012, Modeling and Measurement of the Maximum Pit Size on Ferrous Alloys Exposed to Atmospheric Conditions. (Master's Thesis) University of Virginia, Charlottesville.
21. S. Feliu, M. Morcillo and B. Chico, *Effect of distance from sea on atmospheric corrosion rate*. Corrosion, 1999. **55**(9): p. 883-891.
22. L. Veleva and R.D. Kane, *Atmospheric Corrosion in Corrosion: Fundamentals, Testing and Protection*, Various, Editor. 2003, ASM International: Materials Park, OH. p. 196-209.
23. G.S. Frankel, *Pitting Corrosion in Corrosion: Fundamentals, Testing and Protection*, Various, Editor. 2003, ASM International: Materials Park, OH. p. 236-241.
24. D.A. Jones, *Principles and Prevention of Corrosion*. 2nd ed. 1996: Prentice Hall.

5 Chapter 5 – Summary and Future Work

5.1 Summary

The lack of correlation between corrosion produced by lab accelerated life tests (LALTs) and field tests of organically coated metal alloys is a well-documented problem. The same applies to coated steel. Contributing to discrepancies between lab and field is a general lack of understanding of how differences in environmental severity factors (ESFs), such as chloride and UV, affect the unit processes such as metal corrosion and polymer degradation affecting scribe creep. This body of research endeavored to take the first steps to understand the influence of ESFs on underpaint corrosion and polymer degradation in scribe creep.

Using a “bottom up” approach, this dissertation first compared similarities and differences in corrosion, scribe creep, and polymer degradation of ultra-high molecular weight epoxy resin coated AISI 1018 steel samples tested in standard LALTs, field sites and lab full immersion tests (FIT). This was done using a suite of high-level surveillance methods: electrochemical impedance spectroscopy (EIS), confocal laser scanning microscopy (CLSM), scanning electron microscopy (SEM), Fourier Transform Infrared Spectroscopy (FTIR), X-Ray diffraction (XRD), and Raman spectroscopy. These methods enabled identification of corrosive changes that might not be detected with low fidelity surveillance methods. This study thus improved our ability to draw comparisons between LALT, FIT and field tests.

Next, fractional factorial design of experiment in which ESFs were systematically varied in non-standard LALTs was performed to better understand the effects of individual ESFs on scribe creep, underpaint corrosion, and changes in electrical properties of the coated system. The effect of UV light, temperature, relative humidity, chloride, and wet/dry cycling were investigated using the methods described above. Differences in corrosion morphology, corrosion products formed, and rates of scribe creep were examined. Statistical analysis of the resulting data demonstrated the relative importance of individual and combined ESFs to scribe creep.

Lastly, data from the non-standard LALTs were used to construct an empirical model of scribe creep which accepted ESFs as inputs to yield scribe creep length and mass loss versus time at fixed ESF levels. The empirical model produced using data from the factorial design assessed the relative strength or potency of individual and combined ESFs on scribe creep of coated steel. A possible interaction between temperature and cycling on scribe creep was seen. By highlighting the ESFs that most greatly impacted scribe creep and processes affecting it, such as mass loss and polymer degradation, the model provided a more in depth understanding of the roles of selected ESFs in scribe creep of polymer coated steel. As the first scribe creep model to incorporate multiple ESFs, the model also serves as a template for creating scribe creep models for other commonly used coating schemes.

5.1.1 Comparison of Standard LALTs, FITs and Field Sites

Results demonstrate a positive correlation between mass loss on bare 1018 steel samples and scribe creep length on coated steel for both standard lab- and field- exposed samples. It

is interesting to note that this trend was found across many standard LALTs. Additionally, there was an inverse correlation between scribe creep length and the low frequency electrochemical impedance of the coating for coated steel near the scribe for lab and field samples. In contrast, the results demonstrate that LALT's without UV radiation did not correlate as well with field exposure in terms of coating degradation. This lack of correlation points to the need for UV radiation to damage the polymer coating. However, UV effects do not govern scribe creep. Comparison of LALT results to full immersion tests (FITs) helped to clarify the mechanism of scribe creep in these lab and field exposures.

There appears to be an “overloading” effect of chloride on the Eponol coating. Exposures with high chloride levels, such as ASTM B-117 and full immersion in 5% NaCl, showed significant corrosion occurring away from the scribe after 10 days, likely at intrinsic coating defects. In contrast, exposures with low chloride levels, such as the ASTM G-85 Annex 5, showed no corrosion far from the scribe even after 15 days. FTIR results showed that high chloride levels have no detectable effect of the degradation of the polymer coating itself. This implies that a high level of NaCl is required to initiate corrosion at pores and defects in the coating away from the scribe.

EIS results combined with scribe creep results for FITs at OCP and -1 V vs. SCE suggest that cathodic disbondment caused by cathodic reactions under the coating was not the dominant factor controlling scribe creep in this system. Chiefly, -1 V polarization suppressed scribe creep suggesting that, unless local cathodic reactions during corrosion are greater than those achieved at -1 V, cathodic delamination is not the driving process controlling scribe creep for this coating/substrate system. It appears that anodic wedging of corrosion

products plays a strong role in scribe creep. It may be that cathodic delamination is dominant in consistently wet conditions like ASTM B-117 while anodic wedging plays a bigger role in cyclic wet/dry conditions where more voluminous corrosion products are formed.

It was shown that ASTM G-85 Annex 5 correlated well with the Kennedy Space Center outdoor marine atmospheric site in terms of scribe creep rate, scribe creep corrosion morphology, and corrosion mechanism. However, the test differed from KSC in terms of coating degradation as observed with EIS and FTIR. The addition of UV to ASTM G-85 Annex 5 produced better correlation with KSC with respect to coating degradation. ASTM G-85 Annex 5+UV correlated the best with KSC of any LALT tested.

The effects of ESFs on mass loss of bare steel were fairly straight forward. However, the effects of ESFs on scribe creep behavior appeared to be more complex. The role of ESFs in scribe creep is further discussed in the next section.

5.1.2 Systematic Analysis of the Roles of ESFs in Scribe Creep

The results of Chapter 2 showed that systematic isolation and evaluation of the effects of ESFs, individually and in combinations, on scribe creep length of coated steel was still needed to more accurately determine how scribe creep is affected by the environment.

Fractional Factorial Design of Experiment proved to be a valid method to quickly and efficiently investigate the effects of ESFs on scribe creep. The ESFs investigated were, temperature, relative humidity, cycling, UV irradiation and chloride.

Results show mass loss was lowest for FFA1 and FFA2, involving low temperature and low cycling, and greatest for FFA4 and FFA6, involving high temperature and high cycling.

Additionally, iron oxide hydroxides (FeOOH) were the main corrosion products formed in FFA exposures, as well in cyclic exposures such as ASTM G-85 Annex 5 and Kennedy Space Center. Additionally, line profiles for all cyclic exposures showed that corrosion products filled the scribe and wedged outward underneath the coating as exposure time increased.

Scribe creep results showed that FFA1, FFA2, FFA3 and FFA5 presented similar scribe creep lengths while FFA4 and FFA6 presented distinctly greater scribe creep lengths compared to the other FFAs. Scribe creep and mass loss were shown to have a positive correlation in all cases. The ratios of scribe creep to mass loss were similar for FFA1, FFA2, FFA3, and FFA5. Ratios of scribe creep to mass loss for FFA4 and FFA6 were significantly higher compared to the ratios for the other FFAs. FFA4 and FFA6 were the only exposures with high levels of both temperature and cycling. This points to a possible interaction between temperature and cycling rate when they are both at high levels. Lastly, high levels of UV were shown to promote coating degradation far from the scribe but were not found to be a strong factor in scribe creep.

The metal cover test samples showed no retardation effect on scribe creep length progression when a metal film was put over the top of the polymer coating as an oxygen

barrier. The reduction of oxygen diffusion did not reduce the scribe creep length. Results suggest that cathodic delamination ahead of scribe creep is not the dominant factor controlling scribe creep. These were consistent with cathodic polarization studies where scribe creep was suppressed by -1 V vs. SCE cathodic polarization.

5.1.3 Statistical Analysis and Modeling of Mass Loss of Bare Steel and Scribe Creep of Coated Steel

Empirical statistical models of scribe creep and mass loss were constructed using data from the fractional factorial design of experiment. Both models were shown to conform to the assumptions inherent in linear regression and were therefore valid.

For mass loss, temperature was found to have the largest effect followed by cycling, relative humidity and chloride. The effect of UV was not found to be statistically significant.

Relative humidity (both levels examined experimentally were relatively high) was found to have a slight negative effect on mass loss. This is consistent with earlier analysis of mass loss in standard LALTs. As relative humidity decreases, the concentration of NaCl in droplets on the metal surface increases, thereby possibly increasing corrosion rate. Other literature has also shown an increase in the corrosion rate of bare iron contaminated with SO₂ as relative humidity decreases.¹

Statistical analysis of the scribe creep data showed that cycling had the largest effect of any of the ESFs tested. Cycling was followed by temperature, relative humidity, UV and chloride. Scribe creep was shown to be insensitive to chloride level within the range of

levels tested. This does not mean that chloride has no effect on scribe creep, just that there is no difference in the effect caused by the levels of chloride tested.

No model was able to accurately describe the mass loss of coated steel when FFA4 and FFA6 were included. FFA4 and FFA6 were the only FFA exposures to have both high cycling and high temperature. This points to a possible interaction between temperature and cycling rate, such that simultaneous combination of these drivers results in an effect on scribe creep that is greater than a simple addition of their individual effects.

The scribe creep and mass loss models were able accurately predict results for ASTM G-85 Annex for bare and coated steel. However, the mass loss model required a change of $t^{0.5}$ to $t^{0.35}$ to accurately predict mass loss for KSC. The scribe creep model predicted the value for scribe creep for KSC at 6 weeks, but did not agree with observed results at 2 and 4 weeks.

5.2 **Future Work**

This work has opened up many avenues of investigation that could potentially yield new insights into the roles of ESFs on scribe creep of painted metals. One possible avenue is the further investigation of the possible interaction effect of temperature and cycling on scribe creep.

The fractional factorial design of experiment implemented was of resolution (III) meaning that all main effects were distinguishable from each other but may have been confounded by two factor interactions. In order to avoid confounding effects in the future, a new set of

experiments is proposed: a 2^3 full factorial design.^{2,3} The ESFs to be tested would be temperature, cycling and %RH because those factors were shown to have the largest effect on scribe creep. Chloride would be included, but due to the insensitivity of scribe creep to chloride at the levels previously tested, chloride level would not be varied. The test matrix for such a design is given in Table 5.1. The ESF levels, could be the same as used in the previous fractional factorial design, or perhaps modified after careful consideration. For example, raising the low temperature for the exposures may elucidate the temperature at which the interaction begins to be significant. Since this design is a full factorial, there would be no confounding effects between factors, and all possible interactions could be distinguished. Ideally, a 3^3 full factorial design would be implemented with three levels of each ESF, with the high and low levels remaining the same as the previous factorial design and the middle level being in between the high and low levels. However, this design would require 27 experiments to fully implement.

Table 5.1 Test matrix for a 2³ full factorial design.

Run	Temperature (°C)	Cycling	%RH
1	-	-	-
2	+	-	-
3	-	+	-
4	+	+	-
5	-	-	+
6	+	-	+
7	-	+	+
8	+	+	+

This study examined selected ESFs consistent with marine and rural environments. Other important outdoor ESFs such as SO₂, NO₂ and O₃, which are found in urban/industrial atmospheres, and the pH of the solution that impinges on the sample surface, could be examined using the approach developed here.

A second direction for future work would be to take the methods used here and apply them to a full coating system that could be used in real world applications. This system might include an adhesion promoter, primer, base coat and top coat. Longer timeframes would likely be necessary to accomplish this goal. The Eponol system enabled meaningful study through 15 days of exposure on a model coating with a very high initial impedance. This

indicates that, at least initially, the Eponol system had comparable quality to a commercial system.

A fruitful direction for future work would be to investigate the mechanisms of scribe creep in cyclic exposures. For example, investigation of the effects of chloride on scribe creep at low levels. Results from this study put forth the hypothesis that low level chloride collect at the head and can act as a catalyst for scribe creep, similar to the autocatalytic effect of chloride on pitting of steels. Tools such as X-ray photoelectron spectroscopy and energy dispersive X-ray spectroscopy could be employed to see if chloride ions are concentrated at the head or tail of the scribe creep front. SKP could also be used to look for a change in potential ahead of the advancing scribe creep front.

The effects of adhesion on scribe creep in conjunction with the effects of ESFs were not investigated in this study. Further investigation could look at the effects of ESFs on adhesion of the coating to the substrate and what role adhesion plays in the cathodic delamination and anodic wedging mechanisms of scribe creep. Although an investigation of adhesion was beyond the scope of these experiments, this work expands our understanding of the role of ESFs and serves a significant stepping off point from which new experiments can be designed to elucidate the specific corrosive mechanisms at work in scribe creep.

5.3 **Significance**

This work establishes better foundations for understanding the effects of selected ESFs on scribe creep of painted metals. For example, it was shown that in the ASTM B-117 the effect

of chloride is dominant over the effects of other ESFs on substrate degradation while in LALT and field environments that experience wet/dry cycling, cycling becomes the strongest driver of scribe creep. These results validate the use of a “bottom up” approach to standardize LALT design by examining ESFs. If the empirical equations developed are found to apply broadly, ESFs can be targeted for minimization. Additionally, coating design for scribe creep mitigation can be addressed more directly instead of by trial and error. In environmental or lab test scenarios, the same ESFs will not always be appropriate targets for minimization and mitigation of corrosion.

This work also give evidence supporting the idea that scribe creep in coated systems that experience cycling is not dominated by cathodic delamination. Instead, anodic wedging plays an important role. Overall, scribe creep of coated metal in environments that experience wet/dry cycling may be under mixed control and more investigation is warranted. When designing a corrosion resistant coating, combating detrimental effects of cycling and anodic wedging might be more important goal in the adhesion science of the coating than adhesion in the face of cathodic disbondment.

In addition to a better understanding of scribe creep in general, this body of work provides some guidelines that could be used in the construction of future LALTs. For example, although chloride is a strong corrodant of steel, it was shown that including too high of a level in the LALT design can result in global degradation more uniformly across the intact coating that is unlike that seen in field environments. Additionally, cycling was shown to be an important part of any test that seeks to mimic field exposures. If further research once again finds an interaction between temperature and cycling, this will have to be considered

and factored into LALT design. At this time, it appears that the interaction only happens when temperatures and wet/dry cycling are greater than what would be experienced in the field. This should be taken into account when determining the severity of the LALT and determining acceleration factors.

This work demonstrates that fractional factorial design of experiment can be successfully implemented to reduce the time and resources required in an experimental investigation of a complex, multi-step process such as scribe creep with many corrosion drivers. In this dissertation, FFA was able to highlight important trends that can be investigated at higher resolution in the future.

Lastly, this work provides an overall testing approach and framework for many various avenues of exploration of coatings, pretreatments, and adhesion promoters that mitigate or inhibit scribe creep.

5.4 **References**

1. M. Stratmann and H. Streckel, *On the atmospheric corrosion of metals which are covered with thin electrolyte layers—II. Experimental results*. Corrosion Science, 1990. **30**(6–7): p. 697-714.
2. G.E.P. Box, W.G. Hunter and J.S. Hunter, *Statistics for Experimenters*. 1976, New York: John Wiley and Sons.
3. D.C. Montgomery and G.C. Runger, *Applied Statistics and Probability for Engineers*. 3rd ed. 2006, New York: John Wiley and Sons, Inc.

6 Appendix A - Scribe Creep and Underpaint Corrosion on Eponol Coated AA2024-T3

6.1 Summary of Appendix A

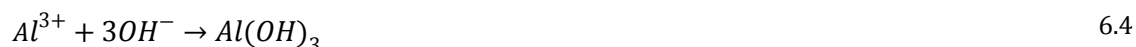
6.2 Background

6.2.1 Mechanism of Scribe Creep on Coated Aluminum

Cathodic delamination does not often occur in aluminum alloys because of a lack of electronic conductivity of the surface oxides, the slow rates of cathodic electron transfer reactions, and a lack of global OH^- production under the coating.¹ Filiform Corrosion (FFC) is a form of surface corrosion that forms long, thin filaments of corrosion under a coating and delaminates and detaches the coating.^{1,2} The filament has an anodic head and a cathodic tail and starts growing from a defect in the coating, like a scratch. The electrochemical reactions that take place are Equation 6.1, the anodic reaction at the head of the filament, and Equation 6.2, which is a secondary reaction near the head upon hydrolytic acidification.¹



Equation 6.3 is the cathodic reaction in the tail of the filament. Then OH⁻ ions form a gelatinous aluminum hydroxide through homogeneous precipitation shown in Equation 6.4.¹



The anodic head of the filament is very acidic (pH=1-3) and the evolution of hydrogen gas (Equation 6.2) occurs in the same area as the anodic dissolution of aluminum.² The tail of the filaments is very basic and Al(OH)₃ is precipitated in the path of the tail (Equation 6.4).¹ The propagation of the filaments has been proposed to be due to anodic undercutting caused by differential oxygen concentration between the front and the back of the head of the filament.²⁻⁴ Figure 6.1 shows a schematic of filiform corrosion on an aluminum alloy.⁵ While some water and oxygen can diffuse through the coating in order for Equation 6.3 to occur,¹ most of the oxygen and water diffuse through the tail of the filament.⁶ Even when an oxygen impermeable metal film was placed over the head and tail of the filament, leaving only the scratch in the coating where the filament originated exposed to air, FFC continued unabated.⁶ It has been calculated that the rate of diffusion through the tail of the filament can be up to ten times greater than diffusion vertically through the coating.⁶ It has been suggested that coating adhesion to the metal substrate determines the corrosion protection of the coating better than the barrier properties of the coating when this mechanism prevails.^{3,4} Often, blisters in the coating of AA2024-T351 are just a cluster of filaments.¹

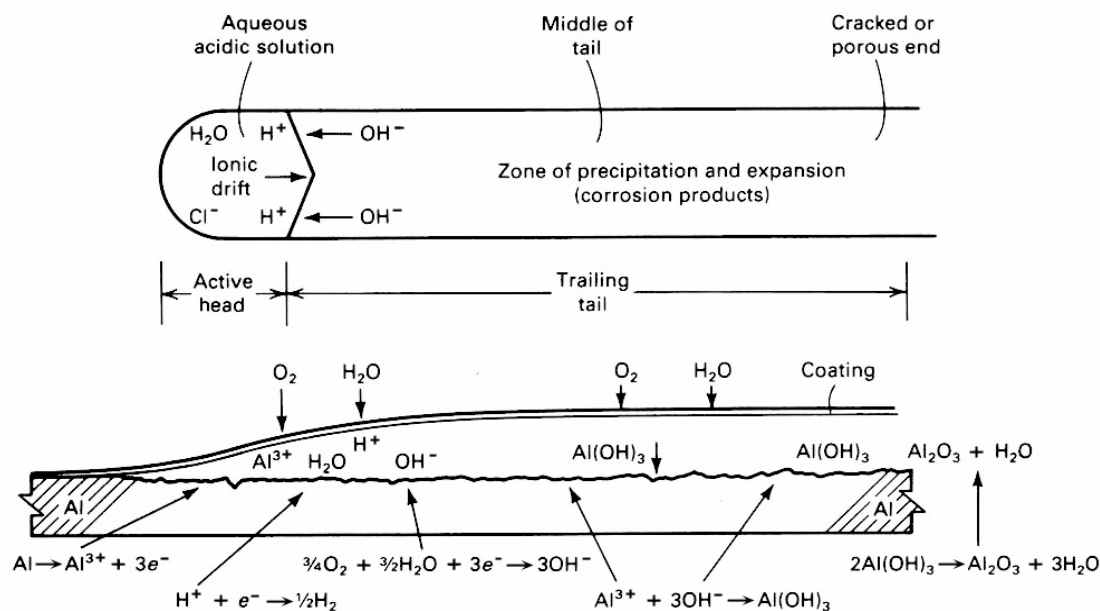


Figure 6.1. Schematic of filiform corrosion on an aluminum alloy.⁵

Certain factors have been shown to affect the growth rate of FCC and scribe creep on coated aluminum alloys. Increasing temperature has been shown to increase scribe creep length on AA2024-T351.^{1,7} Scribe creep on AA2024-T351 has been approximated to be an Arrhenius-type thermally activated behavior that decreases over time. Scribe creep length also decreases over time, and it has been shown that the scribe creep length is proportional to time to the one half power.⁷ Increasing relative humidity (%RH) has been shown to proportionally increase the width of the filaments in FFC.² Filiform corrosion rate is also increased by application of HCl solution at the scratch.¹ The HCl solution promotes anodic undercutting and helps to initiate FFC.¹ Aluminum alloys that contain copper have been shown to support enhanced rates of FFC over copper free alloys.¹ Copper rich inter-metallic particles (IMCs) are cathodic to the aluminum matrix, and re-plated copper has been shown to enhance the overall rate of the oxygen reduction reaction (ORR) on bare AA2024-T351.^{1,8}

Additionally, rates of scribe creep on AA2024-T351 have been shown to be accelerated with higher surface coverage of copper because the ORR occurs preferentially on the Cu-bearing particles.^{1,7} Studies have shown that by limiting the amount of copper available at the surface, either by passivating the Cu bearing IMCs with pretreatments or by decreasing the amount of Cu in the IMCs by keeping the copper in solid solution, will cause a decrease in the scribe creep rate.^{1,7} Studies in the Automotive industry have found that increasing salt levels in LALTs showed no noticeable increase in the corrosion of aluminum alloys.⁹

6.3 **Objective**

The objective of this section of work is to compare and contrast the underpaint corrosion and scribe creep produced by the combination of corrosion drivers present in existing standard LALTs compared to field exposures for coated AA2024-T351. Results were used to generate acceleration factors for field sites with respect to LALTs.

6.4 **Experimental Methods**

6.4.1 **Sample Preparation**

Samples of AA2024-T351 plate measuring 7.62 by 12.7 by 0.3175 cm (3 x 5 x 1/8th inch) were ground with 180, 240, 300, and 600 grit silicon carbide papers to remove any surface oxide, even out any imperfections and create a clean bare surface. The sample was then blown with compressed air to remove any large debris from the grinding. The sample was washed with water and detergent soap and rinsed with Millipore water. After washing, the sample was immediately blown dry with compressed air. Bare samples were then placed in

a desiccator until they were exposed. The samples to be coated were placed in a fume hood. The Eponol (Poly(Bisphenol A-co-epichlorohydrin) glycidyl end-capped, CAS registry number: 25036-25-3. molecular formula: $(C_{18}H_{22}O_3)_n \cdot C_{22}H_{26}O_4$) coating solution was applied to the top of the plate and a Gardco 8 path wet film applicator was used apply the coating to the sample. The 8 path wet film applicator was pulled by hand over the plate. The sample was allowed to cure for 5 days in air and then put into a 60°C oven for 24 hours to finish curing. The wet film thickness was roughly 75 microns (3 mils). The dry film thickness was 30 ± 5 microns (1 mil). After curing, the plate was cut into 2.5 x 2.5 cm (1 x 1 inch) pieces with a band saw. The samples were then scratched by hand with a diamond scribe to give a scribe of 150 ± 50 microns in width, 18 ± 3 mm in length and 10 ± 4 microns in depth into the metal substrate. A schematic of a finished sample in cross section is shown in Figure 6.3. It should be noted that the data for all LALTs is for un-pretreated and coated aluminum samples, while the data from the HI, PJ, and LA field sites is for sample pretreated with Pre-Kote and then coated. The samples exposed to the KSC and BRD field sites were not pretreated before coating.

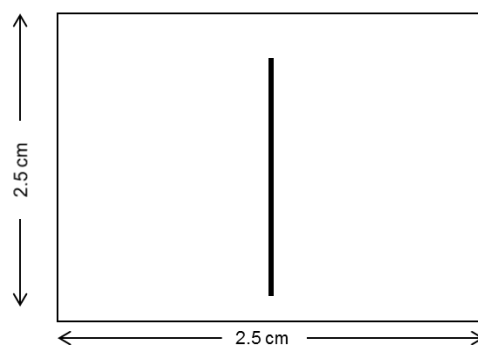


Figure 6.2. Schematic of Eponol coated and scribed AA2024-T351 sample. The sample is a square that is 2.5 cm on a side.

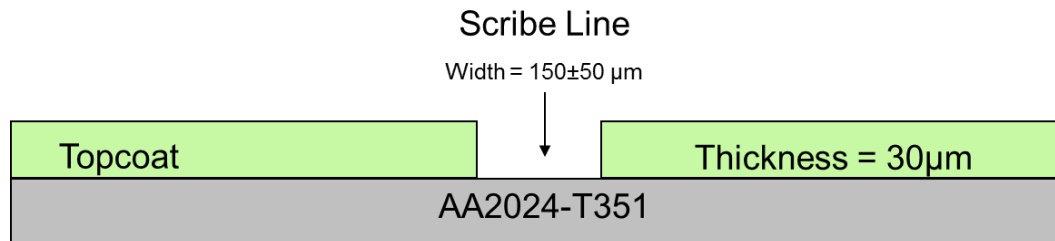


Figure 6.3. Schematic of Eponol coated and scribed AA2024-T351 sample. The substrate is roughly 1 mm thick and the Eponol topcoat is $30\pm 5\ \mu\text{m}$. The scribe line is $150\pm 50\ \mu\text{m}$ in width.

6.4.2 High-Level Surveillance Testing Methods

6.4.2.1 Digital Optical 3D Microscopy (Hirox)

The bare and coated AA2024 aluminum samples were imaged with a Hirox KH-7700 digital microscope in order to examine corrosion morphology. The samples were first imaged with a macro lens to get one image of the entire sample surface. The coated samples then had a 2D tiled image taken at 50x that extended the length of the scratch using the MXG-4050RZ lens. The coated samples then have 3D tiled images taken at 350x that start at the scratch and run perpendicular out from the scratch using the MXG-10C lens with the OL 350 II lens attachment. These 3d tiled images were taken at the same place every time to monitor the progress of the corrosion from the scratch. Higher resolution images (+400x) were taken at various interesting spots on the samples. The 3D images were processed using Mitiani Corporation 3DMeasurement software and with Mountains Map software ¹⁰.

6.4.2.2 Digital Image Analysis (ImageJ)

Images taken with the Hirox were analyzed using ImageJ software ¹¹. The images were imported into ImageJ and converted into 8-bit greyscale images. The image was then converted to binary with the threshold selected to show all the pits as black areas and everything else as white areas. The Count Particles command was then used and the lower threshold for particle size was 20 μm^2 . The data returned was average particle area, area fraction of particles and particle density.

6.4.2.3 Electrochemical Impedance Spectroscopy

EIS was conducted on coated AA2024-T351 samples that had been exposed to various environments in order to examine the electrical properties of the coatings and detect the evolution of coating defects. The testing was done on a Princeton Applied Research Versastat 4 using the VersaStudio software. A five minute OCP test was run before EIS. A typical EIS scan was acquired in sine mode from 100 kHz to 0.05 Hz with 6 points per decade. Samples were scanned with an AC amplitude of 60 mV to reduce noise. The tests were run in a flat cell containing 0.3 wt% sodium sulfate solution with ambient aeration. The area of the sample tested was a circle with an area of 1 cm^2 . The samples were tested at locations 0.3 cm and 0.75 cm away from the scribe (Figure 6.4). The reference electrode used was saturated calomel reference electrode, the samples were the working electrode, and a platinum mesh was used as the counter electrode.

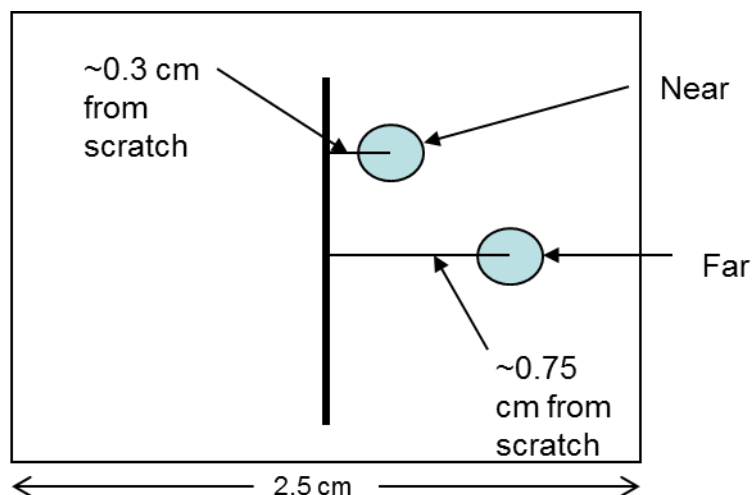


Figure 6.4. Schematic showing locations where EIS was performed on coated and scribed samples.

6.4.2.4 Scanning Electron Microscopy and Energy Dispersive X-Ray Spectroscopy (SEM and EDS)

Scanning electron microscopy (SEM) was conducted on a JEOL 6700F scanning electron microscope. Energy dispersive analysis (EDS) was performed using the same instrument and analyzed using PGT Spirit software.

6.4.2.5 Fourier Transform Infrared Spectroscopy (FTIR)

FTIR analysis of Eponol films was conducted to better understand the effects of ESFs on coating degradation in the form of polymer bond breaking. FTIR analysis enables the detection of degradation of Eponol films exposed on inert substrates to determine the effects of ESFs on the coating itself without any effects due to the substrate. FTIR analysis was performed on Eponol films that had been cast on inert polypropylene substrates and then exposed. For samples analyzed at UVa, the films were removed from the substrate after exposure and placed into a ScienceTech benchtop FTIR spectrometer for analysis. For

samples analyzed at USM, coatings were left on the substrate and spectra were taken from three different locations on the eponol film by securing them to a Smart iTR attachment. The spectra were obtained using a Nicolet 6700 FTIR from Thermo Scientific running Omnic software, in 4000-650 cm^{-1} range. The spectrophotometer was operated in transmission mode. The spectra were recorded at a resolution of 2 cm^{-1} and 32 scans were conducted per location.

6.4.2.6 Confocal Scanning Laser Microscopy

Confocal Scanning Laser Microscopy (CSLM) gives detailed 3D topography information at higher resolutions than can be achieved with the optical 3D system.

6.4.2.7 Nitric Acid Sample Cleaning Procedure

The one bare AA2024-T351 sample exposed to CC+O3 (10-25 ppm) was cleaned with a nitric acid solution after detailed analysis. This was done to remove the surface oxide in order to conduct further analysis on these samples. The sample was cleaned with a 50% nitric acid solution for 30 seconds. The sample was then rinsed in DI water and blown dry with compressed air. The sample was then taken immediately to the SEM for analysis.

6.4.2.8 Differential Scanning Calorimetry

DSC was used to measure the change in the glass transition temperature (T_g) of the Eponol film to gain insight into how different ESFs affected the nature of the Eponol polymer over time. DSC and MDSC measure the amount of heat required to increase the temperature of a

sample. For polymers, it is used to measure the change in glass transition temperature (T_g), or the temperature at which the polymer changes from an amorphous solid to a crystalline solid. The glass transition temperature is important because the properties of the polymer change as it moves from above the T_g to below. For example, above the transition temperature, polymers are amorphous and are generally more flexible and rubbery, while below the T_g they are crystalline and are generally more brittle.¹² Shorter polymer chains, limited crosslinking, and incorporation of plasticizers or residual solvent can lower the T_g , while longer chains, extensive crosslinking and large side groups raise the T_g .¹² Environmental factors can affect the T_g . For example, higher temperatures would cause more residual solvent to evaporate leading to higher T_g , while factors that break the crosslinking or the backbone of the chains themselves, like UV or ozone, would cause T_g to lower.¹² DSC was performed on unexposed and exposed (ASTM D4587, B117, and G85 A3) Eponol 53-BH-35 films on polypropylene. The samples were prepared by using a hollow punch of 6 mm on each of the respective films once they were removed from the substrate. Two to three punches of each sample were loaded in to standard Al DSC pans. A Heat/cool/heat cycle was carried out between -25 °C and 130 °C with a heating rate of 10 °C/min, under a nitrogen atmosphere (flow rate = 50 mL/min); with a TA Instruments DSC Q2000T calorimeter.

Modulated DSC was also performed on the same samples as above following the same procedure of sample preparation but they were loaded into T-zero Al hermetic pans. The conventional modulated DSC run was carried out between -25 °C and 130 °C with a heating rate of 2 °C/min, modulating 60 seconds, under a nitrogen atmosphere (flow rate = 50 mL/min); with a TA instruments DSC Q2000 calorimeter.

6.4.2.9 Thermogravimetric Analysis

TGA was performed on unexposed and exposed samples of Eponol 53-BH-35 on polypropylene. TGA involves heating the sample in a controlled setting and constantly measuring the changing weight. It has been used to measure the amount of residual solvent and the amount of organic content in the polymer. The remaining material after the sample has been heated to the point of complete polymer degradation is inorganic material. The samples were removed from the substrate and then using a hollow punch of 8 mm disks were punched out and two disks were loaded into the sample pan for each run. The sample pan was platinum and the runs were high resolution dynamic and were carried out from room temperature to 500 °C with a ramp rate of 10 °C/min, sensitivity of 1 and resolution of 4°C under a nitrogen atmosphere with a TA instruments TGA Q500 thermogravimetric analyzer.

6.4.3 **Sample Exposure Conditions**

6.4.3.1 LALT Exposure Conditions

The suite of LALT exposure chambers included a QUV™ cyclic condensation (CC/UV) chamber and a salt fog chamber. The salt fog chamber was modified to include UV lights.¹³ The QUV™ allows the use of elevated temperatures, humidity and condensation cycling, and UV exposure in LALTs. These chambers can be used to perform standard LALTs like ASTM B-117 and ASTM D-5894, and also allow for modified versions of standard LALTs. Coated and bare AA2024 samples were exposed in ASTM B-117, ASTM G-85 Annex 3, ASTM G-85

Annex 5, ASTM D-4587 and ASTM D-5894 standardized tests. Samples were also exposed in one non-standard test, a modified ASTM G-85 Annex 5 that included UV light. For this non-standard LALT, all exposure conditions were identical to the ASTM G-85 Annex 5 except for the addition of UV light (wavelength of 340 nm at 0.5 W/m²) for 12 hours per day. Coated and bare AA2024 samples were removed from the exposure chambers and tested with the suite of characterization techniques at 0, 1, 3, 5, 10, and 15 days. After testing, the samples were immediately returned to the exposure chambers. A detailed list of the LALT exposure conditions can be found in Table 6.1.

Table 6.1. List of all standard LALTs used in this study.

Standard LALT	Conditions and Notes	Cl ⁻	UV	Cycling
ASTM B-117	Standard practice for operating salt spray (fog) apparatus. 5% NaCl solution, continuous spray. ¹⁴ ASTM B-117 SW used ASTM synthetic sea water solution in place of the 5% NaCl solution. ToW 75-100%	✓		
ASTM G-85 A3	Seawater acidified test, cyclic. Solution is 42 g of synthetic sea salt and 10 mL glacial acetic acid per liter of solution. 2.8≤pH≤3.0. Test cycle is 0.5 hours spray of this solution followed by 1.5 hours soak at or above 98% RH. ¹⁵	✓		✓
ASTM G-85 A5	Dilute electrolyte cyclic fog dry test. Test consists of two step cycles of 1 hour spray at room temperature and 1 hour dry off at 35°C. Solution of 0.05% sodium chloride and 0.35% ammonium sulfate. ¹⁵	✓		✓
ASTM D-4587	Standard practice for fluorescent UV-condensation exposures of paint and related coatings. 4 hours of UV (340 nm) at 0.89 W/m ² at 60°C followed by 4 hours of condensation (dark) at 50°C. ¹⁶ Condensation comes from the heating of water in a tray below the samples.		✓	✓
ASTM D-5894	Standard practice for cyclic salt fog/UV exposure of painted metal (alternating exposures in a fog/dry cabinet and a UV/condensation cabinet). A combination of ASTM G-85 Annex 5 and ASTM D-4587 Cycle 2. One week of ASTM D-4587 (4 hours of UV (340 nm) at 0.89 W/m ² at 60°C followed by 4 hours of condensation (dark) at 50°C.) followed by one week of ASTM G-85 Annex 5. ¹⁷	✓	✓	✓

Samples were also exposed in non-standard LALTs. These were conducted in a QUV™ cyclic UV exposure chamber that had been modified to allow for the input of ozone gas. The exposure conditions were cyclic condensation (CC) consisting of two hours of condensation at 50°C followed by one hour of dry out also at 50°C, CC+UV (UV added to the one hour dry out during the CC cycling, done at 50°C, all UV exposures were done at an irradiance of 0.68 W/m² centered around 340 nm wavelength), CC+O₃ (0.7-2.5 ppm), CC+O₃ (10-25 ppm), and CC+UV+O₃ (0.7-2.5 ppm). Variations in the ozone levels were caused by the UV light that decomposes ozone, as well as the cooling fans that come on during the dry out phase to cool the UV bulbs. A summary of nonstandard LALT exposure conditions can be found in Table 6.2.

Table 6.2. List of all non-standard LALTs used in this study.

LALT designation	CC (2 hour condensation + 1 hour dry out)	UV (irradiated during dry out. Wavelength is centered at 340 nm with an intensity of 0.68 W/m ²)	O ₃ (pumped into the chamber continuously)
CC	✓	none	none
CC+UV	✓	✓	none
CC+O ₃	✓	none	0.7-2.5 ppm
CC+O ₃	✓	none	10.25 ppm
CC+UV+O ₃	✓	✓	0.7-2.5 ppm

6.4.3.2 Field Exposure Conditions

Samples have also been deployed at various sites around the country for comparison to standard LALTs. A list of these sites and the site characterization data can be found in Table 6.3.

Table 6.3. Environmental severity factors for field sites.

Site Location	Mean Temp °C	% ToW	Mean RH (%)	Mean O ₃ Concentration (ppb)	Mean UV (W/m ²)	Mean Cl ⁻ dep rate (µg/cm ² /hr)	Mean Cl ⁻ dep rate (mg/m ² /day)
Coconut Island, Hi	26.2	14	75.5	-	10.11	0.30	71.18
Los Angeles, CA	17.5	-	70.3	70*	-	-	-
Point Judith, RI	10	-	77.9	72.5	-	0.051	12.2
Charlottesville, VA	15.6	-	64.6	47*	-	0.002	0.48
Kennedy Space Center, FL	23.6	-	72.0	75.3*	-	0.8	192

Note: “-” indicates that the data is not available. “*” indicates that data were taken from nearby NOAA site, not taken directly at exposure site.

6.5 **Results**

6.5.1 **Scribe Creep Analysis**

Image analysis was also performed in order to determine the scribe creep length over time for Eponol coated AA2024-T351 samples. Figure 6.5 shows an example of how scribe creep over time is tracked visually. Figure 6.5 shows the progression of scribe creep during exposure at KSC. Figure 6.6 shows scribe creep behavior for BRD. Figure 6.7 is of samples

exposed in the ASTM B-117. Figure 6.8 and Figure 6.9 show the behavior for ASTM G-85 Annex 3 and Annex 5, respectively. Figure 6.10 shows the scribe creep behavior of samples exposed in ASTM D-5894. Figure 6.11 shows the behavior of samples exposed in the non-standard LALT CC+UV+O₃ (0.7-2.5 ppm). Figure 6.12 shows a visual comparison of scribe creep for all LALTs and Figure 6.13 shows a visual comparison for field sites. The results are shown in graphical form (Figure 6.14). It can be seen from these figures that ASTM D-5894 and ASTM G-85 Annex 5 best match with KSC for appearance of corrosion at and around the scribe. The lack of scribe creep seen for samples exposed at BRD is most likely due to the mild rural/suburban nature of the site. The samples exposed at PJ, HI and LA were so degraded that it was impossible to get accurate scribe creep data.

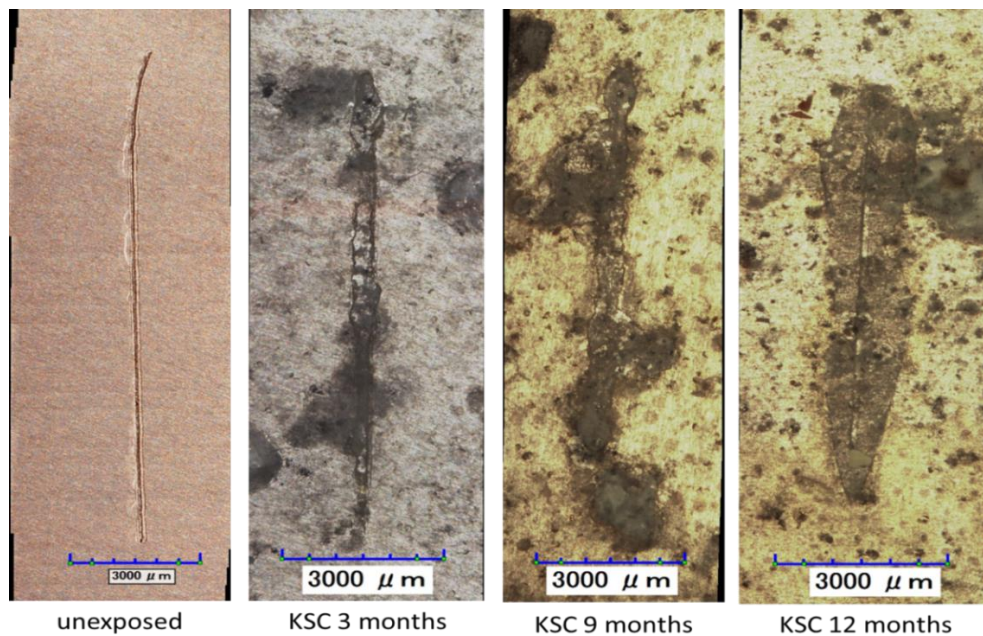


Figure 6.5. Optical Images of scribe creep over time for Eponol coated AA2024-T351 exposed at KSC.

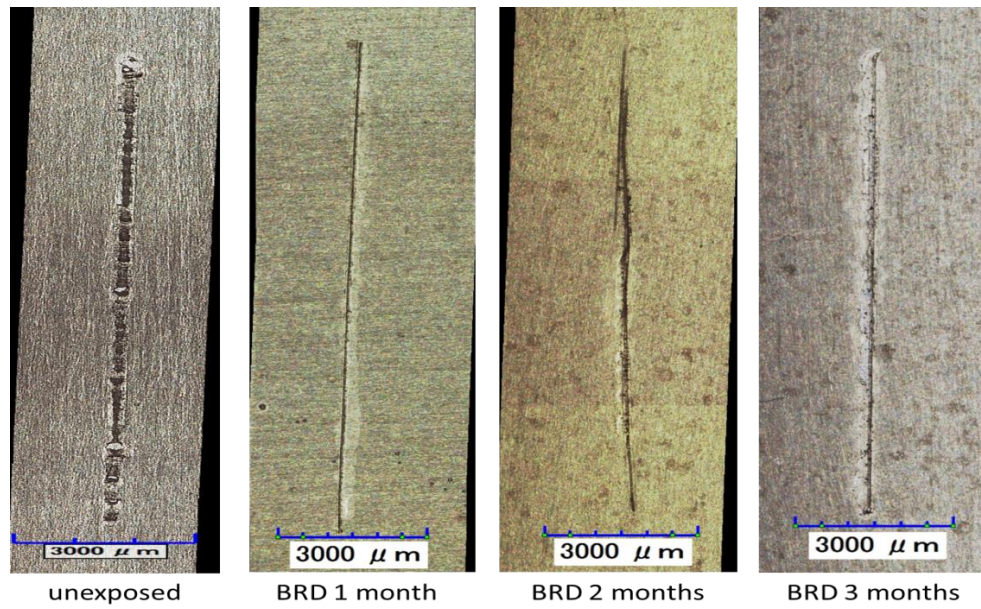


Figure 6.6. Optical Images of scribe creep over time for Eponol coated AA2024-T351 exposed at BRD.

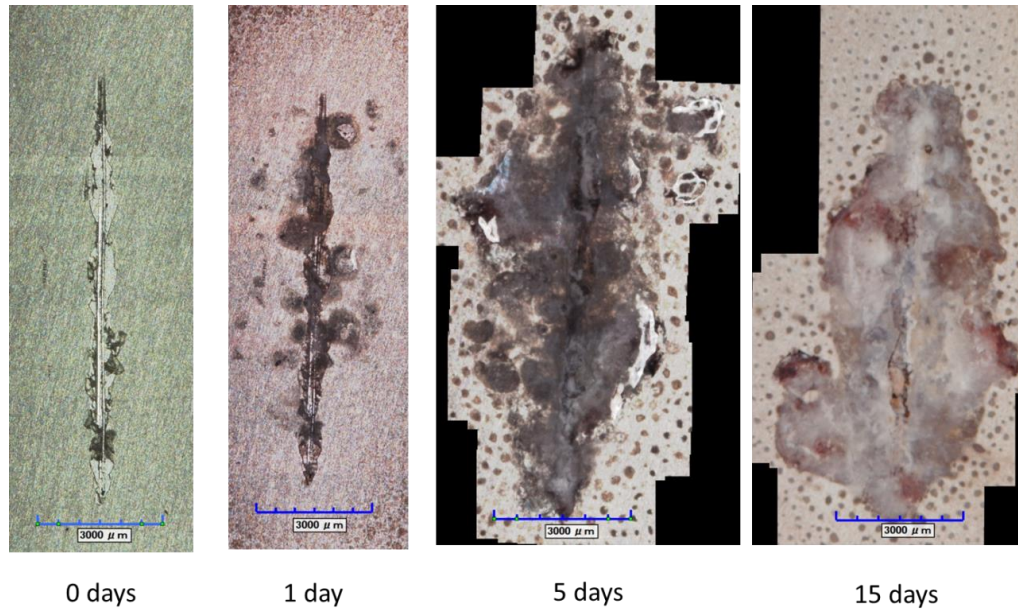


Figure 6.7. Optical images of Eponol coated AA2024-T351 exposed in ASTM B-117.

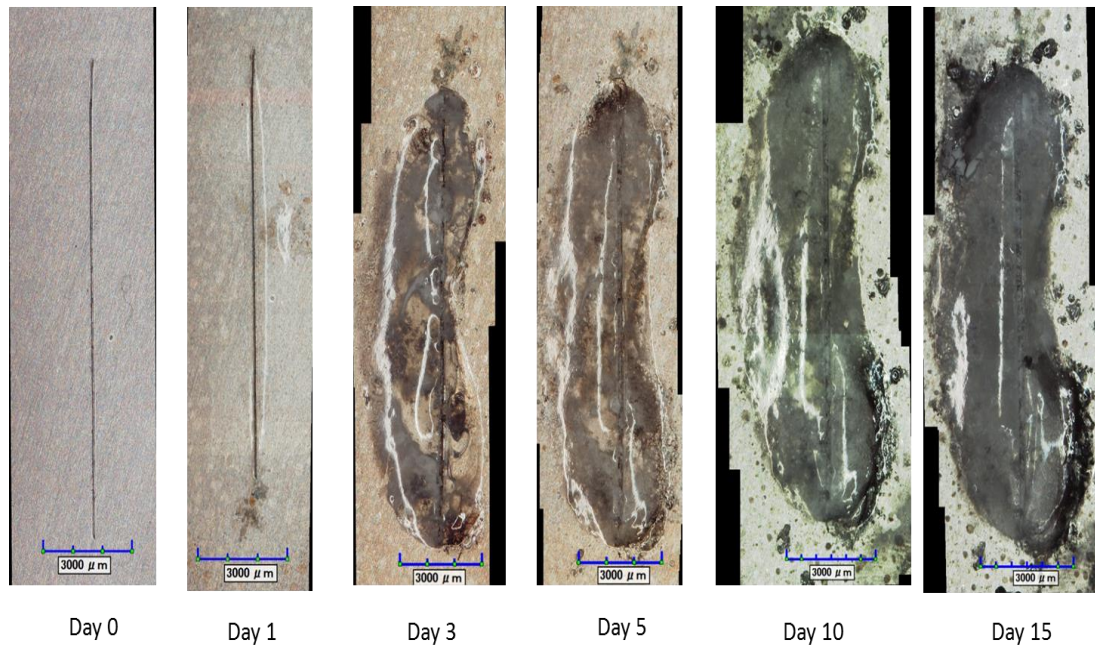


Figure 6.8. Optical Images of scribe creep over time for Eponol coated AA2024-T351 exposed to ASTM G-85 Annex 3.

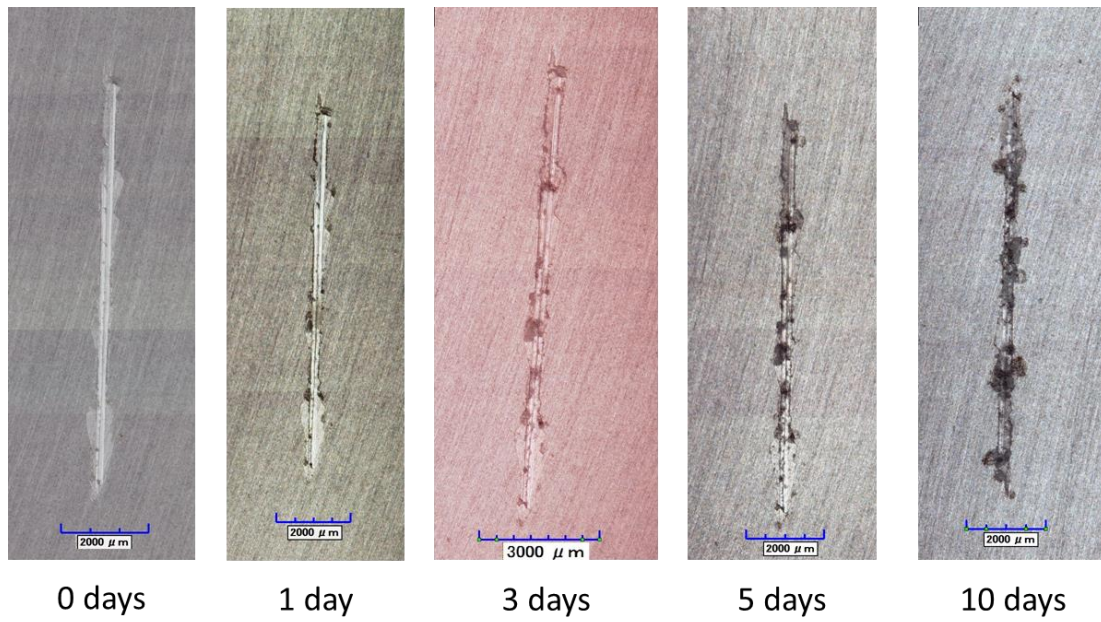


Figure 6.9. Optical images of the scribe on Eponol coated AA2024-T351 exposed to ASTM G-85 Annex 5.

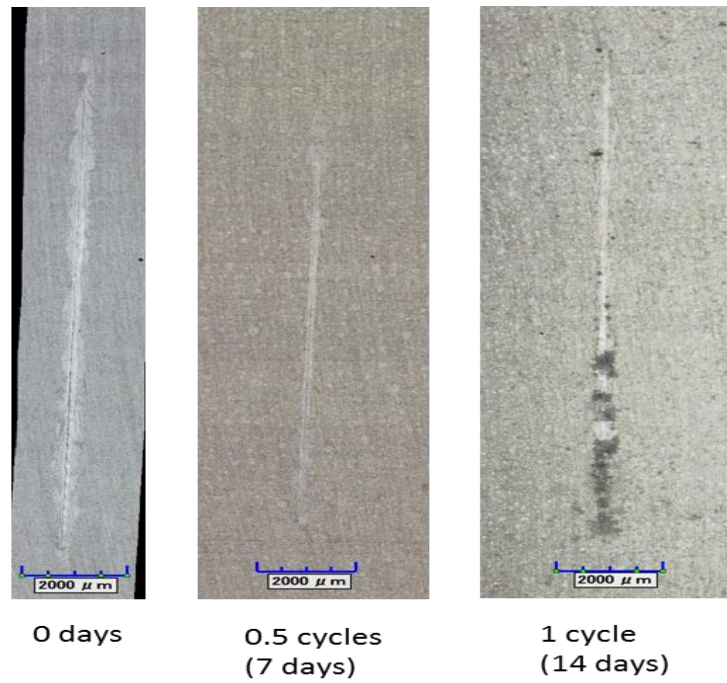


Figure 6.10. Optical images of the scribe on Eponol coated AA2024-T351 exposed to ASTM D-5894.

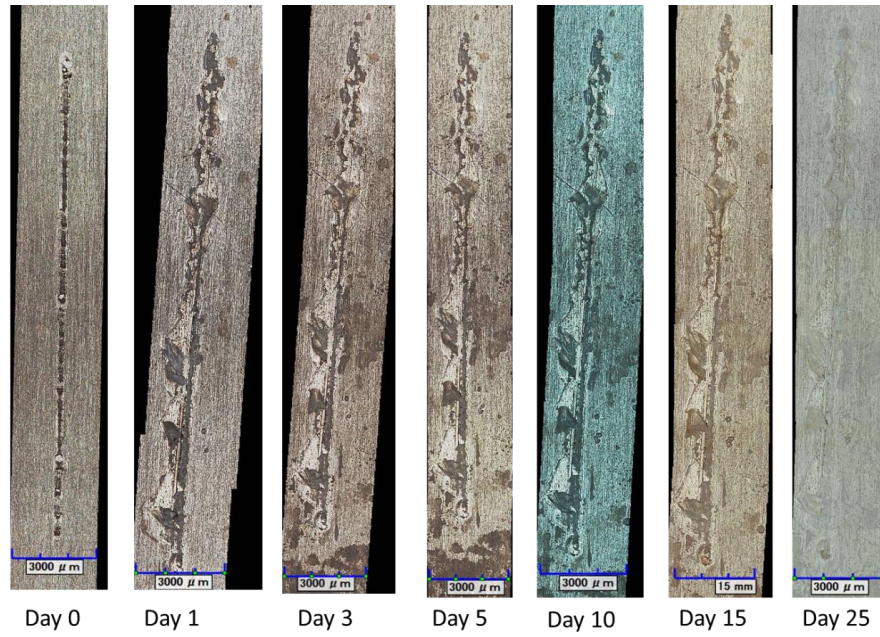


Figure 6.11. Optical images of the scribe on Eponol coated AA2024-T351 exposed to CC+O₃ (0.7-2.5 ppm).

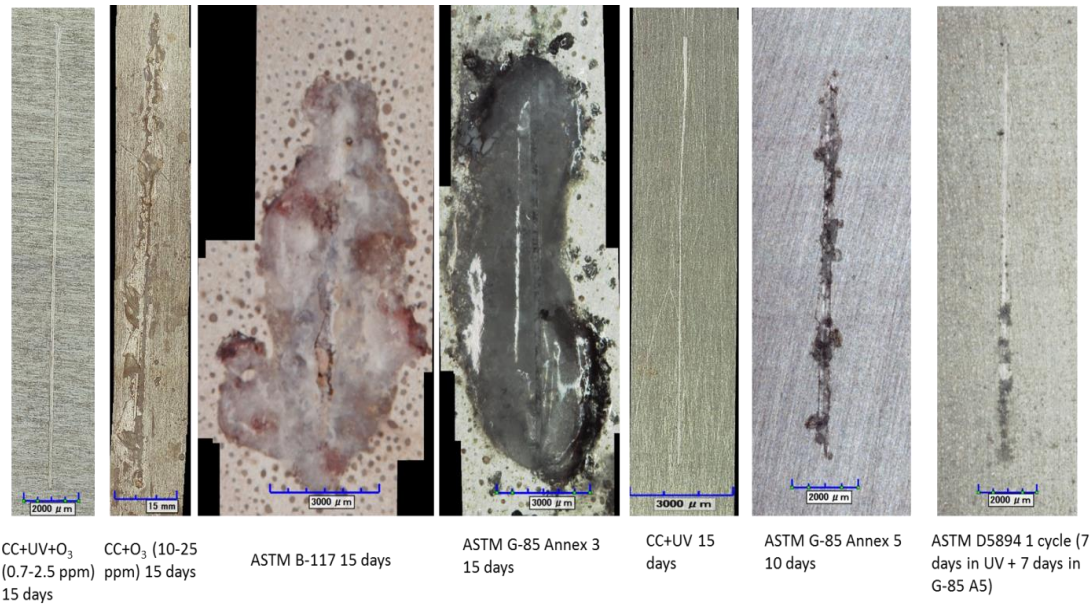


Figure 6.12. Optical images of eponol coated AA2024-T351 exposed in various LALTs showing the extent of scribe creep after 15 days.

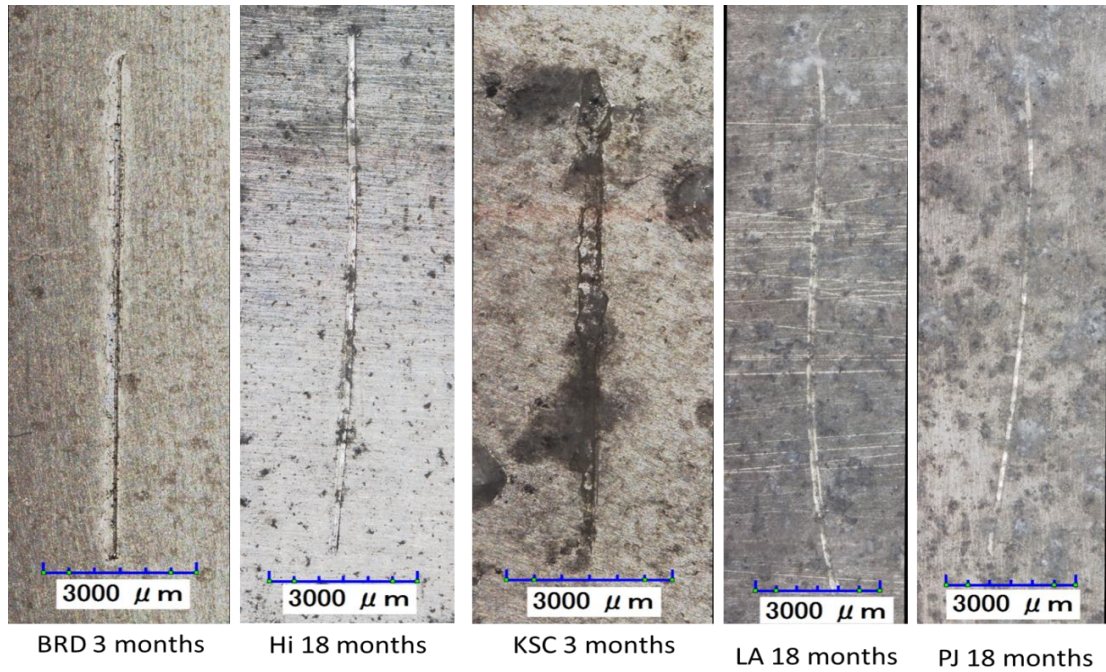


Figure 6.13. Optical images of eponol coated AA2024-T351 exposed at various field sites showing the extent of corrosion and scribe creep over time.

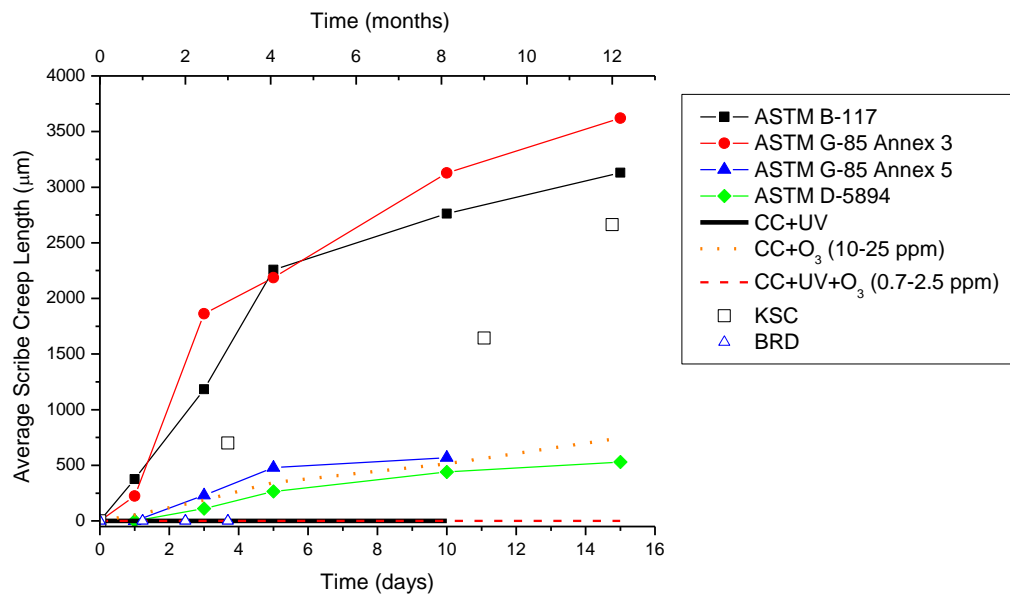


Figure 6.14. Scribe creep length over time for Eponol coated AA2024-T351 for all LALTs and field sites. The KSC and BRD data points correspond to the upper X axis, as indicated by the arrows.

From the scribe creep data obtained, acceleration factors were be calculated and are presented in Table 6.4. Acceleration factors were calculated based upon the time taken to reach a scribe creep length of 3000 μm . It should be noted that some LALTs produced no noticeable scribe creep and were therefore omitted from the table. The LALTs that produced no noticeable scribe creep obviously do not behave like KSC in that manner. Additionally, no noticeable scribe creep was seen on samples exposed at BRD, so acceleration factors with respect to BRD were not calculated. The other field sites (Hi, LA, PJ) were omitted because the overall high degradation of the coating made it difficult to determine if scribe creep had occurred.

Table 6.4. Acceleration factors for LALTs with respect to KSC based on scribe creep length.

Environment	AF wrt KSC
CC+O ₃ (10-25ppm)	3.3
G-85 A3	21
G-85 A5	3.5
B-117	14
D-5894	1.9

6.5.2 Pitting Analysis

Optical, CLSM and Hirox imaging of bare AA2024-T351 exposed to different environments indicated different pit morphologies as a function of standard lab and field environments. All samples were rinsed in DI water and dried before imaging. Samples exposed in high ozone environments had a high density of small pits, i.e., samples exposed in CC+O₃ (10-25 ppm) for 5 days had a pit density of 7.9×10^3 pits/cm² but an average pit area of only 165 μm^2 . (Figure 6.15, Figure 6.16 and Table 6.5), while samples exposed at field sites shows a

small number of large deep pits i.e., samples exposed at BRD had pit a pit density of 53.2 pits /cm² and an average pit area of 367 μm² (Figure 6.17 and Table 6.5). Image comparisons can be seen for samples exposed at field sites (Figure 6.18 and Figure 6.19) and for samples exposed in LALTs (Figure 6.20).

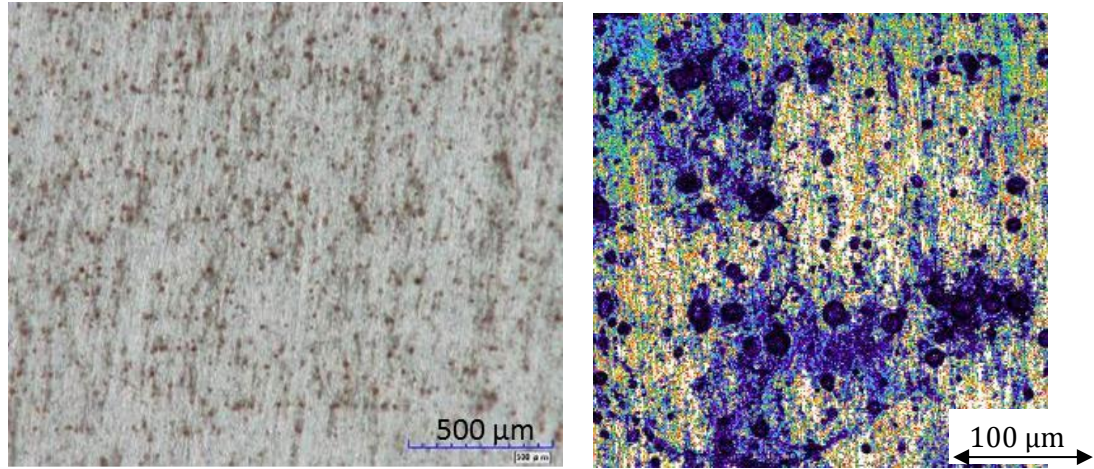


Figure 6.15. Optical image (left) and CSLM image (right) of pitting on bare AA2024 exposed to CC+O₃ (10-25 ppm) for 5 days. All samples rinsed in DI water before imaging.

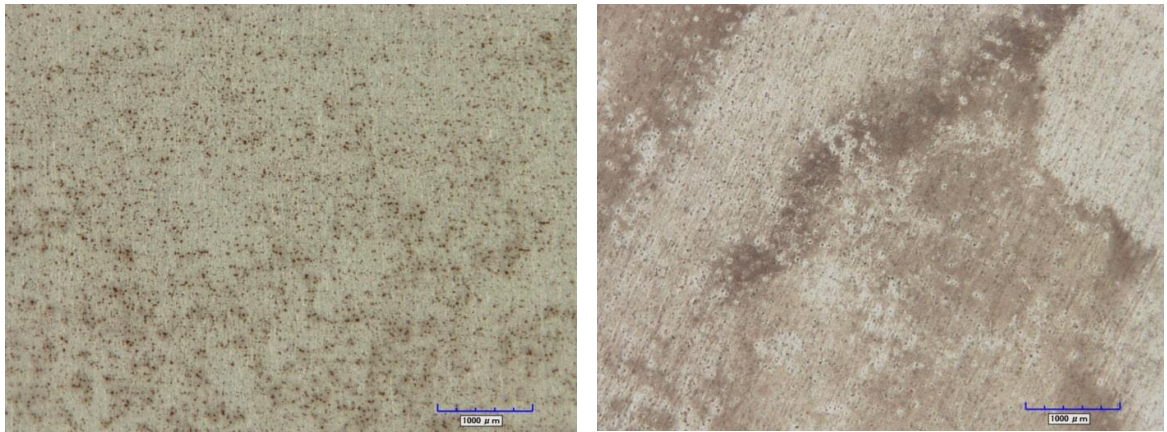


Figure 6.16. Optical images of pitting on bare AA2024-T351 exposed in CC+O₃ (0.7-2.5 ppm) for 15 days (left) and CC+O₃ (10-25 ppm) for 5 days (right). All samples rinsed in DI water before imaging.

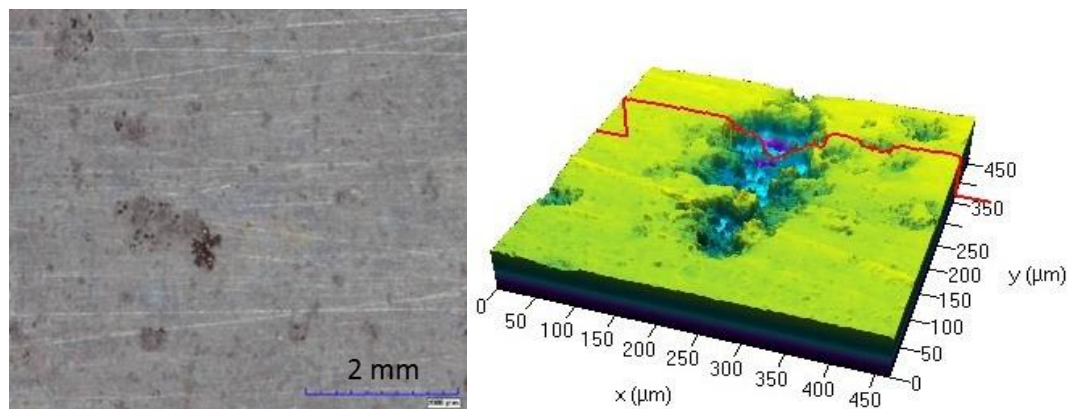


Figure 6.17. Optical image (left) and CLSM image (right) of pitting on bare AA2024 exposed at LA for 9 months. All samples rinsed in DI water before imaging.

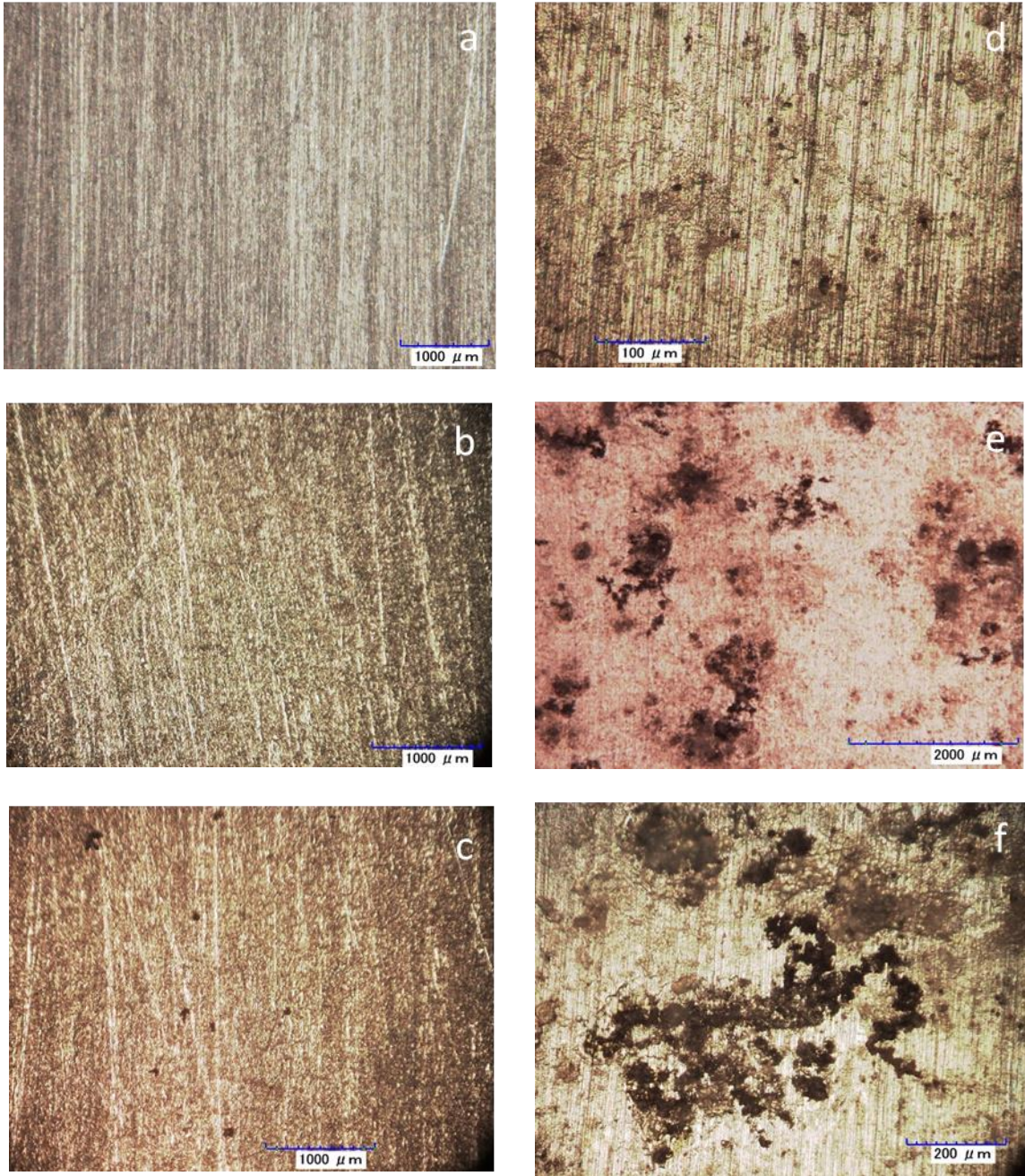


Figure 6.18. Optical images of pitting on bare AA2024-T351. a) unexposed sample, b) exposed at BRD for 1 month, c) Exposed at BRD for 3 months, d) Exposed at KSC for 1 month, e) exposed at KSC for 3 months, f) exposed at KSC for 3 months. All samples rinsed in DI water before imaging.

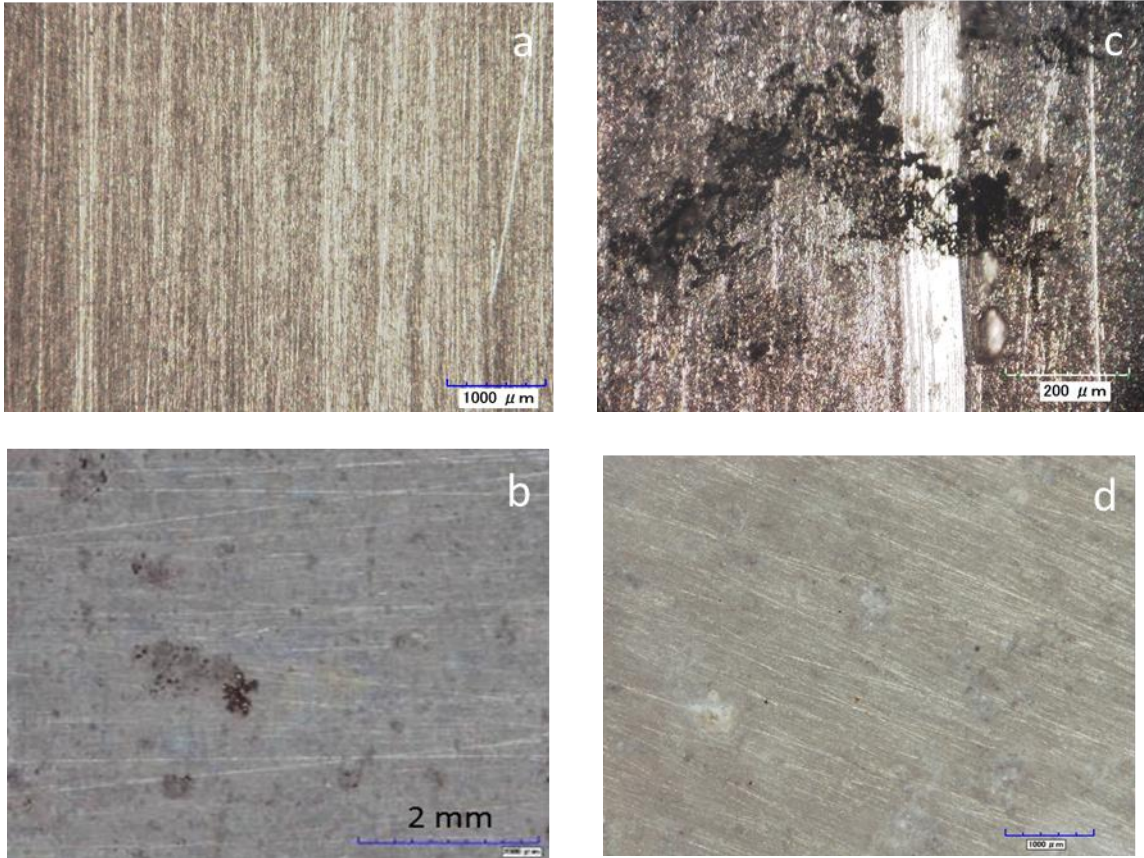


Figure 6.19. Optical images of pitting on bare AA2024-T351 a) unexposed, b) exposed at LA for 9 months, c) exposed at KSC for 3 months, d) exposed at PJ for 9 months. All samples rinsed in DI water before imaging.

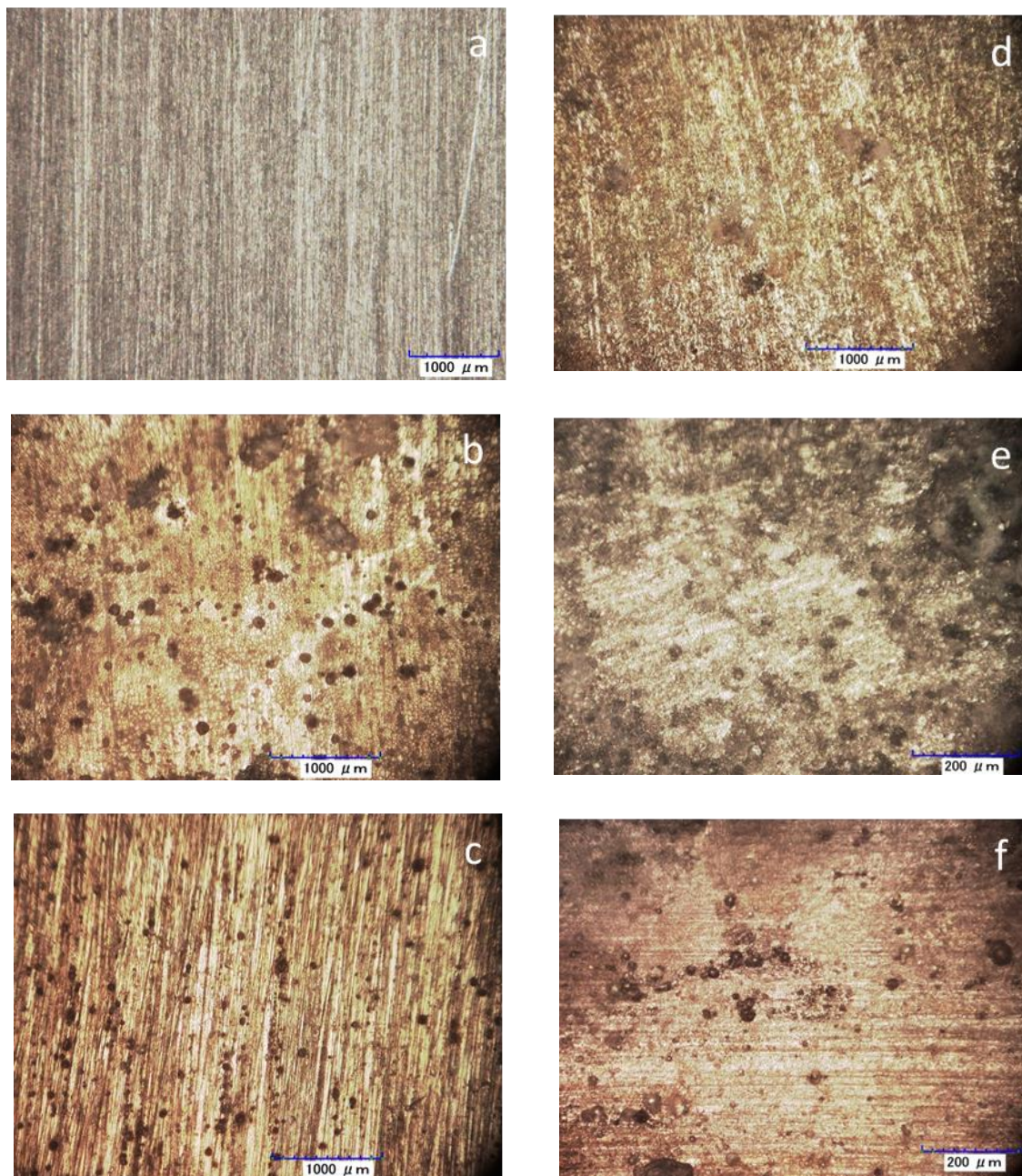


Figure 6.20. Optical images of pitting on bare AA2024-T351 a) unexposed, b) exposed in ASTM D-5894 for 1 cycle (14 days), c) exposed in ASTM D-4587 for 15 days, d) exposed in ASTM G-85 Annex 5 for 10 days, e) exposed in ASTM G-85 Annex 3 for 15 days, f) exposed in ASTM B-117 for 15 days. All samples rinsed in DI water before imaging.

In order to perform a quantitative measurement of pitting across the different exposure conditions, image analysis was performed using ImageJ software ¹¹. An optical image, like the one in Figure 6.21, was converted into a binary black and white image. The image was then processed to determine, total number of pits, total area of pits, average area per pit and the area fraction of pits. The results can be seen in Table 6.5. Using the results obtained from ImageJ, histograms were also constructed of the distribution of pit sizes. Due to the difference in the size of the pits the bins are not the same size for each graph. However, the general trends can be seen. Namely, KSC and ASTM B-5894 both show large numbers of small pits but then have long tails in pit size distributions indicating a few pits that are much larger than the rest (Figure 6.22 and Figure 6.23). ASTM B-117 shows a much smaller tail in pit size distribution and a more normal distribution (Figure 6.24).

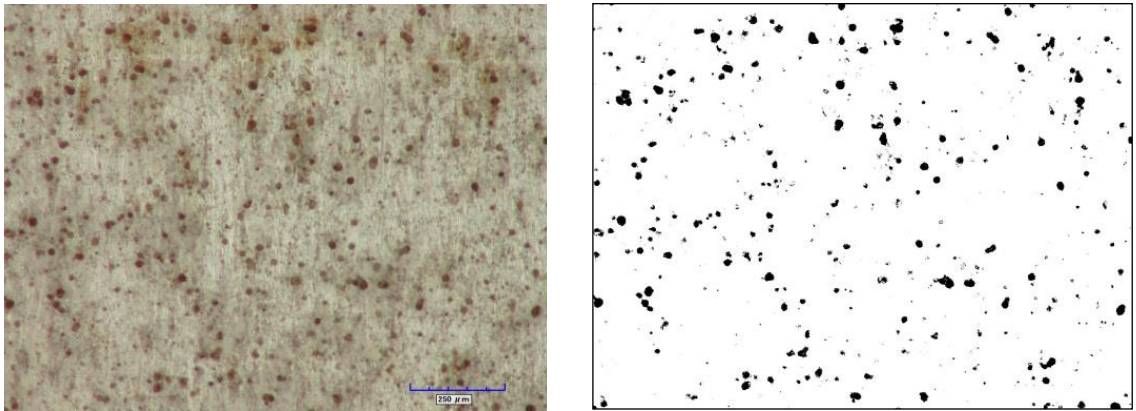
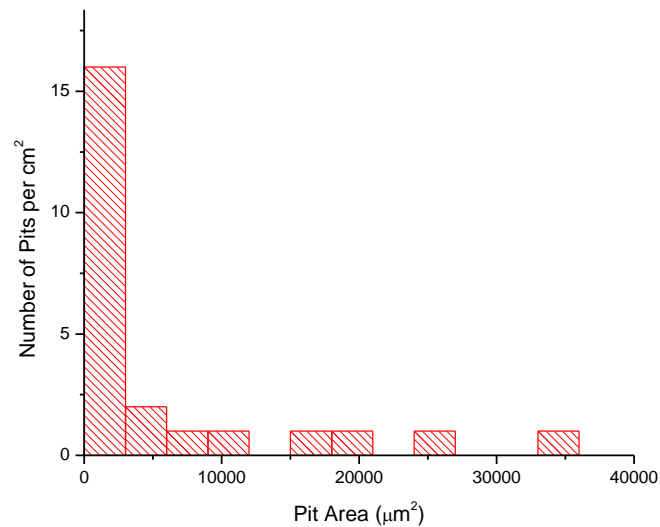


Figure 6.21. Optical image (left) and binary image (right) of pitting on bare AA2024-T351 exposed to CC+UV+O₃ (0.7-2.5 ppm) for 15 days. All samples rinsed in DI water before imaging.

Table 6.5. Summary of Image Analysis of Pitting on bare AA2024-T351

Exposure	Average Pit Area (μm^2)	Area Fraction	Pit Density (pits/ cm^2)
CC+UV+O ₃ (0.7-2.5 ppm) 15 days	289.5	5.8	2×10^4
CC+O ₃ (10-25 ppm) 5 days	165	1.3	7.9×10^3
CC+UV 15 days	160.1	0.1	624.6
CC 15 days	90	0.3	3.3×10^3
ASTM G-85 Annex 5 15 days	331.5	0.6	1.8×10^3
ASTM D-5894 15 days	249.1	0.9	3.6×10^3
ASTM D-4587 15 days	99	0.3	3.0×10^3
ASTM B-117 15 days	102	1.3	1.3×10^4
KSC 3 months	954	10.2	1.1×10^4
BRD 1 month	0	0	0
BRD 3 months	376	0.02	53.2
PJ 3 months	228	0.8	3.5×10^3
LA 3 months	137	0.3	2.2×10^3
Hi 3 months	162	0.4	2.5×10^3

Note: Samples exposed in ASTM G-85 Annex 3 were too corroded to obtain any meaningful pitting data.

**Figure 6.22. Histogram of pit area for bare AA2024-T351 exposed at KSC for 3 months.**

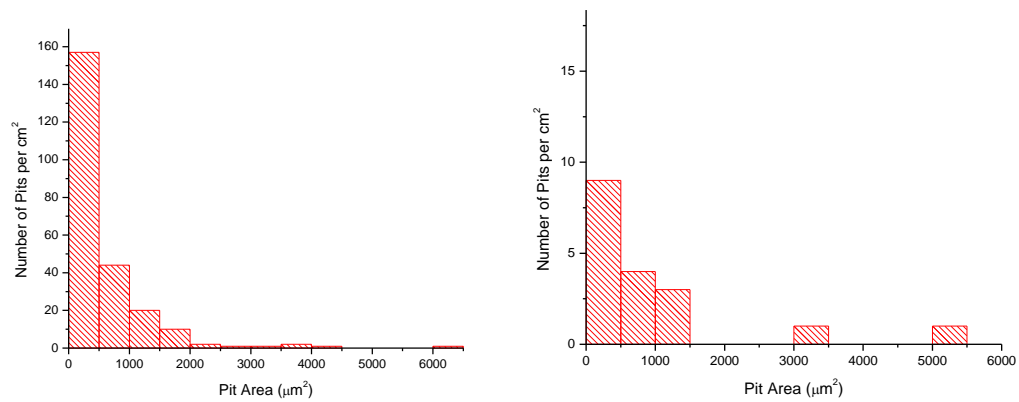


Figure 6.23. Histograms of pit area for bare AA2024-T351 exposed in ASTM D-5894 for 1 cycle (14 days) (left) and for samples exposed at KSC for 3 months (right). Note that the x axis scales are equal in this figure and that the x axis scales for samples exposed at KSC is different in this figure compared with Figure 6.22.

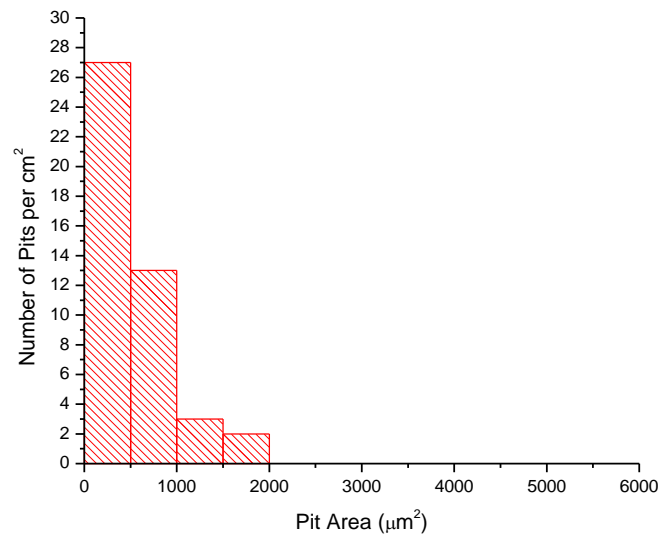


Figure 6.24. Histogram of pit area for bare AA2024-T351 exposed in ASTM B-117 for 15 days.

6.5.3 Corrosion Analysis by SEM and EDS

During analysis of optical images, images from samples exposed in high ozone (10-25 ppm) showed different pit morphologies that were not seen in other exposures. As can be seen in Figure 6.25, there are gray spots that were not identified at first. This sample was cleaned for 30 seconds in a 50% nitric acid solution to remove the surface oxide for further analysis. SEM (Figure 6.26) and EDS (Figure 6.27) analysis later showed these to be pits that had been filled with oxide deposits.

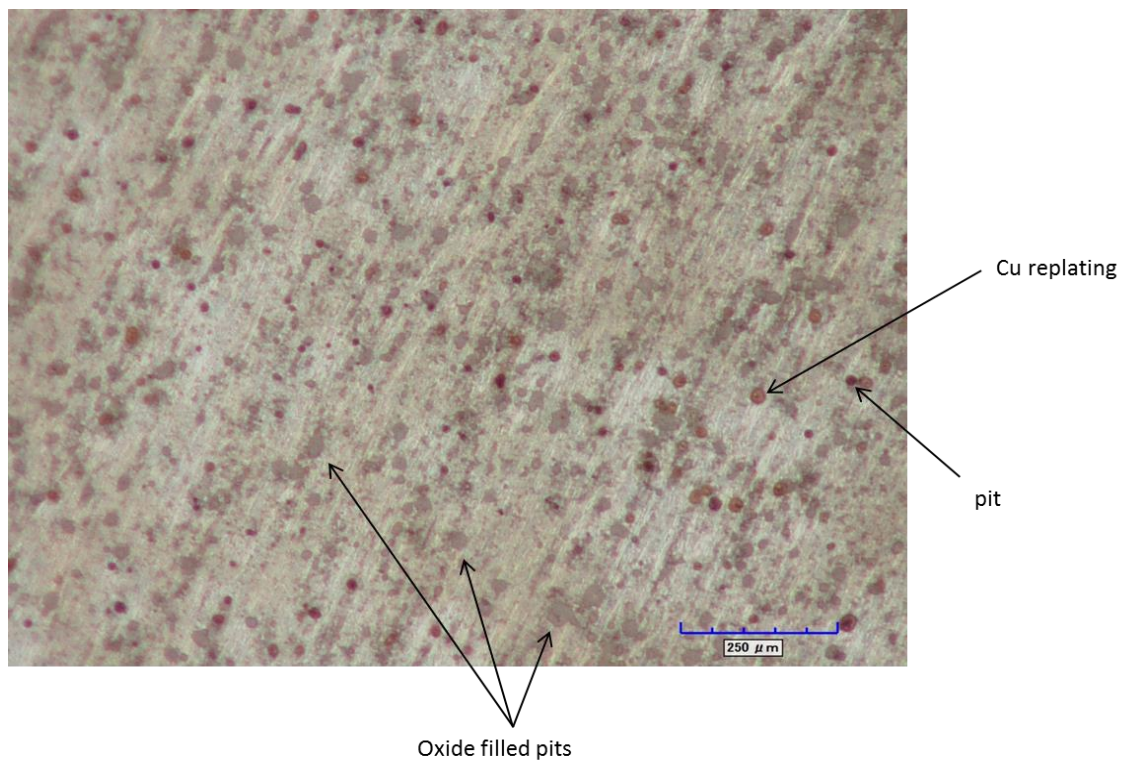


Figure 6.25. Optical image of AA2024-T351 exposed in CC+O₃ (10-25 ppm) for 5 days showing open pits, copper replating and oxide filled pits. Sample was rinsed with DI water before imaging.

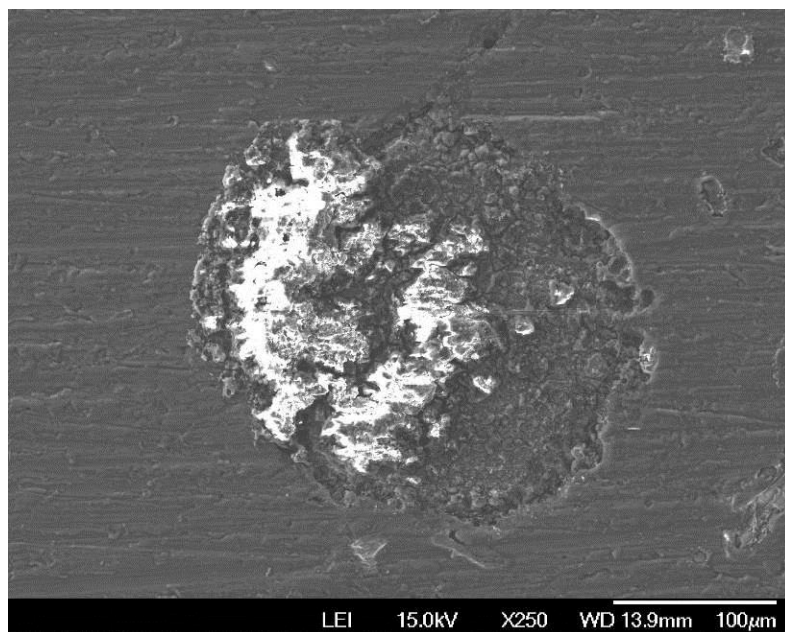


Figure 6.26. SEM image of pit that is filled with oxide. Sample exposed in CC+O₃ (10-25 ppm) for 5 days. Sample was rinsed with DI water before imaging.

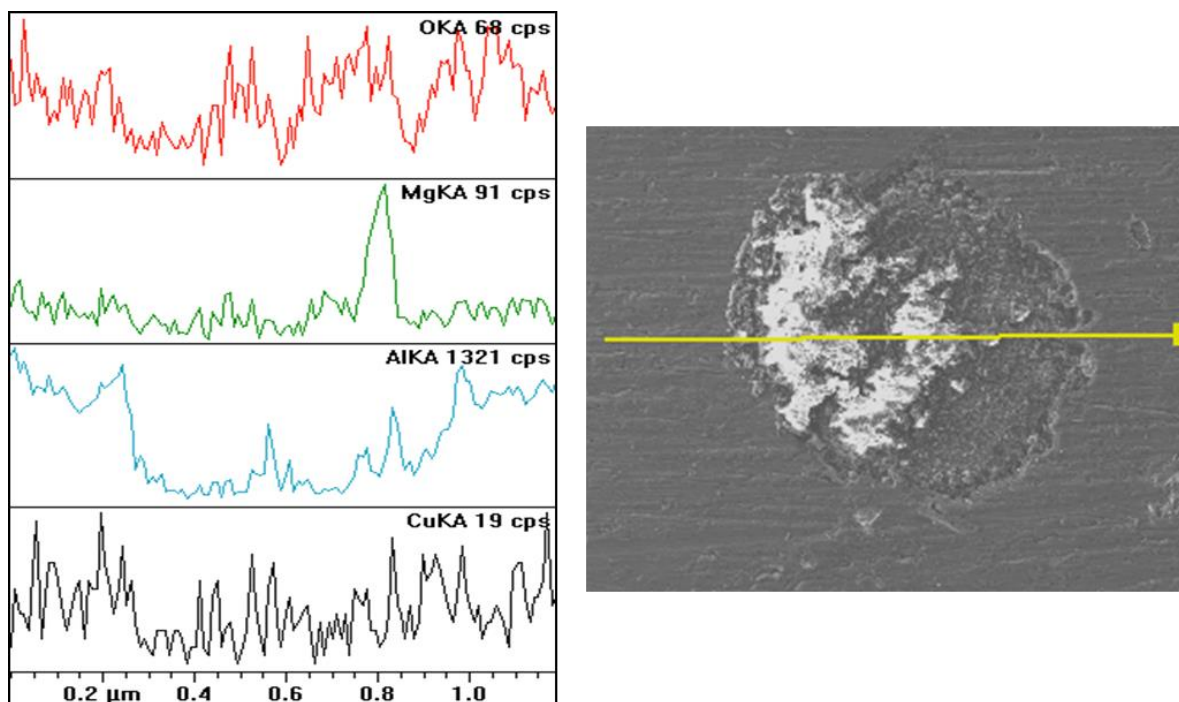


Figure 6.27. EDS linescan of oxide filled pit of a bare AA2024-T351 sample exposed in CC+O₃ (10-25 ppm) for 5 days. The spectra on the left show the relative abundances of oxygen, magnesium, aluminum and copper. The image on the right shows the length and direction of the scan. Sample was rinsed with DI water before imaging.

Pits exposed to high ozone (10-25 ppm) grow outward by undercutting the surface oxide layer. Figure 6.28 shows the pits that have grown down into the metal and have undercut the surface oxide which results in eventual collapse of the unsupported oxide. It is unclear at this time if this process creates the oxide filled pits.

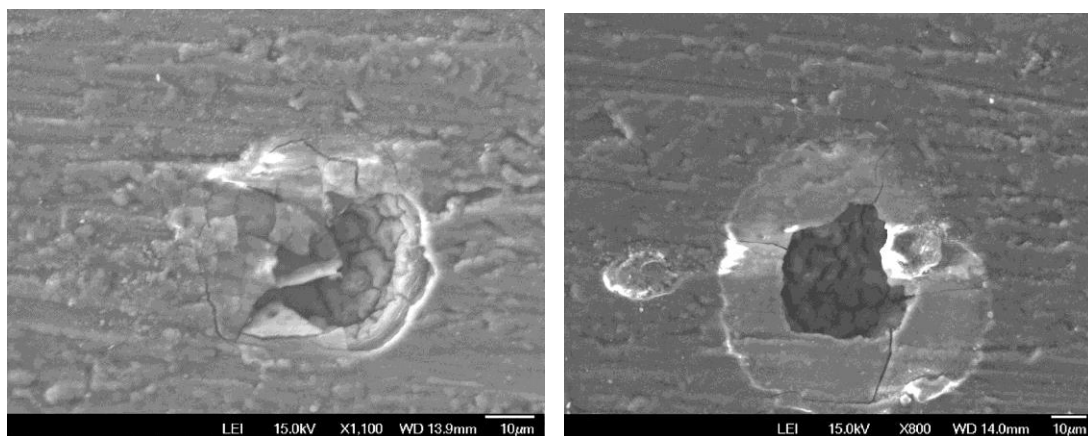


Figure 6.28. Images of small pits growing by undercutting the surface oxide layer on bare AA2024-T351 exposed to CC+O₃ (10-25 ppm) for 5 days. Sample was rinsed with DI water before imaging.

Samples exposed to CC+O₃ (10-25 ppm) were immersed in a 60% nitric acid solution to remove the surface oxide. This was done to these samples to determine the nature of the filled pits and the material filling the pits. These samples were imaged in the SEM and the results can be seen in Figure 6.29. The images show both smooth pits and rough pits. The lower left image of Figure 6.29 shows pits growing underneath the surface oxide.

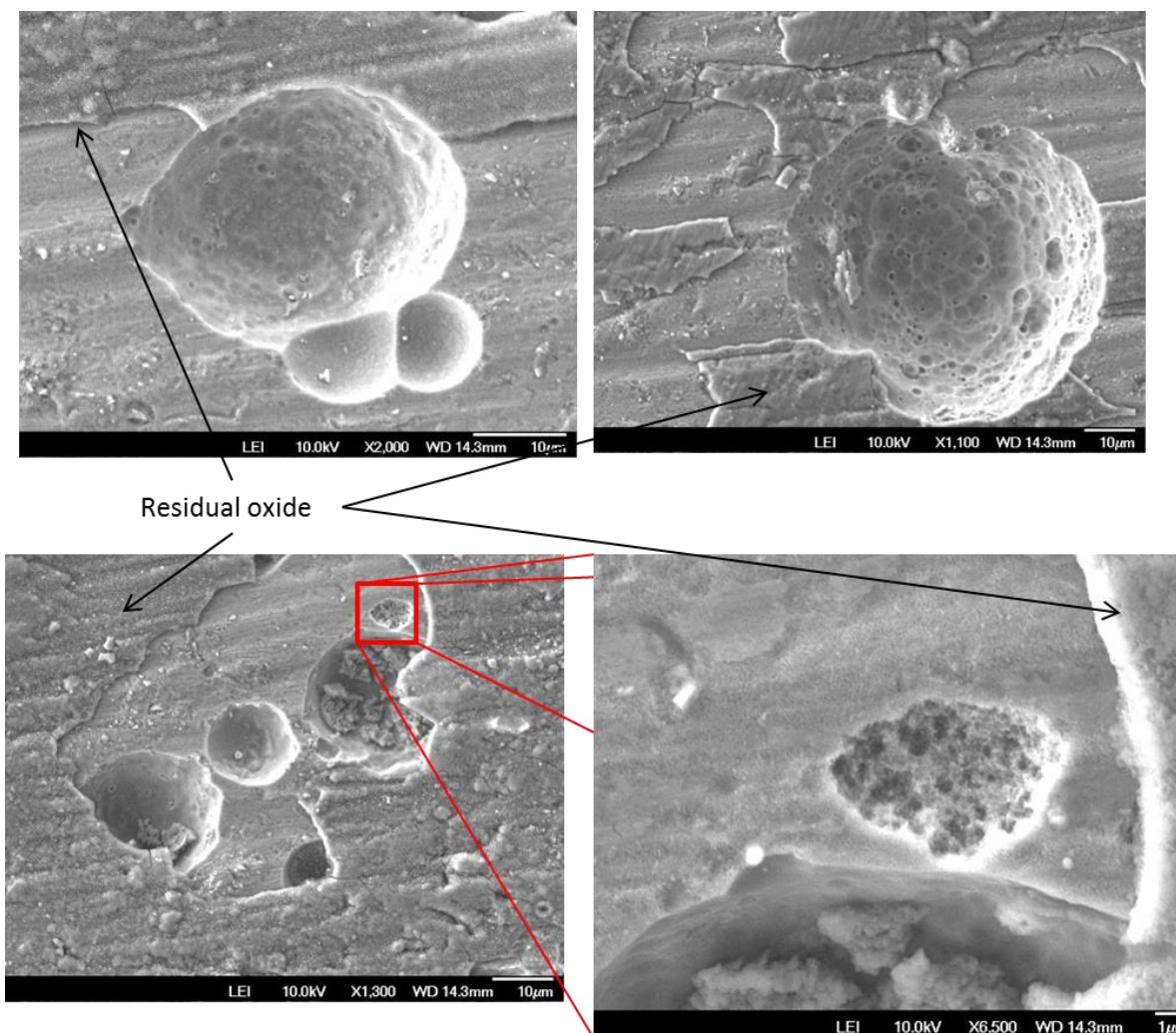


Figure 6.29. SEM images of AA2024-T351 exposed in CC+UV+O₃ (0.7-2.5 ppm) for 15 days and then immersed in 60% nitric acid solution to remove the surface oxide. Sample was rinsed with DI water before imaging.

SEM imaging of samples exposed in different conditions also showed the differences in pit morphology between differing exposure conditions. Samples exposed in high ozone showed a large number of small pits (Figure 6.15, Figure 6.28). Samples exposed in CC+UV+O₃ (0.7-2.5 ppm) showed fewer pits that were larger than the pits in the high ozone exposure (Figure 6.21, Table 6.5). These samples also showed many small surface oxide particles that were absent from the samples exposed to high ozone without UV (Figure

6.30). Samples exposed at field sites showed pits that were very different from the LALT exposed samples. Figure 6.31 shows the cracked and broken morphology that was commonly seen in samples exposed at field sites. These pits were generally larger and farther apart than the pits in LALT exposed samples. Subsequent EDS analysis showed an abundance of sodium in the pit indicating the presence of sodium chloride.

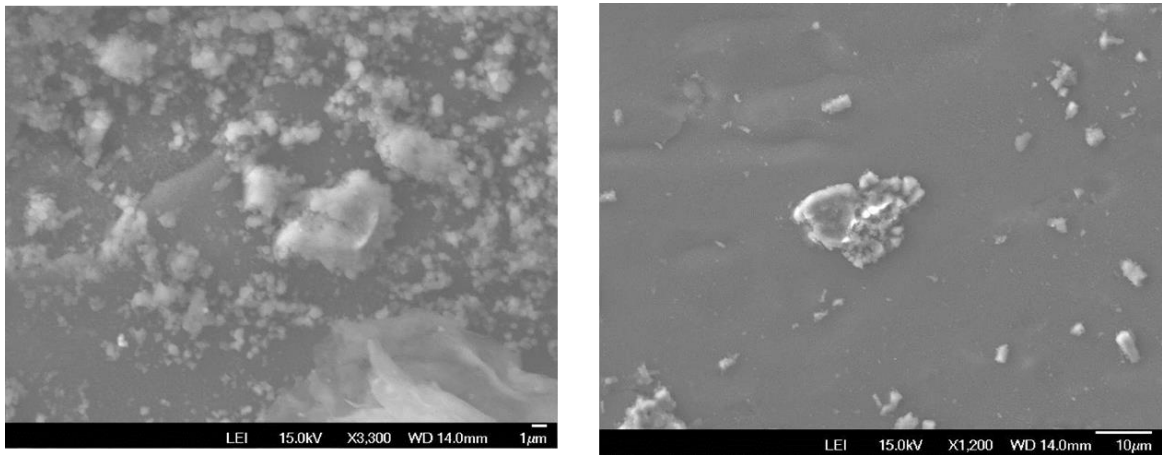


Figure 6.30. SEM images of bare AA2024-T351 exposed to CC+UV+O₃ (0.7-2.5 ppm) for 15 days showing oxide particles on the surface of the sample. The particles were absent from samples exposed in other conditions. Sample was rinsed with DI water before imaging.

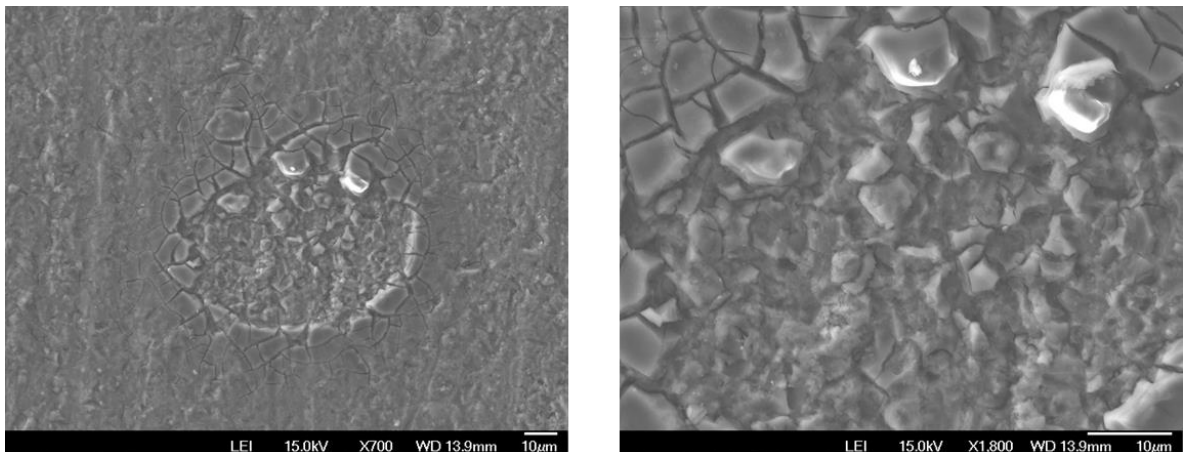


Figure 6.31. SEM images of bare AA2024-T351 exposed at LA for nine months showing pit morphology characteristic of samples exposed at field sites. Sample was rinsed with DI water

before imaging.

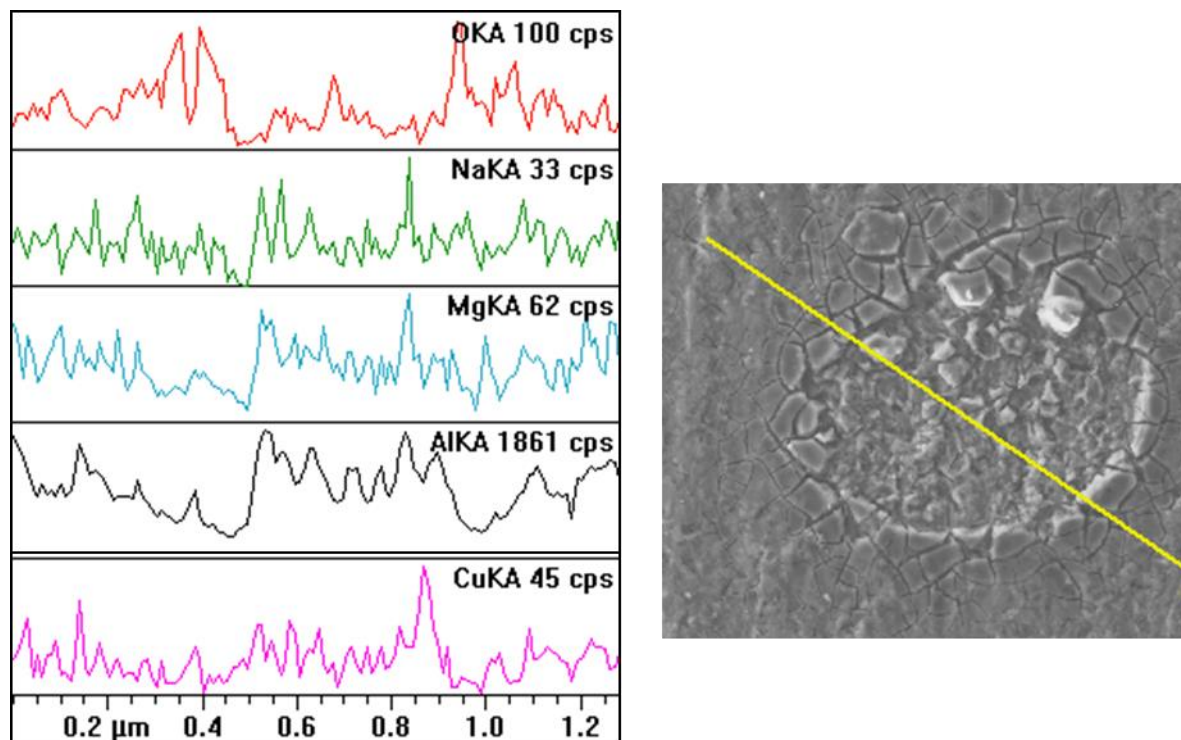


Figure 6.32. EDS spectra (right) of a pit on bare AA2024-T351 exposed at LA field site for 9 months. The image on the right shows the direction of the scan. Sample was rinsed with DI water before imaging.

6.5.4 Coating Analysis

6.5.4.1 Electrochemical Impedance Spectroscopy Analysis

AA2024-T351 samples exposed to various LALTs and field environments listed in Table 1.5 and Table 1.6 were examined by EIS. The EIS data has been obtained from the LALTs and the field sites over exposure times. EIS scans were performed at two locations on the sample, near to the scribe and far from the scribe (see Figure 6.4). The EIS data is presented

below, starting with KSC (Figure 6.33) and BRD (Figure 6.34). KSC shows degradation of the coating electrical properties nearly equally both near to and far from the scribe. This is indicative of an ESF that attacks the coating specifically and only moderate corrosion conditions that attack the bare metal at the scribe. LALTs that have no ESF that attacks the coating specifically, like ASTM B-117 and ASTM G-85 Annex 5, show more coating degradation near to the scribe where corrosion occurs than far from the scribe (Figure 6.35 and Figure 6.37). Thus, one significant difference is whether ESFs affect the coating or induce corrosion which is reflected by scribe creep and particularly a drop in EIS parameters near the scribe. Samples exposed in ASTM G-85 Annex 3 show nearly equal drop in EIS parameters near to and far from the scribe, this is most likely due to the acidic nature of the test. The non-standard LALTs show nearly equal degradation both near and far for all tests incorporating either UV or ozone (Figure 6.40 through Figure 6.42). Acceleration factors were calculated for the LALTs based on the low frequency impedance values ($Z_{|0.01|}$). The acceleration factors are reported in Table 6.6.

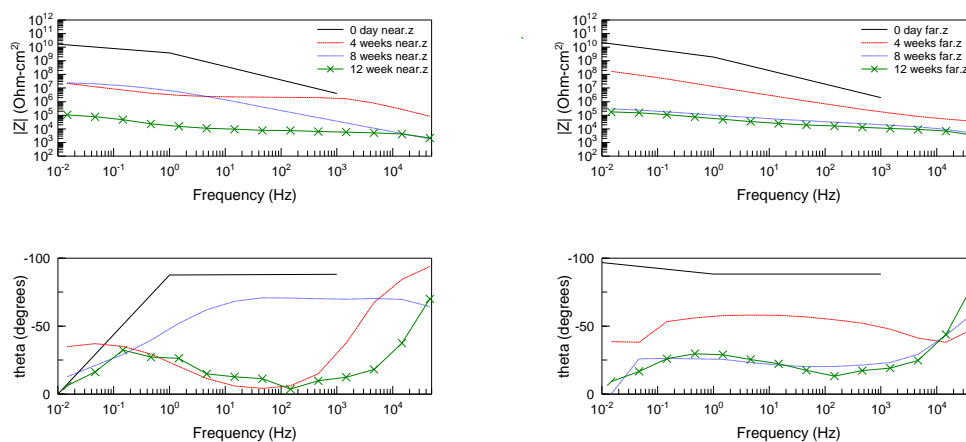


Figure 6.33. EIS data for coated AA2024 exposed at Kennedy Space Center, FL. Left is near and right is far.

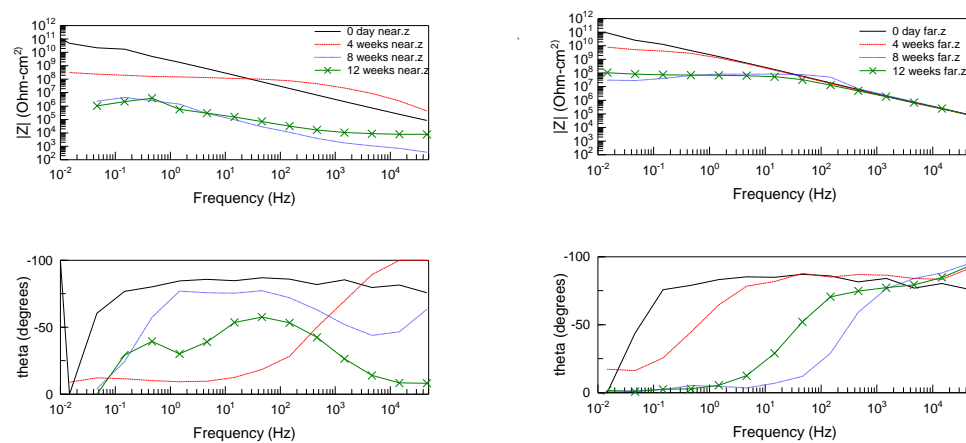


Figure 6.34. EIS data for coated AA2024 exposed at Birdwood Golf Course, Charlottesville VA (BRD). Left is near and right is far.

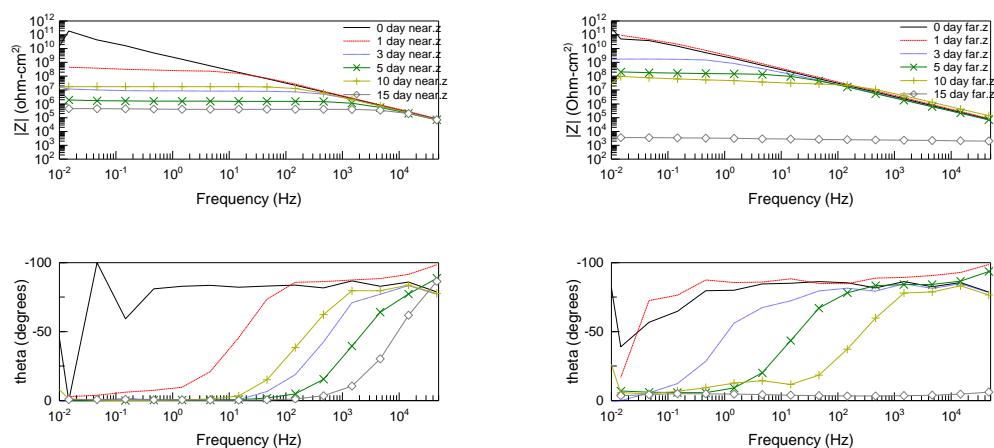


Figure 6.35. EIS data for coated AA2024 exposed to ASTM B-117. Left is near and right is far.

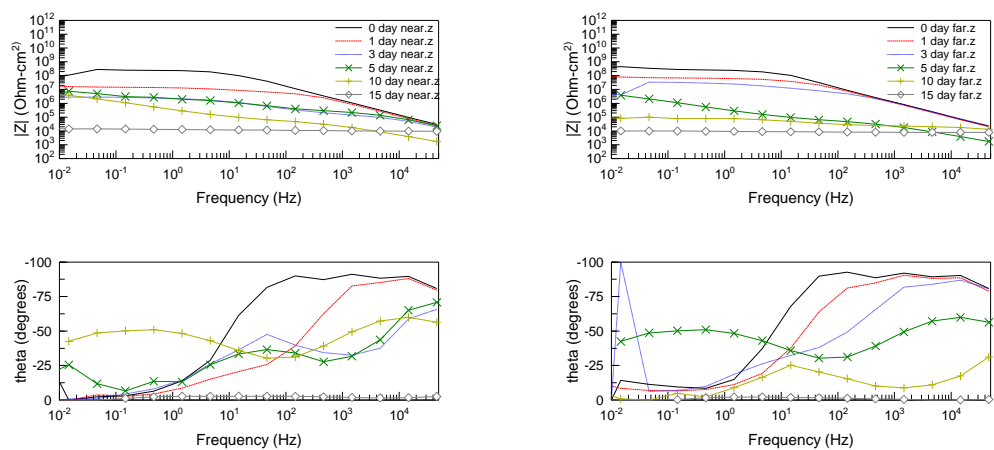


Figure 6.36. EIS data for coated AA2024 exposed to ASTM G-85 Annex 3. Left is near and right is far.

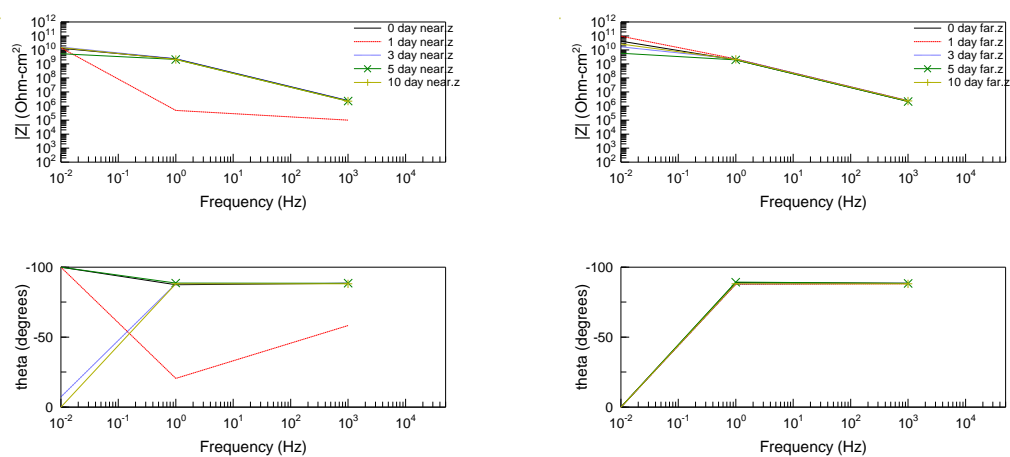


Figure 6.37. EIS data for coated AA2024 exposed to ASTM G-85 Annex 5. Left is near and right is far.

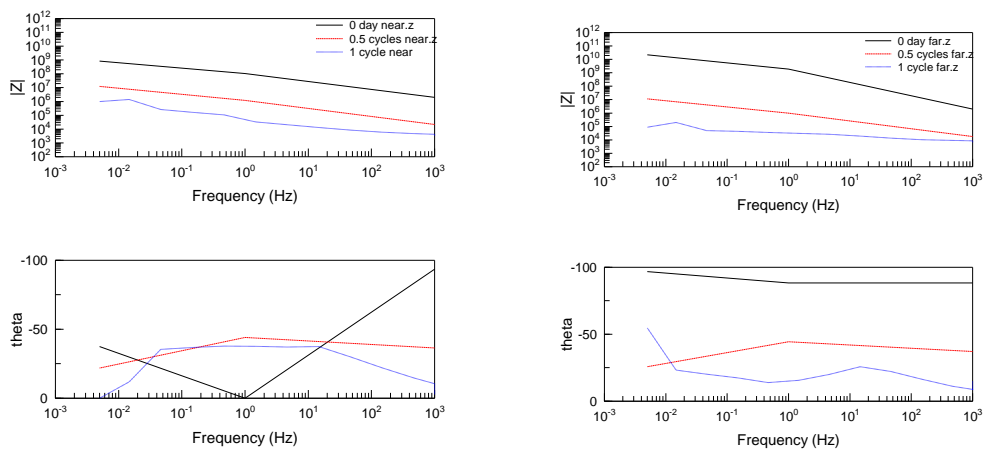


Figure 6.38. EIS data for coated AA2024 exposed in ASTM D-5894. Left is near and right is far.

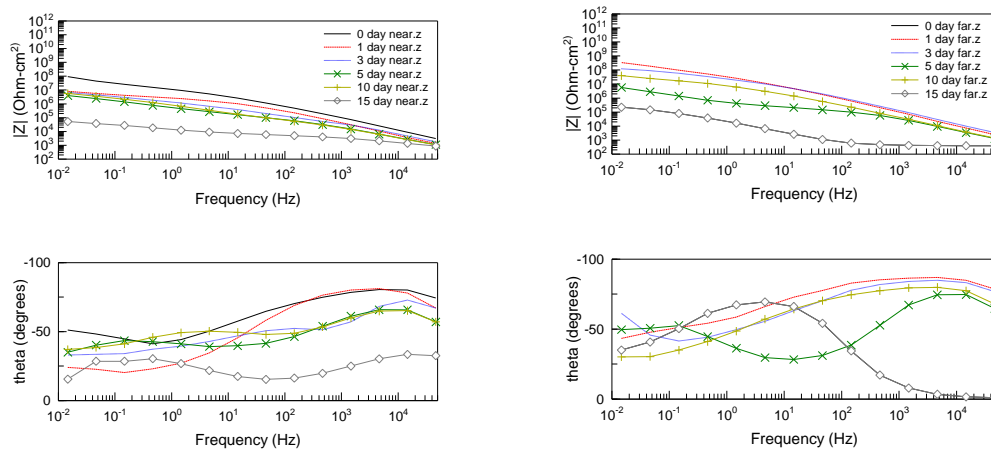


Figure 6.39. EIS data for coated AA2024 exposed to CC. Left is near and right is far.

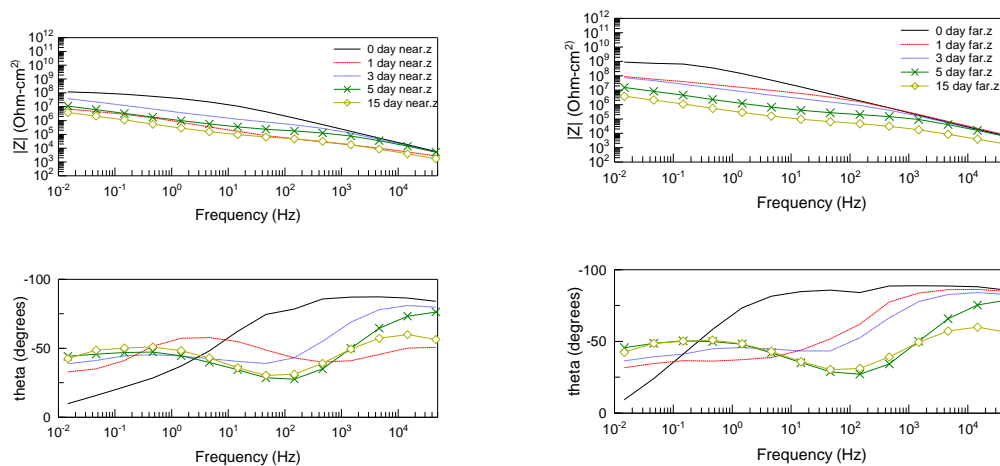


Figure 6.40. EIS data for coated AA2024 exposed to CC+UV. Left is near and right is far.

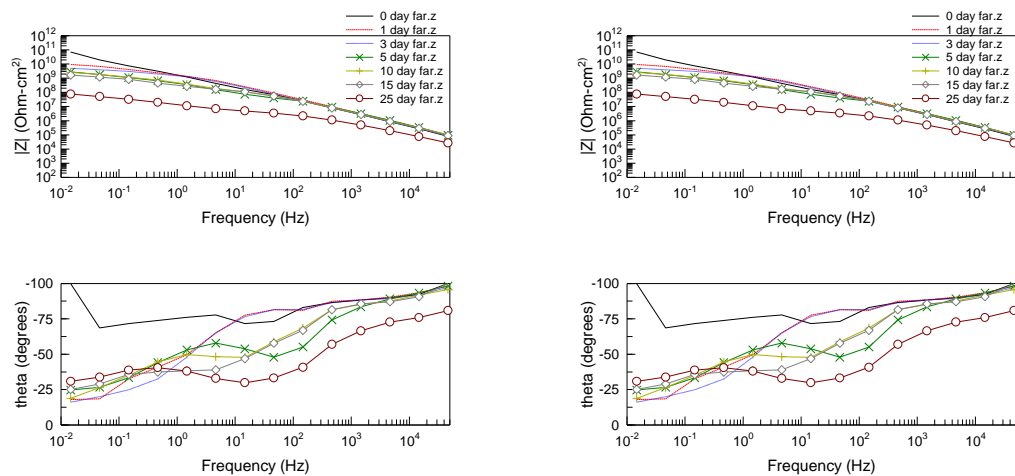


Figure 6.41. EIS data for coated AA2024 exposed to CC+O₃ (0.7-2.5ppm). Left is near and right is far.

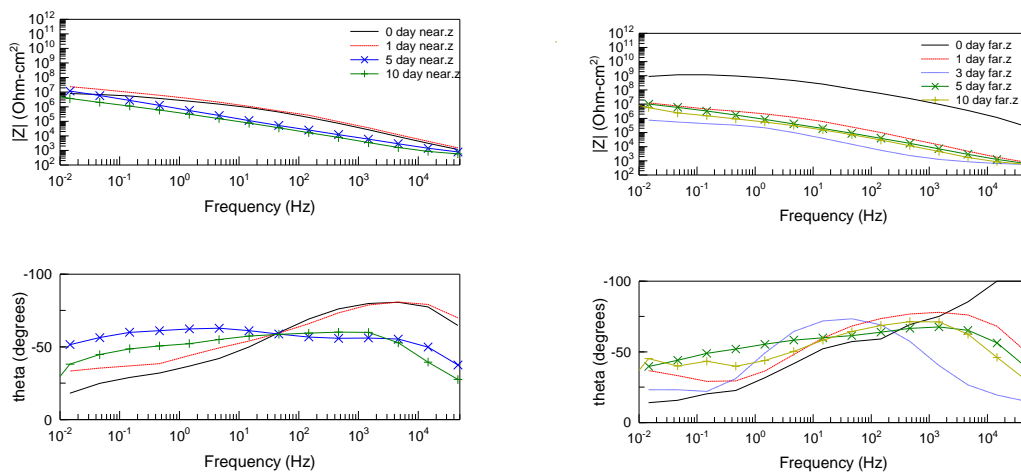


Figure 6.42. EIS data for coated AA2024 exposed to CC+UV+O₃ (0.7-2.5ppm). Left is near and right is far.

Table 6.6. Acceleration factors for AA2024-T351 based on low frequency impedance ($Z_{0.01}$).

Test	AF wrt BRD	AF wrt KSC	AF wrt Hi	AF wrt LA	AF wrt PJ
CC+UV	5.6	2.8	3.27	3.83	2.13
CC+O3(10-25ppm)	16.8	8.4	9.8	11.5	6.4
CC+O3(0.7-2.5ppm)	3.36	1.68	1.96	2.3	1.28
CC+UV+O3(0.7-2.5ppm)	11.2	5.6	6.53	7.7	4.27
ASTM G-85 A3	16.8	6.3	9.8	11.5	6.4
ASTM G-85 A5	4.48	1.68	2.61	3.07	1.71
ASTM B-117	9.6	3.6	5.6	6.57	3.66
ASTM D-5894	12	4.5	7	8.2	4.6

EIS data can provide a wealth of information. In addition to the change in the electrical resistance of the coating over time (previous EIS plots), the saddle frequency method was used to determine the defect area of the coating.¹⁸ The coated metal was modeled as an equivalent circuit (Figure 6.43). Constant Phase Elements (CPEs) were used instead of ideal capacitors because of the tendency for coatings to behave somewhere between a pure capacitor and a pure resistor.¹⁹ $R(\text{soln})$ is the solution resistance, $R(\text{pore})$ and CPE2 are the pore resistance and coating capacitance respectively, and the R_{dl} and CPE1 are the resistance and capacitance of the solution double layer that forms at the solution/coating interface. Pore resistance is the electrical resistance of the pores in the coating.^{18, 20} As the size and defective nature of the pores increases, the resistance of the pores decreases.

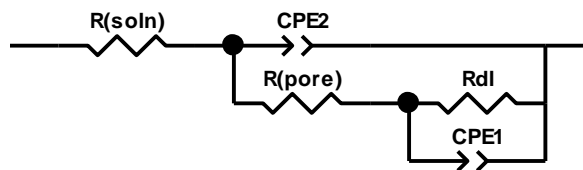


Figure 6.43. The equivalent circuit model for an organically coated metal. $R(\text{soln})$ is the solution resistance, $R(\text{pore})$ is the resistance of the pores in the coating, R_{dl} is the double layer resistance, $CPE2$ is the coating capacitance and $CPE1$ is the double layer capacitance.

Figure 6.44 shows the EIS results of a computer simulation of the circuit in Figure 6.43 with increasing pore area over time. From Figure 6.44, it can be seen that as the pore resistance of the coating decreases over time, the saddle frequency decreases as well. This indicates that the number, size, and defective nature of pores is increasing which corresponds to increase in the defect area of the coating.

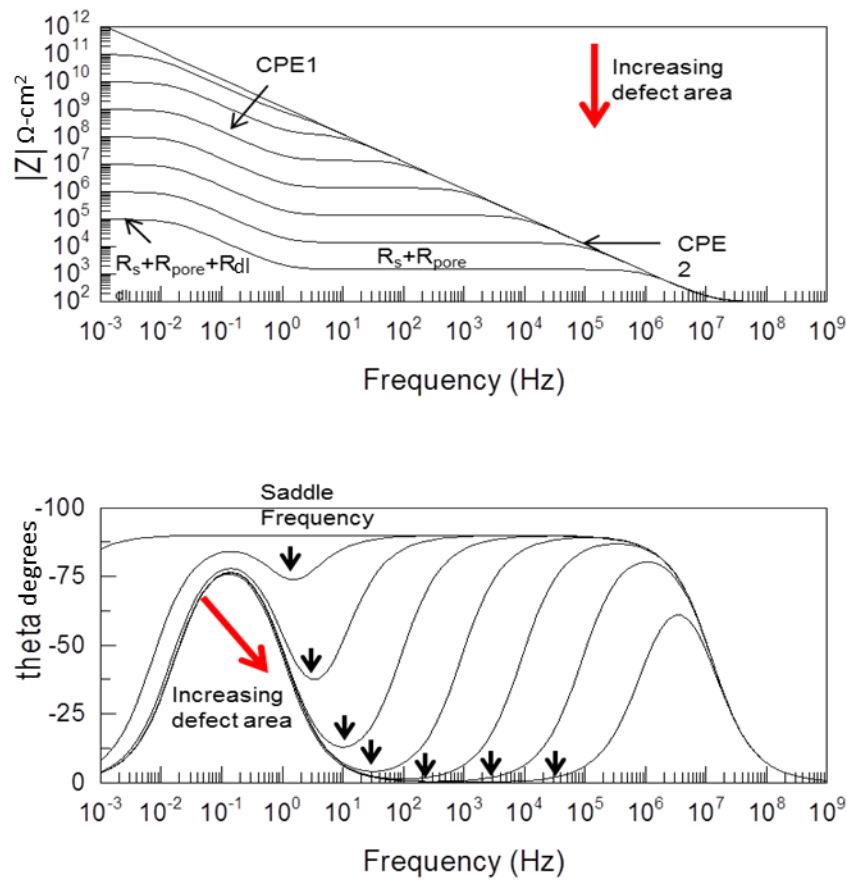


Figure 6.44. Example of the data that can be obtained from EIS. Saddle frequency decreases as R_{pore} decreases. For this simulation, R_s was $10 \Omega\text{-cm}^2$, R_{pore} varied from 10^{12} to $10^3 \Omega\text{-cm}^2$, R_{dl} varied from 10^8 to $10^4 \Omega\text{-cm}^2$, and the total area was 1 cm^2 .

From the phase angle plots (the lower plots on the EIS figures), the saddle frequency was determined. These data were graphed for LALT and field exposed samples and is presented in Figure 6.45. The change in saddle frequency over time shows an increase in pore area over time that is undetectable by visual methods. This data also enabled the calculation of acceleration factors by comparing the change in saddle frequency over time (Figure 6.45).

Acceleration factors were calculated by comparing the time to reach a saddle frequency of 10 kHz for LALTs to field sites. This was done for each field site with respect to each LALT used and the results can be seen in Table 6.7.

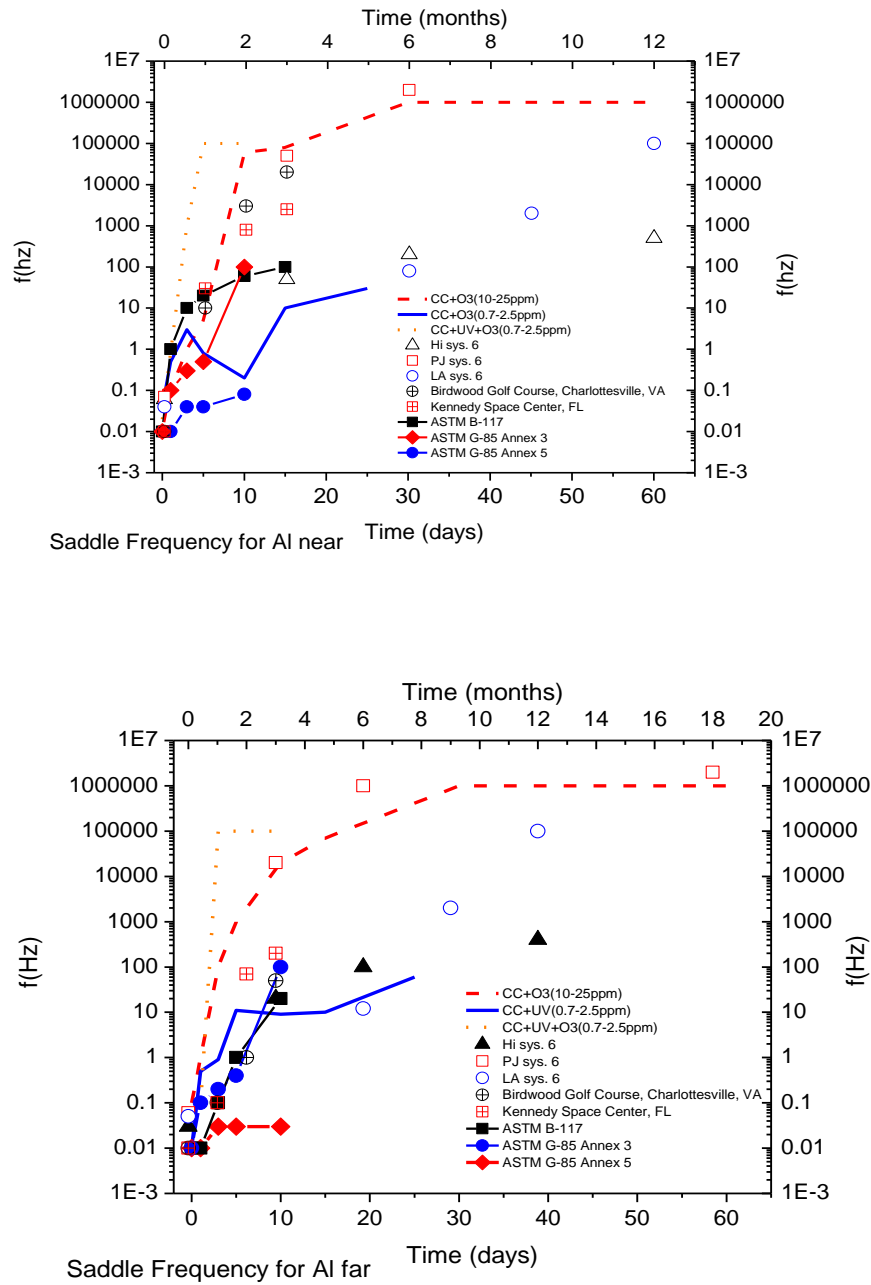


Figure 6.45. Saddle frequency plots for coated AA2024 exposed to various environments. The top plot is data taken from the Near location. The bottom plot is data taken from the Far location. Open symbols represent data for samples exposed at field sites; time is on the top axis for the field sites.

Table 6.7. Acceleration factors for AA2024-T351 based on saddle frequency.

Environment	AF wrt BRD	AF wrt KSC	AF wrt Hi	AF wrt LA	AF wrt PJ
CC+UV	6	5	16	10	3
CC+O3(10-25ppm)	18	15	29	30	7.83
CC+O3(0.7-2.5ppm)	9	7.5	24	15	4.5
CC+UV+O3(0.7-2.5ppm)	36	30	155	95	25
ASTM G-85 A3	6.4	5.36	17.14	10.7	3.21
ASTM G-85 A5	1	0.83	5.7	3.45	0.825
ASTM B-117	2.57	2.14	8	5	1.2
ASTM D-5894	12.8	10.7	34.2	21.4	6.4

By fitting the data from the samples to the equivalent circuit in Figure 6.43 using the parameters CPE1, CPE2, R_{pore} and R_{dl} , values for R_{pore} were calculated. The Z-view software package iteratively changes the parameters of the equivalent circuit until a fitting curve is found.¹⁹ An example of such a fit is given in Figure 6.46. R_{pore} values were determined which shows the specific degradation of the electrical resistance of the coating over time (Figure 6.47).

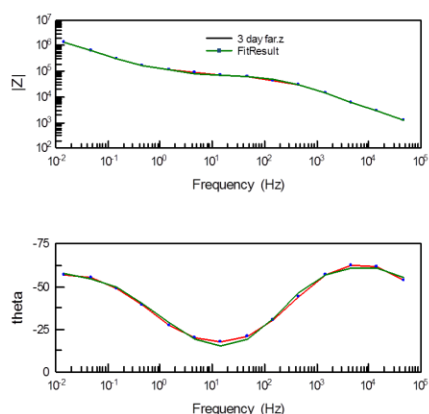


Figure 6.46. EIS data and equivalent circuit fit Eponol coated AA2024-T351 exposed to CC+O₃ (0.7-2.5 ppm) for 3 days. Data taken at the far location (see Figure 6.4).

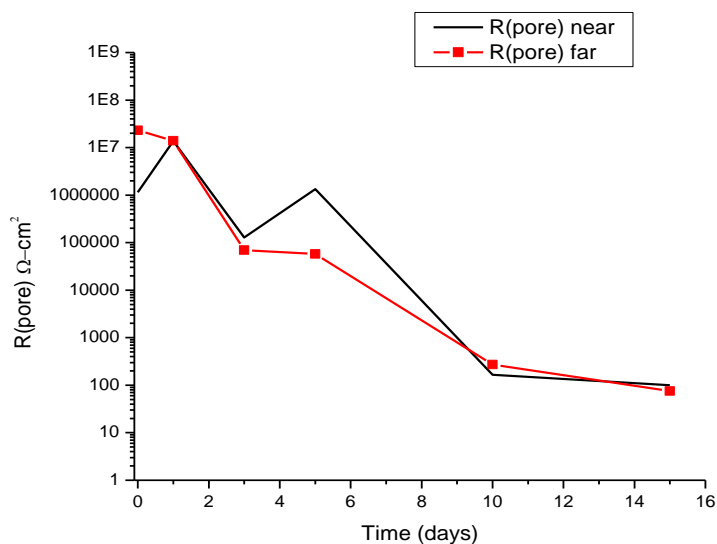


Figure 6.47. R_{pore} values for Eponol coated AA2024-T351 exposed in CC+O₃ (0.7-2.5 ppm). EIS scans were performed near and far from the scribe and then fit to an equivalent circuit to obtain R_{pore} .

It was shown previously that the breakpoint frequency method^{18,20} and data fitting can be used to obtain R_{pore} values for the coated AA2024-T351. With R_{pore} the defect area of the

coating can be calculated using Equation 6.5, where A_d is the defect area, ρ is the intrinsic resistivity of the coating (assumed to be $10^6 \Omega\text{-cm}$), and d is the thickness of the coating ($30 \mu\text{m}$). Graphing Equation 6.5 shows the relationship between pore resistance and defect area of the coating (Figure 6.48). Figure 6.48 also demonstrates the ability of EIS to detect changes in R_{pore} and thus, defect area long before the defect area becomes large enough to be visible to the naked eye.

$$A_d = \frac{\rho \cdot d}{R_{\text{pore}}} \quad 6.5$$

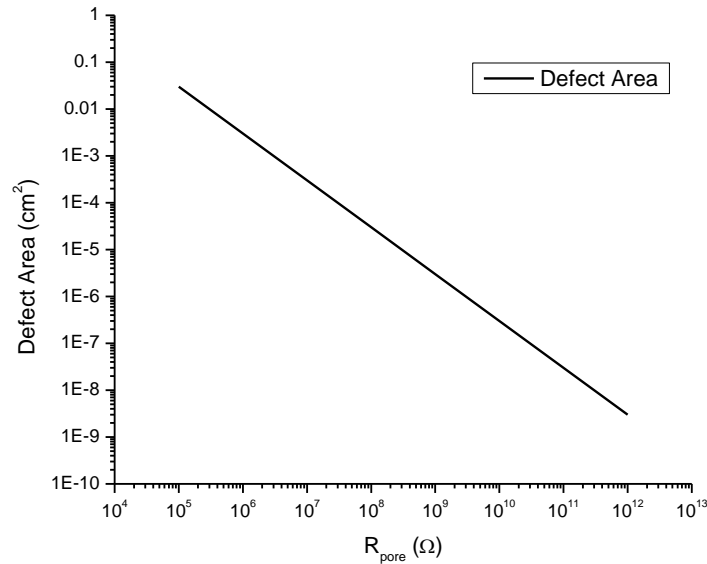


Figure 6.48. Graph of Equation 6.5 showing the increase in electrical defect area associated with the decrease of R_{pore} .

Additionally, the importance of saddle frequency can be seen in Figure 6.49. The relationship between saddle frequency and electrical defect area of the coating can be seen.

There are also two other parameters, f_{45} (low) and f_{45} (high), also called the lower and

higher breakpoint frequencies. These parameters are determined from the plot of Phase angle (the lower plot in Figure 6.44) where the curves cross a line drawn at -45 degrees. The lower breakpoint frequency (f_{45} (low)) is dependent on defect area for very small defects when f_{45} (high) cannot be resolved, while f_{45} (high) is always dependent on defect area and becomes resolvable as the defect area increases.¹⁸

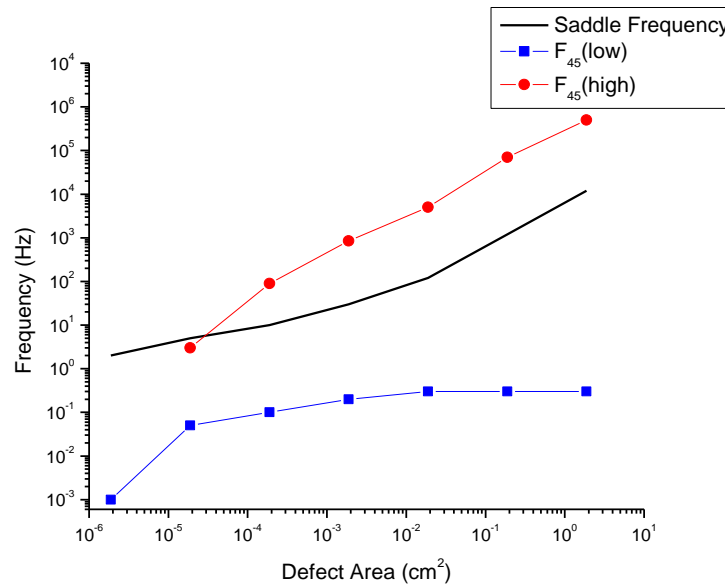


Figure 6.49. Plot of saddle frequency and high and low breakpoint frequency (f_{45}) for the model presented in Figure 6.44. The parameters are identical; R_s was 10 $\Omega\text{-cm}^2$, R_{pore} varied from 10^{12} to 10^3 $\Omega\text{-cm}^2$, R_{dl} varied from 10^8 to 10^4 $\Omega\text{-cm}^2$, and the area was 1 cm^2 .

6.5.4.2 Fourier Transform Infrared Spectroscopy Analysis

Fourier Transform Infrared Spectroscopy (FTIR) has been performed on 30 μm thick Eponol coatings on polypropylene substrates exposed to various standard LALTs and at various field sites. The polypropylene substrate is inert in these tests and thus has no effect on the degradation of the coating. The results, shown in Figure 6.50, show that there is no

degradation of the Eponol coating after 15 days of exposure in ASTM B-117 or ASTM G-85 Annex 5. Figure 6.51 shows ASTM B-117 and ASTM G-85 Annex 3, as well as two samples exposed at KSC for 2 and 5 months. There is a noticeable difference between the samples exposed at KSC and the other samples. In the KSC samples there is a decrease in intensity of the 2963 and 2920 cm^{-1} peaks, a new peak appears at 1717 cm^{-1} , the 3362 cm^{-1} peak broadens and a shoulder appears on the 1609 cm^{-1} peak.

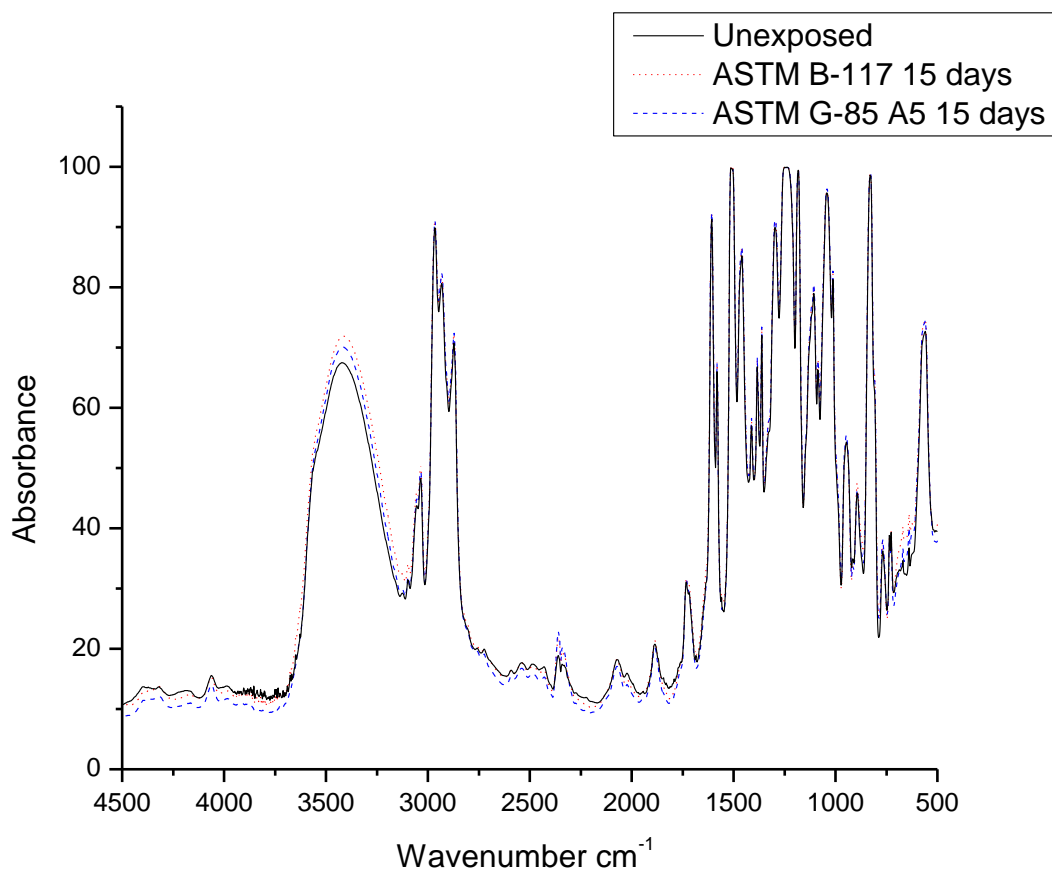


Figure 6.50. FTIR spectra of Eponol films exposed in ASTM B-117 and G-85 A5 for 15 days. Data taken at UVa.

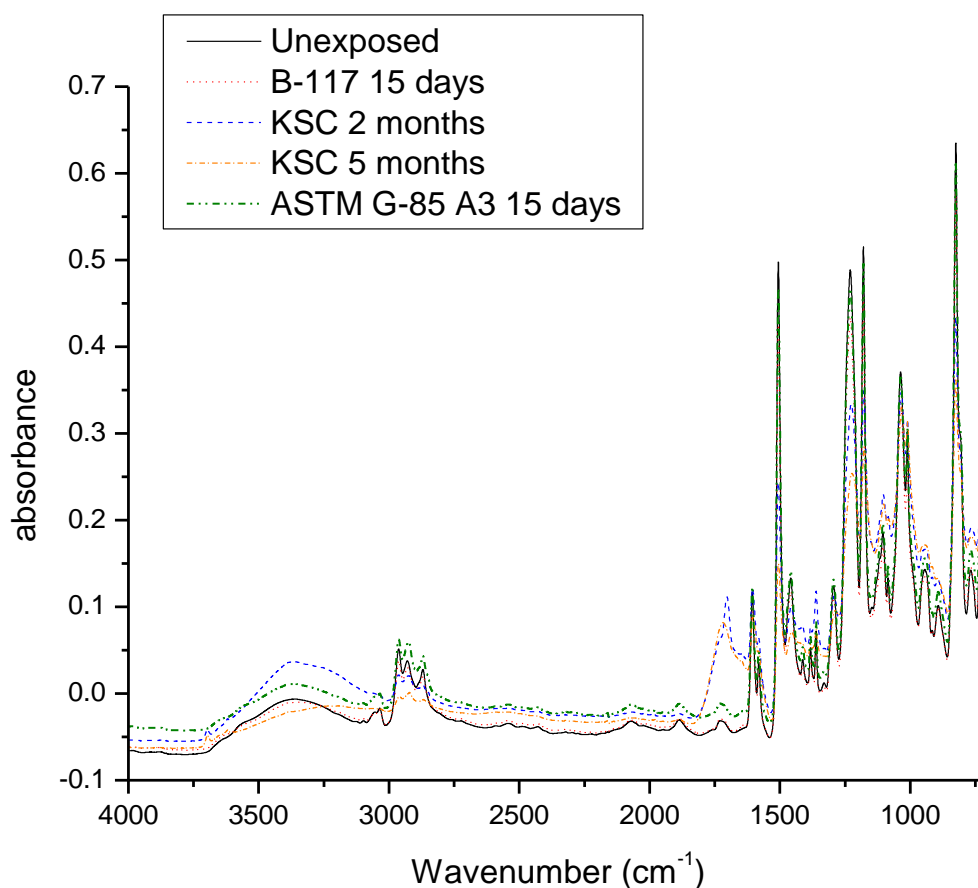


Figure 6.51. FTIR spectra of Eponol films exposed in various conditions. Data taken at USM.

6.5.4.3 Differential Scanning Calorimetry Analysis

USM has also performed Differential Scanning Calorimetry (DSC) and modified Differential Scanning Calorimetry (MDSC) on Eponol films exposed in various LALTs. DSC and MDSC measure the amount of heat required to increase the temperature of a sample. For polymers, it is used to measure the change in glass transition temperature (T_g), or the temperature at which the polymer changes from an amorphous solid to a crystalline solid.

The glass transition temperature is important because the properties of the polymer change as it moves from above the T_g to below. For example, above the transition temperature, polymers are amorphous and are generally more flexible and rubbery, while below the T_g they are crystalline and are generally more brittle.¹² Shorter polymer chains, limited crosslinking, and incorporation of plasticizers or residual solvent can lower the T_g , while longer chains, extensive crosslinking and large side groups raise the T_g .¹² Environmental factors can affect the T_g . For example, higher temperatures would cause more residual solvent to evaporate leading to higher T_g , while factors that break the crosslinking or the backbone of the chains themselves, like UV or ozone, would cause T_g to become lower.¹²

Table 6.8. DSC and MDSC results showing the glass transition temperature for eponol exposed to various conditions.

Sample	DSC			MDSC	
	T_g (°C)	Onset (°C)	Aging Peak Area (J/g)	T_g (°C)	Onset (°C)
Unexposed	72.63	69.16	117.7	62.41	55.76
ASTM B-117	73.33	69.58	96.22	60.19	58.56
ASTM D-4587	74.38	70.16	95.05	61.81	56.72
ASTM G-85 A3	71.28	66.78	72.64	57.26	52.57

6.5.4.4 Thermogravimetric Analysis

USM has also run Thermogravimetric Analysis (TGA) on samples exposed in ASTM B-117, G-85 A3 and ASTM D-4587 as well as unexposed samples. TGA involves heating the sample in a controlled setting and constantly measuring the changing weight. Continuous heating of the sample eventually drives off all organic material. It has been used to measure the amount of residual solvent and the amount of organic content in the polymer. The

remaining material is inorganic material. The data is shown in Table 6.9. The weight loss numbers in the table are total values i.e., for the ASTM G-85 A3, 76.3% of its weight after the residual solvent had been driven off was organic material and the remainder was non-organic. Generally, a higher amount of inorganic solids indicates that the coating was damaged and there was ingress of inorganic matter, such as salts. However, it is unclear at this time if the large amount of inorganic material remaining in the samples exposed to ASTM G-85 Annex is due to high levels of salts that were in the polymer itself, or if the acidic nature of the test altered the polymer structure in some way.

Table 6.9. TGA results on Eponol films showing the amounts of residual solvents, organic material and inorganic material.

Sample	Weight Loss (from RT to 300°C)	Weight Loss (from 300°C to complete degradation and loss of organic material)
ASTM D-4587	6.6%	85.9%
Unexposed	8.9%	94.9%
ASTM B-117	7.0%	90.3%
ASTM G-85 A3	6.8%	76.3%

6.6 **Discussion**

6.6.1 **Visual Analysis**

From the visual data presented earlier in this section, it can be seen that the ASTM G-85 Annex 5 and the ASTM D-5894 best match with KSC (Figure 6.5, Figure 6.9, and Figure 6.10). The ASTM B-117 and ASTM G-85 Annex 3 appear to match with KSC for short time

scales; but as time progresses scribe creep in the LALTs progress much more rapidly than is seen at KSC.

6.6.2 EIS Analysis

EIS data shows that ASTM B-117 and ASTM G-85 Annex 5 cause very little environmental damage to the coating itself (Figure 6.35 and Figure 6.37). KSC shows that most of the damage detected by EIS is coming from the field environment and is not due to scribe creep or the degradation of the substrate (Figure 6.33). This is most similar to the ASTM D-5894 (Figure 6.38), the ASTM G-85 Annex 3 (Figure 6.36) and the non-standard LALTs that contain UV and ozone (Figure 6.40, Figure 6.41, Figure 6.42).

6.6.3 Importance of UV

Table 6.7 demonstrates the importance of UV as part of an accurate LALT. The ASTM D-5894 has cycles consisting of one week in ASTM G-85 Annex 5 and one week in ASTM D-4857 (one week of four hours of UV exposure (340 nm) at 0.89W/m² at 60°C and four hours of CC at 50°C in the dark). The major difference between the G-85 Annex 5 and the ASTM D-5894 is that samples exposed in the ASTM D-5894 are exposed to UV light. As can be seen in Table 6.7, the addition of UV light increases the degradation of the coating roughly by a factor of five.

Figure 6.53 shows an example of damage that occurs when Eponol films are exposed to UV. The decrease in intensity of the 2963 and 2920 cm⁻¹ peaks show degradation of CH, CH₂, and CH₃ bonds in the coating.²¹⁻²⁵ The appearance and increase of a peak at 1717 cm⁻¹ is

caused by the formation of carbonyls and aldehydes which are products of degradation of the aliphatic carbon bonds in the coating.²¹⁻²⁵ UV irradiation breaks bonds and allows water to enter the polymer where damage has occurred. The broadening of the peak at 3362 cm^{-1} and the appearance of a shoulder at 1609 cm^{-1} indicate an increase in OH bonds.²¹⁻²⁵ This is due to the increase in water in the coating due to degradation caused by UV exposure.²² [ENREF 7 22](#)

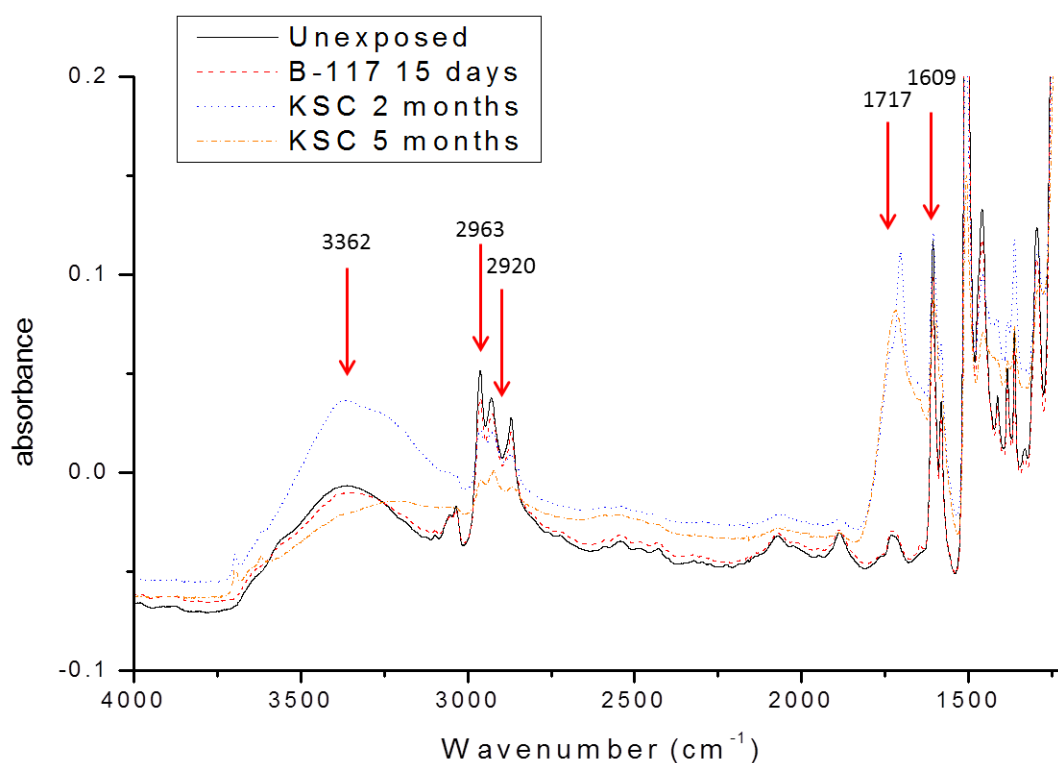


Figure 6.52. FTIR spectra of Eponol films on inert polypropylene substrates exposed in various conditions. Arrows indicate peaks that are expected to change with exposure to UV.

The DSC and MDSC data (Table 6.8) shows the changes in T_g that have occurred. Although the sample exposed to ASTM D-4587 was exposed to UV and would therefore be expected to

have the lowest T_g , the samples exposed to B-117 and G-85 A3 have lower T_g numbers. This is believed to be because the B-117 and G-85 A3 samples have more entrapped water that plasticizes the polymer. D-4587 may be showing the net effect on T_g from two opposite factors. The high temperature of the D-4587 (60°C) is continuing to drive off solvent from the film which increases T_g . However, the UV light degrades the polymer which lowers the T_g .

The TGA data (Table 6.9) shows that the unexposed samples have the least amount of inorganic remnants, as would be expected. ASTM G-85 A3 has the most non-organic remnants. However, the reason behind this remains unclear. It may be due to the sample accumulating more salts than the others during exposure, but why that would happen is not clear.

6.6.4 Role of Chloride

Comparing the visual images of KSC (Figure 6.5) to ASTM B-117 (Figure 6.7), it can be seen that the ASTM B-117 suffers from scribe creep to a larger extent than is seen for KSC. Noticeable scribe creep doesn't appear at KSC until 1 year of exposure. Except for the ASTM G-85 Annex 3, which is acidified and thus not a one to one comparison, not other LALT suffers from visually noticeable scribe creep. Chloride, then, plays a role in scribe creep. Its effect is most likely due to the damage to the substrate in the form of corrosion caused by the chloride leading to scribe creep. However, the noticeable differences in the scribe creep rates between KSC and ASTM B-117 suggest that the high level of chloride in the ASTM B-117 (5%) may be too severe and cause the scribe creep to dominate over other forms of corrosion. Scribe creep as the dominant form of corrosion is not what is seen in the field.

6.6.5 Analysis of Corrosion on Bare AA2024-T351

The SEM analysis of corrosion/pitting morphology on bare aluminum samples shows a distinct difference between LALTs and field exposures. LALTs with high ozone and UV exposures showed a high number of small pits evenly spaced across the surface of the samples, while field exposed samples showed relatively few but very large pits. This can be seen in both Table 6.5 and in Figure 6.53 below. Samples with low ozone and UV showed little pitting. UV is a major ESF that field samples are exposed to, but these results show that UV alone cannot be causing the difference in morphology seen between LALT and field exposed samples from the standpoint of corrosion. No samples were exposed in LALTs that had UV, cycling and chloride in a manner that mimicked the field exposures. The ASTM D-5894 does have a period of time in exposed to chloride and a period of time exposed to UV. However, the UV exposure comes before the chloride exposure. Also, due to the very harsh nature of the UV in the ASTM D-5894, the samples were only exposed to UV once during the course of testing. This leads to the conclusion that ESFs like chloride, cycling and UV may have confounding effects that cause the discrepancies between LALT and field exposed samples.

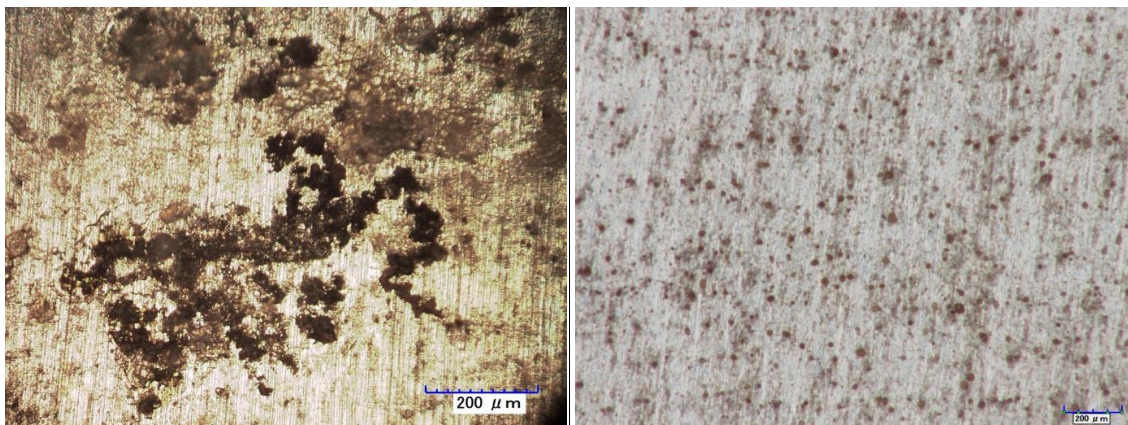


Figure 6.53. Optical images showing the comparison of pitting/corrosion morphology on bare AA2024-T351 exposed at KSC (left) and in CC+UV+O₃ (0.7-2.5 ppm) (right).

6.7 Conclusions

The ASTM D-5894 best matches the degradation of the coating and substrate seen in the field. Visually, it appears similar to KSC (Figure 6.5 and Figure 6.9). Additionally, EIS shows degradation of the coating both near to and away from the scribe that mimics what is seen in samples exposed in the field. However, ASTM B-117 does not mimic the field results for Eponol coated AA2024-T351 (Figure 6.7). The coating was not damaged in the ASTM B-117 in the same way that is was in field results due to a lack of ESF (like UV) that attacks the coating specifically. The ASTM B-117 has a high level of chloride such that in general the scribe is attacked more than is seen in the field while the coating is attacked less. Field exposures are naturally subjected daily wet/dry cycles, and standard and non-standard tests with cycling appeared to mimic the field better than the ASTM B-117 which has no cycling.

6.8 **References**

1. D.E. Little, 2006, ROLE(S) OF PRETREATMENT, INHIBITORS, AND OTHER PROCESS STEPS THAT EFFECT SURFACE COMPOSITION ON THE UNDER-PAINT CORROSION OF AN Al-Cu-Mg ALLOY 2024-T3. University of Virginia, Charlottesville.
2. A. Bautista, *Filiform corrosion in polymer-coated metals*. Progress in Organic Coatings, 1996. **28**(1): p. 49-58.
3. G. Grundmeier, W. Schmidt and M. Stratmann, *Corrosion protection by organic coatings: electrochemical mechanism and novel methods of investigation*. Electrochimica Acta, 2000. **45**(15-16): p. 2515-2533.
4. J.V. Kloet, W. Schmidt, A.W. Hassel and M. Stratmann, *The role of chromate in filiform corrosion inhibition*. Electrochimica Acta, 2004. **49**(9-10): p. 1675-1685.
5. C. Hahin and R.G. Buchheit, *Filiform Corrosion*, in *ASM Handbook - Corrosion: Fundamentals, Testing, and Protection*, S.D. Cramer and B.S. Covino Jr., Editors. 2003, ASM. p. 248.
6. R.T. Ruggeri and T.R. Beck, *An Analysis of Mass Transfer in Filiform Corrosion*. Vol. 39. 1983: NACE. 452-465.
7. D.A. Little, M.A. Jakab and J.R. Scully, *Effect of surface pretreatment on the underpaint corrosion of AA2024-T3 at various temperatures*. Corrosion, 2006. **62**(4): p. 300-315.
8. G.O. Ilevbare and J.R. Scully, *Mass-Transport-Limited Oxygen Reduction Reaction on AA2024-T3 and Selected Intermetallic Compounds in Chromate-Containing Solutions*. Corrosion, 2000. **55**(2): p. 134.
9. N. LeBozec and D. Thierry, *Influence of climatic factors in cyclic accelerated corrosion test towards the development of a reliable and repeatable accelerated corrosion test for the automotive industry*. Materials and Corrosion-Werkstoffe Und Korrosion, 2010. **61**(10): p. 845-851.
10. *MountainsMap*. 2005-2012, Digital Surf: Besancon, France.
11. W.S. Rasband, *ImageJ*. 1997-1212, U.S. National Institutes of Health: Bethesda, Maryland.
12. R. Overney, C. Buenviaje, R. Luginbühl and F. Dinelli, *Glass and Structural Transitions Measured at Polymer Surfaces on the Nanoscale*. Journal of Thermal Analysis and Calorimetry, 2000. **59**(1): p. 205-225.
13. Y. Wan, E. Neiser and R.G. Kelly, *Modification of ASTM Standard B117 Salt Spray Corrosion Test for Improved Correlation to Field Measurements*, in *DoD Corrosion Conference*. 2011: Palm Springs, Ca.
14. ASTM Standard B117 2007a, "Standard Practice for Operating Salt Spray (Fog) Apparatus," ASTM International, West Conshohocken, PA, 2007, DOI: 10.1520/B0117-11, www.astm.org
15. ASTM Standard G-85, 2011, "Standard Practice for Modified Salt Spray Testing," ASTM International, West Conshohocken, PA, 2002, DOI: 10.1520/G0085-11, www.astm.org
16. ASTM Standard D4587, 2011, "Standard Practice for Fluorescent UV-Condensation Exposures of Paint and Related Coatings," ASTM International, West Conshohocken, PA, 2011, DOI: 10.1520/D4587-11, www.astm.org
17. ASTM Standard D5894, 2001, "Standard Practice for Cyclic Salt Fog/UV Exposure of Painted Metal, (Alternating Exposures in a Fog/Dry Cabinet and a UV/Condensation

- Cabinet)," ASTM International, West Conshohocken, PA, 2010, DOI: 10.1520/D5894-10, www.astm.org
18. H.P. Hack and J.R. Scully, *Defect Area Determination of Organic Coated Steels in Seawater Using the Breakpoint Frequency Method*. Journal of the Electrochemical Society, 1991. **138**(1): p. 33-40.
 19. D. Johnson, Z-view. 1990-2012, Scribner Associates.
 20. F. Mansfeld and C.H. Tsai, *Determination of Coating Deterioration with Eis .1. Basic Relationships*. Corrosion, 1991. **47**(12): p. 958-963.
 21. P. Musto, G. Ragosta, M. Abbate and G. Scarinzi, *Photo-oxidation of high performance epoxy networks: Correlation between the molecular mechanisms of degradation and the viscoelastic and mechanical response*. Macromolecules, 2008. **41**(15): p. 5729-5743.
 22. C. Konecki, RE: UVa-Southern Miss ATR-FTIR 8-23-12.pptx. 2012.
 23. M. Diepens and P. Gijsman, *Photodegradation of bisphenol A polycarbonate*. Polymer Degradation and Stability, 2007. **92**(3): p. 397-406.
 24. N. Nagai, H. Okumura, T. Imai and I. Nishiyama, *Depth profile analysis of the photochemical degradation of polycarbonate by infrared spectroscopy*. Polymer Degradation and Stability, 2003. **81**(3): p. 491-496.
 25. A. Rivaton, B. Mailhot, J. Soulestin, H. Varghese and J.L. Gardette, *Comparison of the photochemical and thermal degradation of bisphenol-A polycarbonate and trimethylcyclohexane-polycarbonate*. Polymer Degradation and Stability, 2002. **75**(1): p. 17-33.